ABSTRACT

Title of dissertation:	FROM TANTRUMS TO TRANSFORMATIONS: AGN TRANSIENTS DISCOVERED WITH ZTF
	Sara Evalyn Frederick Doctor of Philosophy, 2021
Dissertation directed by:	Dr. Suvi Gezari Space Telescope Science Institute, Maryland

This dissertation work has consisted of searches for extreme AGN-related outbursts during Phase I of the Zwicky Transient Facility (ZTF) survey, which has been a ground-breaking wide-field instrument for the real-time detection and regular cadence monitoring of transients in the Northern Sky. Transients found to be nuclear through photometric filtering were vetted by humans and coordinated for prompt follow-up with various rapid robotic, spectroscopic, and high energy resources, to understand the nature of the galaxy centers undergoing flares and the appearance of spectral features. Findings from this unprecedentedly high-volume data stream were often serendipitous, and led to surprising new avenues for study, including 1) the establishment of a new observational class of quiescent galaxies caught turning into quasars, 2) the discovery of a preponderance of smooth and high-amplitude optical transients hosted in NLSy1s, and 3) a framework for distinguishing extreme AGN variability from other transients in AGN. We present the results of these observations, including candidates for TDEs in AGN, changing-look

AGN caught "turning-on", as well as members of the new emerging observational class of flares in Narrow-Line Seyfert 1 (NLSy1) galaxies associated with enhanced accretion (Trakhtenbrot et al. 2019). We compared the properties of these samples of flares to previously reported changing-look quasars and Seyfert galaxies, confirmed that they are a unique observational class of transients related to physical processes associated with the central supermassive black hole's accretion state, and considered the observations in the context of the physical interpretations for a range of related transients from the literature. With these unique sample sets, we also aim to understand why we have found certain galaxy types to preferentially host the sites of such rapid enhanced flaring activity, and attempt to map out the innermost environment of the accretion events. These pathfinding studies enabled with ZTF have the potential to guide how these exceptional moments of AGN evolution will be systematically discovered in future large area surveys such as the Vera C. Rubin Observatory.

FROM TANTRUMS TO TRANSFORMATIONS:
AGN Transients
Discovered with
the Zwicky Transient Facility

by

Sara Evalyn Frederick

Dissertation submitted to the Faculty of the Graduate School of the
University of Maryland, College Park in partial fulfillment
of the requirements for the degree of
Doctor of Philosophy
2021

Advisory Committee:
Professor Suvi Gezari, Chair and Research Advisor
Professor Richard Mushotzky
Professor Sylvain Veilleux
Dr. Stephanie LaMassa
Professor Kara Hoffman, Dean's Representative

© Copyright by
Sara Evalyn Frederick
2021

Preface

A portion of this dissertation was previously published as first-author peer-reviewed journal articles and presented at professional conferences and collaboration meetings, with contributions from co-authors, builders, and members of the Black Holes Science Working Group of the ZTF collaboration who made this work possible, including (but not limited to) Matthew Graham, Shri Kulkarni, Dan Stern, Sjoert van Velzen, Jesper Sollerman, Daniel Perley, Tiara Hung, Charlotte Ward, and many others.

In order of publication:

Chapter 2 has been published in the Astrophysical Journal, Volume 883, Issue 1 as “A New Class of Changing-Look LINERS.”

Chapter 3 has been accepted for publication in the Astrophysical Journal as “A Family Tree of Optical Transients in Narrow-line Seyfert 1 Galaxies”.

Preliminary results of Chapter 4 have been presented at the Joint Space-Science Institute (JSI[1]) Fall 2019 Meeting in Annapolis, Maryland, the Spring 2020 ZTF Virtual Collaboration Meeting hosted by Humboldt-Universität zu Berlin, and the Winter 2021 237th “Virtually Anywhere” American Astronomical Society Meeting. It will be submitted for publication in the Astrophysical Journal in the Fall of 2021.

[1]https://jsi.astro.umd.edu/

Dedication

To my loving and proud parents, to my grandparents for modeling meaningful life-long hard work in pursuit of scholarship, and to scholars-in-training who aspire to pave divergent paths while lifting others as you climb: You are our universe's past and future ancestors, and this science is for you.

Acknowledgments

The recipe for my success included countless benefactors and support structures sometimes but not always baked into the systems and institutions I navigated. Thank you so much, to all of you, for seeing something in my journey worth attending to as I figured out my path.

My parents Maria Pineda and Steve Frederick for believing in me, for the care packages, for editing my draft text, and for supporting my academic journey even when it kept us apart. And to my extended family, especially my grandparents Julio and Elia Pineda and Harold and Thelma Frederick, for my mind, storytelling skills, culture, bloodline, and your unconditional pride (even calling me *"Doctora"* before I had the papers signed). Even from a distance, you cured me when I needed family, community, and love.

My various formal and informal advisors, especially Suvi Gezari, Erin Kara, Stephen Privitera, and Sjoert van Velzen, for positive examples, for your patience and guidance, as well as professional networking and development resources. I can't thank you enough for your time, skills, code, enthusiasm, advice, and persistent attention. To the physicists like me I could look up to, the LUMA and MITES programs and especially Prof. Peter Gonthier, for taking a chance on the one external student who applied to your research program, for taking me under your wing and making me feel like I belonged in your home, your lab, at NASA Goddard, and in the field of astrophysics. And to the ZTF collaboration team, especially Thomas Kupfer, Umma Rebbapragada, Matthew Graham, Shri Kulkarni, and Roger Smith,

for facilitating training, funding, experiences, and friendships that made me a better, more confident, and connected scientist.

All the supportive, curative counter-spaces I stumbled into, including but not limited to MICA, LASC, MBSA, PAARC, CMRS, the now dismantled MD Food Co-op, and to the navigators who welcomed me graciously into these spaces, especially to Lisa Warren, Ghonva Ghauri, Dorothy Kou, Dr. Naliyah Kaya and for the many discussions on identity, indigeneity, art, social justice, academia, and activism that sustained and nourished me throughout my time on the UMD campus.

To all the change leaders I had the honor to overlap with within the Maryland Astronomy Department, who strove every day to prioritize the success of every scientist, including but certainly not limited to Amy Steele, Laura Blecha, Alice Olmstead, Katie Jameson, Ashley Wilkins, Stuart Vogel, Barbara Hansborough, Derek Richardson, Krista Smith, Brian Morsony, Taro Shimizu, and many, many more. My personal and professional growth was directly related to actions you had the vision to prioritize, personal privileges you fought to dismantle, examples and norms you set, and doors you opened so I could walk through. I saw and benefited from your efforts, and it was truly an honor to look up to you all as role models in the educational, social justice, and research spaces in which we co-existed. Thank you for being gracious friends, as well as my role models and career mentors. Additionally, to the business and administrative staff at the University of Maryland for your patience with and kindness toward me, and for upholding and improving the department, college, and university through your vital work, especially Dorinda Kimbrall, Natalie Rowe, Susan Lehr, John Cullinan, and Adrienne Newman.

All the unofficial host families who took me in, stored my belongings, shared hand-me-down housewares and life advice, invited me to hot meals and religious services on holidays, and made sure I never went hungry or lonely in between, especially the Fosters, the Louies, the Ritonias, and the Gershteyns. Thank you for welcoming me into your lives, and making my time away from home much more enjoyable.

My tabletop gaming families, especially game runners Elece Smith, Zak Glennon, Teal, and Joe DeMartini: for hosting inclusive campaigns and for the long nights we collectively clung to normalcy during the Covid-19 pandemic.

Pooja Suresh for being a sister I never had, for lending me Physics GRE study materials and passing along advice from your PhD-educated Dad, and for giving me a brilliant physicist to look up to and to talk through milestones for hours as we went on this grad school journey together. Where would I be without you?

Finally, acknowledgements would not be complete without expressing gratitude to the sanitation and maintenance staff in my various workplaces for enabling this work, and last but certainly not least to the original stewards of the various dispossessed locations which I occupied while completing this dissertation, for preserving and defending these places for generations, including but not limited to the Maya, Sami, Gaels, Cheyenne, Oglala Sioux, Arapaho, Piscatawey, Pamunkey, Hopi, Pueblo, Apache, Duwamish, Tongva, Carib, and Taino people of the contemporary and ancestral land now called Honduras, Sweden, Scotland, and the United States of (Northern) America, also known as Turtle Island, in states and territories including land that is known as Nebraska, Maryland, Washington D.C., Arizona, Washington,

California, and the Virgin Islands.[2]

Thank you all.

[2] https://native-land.ca/

Table of Contents

List of Tables

List of Figures

List of Abbreviations

AGN	Active Galactic Nucleus
BH	Black Hole
BOSS	Baryon Oscillation Spectroscopic Survey
CLAGN	Changing-look AGN
CL-LINER	Changing-look LINER
DESI	Dark Energy Spectroscopic Instrument
DRW	Damped Random Walk
FPM	Focal Plane Module
HST	Hubble Space Telescope
IR	Infrared
LIER	Low-ionization Emission Line Region
LINER	Low-ionization Nuclear Emission Line Region
MIR	Mid-infrared
MSIP	Mid-Scale Innovations Program
NASA	National Aeronautics and Space Administration
NLSy1	Narrow-Line Seyfert 1 Galaxy
NuSTAR	Nuclear Spectroscopic Telescope Array
P48	Palomar Oschin 48-inch Schmidt Telescope
P60	Palomar 60-inch SED Machine
SDSS	Sloan Digital Sky Survey
SMBH	Supermassive Black Hole
SN	Supernova
SPIDERS	SPectroscopic IDentfication of ERosita Sources
Sy	Seyfert galaxy type
TDSS	Time-Domain Spectroscopic Survey
TESS	Transiting Exoplanet Survey Satellite
TNS	Transient Name Server
ToO	Target of Opportunity
UV	Ultra-violet
XMM	X-ray Multi-Mirror Mission

Table 1: Abbreviations Used In This Thesis

For more abbreviations related to software and facilities, see Appendix A.

Chapter 1: Introduction

1.1 Introduction to Supermassive Black Holes (SMBHs) and Active Galactic Nuclei (AGN)

Black holes (BHs) are mathematically a singularity in space-time, and astrophysically the runaway gravitational collapse of dense remnants of the explosive end states of massive stars tens to hundreds of times the mass of the sun. The scaled-up counterparts to these stellar mass black hole systems are supermassive black holes (SMBHs), which are typically millions to billions of times Solar. These black holes have more mysterious origins for growth to these sizes, yet are found to comprise the centers of nearly all moderate to large sized galaxies — some with companion SMBHs, and others largely dormant in the current era / nearby universe (for example the BH located at the Milky Way's galactic center, Sagittarius A*). Stellar mass black holes actively accreting[1] from supergiant stellar companions as persistent sources of high-energy radiation, so-called X-ray binaries, have supermassive counterparts in the form of active galactic nuclei (AGN), which occupy roughly 10% of galaxies. The AGN engine is thought to be driven by accretion of a reservoir of primarily gaseous ionized material gravitationally drawn from the surrounding host galaxy into a disk around the central SMBH.

[1] Accretion refers to the accruing of matter through gravitational force leading to the black hole's growth.

1.1.1 Anatomy of an AGN

The accretion onto the central SMBH taking place in AGN is the most efficient natural conversion of mass to energy known. AGN are also the most luminous persistent sources of electromagnetic radiation in the observable universe, spanning wavebands from gamma-rays to radio. Among the most massive types of AGN systems ($\gtrsim 10^8 M_\odot$), quasars (historically shortened from "quasi-stellar objects"[2]) can reach luminosities[3] of 10^{47} erg s^{-1}. These outshine the combined light from all the tens of billions of stars occupying their host galaxies. Over the lifetime of the quasar, this output can surpass the gravitational binding energy of the galaxy by two orders of magnitude (Silk & Rees, 1998).

AGN produce radiation at all wavelengths, representing many diverse energetic processes: from gamma rays due to annihilation of near-relativistic energetic particles near the event horizon, to UV/optical photons from viscous heating of the infalling material, to X-rays as a result of magnetically confined plasma, to synchrotron radiation produced by jets launched as a result of strongly wound magnetic field lines coupled to the black hole spin. Section 1.2.1 discusses in detail the classification scheme for AGN types based on observed radiation. This dissertation focuses mainly on optically-selected, radio-quiet, UV- and X-ray-bright sources, and therefore this section focuses on the primary source of that emission — the complex structures formed by the accretion flow. Information about these components is partially derived from intensive studies across many wavelengths of stellar mass black hole systems, which accrete from nearby giant stars rather than a reservoir of gas in a host galaxy's center, and therefore provide a solid theoretical basis upon which to build this work (see e.g. Ruan et al. 2019a, Figure 1.1). However, ways in which this scaling by mass can break down are discussed further in Section 1.2.

[2]QSOs, or quasi-stellar objects, are named due to their brightness in visible wavelengths being historically confounded with stellar sources despite being millions of times more distant.

[3]Luminosity refers to the intrinsic rate of energy release due to radiation of a source.

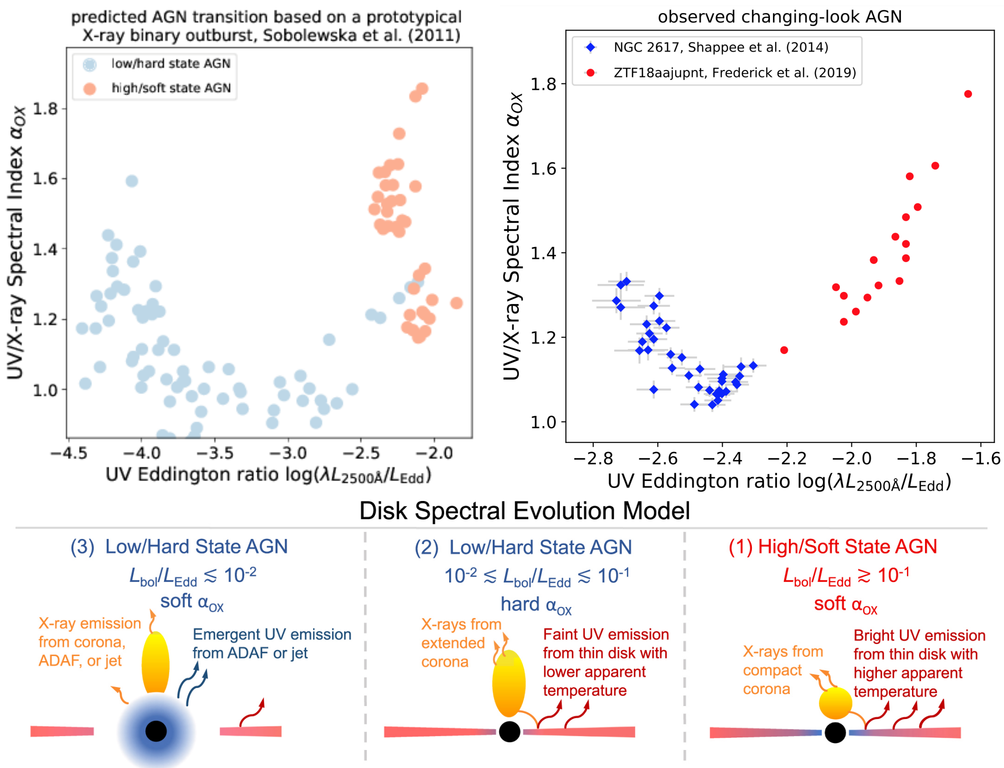

Figure 1.1: Upper panels: An example of how the accretion behavior of an SMBH in an AGN system may be described by that of an X-ray binary. Figures from Ruan et al. (2019a,b) show the predicted α_{OX} (ratio of UV and X-ray flux densities) and Eddington ratio (accretion rate parameter) evolution in AGN analogous to an X-ray binary outburst (upper left). Comparison to changing-look AGN (including a changing-look LINER presented in Chapter 2) appears to show it following the shape of the XRB outburst evolution through this parameter space (upper right). Lower panel: Diagram of accretion onto a black hole. One such interpretation of the Ruan et al. (2019b) result is based on a scaled model of the spectral evolutionary sequence through accretion states defined by luminosity and Eddington rate. Components such as the X-ray emitting corona and the UV emitting disk are described in the following Section.

As particles sink toward the black hole gravitational well following general relativistically curved trajectories along space-time, they flatten on average due to momentum conservation into a disk-like structure known as the accretion disk. The matter approaching the event horizon — the so-called "point of no return" — of the black hole is high temperature ($T \sim 10^4$ K), viscous and turbulent, and threaded by strong magnetic field lines. As such, it is an ideal and sensitive laboratory for physics in extreme regimes of gravity and temperature far beyond what can be achieved on Earth.

Observables from AGN can be decomposed into a number of interrelated components, relevant at differing energies, centered on a supermassive black hole surrounded by hot plasma and a radiatively-efficient geometrically thin and optically thick accretion disk emitting primarily in the optical-UV (Malkan, 1983). We review a subset of relevant components in the following sections.

1.1.1.1 The X-ray Emitting Corona

A tenuous component called the corona emits X-rays from above and below the innermost accretion flow, and may result from the confluence of plasma flowing along magnetic field lines threading the disk (Galeev et al., 1979; Merloni & Fabian, 2001). Again, this dissertation focuses on modes of accretion in radio-quiet systems, although some AGN may display evidence for disk winds in addition to radio and gamma ray emitting synchrotron powered jets. These are powered by the Blandford-Znajek mechanism, which magnetically extracts angular momentum from the spanning black hole and converts its rotational energy to electromagnetic power (Blandford & Znajek, 1977), and thought in some models to be connected to the corona as the base of a weak or failed jet (e.g. Wilkins et al. 2015). The exact geometry of the corona has not yet been unambiguously measured for any system. In the lamp-post geometry, the X-ray emitting region is approximated as a point source above a thin disk and along the axis of azimuthal symmetry. This model is not as physical as those accounting for the emissivity structure of a geometrically extended corona, but has been shown to describe observed accretion disk irradiation profiles well, so this is what is often assumed. This hot component is required based on the temperature of the disk (assuming it is emitting as a blackbody) being too cold to explain observed X-ray emission from its vicinity (Ghisellini, 2013). Observed X-ray energies ($\sim$ 100 keV) indicate thermal temperatures of the system of $T \geq 10^7$ K. The intrinsic X-ray emission from the corona has a spectrum in the form of a power law.

1.1.1.2 The Soft X-ray Excess

Primarily in high-mass-accretion-rate AGN, a soft-X-ray excess in flux below $\sim$1-2.5 keV is observed to deviate from the power law continuum at varying strengths, depending somewhat on the level of absorption affecting the observation (Arnaud et al., 1985; Singh et al., 1985; Turner & Pounds, 1989).

This "soft excess" can be modeled physically as a reflection component made up of emission lines from the inner ionized disk which have been relativistically broadened beyond identification (Crummy et al., 2006; Gierliński & Done, 2004), an inner Compton upscattering region of the disk powered by the accretion flow (Done et al., 2012), or an additional power law component due to the launching of a jet (Chatterjee et al., 2009; Kataoka et al., 2007) or a number of other diverse ideas that have been proposed; however, its origin remains largely mysterious and best-fit models are largely degenerate (Lohfink et al. (2012); Page et al. (2004).

1.1.1.3 Gas Clouds and Obscuring Structures in AGN

The AGN systems display spectroscopic evidence for additional cloud-like nuclear structures in the infrared (IR), optical and X-rays called the broad line emitting region (BLR)[4], the narrow line region (NLR), and the clumpy, dusty molecular torus encircling the accretion flow, the radius of which is set by the sublimation temperature of the dust. These components are all discussed further in Section 1.2.1. A subset of AGN displaying broad lines show double-peaked profiles, which can be interpreted in the context of either a Keplerian disk model (e.g. Eracleous & Halpern 2003), or a dual AGN scenario in rare instances that they cannot be explained as a result of typical disk dynamics (e.g. Véron-Cetty & Véron 2000.) Obscuration by gas and dust along the line of sight to the accretion flow in the form of outflowing winds also affect AGN spectra in complex ways that present a challenge to disentangle and interpret. For these structures spanning large ranges in mass and intrinsic physical separation, time resolution is much higher than spatial resolution. Therefore, time-domain investigations such as those laid out here are crucial for a complete understanding of AGN phenomena.

1.1.2 AGN Variability

High energy radiation from the innermost regions of AGN can show variability on timescales down to minutes and even seconds. Decades long observation campaigns of well-studied, relatively nearby AGN have shown that the optical variability caused by the chaotic accretion process can be modeled well by a damped random walk (DRW; e.g. Kelly et al. 2009). Most rapid[5] variability will occur on the orbital timescale (a.k.a. the dynamical time scale), where r_S is the Schwarzschild radius or $r_S = \frac{2GM_{\rm BH}}{c^2}$

$$t_{orb} = \frac{2\pi R}{v_\phi} = 2\pi\sqrt{\frac{R^3}{GM}} = 1.1\ \mathrm{days}(\frac{\mathrm{M_{BH}}}{10^8\mathrm{M_\odot}})(\frac{\mathrm{R}}{100\ \mathrm{r_S}})^{3/2} \tag{1.1}$$

[4]This refers to the nuclear region producing broad hydrogen Balmer series emission lines observed in optical spectra of AGN.

[5]In this case, the term "rapid" for AGN is relative and refers to phenomena that is observable on human timescales.

[6] or the light-crossing time, although propagating fluctuations, accretion disk instabilities, and variable obscuration can also contribute (see discussion in Section 1.2.4 of this Chapter).

Accreting stellar mass black hole systems are observed to display variability in both brightness and spectral slopes on predictable cycles related to drastic changes in accretion states lasting tens of days (populating the so-called "turtle head" diagram). Scaling viscous timescales[7] simply from such systems, we may expect to observe more extreme forms of variability from AGN related to changes in accretion states on the order of thousands to hundreds of thousands of years (Lawrence, 2018; Siemiginowska et al., 1996).

1.2 Changing-look AGN: A Unique Challenge to AGN Theory

1.2.1 The AGN Unification Scheme and Select Host Galaxy Types

Broad and narrow line regions of AGN are named as such due to the observations of widths of Hydrogen features observed in spectra of the regions probed by these components, thought to be clouds of gaseous material. Type 1 and 2 AGN are classified according to the presence or absence of these lines, thought to be signatures of velocity broadening due to proximity of the clouds to the strong gravity near the central SMBH. A FWHM of 2000 km s^{-1} is usually quoted as the boundary for defining Type 1 vs. Type 2 AGN.

Antonucci (1993) presented a unification scheme (see Figure 1.2) following observations of type 2 AGN in polarized light which showed their spectra looked much like that of type 1 AGN. From this evidence, it was established that the

[6] This timescale is only accurate many gravitational radii ($r_G = \frac{GM}{c^2}$) from the black hole, before general relativistic effects become important.

[7] The viscous timescale is the time required to diffuse momentum via thermal collisions of gas particles in a hot medium, $t_{\rm visc} = 10^7$ seconds $\alpha^{-1}(\mathrm{r}/10\mathrm{h_d})^2(\mathrm{R}/3\mathrm{r_S})^{3/2}(\mathrm{M_{BH}}/10^8\mathrm{M_\odot})$, where h_d is the disk thickness.

view along the line of sight to the observer was the source of the discrepancy, that narrow line AGN were obscured by the torus and broad line AGN were being viewed closer in to the central SMBH (Rowan-Robinson, 1977; Sheng et al., 2017; Urry & Padovani, 1995). Therefore, for many decades, Seyfert Type 2 galaxies were thought to be obscured due to being observed at high inclination angles to the torus.

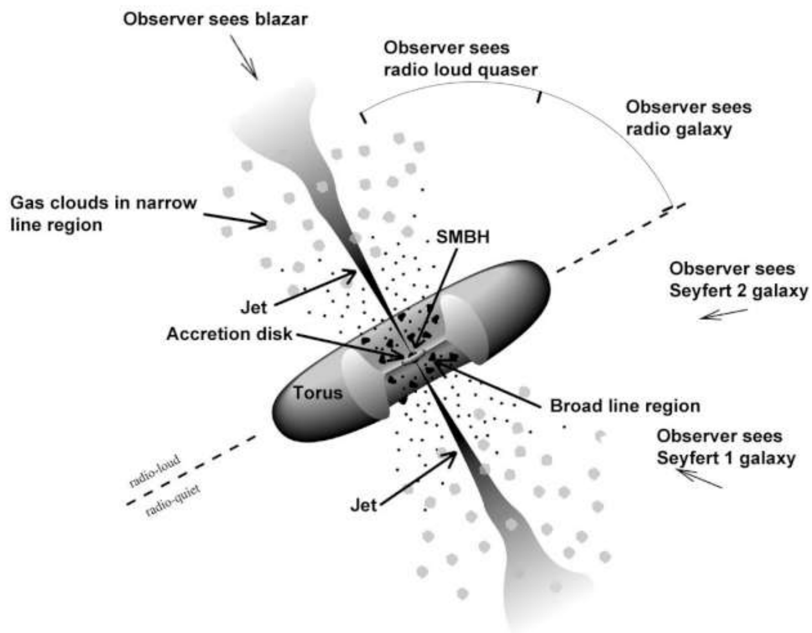

Figure 1.2: The unification model of AGN, adapted from Urry & Padovani (1995), is based on orientation to the line of sight to the observer as well as by the presence or absence of components such as a radio-loud jet.[9]

Under this unification model, the diverse zoo of AGN observational classes: Quasars, QSOs, Seyfert galaxies, BL Lac objects, blazars, can all be described by the same unified model: that all AGN are powered by the same mechanism with differences in the vantage point to the observer of the various physical components contributing persistent emission across the electromagnetic spectrum comprising

[9]Figure hosted at `https://fermi.gsfc.nasa.gov/science/eteu/agn/figure1.jpg`.

the accretion flow (e.g. gas, dust) and/or a jet (e.g. plasma, magnetic fields). See Section 1.1.1 for more details about these components.

In the following sections we focus on introducing the host galaxy types most relevant for the work laid out in this thesis.

1.2.2 Intermediate AGN Type Classifications

Many AGN spectra do not fall neatly into either a type 1 or type 2 subclass. Therefore, the presence or absence of broad components in the highest order Balmer emission lines in the series, Hα and Hβ, defines a number of intermediate type designations between broad (1) and narrow (2). Osterbrock (1981) specified the difference between Seyfert 1.5, 1.8 and 1.9 as follows:

- Type 1.9 — only a broad component in the Hα line, narrow higher order Balmer lines.
- Type 1.8 — broad component in the Hα line, a relatively weak broad component in Hβ.
- Type 1.5 — strength of broad components are comparable between Hα and Hβ.

Winkler (1992) expanded upon this scheme to quantitatively distinguish the subtypes based on the flux ratio of Hβ to [O III]λ5007, with cutoff classes at 0.33, 2.0 and 5.0 (including Type 1.2). At times these intermediate labels have also classified non-Seyfert objects such as low ionization nuclear emission line region galaxies (LINERs) based on the appearance of weak emission lines in their stellar dominated optical spectra (see Section 1.2.4 for a full description of this class).

1.2.3 Narrow Line Seyfert 1 Galaxies

Narrow-line Seyfert 1 type galaxies (or NLSy1s), are a separate class of highly X-ray variable AGN with observed Balmer line widths approximately intermediate between 1000 and 2000 km s^{-1} (Goodrich, 1989). They therefore have derived virial black hole mass ($M_{\rm BH,vir}$) estimates (Shen et al., 2011) systematically smaller than that of normal Seyfert type 1 AGN,

$$M_{\rm BH,vir} = 1.5 \times 10^5 \left(\frac{R_{\rm BLR}}{\text{light days}}\right) \left(\frac{\text{FWHM(H}\beta)}{10^3\text{kms}^{-1}}\right)^2 M_\odot$$

where $R_{\rm BLR} = 32.9(\frac{\lambda L_{5100A}}{10^{44}\text{ergs}^{-1}})^{0.7}$ light days and L_{5100A} is the luminosity density at 5100 Å (Kaspi et al., 2000).

Although multiwavelength evidence points to NLSy1s accreting close to the Eddington limit[10] (e.g. Xu et al. 2012, Netzer & Trakhtenbrot 2007 and references therein), the virial black hole mass based on Hβ measurements from which this property has partially been derived has been posited to be due to an inclination effect by Rakshit et al. (2017) (see Section 2.3.3 for further discussion and explanations). NLSy1s often display relatively prominent Fe II complexes in their optical spectra (Osterbrock & Pogge, 1985; Rakshit et al., 2017), which, when explained by an increased covering factor of the BLR (Véron-Cetty & Véron, 2000), is in agreement with the high accretion rate interpretation along the axes of the eigenvector relation classification scheme for AGN that also depends upon orientation (e.g. Shen & Ho 2014).

NLSy1s are often more variable in the X-rays than the optical. However, during the ASASSN survey, Trakhtenbrot et al. (2019a) reported on a nuclear optical transient with persistent UV-bright emission in a NLSy1 host galaxy and associated it with two other similar events in the literature. The multiwavelength properties

[10] The Eddington limit is the accretion rate at which the radiation force emitted from the accreting body balances the gravitational force on the accreted matter.

of this transient did not fit within the framework of previously known transient phenomena that are unrelated to AGN variability such as a tidal disruption event (TDE) or supernova (SN), and was instead interpreted as an dramatic enhancement in accretion rate in a pre-existing AGN. Kankare et al. (2017) had previously reported on a similar population of flaring events occurring within NLSy1 galaxies. In Chapter 3 we report several more of these events occurring in known and candidate NLSy1s discovered by ZTF.

1.2.4 The Heterogeneous Population of Low Ionization Nuclear Emission Line Regions (LINERs)

The optical spectra of star forming galaxies with strong Balmer lines and low ionization spectral features can often be confused for narrow-line AGN. The Baldwin, Phillips & Terlevich, or BPT, diagram (Baldwin et al. 1981, Figure 1.3) helps to distinguish these along with a third galaxy type: LINERs, or low ionization nuclear emission line regions.

LINERs, as their name implies, display narrow low excitation emission lines, as well as a weak nonthermal continuum. We show an example LINER host galaxy SDSS spectrum compared with a quasar spectrum in Figure 1.5. Some UV, X-ray, and radio studies showing compact and variable emission may indicate a low luminosity AGN underlying the stellar continuum (e.g. Maoz 2007). They are the largest local AGN subpopulation, representing nearly 30% of all nearby galaxies (Heckman, 1980).

A separate class of "LIERs" have emerged, with low-ionization emission not from the nucleus of the galaxy but rather from processes in non-nuclear stellar populations which result in the same empirical line ratios as LINERs (Belfiore et al., 2016).

The observational subclasses of AGN determined by emission line features dis-

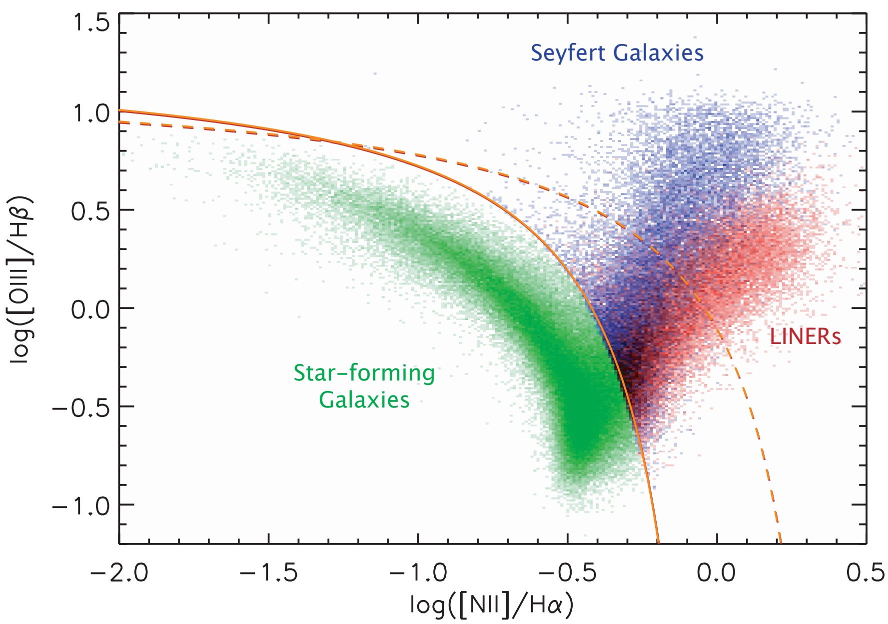

Figure 1.3: Galaxies from the Sloan Digital Sky Survey (SDSS) categorized based on the Baldwin, Phillips & Terlevich (BPT) emission line ratio diagnostic diagram.[12] Additional mappings from Kauffmann et al. (2003) and Kewley et al. (2001) are shown here in orange. This combined classification scheme serves to distinguish galaxies displaying primarily stellar emission (star-forming galaxies) from accretion onto supermassive black holes as the dominant emission mechanism (LINERs and Seyfert galaxies).

cussed in this section divide the population of radio-quiet AGN. AGN are more broadly divided by their emission characteristics, into the so called "radiative-mode," "wind-mode," or "quasar-mode" for those with higher accretion rates and luminosities primarily from a disk[13], and those dominated by outflows or jets in the "radio-mode". The presence or absence of strong radio emission from an AGN may be linked to the black hole spin parameter (e.g. Véron-Cetty & Véron 2000 and references therein). This physical property may also play an analogous role in distinguishing LINERs, and may play a role in hosting environments conducive to accretion state changes such as in changing-look AGN (Dodd et al. 2021; see also Section 1.2).

UV and X-ray studies of LINERs indicate that they may be weak i.e. low-accretion-rate or low-radiative-efficiency analogs of Seyfert AGN, and therefore lower density accretion disks (e.g. Nemmen et al. 2014), although this notion was challenged by Maoz (2007) who argued for the pure thin disk scenario based on UV/X-ray observations of LINER nuclei.

1.2.5 Review of Changing-Look AGN

According to the AGN unification scheme laid out in Section 1.2.1, type 2 AGN are obscured by a dusty molecular torus, and expected to not display variability. Five decades ago, Seyfert 2 Mrk 6 displayed optical continuum variations accompanied by the dramatic appearance of broad Balmer emission lines, changing its optical taxonomy to a type 1 (Khachikian & Weedman, 1971; Pronik & Chuvaev, 1972). In subsequent years, several more puzzling contradictions to this framework emerged.

Changing-look AGN[14] (CLAGN) demonstrate large-amplitude optical and/or X-ray variability accompanied by a spectrum that completely changes its heretofore

[13] See Section 2.2.1 for further discussion on empirical distinctions between quasars and other AGN such as Seyfert galaxies.

[14] Optical changing-look AGN are distinct from X-ray AGN that exhibit "changing-look" transitions between Compton-thick and -thin classes.

dichotomous empirical classification from a broad-line AGN with a blue continuum, to an active galaxy with narrow emission lines (or vice-versa).

A small number of changing-look AGN had been discovered in the mid 20th century, however the advent of systematic searches through large scale photometric and spectroscopic surveys for extremely variable quasars such as PanSTARRs and TDSS/SDSS greatly improved on this number (MacLeod et al., 2016; Ruan et al., 2016; Rumbaugh et al., 2018).

The first changing look quasar SDSS J015957.64+003310.5 (redshift $z = 0.31$) was reported by (LaMassa et al., 2015). Previously a Type 1 AGN in SDSS, it was found in a subsequent SDSS BOSS (Dawson et al., 2013) epoch to have transitioned to a Type 1.9 AGN in a 9 year period. The source was also detected by both archival Chandra and XMM-Newton observations within the Stripe 82X survey (LaMassa et al., 2013a,b). They systematically ruled out other explanations for the dramatic spectroscopic and continuum transition such as obscuration by an orbiting cloud of gaseous material. They also linked CLAGN to an evolutionary theory of the unified AGN intermediate types being on an evolutionary track dependent on accretion rate and black hole mass, which we confirm in Section 2.3.5 for the sample presented in this dissertation. Elitzur et al. (2014) predict a natural sequence (shown in Figure 1.4) in which AGN transition from type 1 to 1.2/1.5 to 1.8/1.9 due to a change in accretion rate and the availability of ionizing radiation affecting the emission line intensities.

Another of the known CLAGN, iPTF16bco (Gezari et al., 2017) was caught "turning-on" in the iPTF survey into a broad-line quasar from a LINER galaxy (Figure 1.5). iPTF16bco was one of only three cases of a CLAGN in a LINER out of the nearly 70 known CLAGN at the time.Furthermore, as a LINER, iPTF16bco had a lower inferred accretion rate in its low state ($L/L_{\rm Edd} \lesssim 0.005$, Gezari et al., 2017) compared to the majority of previously discovered CLAGN (MacLeod et al., 2019), implying a much more dramatic transformation.

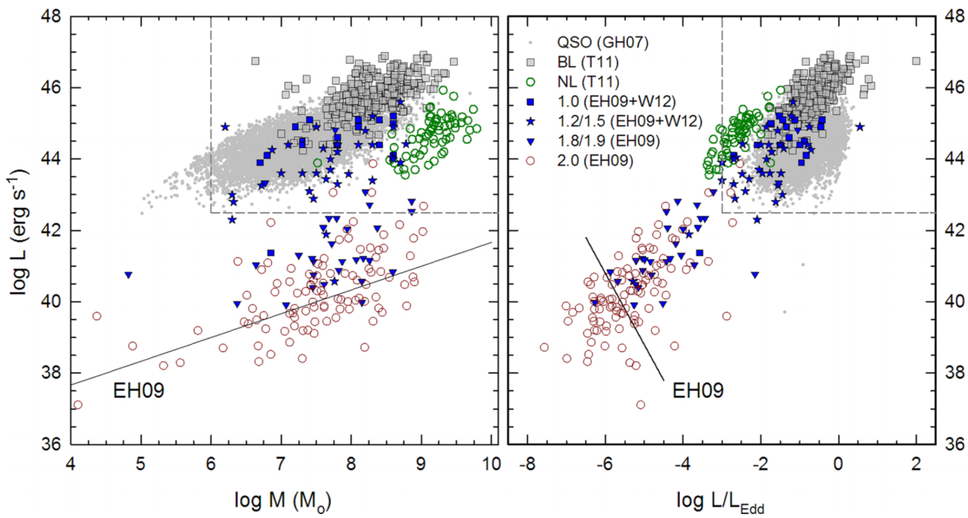

Figure 1.4: Posited transition between AGN spectral types through L vs. $M_{\rm BH}$ and $\dot{M}$ parameter spaces, from type 1 (blue, filled) to type 2 (red open circles), driven by the accretion rate and resulting in this luminosity-emission relation. We trace the relatively rapid (years long) evolution from LINER to type 1 QSO through this same parameter space for the CL-LINER sample presented in Chapter 2, some increasing in luminosity by at least an order of magnitude during the transition. From Elitzur et al. (2014).

These discoveries of unique objects were followed by a slew of observational studies across the wavebands to understand what each AGN emission region could illuminate about the changing-state mechanism, e.g. Parker et al. (2016); Stern et al. (2018), in tandem with theoretical explorations into how other established fields, such as stellar mass BHs, could inform interpretation of these AGN events, (Noda & Done, 2018; Ross et al., 2018). These studies bolstered the idea that CLAGN were in fact driven by changes in the accretion rate and that they could occur on human timescales. In the meantime, a growing number of continuing systematic searches proved the commonality and heterogeneity of these systems in Seyfert AGN and quasars.

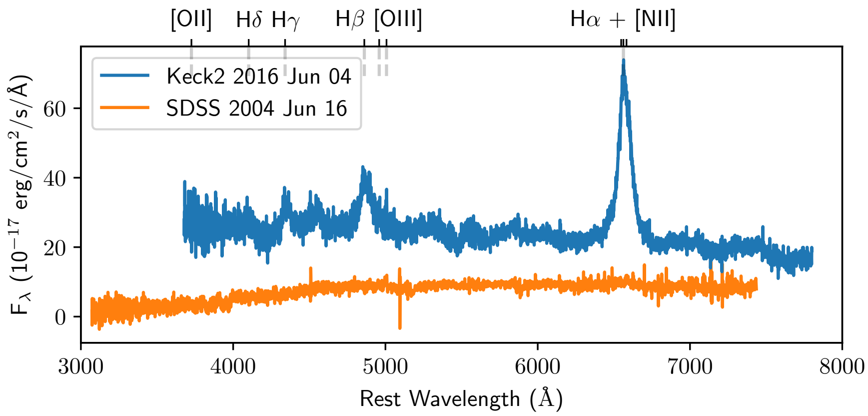

Figure 1.5: Comparison of early and follow-up spectra of iPTF 16bco showed the appearance of broad lines where there were previously none, in concurrence with a smooth, slowly rising blue light curve with a plateau in the final months of the intermediate Palomar Transient Facility Survey.

These observations challenge the established theory of the AGN unification scheme, which attributes these spectral differences solely to the orientation of the line of sight to an obscuring toroid of gas and dust (Antonucci 1993; See Section 1.1.1 for more details). Typically, the difference between type 1 and type 2 AGN has been explained in this way by geometry alone, but such changes necessitate a paradigm shift. However, the mechanism behind these changes are not well understood (e.g. Stern et al. 2018). Recent studies have shown that these transformations from one AGN subtype to another in a single object, observed on human timescales, are more rapid than expected from accretion theory by a factor of ten thousand (e.g. Lawrence 2018). Evidence suggests these events may be the results of environmental changes due to instabilities propagating through the accretion flow (e.g. Ross et al. 2018; Yan et al. 2019; see Figure 1.6), but the triggering mechanism driving these sudden flares is not well understood.

The nature of the CLAGN spectral transformation is most often attributed to

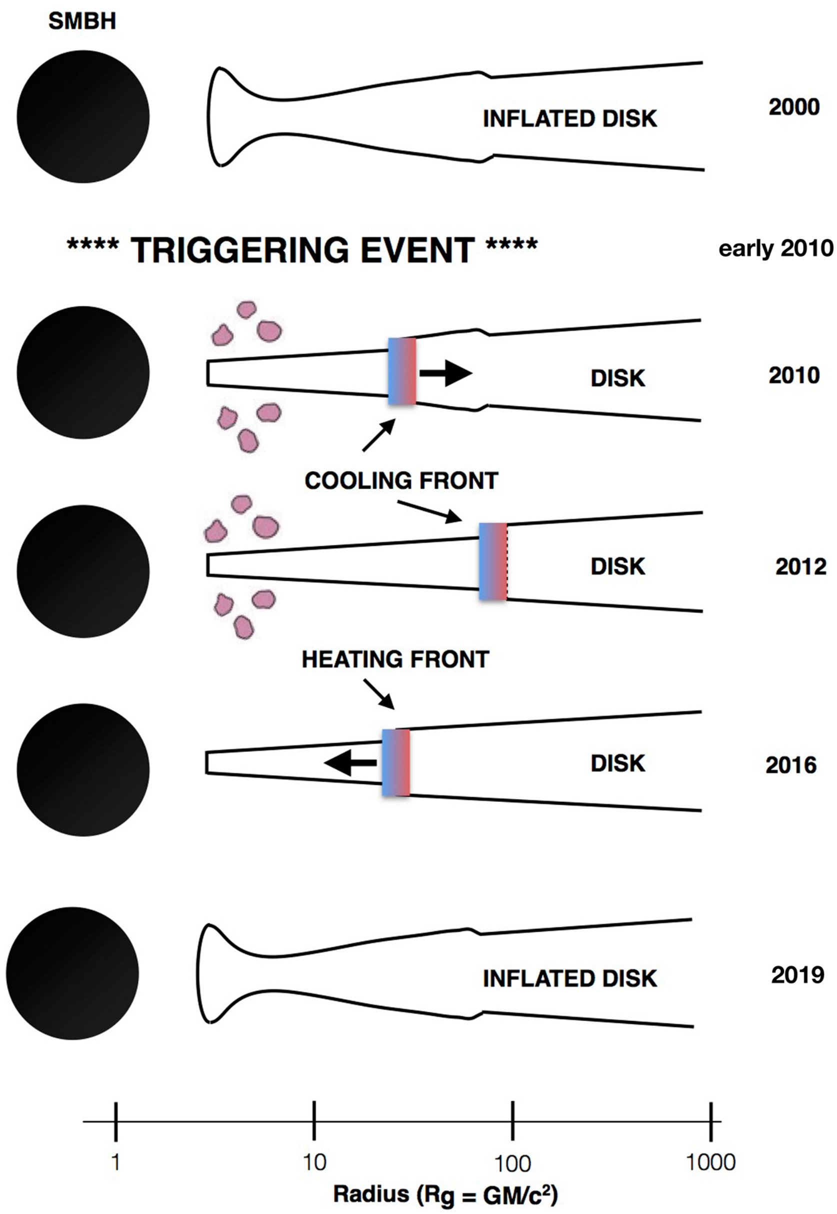

Figure 1.6: Model from Figure 4 in Ross et al. (2018) illustrating possible accretion modes throughout several years of follow-up observations for changing-look quasar SDSS J110057.70-005304.5. The physical mechanism for triggering propagating thermal fronts throughout the disk is not well understood, however, such an unstable configuration may explain the years- to decades-long timescales for transitions between spectral classifications observed in changing-look AGN.

changes in accretion rate (e.g. Elitzur et al. 2014, LaMassa et al. 2015, MacLeod et al. 2016, Gezari et al. 2017, Rumbaugh et al. 2018). Shappee et al. (2014) proposed that observed X-ray through NIR lags in CLAGN were the result of reprocessing of variable X-ray illumination of the accretion disk, and Sheng et al. (2017) reported mid infrared variability lagging that of the optical in support of dust reprocessing.

Tidal disruption events, which occur when a star is tidally destroyed by the gravitational influence of a black hole, are another way a dormant SMBH might feed sporadically on stars, although TDEs likely also occur in variable AGN hosts Jiang et al. (2019); Merloni et al. (2015). Although ZTF has vastly improved our knowledge of this accretion event type in the last 3 years (see van Velzen et al. 2020b and references therein) many hurdles to observing TDEs in the foreground of AGN hosts remain, and they are therefore often found serendipitously (see Sections 1 and 4.4.3 of Chapter 3 for further discussion.) However, MacLeod et al. (2016); Ruan et al. (2016) and others showed that TDEs could not fully explain CLAGN, in part due to the existence of CLAGN growing fainter rather than brighter in nearly equal (albeit small) numbers.

Still, theoretical challenges abound for all proposed scenarios, and further observations are needed to examine the full range of multi-wavelength phenomena occurring during these accretion state changes and within their hosts.

1.3 Overview of Thesis Work

1.3.1 Why Study AGN with ZTF?

Astronomers more interested in transients fondly refer to AGN as the "extragalactic vermin" of the sky, and often much effort goes into rejecting them from surveys as uninteresting sources that nevertheless persistently "go bump in the night". However, difference imaging is well situated to pick out significant variability above the low level baseline stochasticity of most broad line AGN, or to pick out variability from AGN which are not typically extremely variable in the optical (e.g. NLSy1s and other narrow-line AGN). ZTF autonomously provides densely sampled epochs, and therefore is able to identify individual features in light curves. The vast amount of archival optical spectroscopy made available by the Sloan Digital Sky Survey (SDSS) coupled with the Spectral Energy Distribution Machine (SEDM) robotic spectrograph's capabilities to pick out broad lines in follow-up spectra makes the Zwicky Transient Facility the perfect search engine for discovering CLAGN sources in real time. For example, 16bco was discovered serendipitously in the final months of a search for tidal disruption events (TDEs) in the intermediate Palomar Transient Factory (iPTF) survey to be a quasar turning on from a quiescent, early-type, LINER-like galaxy (Figure 1.5; Gezari et al. 2017), along with a similar source discovered in archival data by Yan et al. (2019). They predicted several more of these sources would be discoverable in the order-of-magnitude increase in survey volume achievable by ZTF. Current detection methods are also well-suited for finding this particular class of CLAGN turning on, due to the high percentage of quiescent types comprising galaxies in the nearby Universe" (Dodd et al., 2021).

1.3.2 Summary of Chapters

This dissertation consists of multiwavelength real-time investigations of extreme transients associated with sudden changes in the environments of the SMBHs in galaxy centers. Possible modes of SMBH accretion we ascribe to these outbursts span from the tidal disruption of stars in AGN, to the curious established and growing class of CLAGN. CLAGN demonstrate large-amplitude optical and/or X-ray variability accompanied by a spectrum that completely changes its heretofore dichotomous empirical classification from a broad-line AGN with a blue continuum, to an active galaxy with narrow emission lines (or vice-versa), challenging the AGN unification scheme based on the orientation of the line of sight to an obscuring torus. These transformations from one AGN subtype to another, observed on human timescales, are more rapid than expected from accretion theory by a factor of ten thousand. Evidence suggests these events are the results of accretion state changes due to instabilities in a pre-existing disk, but the mechanism driving these sudden changes is not well understood.

With the ZTF Northern Sky Survey, coupled with data from various spectroscopic and photometric follow-up resources (primarily the Lowell Discovery Telescope), we sought to understand the nature of the AGN undergoing flares and the appearance of spectral features. Informed by an archival iPTF pilot study of CLAGN, and with ZTF's upgraded suite of automated telescopes monitoring the entire Northern sky and streaming millions of data points from new events on a nightly cadence, we have been able to study an unprecedented volume of dramatic activity from galaxy centers in real time.

This work has made two main contributions to the field of AGN time-domain science, with discoveries resulting in a paradigm shift about the timescales and host galaxies of extreme accretion state changes:

1. Establishing a new observational class of quiescent galaxies caught turning into quasars, and

2. Linking a (separate) new observational class of unusually smooth and rapid outbursts to a subclass of active host galaxies undergoing enhanced accretion, while more than tripling the number of such known events in the literature.

Both transient classes emerged from ongoing searches for CLAGN and TDE phenomena, and are associated with subtypes of AGN with interesting, and still not fully understood, properties. We found that the former class of objects display spectroscopic transformations more dramatic by an order of magnitude when hosted in low ionization nuclear emission line region (LINER) galaxies, and the latter occur preferentially in Narrow-Line Seyfert 1 (NLSy1) galaxies. Chapter 2 of this dissertation was published in a first-author Astrophysical Journal article entitled "A New Class of Changing-look LINERs" (Frederick et al., 2019). Chapter 3 of this dissertation, (Frederick et al., 2020) entitled "A Family Tree of Optical Transients from Narrow-Line Seyfert 1 Galaxies," links novel findings to other NLSy1-associated transients in the literature, and provides a framework for spectroscopically classifying such flares in future wide-field surveys.

The fourth chapter of this dissertation, entitled "The X-ray View of a New Class of Changing-look LINERs" (Frederick et al. 2021, in prep.), includes the 3-year catalog of this new class of objects discovered with ZTF, never-before-seen at high X-ray energies, and describes the results of a year-long joint XMM-Newton and NuSTAR observing program entitled "The First X-ray View of a New Class of Changing-Look AGN with XMM and NuSTAR" (PI: Frederick). To complement the hard X-ray data, we also collected target-of-opportunity UV and X-ray observations of this growing sample with the Neil Gehrels Swift Observatory, as well as multi-epoch optical spectroscopic follow-up with the Gemini GMOS-N Observatory, as part of a proposal entitled "The Real-Time Appearance of the BLR in a New Class of Changing-Look LINERs Discovered by ZTF" (PI: Frederick), for which multi-epoch optical spectra were collected in early 2020. This ongoing study will test physical mechanisms driving this new class of changing-look LINERs by mapping the structure of the accretion flow state changes.

In summary, in Chapter 2, we establish a new class of changing-look LINERs and present follow-up observations for a candidate state transition that was discovered to be occurring in real-time. In Chapter 3, we link a number of optical transients in AGN to NLSy1 host galaxies, including a changing-look LINER from the sample presented in Chapter 2, and provide a framework for classification in future surveys. In Chapter 4, we present preliminary analysis of X-ray follow-up observations of the full CL-LINER sample. Chapter 5 summarizes the findings of this dissertation and discusses next steps for this work.

ZTF, using difference imaging as a discovery mechanism, has allowed for real-time detection and rapid multiwavelength follow-up of events related to accretion onto supermassive black holes like never before. In this dissertation, we establish that certain nuclear environments are more conducive to hosting these newly discovered dramatic transients, not only to better understand the accretion phases of their evolution, but also to improve the efficiency of upcoming generations of real-time searches for the most dramatic AGN outbursts with large-area facilities such as the Vera C. Rubin Observatory and the fifth Sloan Digital Sky Survey.

Chapter 2: A New Class of Changing-Look LINERs

We report the discovery of six active galactic nuclei (AGN) caught "turning on" during the first nine months of the Zwicky Transient Facility (ZTF) survey. The host galaxies were classified as LINERs by weak narrow forbidden line emission in their archival SDSS spectra, and detected by ZTF as nuclear transients. In five of the cases, we found via follow-up spectroscopy that they had transformed into broad-line AGN, reminiscent of the changing-look LINER iPTF16bco. In one case, ZTF18aajupnt/AT2018dyk, follow-up *HST* UV and ground-based optical spectra revealed the transformation into a narrow-line Seyfert 1 (NLS1) with strong [Fe VII, X, XIV] and He II $\lambda 4686$ coronal lines. *Swift* monitoring observations of this source reveal bright UV emission that tracks the optical flare, accompanied by a luminous soft X-ray flare that peaks $\sim$60 days later. *Spitzer* follow-up observations also detect a luminous mid-infrared flare implying a large covering fraction of dust. Archival light curves of the entire sample from CRTS, ATLAS, and ASAS-SN constrain the onset of the optical nuclear flaring from a prolonged quiescent state. Here we present the systematic selection and follow-up of this new class of changing-look LINERs, compare their properties to previously reported changing-look Seyfert galaxies, and conclude that they are a unique class of transients related to physical processes associated with the LINER accretion state.

2.1 Introduction

The observed diversity in the optical spectra of AGN, with well-defined systematic trends known as the eigenvector relations, are understood to be a function of both orientation as well as accretion rate (e.g. Shen & Ho 2014). "Changing-look" active galactic nuclei (CLAGN) are a growing class of objects that are a challenge to this simple picture, in that they demonstrate the appearance (or disappearance) of broad emission lines and a non-stellar continuum, changing their classification between type 1.8-2 (narrow-line) to type 1 (broad-line) AGN (or vice versa) on a timescale of years. The nature of this spectral transformation is most often attributed to changes in accretion rate (MacLeod et al., 2016; Oknyansky et al., 2016; Ruan et al., 2016; Runnoe et al., 2016; Shappee et al., 2014; Sheng et al., 2017), but the mechanism(s) driving these sudden changes is still not well understood (e.g. Lawrence 2018; Stern et al. 2018).

One of the known changing-look quasars (CLQs), iPTF16bco (Gezari et al., 2017), was caught "turning-on" in the iPTF survey into a broad-line quasar from a low-ionization nuclear emission-line region galaxy (LINER). LINERs are distinguished from Seyfert 2 (Sy 2) spectra via the relatively strong presence of low-ionization or neutral line emission from [O I] λ6300, [O II] λ3727, [N II] $\lambda\lambda$6548, 6583, and [S II] $\lambda\lambda$6717, 6731; a lower [O III] λ5007/Hβ flux ratio; and a lower nuclear luminosity. However, the status of LINERs as low-luminosity AGN remnants is a topic of debate, as weak emission in some LINERs could also be powered by shocks, winds, outflows, or photoionization from post-AGB stellar populations (Bremer et al., 2013; Filippenko, 1996; Ho et al., 1993; Singh et al., 2013). LINER galaxies are the largest AGN sub population, and may constitute one-third of all nearby galaxies (Heckman, 1980; Ho et al., 1997b), yet iPTF16bco was one of only three cases of a CLAGN in a LINER out of the nearly 70 known CLAGN at the time.[1] Furthermore, as a LINER, iPTF16bco had a lower inferred accretion rate in its low state ($L/L_{\rm Edd} \lesssim 0.005$, Gezari et al., 2017) compared to the majority of previously discovered CLAGN (MacLeod et al., 2019), implying a much more dramatic transformation.

We report the discovery of six new CLAGN, all classified as LINER galaxies by their archival SDSS spectra, detected as nuclear transients by the Zwicky Transient Facility (ZTF; Bellm et al. (2019a); Graham et al. (2019)), and spectroscopically confirmed as "changing-look" to a NLS1 or broad-line (type 1) AGN spectral class. One of these nuclear transients, ZTF18aajupnt, was initially classified as a candidate tidal disruption event (TDE) from the presence of Balmer and He II emission lines (Arcavi et al., 2018). Here, we show that the ZTF light curve, together with our sequence of follow-up optical spectra and UV and X-ray monitoring with *Swift* and follow-up UV spectra with *HST*, are more consistent with a CLAGN classification. It was previously thought that, although they are commonly found in Seyferts, coronal emission lines (such as [Fe VII] λ6088) should never be exhibited by LINER-like galaxies by definition (e.g. Corbett et al. 1996). However, here we also report the surprising appearance of coronal lines coincident with an increase in UV/optical and soft X-ray continuum emission and broad Balmer emission consistent with a NLS1 in this galaxy previously classified as a LINER.

This paper is organized as follows. In Section 2.2, we present our sample selection of nuclear transients in LINERs, information on the host galaxies, ZTF and archival optical light curves, optical spectroscopic observations, and multiwavelength follow-up observations of ZTF18aajupnt, including details of the data reduction involved. In Section 2.3, we introduce a new class of changing-look LINERs, and compare their properties to previously reported Seyfert CLAGN, focusing on the

[1] We note that the other two known so-called CL LINERs, NGC 1097 (Storchi-Bergmann et al., 1993) and NGC 3065 (Eracleous & Halpern, 2001) are, or are reminiscent of, transient double peaked emitters, which may be distinct from changing-look AGN.

particularly interesting case of ZTF18aajupnt, which transformed from a LINER to a NLS1. In Section 2.4 we discuss the results of our analysis, the conclusions of which are summarized in Section 2.5.

Throughout the paper we use UT dates, and assume the following cosmology for luminosity calculations: $H_0 = 70$ km s^{-1} Mpc^{-1}, $\Omega_\Lambda = 0.73$ and $\Omega_M = 0.27$. We have corrected for Galactic extinction toward the sources where explicitly stated. All magnitudes are in the AB system, and all uncertainties are at the 1σ level unless otherwise noted. We adopt the definition for a quasar from the SDSS DR7 quasar catalog (Schneider et al., 2010), as having an apparent i-band PSF magnitude fainter than 15 and an absolute i-band magnitude brighter than -22.

2.2 Discovery and Observations

2.2.1 Sample Selection Criteria

We selected CLAGN candidates first flagged as nuclear transients in the ZTF alert stream (described further in Section 2.2.2) and with a cross-match within $1\farcs0$ of a LINER or type 2 Seyfert galaxy in the Portsmouth Catalog's narrow-line ratio BPT classifications[2] (Bolzonella et al., 2000; Thomas et al., 2013). Those classifications, described further in Section 2.3.1, are based on stellar population and emission line fits to SDSS DR12 spectra, performed with Penalized Pixel Fitting (`pPXF`; Cappellari (2016); Cappellari & Emsellem (2004)) and Gas and Absorption Line Fitting (`GANDALF`; Sarzi et al. (2017)), respectively. In this study, we focus on the "LINER CLAGN" that emerged as a new class of changing-look AGN and display the most dramatic spectral variability of the CLAGN in our ZTF sample (we reserve discussion of the complementary sample of Seyfert CLAGN for a forthcoming publication).

[2] `https://www.sdss.org/dr12/spectro/galaxy_portsmouth/#kinematics`

2.2.2 ZTF Light Curve

ZTF surveys the extragalactic[3] Northern Sky in two modes: a public Mid-Scale Innovations Program (MSIP) survey of 15,000 deg^2 of sky every 3 nights in g and r filters, and a high-cadence ZTF partnership survey of 3400 deg^2 with a dense cadence of 6 epochs each in g and r filters per night. It also surveys in i-band every 4 nights with a footprint of 10725 deg^2 (Bellm et al., 2019b). PTF and iPTF (2009−2016; Law et al. (2009); Rau et al. (2009)) also utilized Palomar Observatory's Samuel Oschin 48" Schmidt telescope; the camera upgrade for ZTF has a 47 deg^2 FoV and reaches 20.5 r-band mag in 30 seconds exposures, with a more efficient areal survey speed of 3760 deg^2 hr^{-1}. Images are processed each night by the Infrared Processing and Analysis Center (IPAC) pipeline (Masci et al., 2019), where difference imaging and source detection are performed to produce a transient alert stream (Patterson et al., 2019), distributed to the GROWTH Marshal (Kasliwal et al., 2019) and other brokers via the University of Washington Kafka system. van Velzen et al. (2019) presented details of the nuclear transients filtering procedure.

All transients in the sample were discovered in 2018 between April and November, all in the ZTF MSIP survey (specific dates are summarized in Table 2.1). ZTF18aajupnt[4] was also detected in the ZTF Partnership survey on 2018 May 31, and (as it was detected in both surveys in the same night) was registered publicly to the Transient Name Server (TNS) as AT2018dyk. Transients were required to have a real-bogus (RB) score ≥ 0.5 as classified by ZTF machine learning (Mahabal et al., 2019). Further details on the transients, including discovery difference absolute magnitudes, are in Table 2.1.

[3] Additional public and private allocations are made to survey the Galactic Plane at higher cadence. See Bellm et al. (2019b) for details.

[4] As ZTF given names are typically a mouthful of letters (appropriately so, due to the requirement of naming upwards of a million alerts per night), the ZTF Black Holes Working Group has informally begun naming TDEs from a fictional world with no shortage of characters: HBO's *Game of Thrones*. As it was initially thought to be a TDE, ZTF18aajupnt was affectionately dubbed "Tyrion Lannister".

Table 2.1: Basic data for the changing-look LINER sample. We list redshifts from the Portsmouth SDSS DR12 catalog (Thomas et al., 2013), which is described in Section 2.2.1. Transition timescales δt are roughly constrained based on the time delay between the onset of variability detected in the host in the archival light curves, and the time of the first spectrum taken in the type 1 AGN state. Estimates of star formation rate by Chang et al. (2015) are from SDSS+WISE SED model fitting. Δm is the variability magnitude change defined in Eq. 3 of Hung et al. (2018) as $\Delta m = -2.5\log(10^{-\mathrm{m_{r,host}}/2.5} + 10^{-\mathrm{m_r}/2.5}) - \mathrm{m_{r,host}}$, where m_r represents the brightest, transient r-band magnitude in the difference-imaging light curve. ZTF18aajupnt, described further in Section 2.3.6 is the least luminous transient, and has the nearest host of the sample.

Name	RA (hh:mm:ss.ss)	Dec (dd:mm:ss.ss)	z	D_{Lum} (Mpc)	Discovery Date	$M_{\mathrm{Discovery}}$ (mag)	δt (yr)	Host Type[5]	log SFR [$M_{\odot}$ yr^{-1}]	Δm_{var} (mag)	High State
ZTF18aajupnt[6]	15:33:08.01	+44:32:08.2	0.0367	158	2018 May 31[7]	−16.59	<0.3	Spiral (SBb D)	0.177	−0.18	NLS1
ZTF18aasuray[8]	11:33:55.83	+67:01:08.0	0.0397	171	2018 May 10	−17.80	<6.8	Spiral (SBa(r)[9])	0.147	−0.06	Seyfert 1
ZTF18aahiqfi[10]	12:54:03.80	+49:14:52.9	0.0670	296	2018 April 8	−18.25	<0.6	Elliptical	−0.058	−0.12	quasar
ZTF18aaidlyq[11]	09:15:31.06	+48:14:08.0	0.1005	457	2018 April 11	−19.09	<0.7	Spiral (Sb D)	0.092	−0.29	quasar
ZTF18aaabltn[12]	08:17:26.42	+10:12:10.1	0.0458	199	2018 Sept 15	−17.62	<2.6	Elliptical	0.227	−0.81	quasar
ZTF18aasszwr[13]	12:25:50.31	+51:08:46.5	0.1680	813	2018 Nov 1	−20.40	<5.3	Elliptical	1.267	−0.72	quasar

The optical photometry for ZTF18aajupnt, ZTF18aasuray, ZTF18aahiqfi, ZTF18aaidlyq, ZTF18aasszwr, and ZTF18aaabltn is comprised of 398, 200, 35, 35, 143, and 207 images, respectively, shown in Figure 2.1. We consider only observations with difference image detections classified as real (with RB score$\geq$ 0.5 on a scale where 0 is bogus and 1 is real). The ZTF optical difference imaging light curves show only the transient nuclear emission in the g- and r-bands. The transients are localized to within $0\farcs19^{+0\farcs28}_{-0\farcs19}$ (ZTF18aajupnt), $0\farcs09\pm0\farcs26$ (ZTF18aasuray), $0\farcs11^{+0\farcs33}_{-0\farcs11}$ (ZTF18aahiqfi), $0\farcs06^{+0\farcs33}_{-0\farcs06}$ (ZTF18aaidlyq), $0\farcs10^{+0\farcs20}_{-0\farcs10}$ (ZTF18aasszwr), and $0\farcs15\pm0\farcs15$ (ZTF18aaabltn) of their host galaxy nuclei, well within our nuclear selection criterion of $< 0\farcs5$.

To quantify the amplitude of the flux increase relative to the host galaxy flux, and to compare to variability of CLAGN measured from imaging surveys that do not perform image subtraction, as in Hung et al. (2018), we add the flux of the host galaxy to the transient flux, to get a variability amplitude, $\Delta m_{\mathrm{var}} = m_{r,\mathrm{tot}} - m_{r,\mathrm{host}}$, where $m_{r,\mathrm{tot}} = -2.5\log(10^{-m_r/2.5+-m_{r,\mathrm{host}}/2.5})$, and m_r represents the brightest transient ZTF r-band magnitude and $m_{r,\mathrm{host}}$ is the archival host magnitude from SDSS DR14. We find Δm_{var} values ranging from -0.12 to -0.81 mag for the sources in our sample, with 3 out of 5 below the CLAGN candidate selection criteria of an

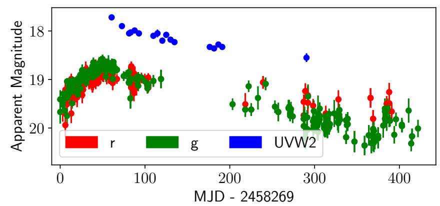

(a) ZTF18aajupnt

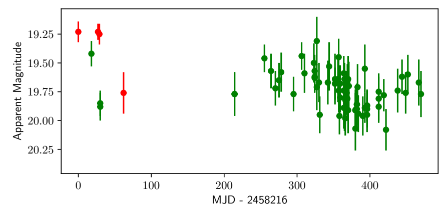

(b) ZTF18aahiqfi

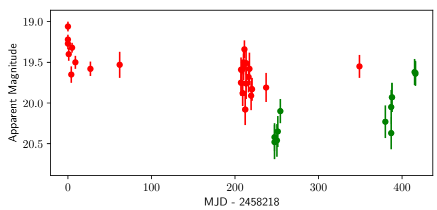

(c) ZTF18aaidlyq

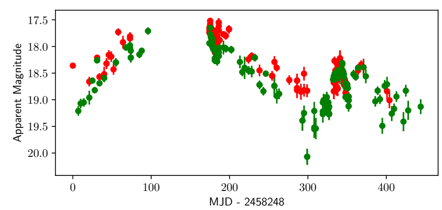

(d) ZTF18aasuray

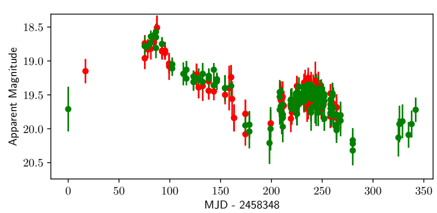

(e) ZTF18aasszwr

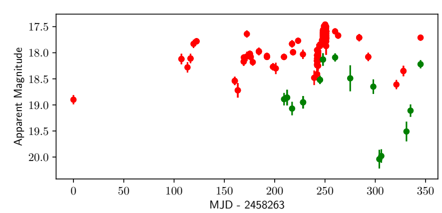

(f) ZTF18aaabltn

Figure 2.1: Light curves of the CL LINER sample. Red points represent r-band difference imaging photometry data taken with the Palomar 48-inch (P48), green points g-band difference imaging photometry, and the blue points are the UVW2 *Swift* photometry in the light curve of ZTF18aajupnt, which tracks the plateau in the optical uncharacteristic of either TDEs or SNe. Note the differences in scale.

amplitude of $\Delta r > 0.5$ mag between SDSS and Pan-STARRS1 imaging observations adopted by MacLeod et al. (2019).

ZTF18aajupnt (AT2018dyk; discussed more in Section 2.2.5), ZTF18aasuray, and ZTF18aasszwr display a slow months-long rise and plateau (although a visibility gap makes this unclear for ZTF18aasuray) with a constant color, and gradual decline, with ZTF18aasszwr exhibiting a second rise and ZTF18aajupnt growing redder in the latest observations. All other transients in the sample show flaring in the light curves (see Figure 2.1) but with less distinct trends, characteristic of broad-line AGN variability viewed in difference imaging (Choi et al., 2014).

2.2.3 Capturing the Transition in Archival Light Curves

Although difference imaging is a useful real-time discovery mechanism for these nuclear transients, archival optical photometric observations can fill in the details of the timing of the transition to its "on" state. With archival light curves extending over a baseline of 13 years from the Catalina Real-time Transient Survey (CRTS; Drake et al., 2009), the All-Sky Automated Survey for Supernovae (ASAS-SN; Kochanek et al., 2017; Shappee et al., 2014)[14], and Asteroid Terrestrial-impact Last Alert System (ATLAS; Tonry et al., 2018), and ZTF aperture photometry from the IPAC pipeline measured from the static images, we uncover an intriguing uniformity in the events (Figure 2.2). Each source in the sample went from lacking any significant variability to flaring dramatically and, for those observed long enough, subsequently declining (ZTF18aaabltn continues to rise smoothly). As not all sources in the sample have peaked, we define the transition timescale for each source reported in Table 2.1 as being from the onset of each flare to the spectroscopic confirmation of the appearance of a blue continuum and broad line emission (except iPTF16bco, for which the onset time was constrained by archival and follow

[14] http://www.astronomy.ohio-state.edu/~assassin

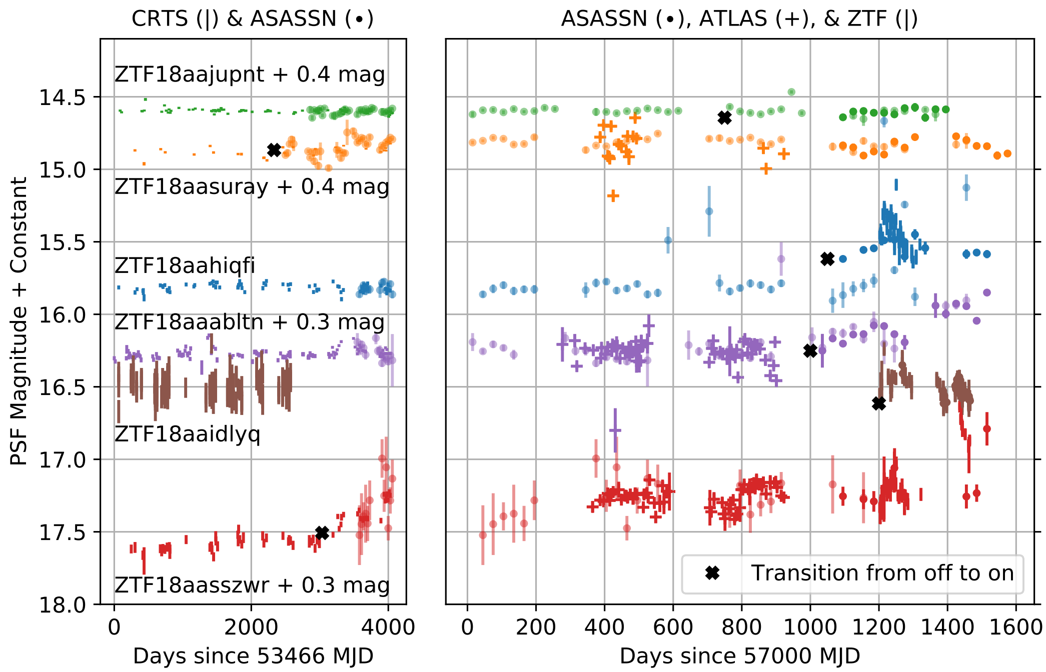

Figure 2.2: Archival light curves of the CL LINER sample summarized in Section 2.2.3. The left panel shows years to decades of quiescence (in the "off" state while these were still LINER galaxies) observed by CRTS, followed by slow flares in the faintest sources ZTF18aasszwr, ZTF18aaabltn, and ZTF18aahiqfi. The right panel shows the rise, flaring, and decline of the sources caught by ZTF+ATLAS+ASASSN g-band observations at these various stages. The estimated transition time listed in Section 2.2.3 for each object is marked by a black "×". When two filters are shown for the same instrument, the redder is shown as more transparent, as in the case of the ASAS-SN g and V photometric points shown.

up X-ray observations; Gezari et al. (2017)). Turn-on timescales, absolute r-band magnitudes at the time of detection with ZTF, variability amplitude relative to the host galaxy flux, and new AGN class following the change are summarized in Table 2.1 for all transients in the sample. We discuss the details of each source's flaring individually below.

ZTF18aajupnt — ZTF-matched aperture photometry in g band shows that ZTF18aajupnt began flaring some time before 2018 March (58200 MJD) ∼2 months prior to discovery in difference imaging on 2018 May 31, and 3 months prior to confirmation of a spectroscopic change. The most recent difference imaging photometry shows a slow decline at constant color. Transition timescale: < 0.3 years, the fastest in the sample.

ZTF18aahiqfi — The rise (seen in ZTF g-band matched photometry) starts approximately at 2017 Sept (58000 MJD), 7 months prior to its spectroscopic change. It peaks around 2018 May (58250 MJD; $\sim$1 month after discovery with ZTF difference imaging on 2018 April 8) and subsequently shows a sharp decline. Prior to this flaring, Catalina Real-time Transient Survey (CRTS shown in the left panel of Figure 2.2; Drake et al. (2009)) observations in V-band and ASAS-SN showed no variability above the 0.1 mag level. Transition timescale: < 0.6 years.

ZTF18aaidlyq — This source displayed a slight flare in ASAS-SN data just after 2017 Sept (58000 MJD), 7 months prior to detection in ZTF difference imaging and 8 months prior to spectroscopic confirmation of the existence of a BLR, but was faint and quiescent in CRTS beginning in 2005 May (note that this source is near a bright star). Transition timescale: < 0.7 years.

ZTF18aasuray — Discovery with ZTF difference imaging occurred on 2018 May 10 and shows a slow symmetric rise and decline lasting 300 days. ZTF18aasuray displayed flaring in ASAS-SN data beginning around 2011 Aug (55800 MJD), 6.8 years prior to spectroscopic confirmation of the changing look which occurred on 2018 June 21. Prior to this flaring, Catalina Real-time Transient Survey (CRTS shown in the left panel of Figure 2.2; Drake et al. (2009)) observations in V-band showed no variability above the 0.1 mag level. Transition timescale: < 6.8 years.

ZTF18aasszwr — The rise is visible in CRTS around 2018 July (56500 MJD), after which it may have plateaued for a time. Most recently there has been a sharp rise and decline around 2018 May (58250 MJD), with the peak reaching > 1 mag above original levels. The transition from quiescence thus happened roughly in real time, and was observed with difference imaging 4 months after the flaring began, with the spectroscopic change confirmed within 5.3 years of the initial rise time, and within 5 months of the onset of the most recent flare. We note that two decades ago, ZTF18aasszwr was a variable (rms = 0.14 mJy) radio source between the NRAO VLA Sky Survey and Faint Images of the Radio Sky at Twenty centimeters (NVSS and FIRST; Ofek & Frail 2011), with a peak flux density at 1.4 GHz of $F_\nu = 2.17$ mJy. Transition timescale: < 5.3 years.

ZTF18aaabltn — CRTS, ATLAS and ASAS-SN show a continuous rise starting around 2016 April (57500 MJD) but this disregards some slight flaring (by 0.2 mag) events at 2008 Nov and just before 2014 Dec (57000 MJD), with both returning to very flat pre-activity levels. This constrains the spectroscopic change to happening within 1000 days (< 2.7 years) of the flare start time, the first large flare occurring within 9 months of being observed to be a LINER in 2007 Feb. Transition timescale: < 2.6 years.

iPTF16bco — CRTS photometry shows a flare beginning around 2012 March (56000 MJD), 8 years after being observed to be a LINER and 4 years prior to discovery and classification of a quasar in iPTF, and the latest ZTF g-band data show it declining rapidly. However, archival XMM Slew Survey observations constrain the onset of the X-ray source detected by Swift in its broad-line state to < 1.1 years before (Gezari et al., 2017). Transition timescale: < 1.1 years.

2.2.4 Host Galaxy Morphology

Images of the six transients' host galaxies from SDSS are shown in Figure 2.3, and basic data including the hosts' names, matched coordinates, redshifts, luminosity distances, morphological types, and star formation rates (SFRs) are summarized in Table 2.1. The SFR estimates by Chang et al. (2015) were obtained through Multi-wavelength Analysis of Galaxy Physical Properties (MAGPHYS; da Cunha et al. (2012)) model fitting of dust extinction/emission, and SEDs constructed from WISE+SDSS (WISE: Wright et al. (2010)) matched photometry of present-epoch galaxies (we note that SFRs for only two AGN in our sample were measured by Chang et al. (2015), the rest did not fit their criteria). The bulges of the LINERs' hosts are similar in apparent color and extent, but the host of ZTF18aaidlyq exhibits evidence for a bar and ring, and the host of ZTF18aaabltn exhibits apparent elongation. The host of ZTF18aajupnt stands out in the sample as the only gas-rich spiral galaxy, and we note that NLS1s typically occur in spiral-type galaxies (Crenshaw et al., 2003). Black hole masses estimated from the host galaxy luminosity, bulge mass, and velocity dispersions derived from the SDSS host imaging and spectra have been measured in Section 2.3.2 and are summarized in Table 2.2.

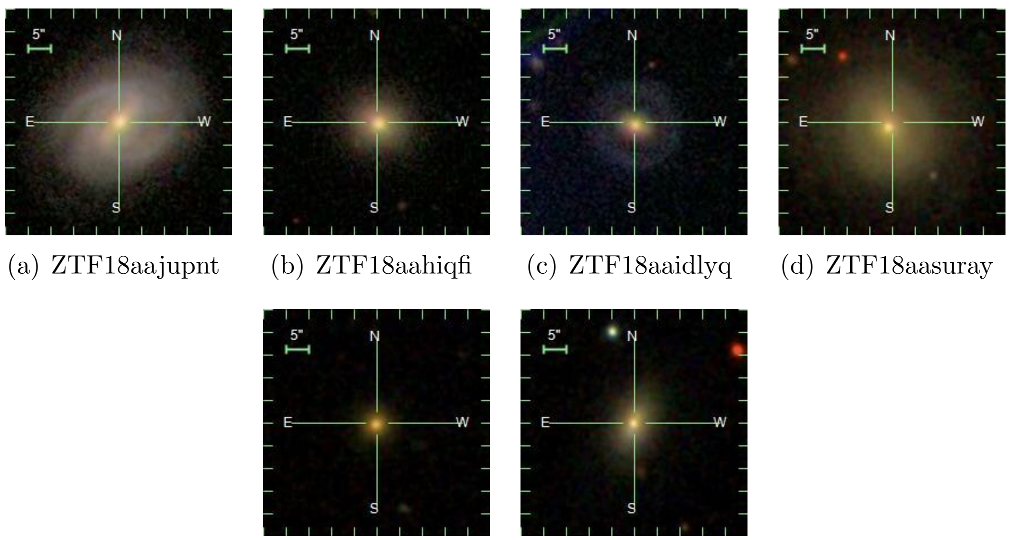

(a) ZTF18aajupnt (b) ZTF18aahiqfi (c) ZTF18aaidlyq (d) ZTF18aasuray

(e) ZTF18aasszwr (f) ZTF18aaabltn

Figure 2.3: Composite *ugriz* color SDSS images of the host galaxies of the changing-look LINER sample. Their individual morphological classifications are listed in Table 2.1.

2.2.5 Optical Spectroscopy

We obtained spectral follow-up of nuclear transients in known LINERS and Sy 2 galaxies as described in Section 2.2.1 to confirm changing-look AGN candidates, as neither "true" narrow-line Sy 2s nor LINERs are expected to vary significantly.

Table 2.2: Properties of the host galaxies of our sample of changing-look LINERs from ZTF and iPTF. We also show $M_{\rm BH}$ calculated in Section 2.3.2 from the host galaxy luminosity, mass, and velocity dispersion, respectively.

Name	$M_{r,\rm host}$ [15] (mag)	log $M_{\rm Bulge}$ [16] $[M_\odot]$	$\sigma_\star$ [17] (km s^{-1})	λL_{5100A} (10^{43} erg s^{-1})	FWHM$_{H_\beta}$ (km s^{-1})	log $M_{\rm BH,M_r}$ [18] $[M_\odot]$	log $M_{\rm BH,Bulge}$ [19] $[M_\odot]$	log $M_{\rm BH,\sigma\star}$ [20] $[M_\odot]$	log $M_{\rm BH,vir}$ $[M_\odot]$	$L/L_{\rm Edd}$ [21]
ZTF18aajupnt	−22.00	10.66±0.15	150	0.49±0.11	939±28	8.0	7.8	7.6	6.4	0.09
ZTF18aasuray	−21.70	10.73±0.15	230	10.6±0.4	4270±218	7.9	7.9	8.4	8.0	0.03
ZTF18aaidlyq	−21.64	-	120	12.7±2.3	7726±458	7.9	-	8.2	8.5	0.06
ZTF18aahiqfi	−21.63	-	210	4.1±0.5	8809±723	7.9	-	7.2	8.3	0.2
ZTF18aasszwr	−22.19	11.19±0.15	180	57.0±1.9	6461±846	8.1	8.3	7.9	8.8	0.5
ZTF18aaabltn	−20.62	-	140	0.8±0.2	5195±648	7.3	-	7.5	8.0	0.2
iPTF16bco	−22.21	-	176	17.3±11.0	4183±213	8.4	-	7.9	8.1	0.05

We observed ZTF18aahiqfi, ZTF18aaidlyq, and ZTF18aasuray with the Deveny spectrograph on the Discovery Channel Telescope (DCT; spectral coverage of 3600-8000 Å) with a 1.″5 wide slit, central wavelength of 5800 Å and exposure times of 2 × 900, 2 × 1200, and 1400 seconds on 2018 April 11, May 06, and June 21, respectively. The DCT spectra were reduced with standard IRAF routines, corrected for bias and flat-fielding, and combined into a single 2D science frame. Wavelength and flux calibration were done via a comparison with spectra of an arc lamp and the flux standard Feige 34, respectively. The spectra have not been corrected for telluric absorption. We found that the Balmer lines of ZTF18aahiqfi, ZTF18aaidlyq, and ZTF18aasuray had gotten dramatically stronger and broader compared to archival SDSS spectra of their hosts, obtained more than a decade prior (in April 2003, Dec 2002, and Feb 2001, respectively).

ZTF18aasszwr and ZTF18aaabltn showed similar striking spectral changes when they were followed up on 2018 Dec 3 and 9 using the Spectral Energy Distribution Machine (SEDM; Blagorodnova et al. 2018) IFU spectrograph on the Palomar 60-inch (P60; Cenko et al. 2006) operating as part of ZTF. Both displayed broader emission lines and bluer continuua compared to archival LINER spectra (from Feb 2007 and Jun 2004, respectively). The SEDM data were reduced with `pySEDM` (Rigault et al., 2019).

See the spectral comparisons for all CLAGN in the sample in Figure 2.4, and zoom-ins of the emission lines in the “off” states in Figures 2.18, 2.19, and “on” states in Figure 2.20 of the Appendix. The hosts of all six transients in this sample were originally classified as LINERs in SDSS, however we re-measured the diagnostic narrow-line ratios in Section 2.3.1, and find that the majority of the sample is on the borderline between a LINER and Seyfert classification.

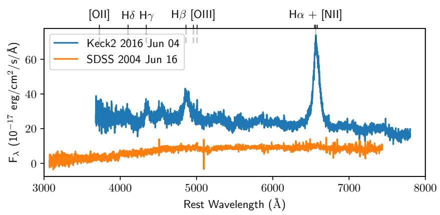

(a) iPTF16bco

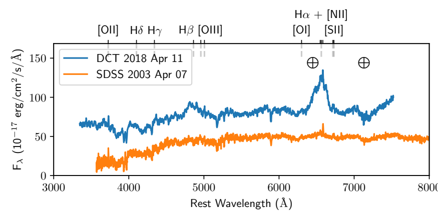

(b) ZTF18aahiqfi

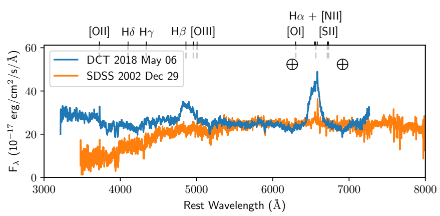

(c) ZTF18aaidlyq

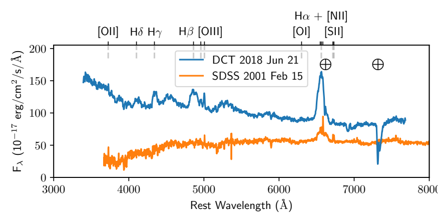

(d) ZTF18aasuray

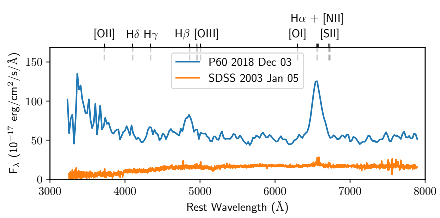

(e) ZTF18aasszwr

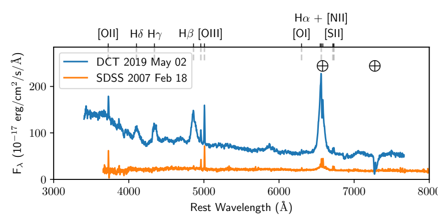

(f) ZTF18aaabltn

Figure 2.4: Comparison of early and follow-up spectra of the other CLAGN in the sample. Note that the Palomar 60-inch "P60" spectra have a difference in aperture affecting the flux measurement by a factor of order unity. Detailed follow-up of ZTF18aajupnt (not shown here) is presented in Figure 2.6.

Due to its similarity to a TDE at early times, we promptly initiated a multi-wavelength follow-up campaign of ZTF18aajupnt which we describe in the following sections. Following the discovery of a blue continuum with the Double Spectrograph (DBSP) of the Palomar 200-inch Hale telescope on 2018 June 12 (PI: David Cook), we monitored ZTF18aajupnt with five additional epochs of optical spectroscopy

Table 2.3: Spectroscopic Legacy and Follow-up Observations of ZTF18aajupnt.

Obs UT	Instrument	Exposure (s)	Reference
2002 July 11	SDSS	28816	Abolfathi et al. (2018)
2018 June 12	Palomar 200" DBSP	2400	This work
2018 July 22	Palomar 60" SEDM	2430	This work
2018 July 30	*Swift* XRT	40400	This work
2018 Aug 7	Keck LRIS	300	This work
2018 Aug 11	*XMM* EPIC pn	11906	This work
2018 Aug 12	Palomar 60" SEDM	2430	This work
2018 Aug 12	FTN FLOYDS-N	3600	Arcavi et al. (2018)
2018 Aug 21	Gemini GMOS-N	600	This work
2018 Sept 1	*HST* STIS	2859	This work
2018 Sept 12	DCT Deveny	2400	This work

with SEDM on Palomar's 60-inch on 2018 July 22 and Aug 12, LRIS on the Keck I telescope on 2018 Aug 7 (PI: Kulkarni), Gemini GMOS-N on 2018 Aug 21 (PI: Hung), and with Deveny on the DCT on 2018 Sept 12 (PI: Gezari). We detail the configurations of the spectroscopic follow-up observations of ZTF18aajupnt in Table 2.3. During this time, its optical light curve plateaued in a manner strikingly similar to iPTF16bco (shown in Figure 2.5). It also surprisingly displayed coronal emission lines (those detected are shown in Figures 2.7 and 2.21) in a heretofore low-ionization nuclear source.

Figure 2.6 shows a complete series of spectra obtained for ZTF18aajupnt, as well as comparisons to some examples of other AGN and transient types, including the class of extreme coronal line emitters (ECLEs) and the luminous SN IIn SN 2005ip which demonstrated strong coronal line emission (Smith et al., 2009). These spectra were reduced with standard pipelines and procedures for each instrument. Measurements of the flux, luminosity, radial velocity, full-width-at-half-maximum (FWHM), and equivalent width of the emission lines, including the coronal emission lines ([Fe XIV] $\lambda 5304$, [Fe VII] $\lambda\lambda 5721, 6088$, [Fe X] $\lambda 6376$ in the spectrum with the highest signal-to-noise detection of the coronal lines is given in Table 2.4. The FLOYDS-N spectrum from 2018 Aug 12 was reported by Arcavi et al. (2018) to

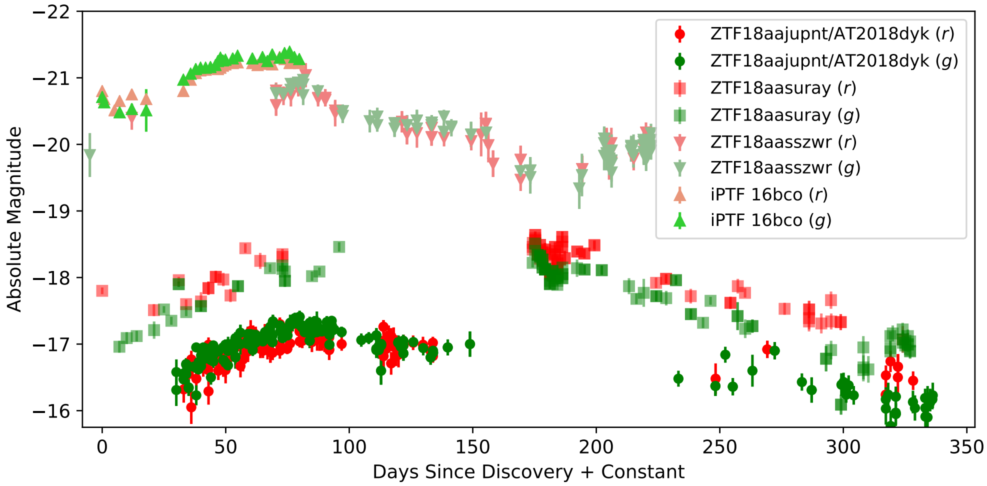

Figure 2.5: Difference imaging light curves of the CL LINERs with the best-sampled P48 observations in the ZTF sample (ZTF18aajupnt, ZTF18aasszwr, and ZTF18aasuray) plotted in absolute magnitude compared to that of CL LINER iPTF16bco (triangle shaped points). ZTF18aasszwr and iPTF16bco are similar in luminosity and more luminous than ZTF18aajupnt and ZTF18aasuray by about 2.5 mag. ZTF18aasuray has a much slower evolution and is constantly redder in color, whereas ZTF18aajupnt reddens ∼280 days into its evolution. The rise of ZTF18aajupnt mirrors that of iPTF16bco, whereas the decline appears slower than but similar in shape to that of ZTF18aasszwr.

have broad Hα, and both broad and narrow Hβ and He II. At that time, a blue continuum was not obvious in their spectrum. However, we show a power-law blue excess is clearly detected in the residuals of the spectra after subtracting a model for the host galaxy light (Figure 2.7).

We have corrected for Galactic extinction in the spectra in Figure 2.6, with color excess $E(B-V) = 0.0164$ mag (from the Schlafly & Finkbeiner (2011) dust map[22]). We use the optical correction curve for $R_V = 3.1$ given by Eqs. 3.a. and b. in Cardelli et al. (1989), such that $f_{\rm corr} = f_{\rm obs} 10^{A_\lambda/2.5}$.

[22] https://irsa.ipac.caltech.edu/applications/DUST/

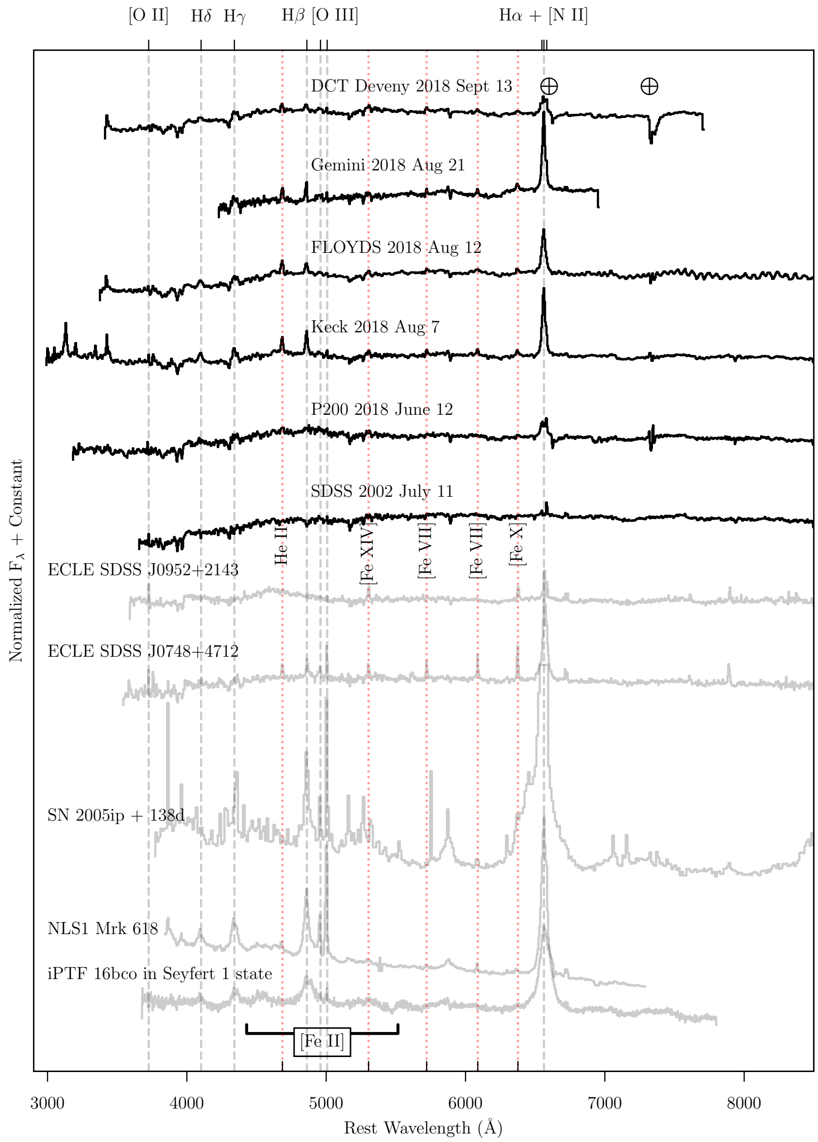

Figure 2.6: Host and follow-up spectra of ZTF18aajupnt, alongside various AGN and coronal line emitters for comparison. AGN emission lines are annotated in gray and are labeled above the figure. Coronal lines are annotated in red and are labeled in the middle of the figure. The flux of the Hα line (only) in SN 2005ip has been truncated for visual purposes (as it lies well above the upper boundary of the plot). Spectra have been rebinned by a factor of four for visual purposes.

2.2.6 UV Imaging and Spectroscopy

We obtained 17 epochs of follow-up imaging of ZTF18aajupnt with the Neil Gehrels *Swift* Observatory's (Gehrels et al., 2004) Ultraviolet/Optical Telescope

Table 2.4: Line measurements for ZTF18aajupnt from fits in Figure 2.21 and used in Figures 2.16, 2.13 and 2.17. The blueshift measured significantly only in Fe X translates to ≈0.0005 c.

	λ (Å)	F_λ (10^{-15} ergs s^{-1} cm^{-2} Å^{-1})	L (10^{39} ergs s^{-1})	v_r (km s^{-1})	FWHM (km s^{-1})	EW (Å)
Hα	6562.80	27.67±0.59	82.4±1.2	57 ± 4	1061 ± 19	56.9 ± 1.5
[NII]λ6548	6548.05	0.21±0.19	0.64±0.37	-612 ± 19	212 ± 59	0.4 ± 0.0
[NII]λ6583	6583.45	1.11±0.15	3.31±0.29	954 ± 10	335 ± 28	7.9 ± 0.2
Hβ	4861.30	9.02±0.32	26.85±0.94	76 ± 8	939 ± 28	18.0 ± 0.7
[OIII]	5006.84	0.96±0.16	2.86±0.47	73 ± 24	489 ± 59	2.1 ± 0.3
HeII	4686.00	3.48±0.29	10.37±0.85	10 ± 28	1157 ± 69	6.7 ± 0.6
[FeXIV]	5304.00	0.45±0.14	1.33±0.40	37 ± 44	546 ± 115	1.0 ± 0.3
[FeVII]λ5721	5721.00	0.81±0.14	2.40±0.41	62 ± 40	795 ± 98	1.6 ± 0.3
[FeVII]λ6088	6088.00	1.08±0.13	3.22±0.39	68 ± 22	600 ± 54	2.3 ± 0.3
[FeX]	6376.00	1.83±0.19	5.44±0.56	-160 ± 36	1301 ± 94	3.9 ± 0.4

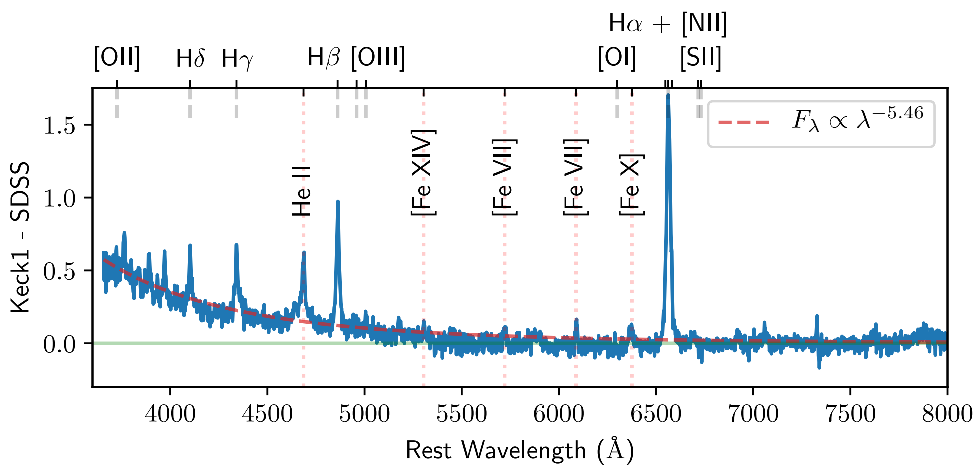

Figure 2.7: Host-galaxy-subtracted Keck1 spectrum of ZTF18aajupnt showing presence of coronal emission lines (red dotted lines) and a blue excess in the residuals. We fit the non-stellar blue continuum with a power law (red dashed line with $\alpha = -5.46$).

(UVOT; Poole et al. (2008); Roming et al. (2005)) from 2018 July 30 to 2019 Mar 17 with 2−3 ks per epoch in the UVW2 filter ($\lambda_{\text{eff}} = 2030$ Å; See Figure 2.1 and 2.8). We detected NUV brightening in the nucleus relative to its archival *Galaxy Evolution Explorer* (*GALEX*; Martin et al. (2005)) All-Sky Imaging Survey (AIS) magnitude

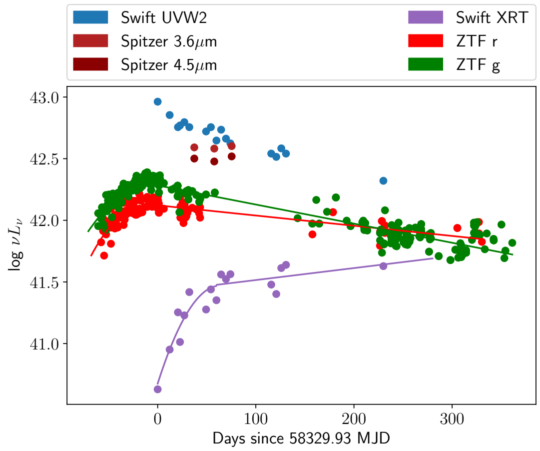

Figure 2.8: The νL_ν light curve of ZTF18aajupnt, comparing *Spitzer* data to concurrent *Swift* UVOT, XRT and ZTF observations. For the *Spitzer* and *Swift* UVOT observations we subtracted the host galaxy light as estimated by WISE and *GALEX* measurements, respectively. To better show the 60-day lag in the X-ray, we fit the rise caught by optical and X-ray observations with an order 2 polynomial and the plateau with linear fits.

of $NUV = 19.0$ mag (measured with a 6 arcsec radius aperture).

The source was initially detected with a *Swift* UVW2 = 17.7 mag (measured within a 5 arcsec radius aperture), which then faded to UVW2 = 18.0 mag 20 days later, and then remained roughly at that UV flux over the next 50 days. Note that while some of the UV flux measured by *Swift* contains a contribution from extended star-formation (detected in the UV out to a radius of 15 arcsec), the fact that it is variable, and brighter than the archival *GALEX* UV central flux indicates that it is associated with the transient. The UV-optical color of ZTF18aajupnt after subtracting off the *GALEX* flux is UVW2$-r$ = -0.45 mag, very similar to iPTF16bco (which had NUV$-r$ = -0.5 mag, already 0.5 mag bluer than the color range of AGN in both *GALEX* and SDSS; Agüeros et al. (2005); Bianchi et al. (2005)).

We obtained UV spectroscopy of ZTF18aajupnt with the Space Telescope Imaging Spectrograph (STIS) FUV and NUV Multi-Anode Microchannel Array (MAMA) detectors aboard the *Hubble Space Telescope* (*HST*) for a 2 ks exposure with 0.″2 slit width, and G140L (λ = 1425 Å) and G230L (λ = 2376 Å) gratings on 2018 Sept 1, 2019 Jan 18 (only in the FUV[23]), and 2019 March 3, shown in Figure 2.9 (Proposal ID: 15331, PI: S.B. Cenko).

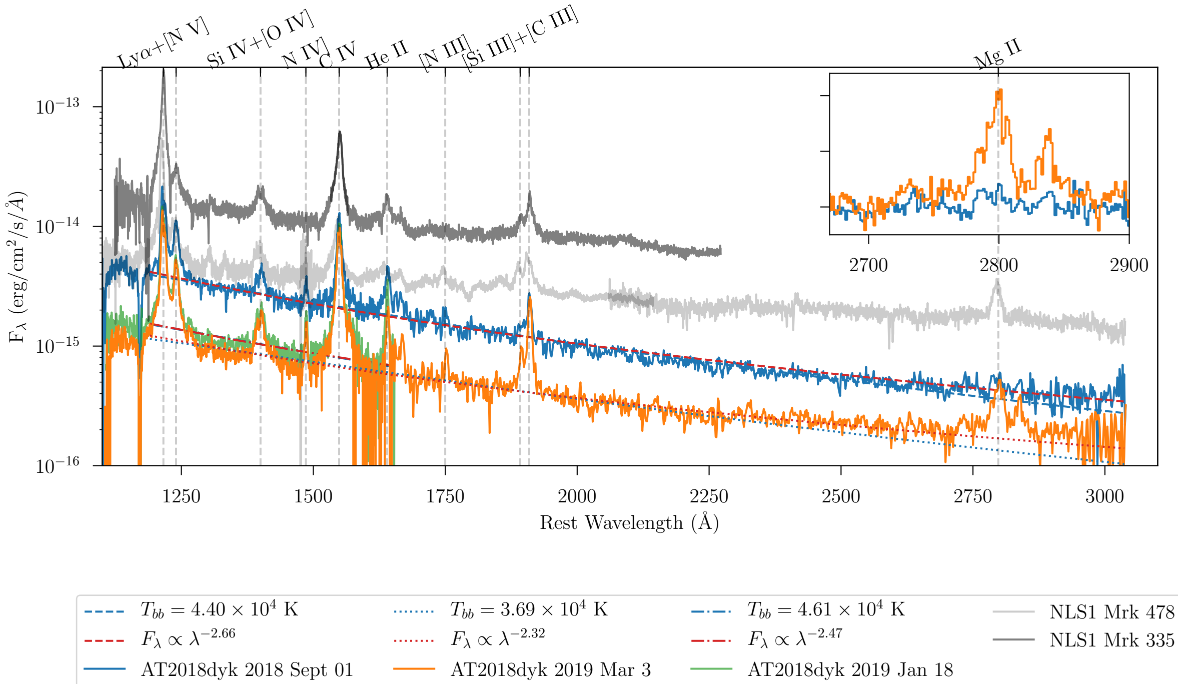

Figure 2.9: *HST* UV spectrum of ZTF18aajupnt compared to two prototypical NLS1s. Note the presence of high-ionization lines He II, N V, O IV, and C IV, and the relative weakness of the low-ionization line Mg II λ2798 in ZTF18aajupnt until later times.

The high spatial resolution of *HST* ($\sim$ 0.″5) enables better isolation of the nuclear emission from the host galaxy light. The UV continuum, when masking the emission lines and correcting for Galactic extinction as in Section 2.2.5, is an equally good fit to both a blackbody (remaining consistent for both observations within $T = (4.5 \pm 0.3) \times 10^4$ K) and a power law with spectral index $\alpha = -2.6 \pm 0.1$ where $F_\lambda = F_{\lambda,0}\lambda^\alpha$ or $\alpha_\nu = -\alpha - 2 = 0.6$, with the continuum $F_{\lambda,0}$ decreasing in flux by a factor of 10.7 over 140 days, while the strength of the emission lines remain

[23]The second HST epoch had no NUV coverage due to losing lock on the guide stars, and was retaken.

roughly at the same level. This blackbody temperature is not unusual for TDEs (e.g. Arcavi et al. 2014; Gezari et al. 2012; Holoien et al. 2016a,b; Hung et al. 2017; van Velzen et al. 2011), and the power-law index is within the range of UV slopes observed in quasars ($-1.5 < \alpha_\nu < 1.5$; Davis et al., 2007), but steeper than the UV slopes observed in NLS1s ($-2 < \alpha_\nu < 0$; Constantin & Shields, 2003). Figure 2.9 shows similarities of the emission features to *HST* Faint Object Spectrograph (FOS) spectra of the prototypical NLS1s Mrk 335 and Mrk 478, noting that compared to the NLS1s, the UV spectrum of ZTF18aajupnt initially has a weaker low-ionization line Mg II λ2798, which tends to exhibit weak responsivity in CLAGN (e.g. Gezari et al. 2017; MacLeod et al. 2016). In the latest *HST*/STIS epoch, $\sim$6 months after the optical peak, a broad multi-component Mg II line profile appeared, reminiscent of recently "awakened" CLAGN Mrk 590 (Mathur et al., 2018). This suggests that a light travel time delay, and not low responsivity, is responsible for Mg II being only marginally detected in the intial observation. This also implies that Mg II is not co-spatial with the Balmer-line emitting region.

Galactic extinction has been corrected in these spectra in the same way as in Section 2.2.5, but instead using the UV correction curve for $R_V = 3.1$ given by Eqs. 4.a. and b. in Cardelli et al. (1989).

2.2.7 X-ray

We observed ZTF18aajupnt concurrently with 17 exposures of *Swift* XRT, detailed in Table 2.5. The XRT data were processed by the XRT Products Page[24] (Evans et al., 2009) using HEASOFT v6.22[25]. We assessed best-fit models utilizing χ^2 statistics and XSPEC version 12.9.1a (Arnaud, 1996). Uncertainties are quoted at 90% confidence intervals. The XRT light curve in the right panel of Figure 2.10 shows that ZTF18aajupnt is a strongly variable X-ray source, caught rising steadily

[24] `http://www.swift.ac.uk/user_objects/`
[25] `https://heasarc.gsfc.nasa.gov/docs/software/heasoft/`

Table 2.5: *Swift UVOT/XRT* photometry for ZTF18aajupnt. Corresponds to right panels of Figures 2.10 and 2.11.

Obs UT	*UVOT/XRT* Exposure times (s)	Count rate (10^{-2} s^{-1})	UVW2 (AB mag)	Unabsorbed $F_{0.3-10\mathrm{keV}}$ (10^{-13} erg s^{-1} cm^{-2})	$L_{2\ \mathrm{keV}}$ (10^{40} erg s^{-1})	$L_{2500\ A}$ (10^{42} erg s^{-1})	α_{OX}
2018 Jul 30	931/941	0.4 ± 0.3	17.72 ± 0.04	1.21	0.56	6.80	-1.15
2018 Aug 12	312/2022	0.8 ± 0.3	17.90 ± 0.06	2.64	1.19	5.70	-1.00
2018 Aug 20	491/3001	1.7 ± 0.3	18.05 ± 0.05	4.43	2.38	5.00	-0.86
2018 Aug 22	298/2252	1.0 ± 0.2	18.03 ± 0.06	2.55	1.37	5.10	-0.96
2018 Aug 27	375/3164	1.6 ± 0.3	17.99 ± 0.06	4.18	2.25	5.30	-0.88
2018 Sep 01	286/2874	2.4 ± 0.3	18.05 ± 0.06	6.48	3.48	5.00	-0.80
2018 Sep 18	807/3006	1.7 ± 0.3	18.10 ± 0.05	5.43	2.51	4.80	-0.85
2018 Sep 23	165/3011	2.5 ± 0.3	18.05 ± 0.08	7.93	3.66	5.00	-0.79
2018 Sep 28	324/1877	2.1 ± 0.4	18.20 ± 0.06	6.47	2.98	4.40	-0.80
2018 Oct 03	353/3149	3.4 ± 0.4	18.08 ± 0.06	10.47	4.83	4.90	-0.74
2018 Oct 08	582/2447	3.1 ± 0.4	18.18 ± 0.05	9.60	4.43	4.40	-0.74
2018 Oct 13	1677/1695	3.4 ± 0.5	18.23 ± 0.04	10.53	4.86	4.20	-0.71
2018 Nov 23	1329/2931	2.8 ± 0.3	18.33 ± 0.05	8.68	4.00	3.90	-0.73
2018 Nov 28	1380/2854	2.3 ± 0.3	18.36 ± 0.05	7.27	3.36	3.80	-0.76
2018 Dec 03	1281/2484	3.8 ± 0.4	18.28 ± 0.05	11.82	5.46	4.10	-0.69
2018 Dec 08	629/2452	4.0 ± 0.5	18.33 ± 0.05	12.54	5.79	3.90	-0.67
2019 Mar 17	191/2874	3.9 ± 0.4	18.55 ± 0.09	12.24	5.65	3.20	-0.64

by an order of magnitude in flux over several months. The coadded spectrum (shown in the left panel of Figure 2.10) is well-modeled by a power law with a spectral index of $\Gamma = 2.82^{+0.35}_{-0.26}$ and assuming a Galactic extinction of $N_{\mathrm{H}} = 1.76 \times 10^{20}$ cm^{-2} (computed by the `NHtot` tool; Kalberla et al. (2005); Schlegel et al. (1998)), with no intrinsic absorption and an observed flux between 0.3−10 keV of (3.0±0.5) $\times 10^{-13}$ erg cm^{-2} s^{-1}.

We then observed ZTF18aajupnt with the *XMM* EPIC pn camera (Strüder et al., 2001) on 2018 Aug 11 for a 12 ks exposure (Observation ID: 0822040701, PI: S. Gezari). We reduced the data using the *XMM-Newton* Science Analysis System (SAS) v16.0 (Gabriel et al., 2004). We extracted products with circular source and background (source-free) regions with radii of 35” and 108”, respectively. To mitigate background flaring and maximize SNR, we filtered the photometry for count rates below 1.75 cts s^{-1}. We also adopted CCD event patterns 0 to 4, corresponding to single- and double-pixel events. We used *XMM Newton* EPIC-pn calibration database files updated as of Sept 2018. We fit the *XMM* EPIC pn data to a simple power law with spectral index $\Gamma = 3.02 \pm 0.15$ and only Galactic extinction, characteristic of a steep soft excess, and consistent with the range of photon indices

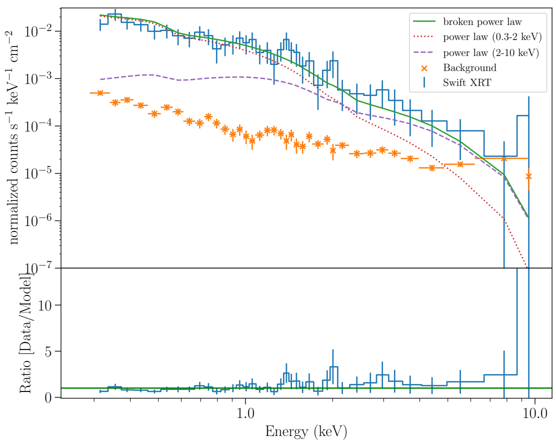

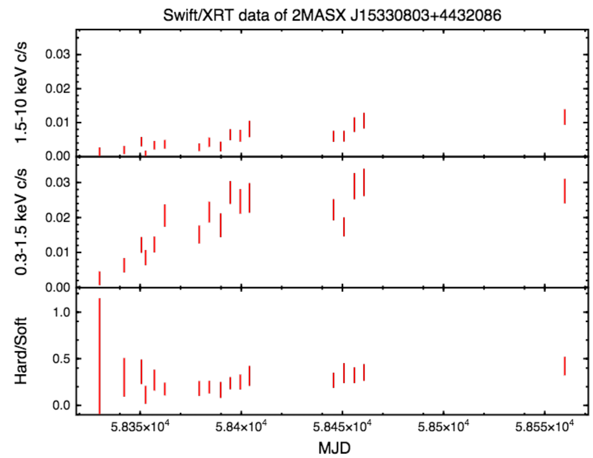

Figure 2.10: Left panel: XRT spectral fit to a broken power law with soft photon index $\Gamma = 2.82^{+0.35}_{-0.26}$ described in Section 2.3.6.4. Right panel: Although a slow rise is evident at the 0.01 counts s^{-1} level in the hard band (defined as 1.5$-$10 keV), the hardness ratio light curve shows that the X-ray flare is primarily soft, i.e. 0.3$-$1.5 keV.

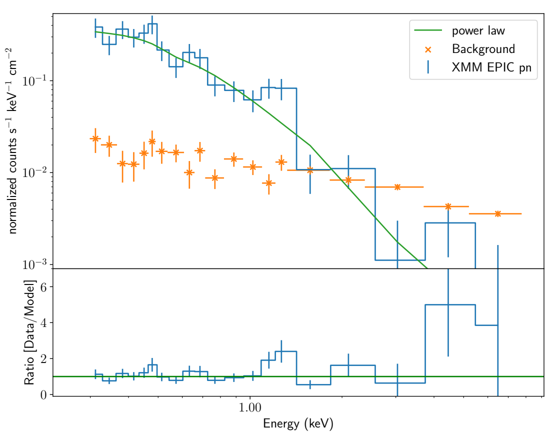

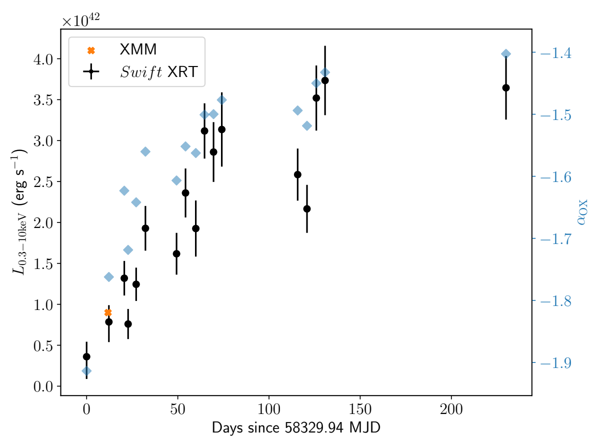

Figure 2.11: Left panel: The *XMM* EPIC pn data of ZTF18aajupnt fit to a simple absorbed power law with spectral index Γ = 3.02$\pm$0.15 shows a prominent, steep soft excess. Right panel: The X-ray luminosity derived from a power law fit with Γ=3 is plotted in comparison with $\alpha_{\rm OX}$ (described in Section 2.3.6.4).

observed for NLS1s ($\overline{\Gamma}$ = 2.8 $\pm$ 0.9; Boller et al., 1996; Forster & Halpern, 1996; Molthagen et al., 1998; Rakshit et al., 2017).

Using the PIMMS count rate calculator[26], the conversion factor between counts and unabsorbed flux is 3.1$\times$10^{-11} for XRT, and 1.5$\times$10^{-12} for *XMM*.

[26] `https://heasarc.gsfc.nasa.gov/cgi-bin/Tools/w3pimms/w3pimms.pl`

2.2.8 Infrared

Spitzer Infrared Array Camera (IRAC; Fazio et al. 2004) observations were triggered for five epochs on 2018 Aug 13 under the approved ToO program (PI: Yan, PID:13251). At each epoch, the data were taken for both 3.6 and 4.5μm, each with a total of 600 seconds exposure time. A 50 point cycling dither pattern was used. The first three epochal data were taken and used for the analysis when this paper was prepared. The coadded and mosaiced images were produced by the standard *Spitzer* pipeline and are directly used by our analysis.

We measured a maximum increase of 0.14 mag compared to archival WISE observations. We correct the difference magnitude for the small difference between the bandpass of the two instruments: 0.19, 0.03 mag for channels 1 and 2, respectively, as measured using stars in the field. In Figure 2.8, we show that this νL_ν at 3.6/4.5 μm (subtracting our estimate of the host galaxy baseline as measured by WISE) is greater than νL_ν in the UV, suggesting a large dust covering factor (the fraction of solid angle from the central source obscured by dust).

NEOWISE data (WISE, Wright et al. 2010) showed there was no variability from the host galaxy of ZTF18aajupnt for 1 year prior to its discovery in ZTF, despite the hint of optical variability observed in June 2016 by iPTF (Section 2.2.2).

2.2.9 Radio

We measure an archival FIRST VLA survey intensity upper limit (including CLEAN bias) of 0.89 mJy beam^{-1} at the location of the host of ZTF18aajupnt in 1997.

2.3 Analysis

2.3.1 Host Galaxy Classification

We compare the SDSS spectra of the LINER hosts, observed more than a decade prior to the changing looks caught by ZTF, with follow-up observations taken using the Palomar 60-inch (P60) telescope and the DCT in Figure 2.4. We fit stellar absorption and narrow emission lines to the host spectra with `pPXF` and results are in Figure 2.12. To distinguish them from star-forming galaxies, Kauffmann et al. (2003) define a galaxy as a Seyfert if

$$\log([\mathrm{OIII}]/\mathrm{H}\beta) > 0.61/(\log([\mathrm{NII}]/\mathrm{H}\alpha) - 0.05) + 1.3.$$

and Kewley et al. (2001) demarcate a Composite galaxy if

$$0.61/(\log([\mathrm{NII}]/\mathrm{H}\alpha) - 0.47) + 1.19 < \log([\mathrm{OIII}]/\mathrm{H}\beta)$$

is true. These functions are represented as the dashed and solid lines (respectively) in the BPT [OIII]/Hβ versus [NII]/Hα narrow-line diagnostic diagram shown in the upper left panel of Figure 2.13. Figure 2.13 also shows various other line ratio diagnostic diagrams involving the line ratios [OIII]/Hβ, [NII]/Hα, [OI]/Hα, and [OIII]/[OII] (Baldwin et al. 1981; Kewley et al. 2001, Kauffmann et al. (2003), Kewley et al. 2006), including the WHAN diagram (Cid Fernandes et al., 2011), accounting for the equivalent width of Hα and the fact that the typical BPT LINER classification contains both "weak AGN" and "retired galaxies" that have ceased star formation.

Analysis of the archival SDSS spectra of the individual sources in this sample finds that all but CLQ iPTF16bco exist in the borderline region between LINER

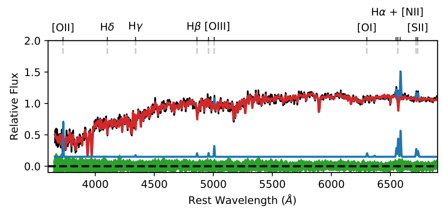

(a) ZTF18aajupnt

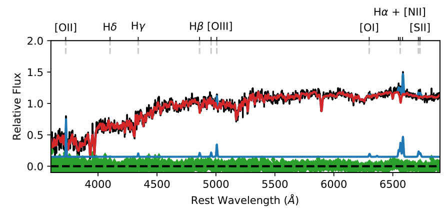

(b) ZTF18aahiqfi

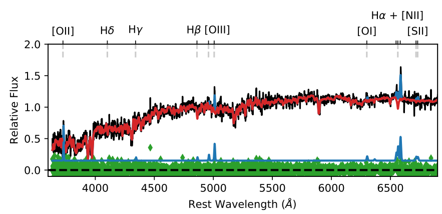

(c) ZTF18aaidlyq

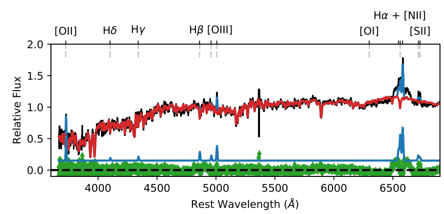

(d) ZTF18aasuray

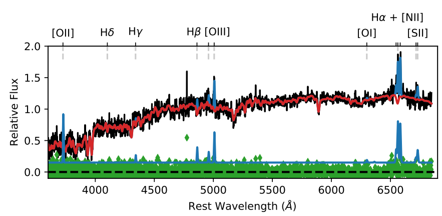

(e) ZTF18aasszwr

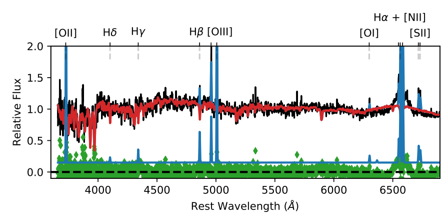

(f) ZTF18aaabltn

Figure 2.12: The SDSS spectra of the host galaxies were fit using the Penalized Pixel-Fitting (`PPXF`) method by Cappellari & Emsellem (2004). Red denotes the stellar population template, blue the emission line fits, and green points the residuals to the total best fit model. Note the poor fit to the [O II] and [O III] emission lines of ZTF18aaidlyq, which are replaced in subsequent analysis by the emission line fits in Figure 2.18. We do not re-analyze iPTF16bco (not shown here) and instead use the analysis from Gezari et al. (2017).

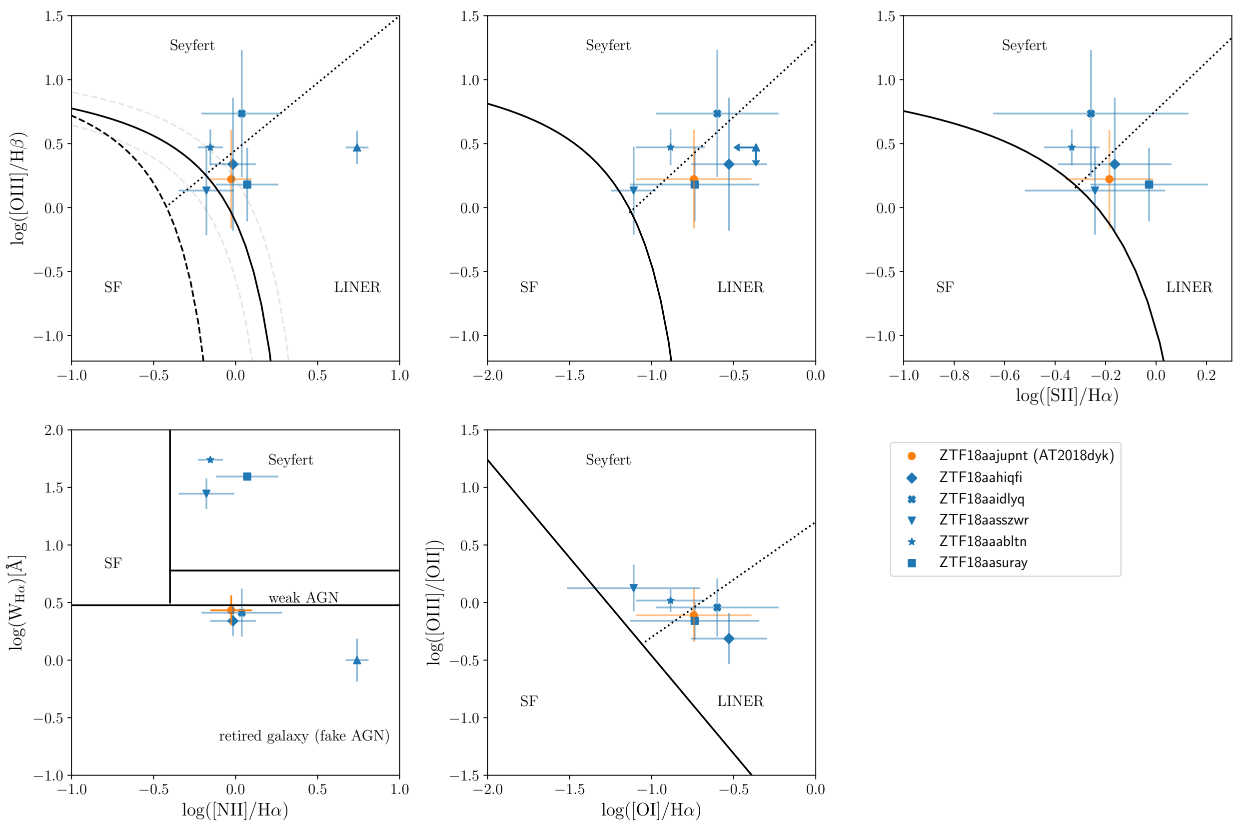

Figure 2.13: Narrow-line diagnostics for the CL LINER sample in the "off" state (i.e. their host galaxies), including iPTF16bco (values from Gezari et al. (2017)). The majority of the sample is on the borderline between a LINER and Seyfert classification. Note differences in scale. Upper limits are used when lines are not significantly detected.
Lower left panel: AGN diagnostic diagram from Cid Fernandes et al. (2011). Only three of the sources in the CL LINER sample require a Seyfert to power the Balmer emission lines in their low state, also indicated by the Hα line profiles requiring broad components, shown in the fits in Figure 2.18.

and Seyfert classifications for all five diagnostics shown in Figure 2.13. According to the diagram of Cid Fernandes et al. (2011), both weak and "fake" AGN scenarios are plausible within the 1σ errorbars for three LINERs in this sample, excluding the host of iPTF16bco, which is considered a retired galaxy in this diagnostic, and the hosts of ZTF18aasszwr and ZTF18aaabltn, which are Seyfert-like (see lower left panel of Figure 2.13).

We note that the broad Hα component of ZTF18aaabltn is not completely gone in the spectrum representing its "off" state. Although it passed the sample selection criteria of being identified as a LINER in the Portsmouth SDSS DR12 catalog (described in Section 2.2.1), re-fitting of the line ratios of ZTF18aaabltn reveals that it is a Seyfert rather than a LINER. As we measured a broad base in Hα, we classify it instead as a Sy 1.9 (this is also consistent with prior radio and X-ray detections of this source). ZTF18aasuray displayed double-peaked broad Balmer emission indicative of an persistent broad line region with unchanging kinematics in both its low and high states. As the peaks did not represent high enough velocities or asymmetric enough profiles to require separate components, we fit a single broad Gaussian base in this source when measuring the narrow line ratios. Unlike ZTF18aaabltn, those measurements were in agreement with the LINER classification.

Similarly to this work, Thomas et al. (2013) also used `pPXF` to fit stellar kinematics and the [S II]/Hα ratio diagnostic from Schawinski et al. (2007) (upper right panel of Figure 2.13) to classify a source as a LINER; however, they used the Gas and Absorption Line Fitting code (`GANDALF` v1.5; Sarzi et al. (2017)) to fit emission lines, whereas we use a simple multi-component Gaussian profile fit to the narrow lines in the stellar-template-subtracted spectra (see Figure 2.18 in the Appendix for these model fits). There may also be a discrepancy stemming from `GANDALF` correcting for dust—the majority of this sample have Balmer decrement $f_{\mathrm{H}\alpha}/f_{\mathrm{H}\beta} > 3.1$, indicative of strong intrinsic reddening. However, we choose not to apply a dust correction since it is an uncertain measurement for this sample, due to the weak emission line intensities.

2.3.2 Black Hole Masses

In order to shed light on the physical differences between the individual AGN in this sample, we estimate the black hole masses of the CLAGN hosts using several methods. The broad Hβ line is the most common virial estimator for BH masses at low redshift ($z \lesssim 0.4$; e.g. Marziani & Sulentic 2012).

$$M_{\rm BH,vir} = 1.5 \times 10^5 \left(\frac{R_{\rm BLR}}{\text{light days}}\right)\left(\frac{\rm FWHM(H\beta)}{10^3 \rm kms^{-1}}\right)^2 M_\odot$$

where $R_{\rm BLR} = 32.9(\frac{\lambda L_{5100A}}{10^{44}\rm ergs^{-1}})^{0.7}$ light days (Kaspi et al., 2000). We also calculate $M_{\rm BH}$ from the host galaxy luminosity following McLure & Dunlop (2002) such that

$$M_{\rm BH,M_r} = -0.5 M_{r,\rm host} - 2.96,$$

and the host bulge stellar mass using the relation from Häring & Rix (2004)

$$\log(M_{\rm BH,Bulge}[M_\odot]) = \log(0.0014 \rm M_{Bulge}[M_\odot]),$$

and computed and from the stellar velocity dispersion ($\sigma_\bigstar$) measured from the SDSS spectrum using the `pPXF` method) using the $M_{\rm BH} - \sigma$ relation from Tremaine et al. (2002)

$$\log M_{{\rm BH},\sigma\bigstar}[M_\odot] = 8.13 + 4.02 \log(\sigma_\bigstar / 200 \text{ km s}^{-1}).$$

The results of these measurements are summarized in Table 2.2, and discussed further in Section 2.3.3.

2.3.3 Comparison to Tidal Disruption Events

It is important to compare the properties of this class of AGN "turning-on" from quiescence with a related phenomenon of tidal disruption events (TDEs). When a star passes close enough to a central black hole to be ripped apart by tidal forces, roughly half of the stellar debris will remain bound to the black hole and provide a fresh supply of gas to accrete onto the black hole. The evolution of the flare of radiation from a TDE is regulated by the fallback timescale ($t_{\rm fb}$), the time delay for the most tightly bound debris to return to pericenter after disruption, and the circularization timescale, which is dependent on the efficiency at which the debris streams shock and circularize due to general relativistic precession. Interestingly, the virial black hole mass for all the CL LINERS in the iPTF/ZTF sample are above the black hole mass for which a solar-type star can be disrupted outside the event horizon ($M_{\rm BH} \lesssim 10^8\ M_\odot$). The only exception is ZTF18aajupnt, which as a NLS1 in its "on" state, thus with narrower lines, naturally implies a smaller black hole mass with this method. However, the black hole mass inferred from the host galaxy velocity dispersion and bulge mass suggest a larger black hole mass of $\log(M_{\rm BH}/M_\odot) = 7.6 - 7.8$. This trend of the black hole mass from the virial method being much smaller is consistent with the work of Rakshit et al. (2017), who suggest that the smaller Balmer line widths measured in NLS1s which lead to lower BH masses are due to the geometrical effects of being viewed more face-on ($\langle i \rangle = 26°$) compared to normal broad line Sy 1s ($\langle i \rangle = 41°$). This claim is backed up by spectropolarimetric studies of NLS1s (Baldi et al., 2016). Alternately, Marconi et al. (2008) suggested that in rapidly accreting objects (including NLS1s), enhanced ionizing radiation pressure could also lead to underestimates of virial black hole mass estimates.

It is also possible that these transitioning AGN do not obey the radius-luminosity relation established from reverberation mapping studies of Seyfert galaxies. If we instead use the black hole mass estimates from the host galaxy velocity dispersion, luminosity, and/or stellar mass, we find that the CL LINER sample have black hole masses of $\log(M_{\rm BH}/M_\odot) \sim 7 - 8$, close to, but not necessarily exceeding the upper mass limit for the tidal disruption of a solar-type star.

We can also compare the light curves and spectra of our CL LINERs to TDEs. The quiescence in the light curves before the onset of their flaring activity, their blue colors ($g - r < 0$) during the flaring in most of the cases, as well as their smooth decline from peak are generally consistent with the TDE scenario. The main distinction is in their spectral properties at peak. The five objects caught transitioning from a LINER to a type 1 AGN show spectra in their "on" state that are almost indistinguishable from normal quasars, besides the relative weakness of [O III]. In contrast, TDEs exhibit exclusively broad emission lines; broad He II λ4686 emission, and/or broad Hα and Hβ lines, and sometimes broad He I, but with line luminosities of $\lesssim 10^{41}$ ergs s^{-1} (Arcavi et al., 2014; Brown et al., 2016; Holoien et al., 2018; Hung et al., 2017), well below the CL LINERs (see Figure 2.14). Furthermore, the X-ray spectra of the CL LINERs with X-ray observations in their "on" state, iPTF16bco and ZTF18aajupnt, are well described by a power-law, with $\Gamma = 2.1$ (Gezari et al., 2017) and $\Gamma = 3.0$, respectively, and are clearly distinct from the extremely soft blackbody spectra with $kT \sim 0.04 - 0.10$ keV characteristic of both optically and X-ray selected TDEs (Komossa, 2002; Miller et al., 2015; van Velzen et al., 2019). We present a more detailed comparison of the observed properties of ZTF18aajupnt with TDEs in Section 2.3.6.

2.3.4 Comparison to Seyfert CLAGN

We measure the Hα and [O III] λ5007 luminosities for this sample in their "on" state in Figure 2.17 and compare to that of SDSS Sy 1s (including NLS1s; Mullaney et al. (2013)) and quasars (Shen et al., 2011). All AGN in this sample display [O III] λ5007 luminosities significantly below average for their observed broad Hα luminosity in their "on" state, consistent with the findings of Gezari et al. (2017), that CLQs with appearing (disappearing) broadlines were in general closer to the fringe (average) of the quasar distribution. However, for ZTF18aasszwr and ZTF18aaabltn, only upper limits of [O III] were possible due to the low SNR for narrow lines of the low-resolution ($R \sim 100$) follow up spectra.

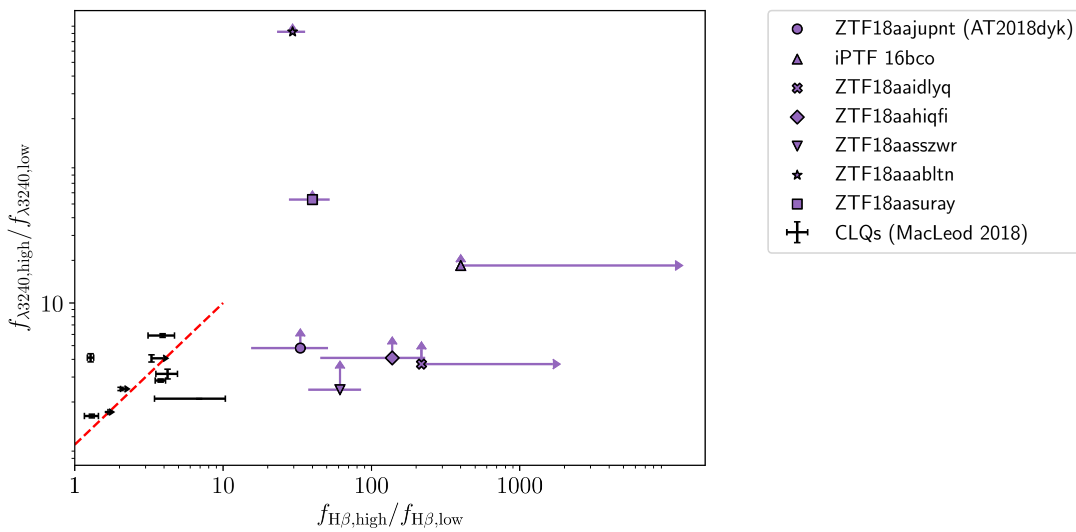

Figure 2.14: Ratio of continuum flux change as a function of broad line flux change for our changing-look LINER sample (filled shapes) in comparison to changing-look Seyferts. ZTF18aajupnt (purple circle), is intermediate in flux ratio and Hβ ratio space between Seyfert CLAGN (black, lower left) and the other CL LINERs in this sample. The red dotted line denotes a 1:1 ratio between the continuum and Hβ fluxes. iPTF16bco, ZTF18aasuray, ZTF18aasszwr, iPTF16bco are outliers in differential continuum space (although we collected spectra of the latter two with an IFU spectrograph that can be unreliable at bluer wavelengths), and iPTF16bco, ZTF18aaidlyq, and ZTF18aahiqfi are outliers in Hβ luminosity space compared to that of the Seyfert CLAGN. All have much larger (by a factor of > 10) changes in broad line flux than the changing-look Seyfert sample. The $f_{\lambda 3240}$ ratio measurements are represented as lower limits, as there is stellar contamination in the low (LINER) state. Adapted from Figure 6 in MacLeod et al. (2019).

MacLeod et al. (2019) systematically obtained spectra for highly-variable candidate CLQs (defined as type 1 AGN transitioning to type 2s or vice versa) within the SDSS footprint, requiring Pan-STARRS 1 variability exceeding $|\Delta g| > 1$ mag and $|\Delta r| > 0.5$ mag. We find agreement with their measured positive correlation between broad emission line and continuum flux changes, but find that our sample of CL LINERs is more extreme in the parameter space of continuum and Hβ flux ratios (ranging from 2−800 and 12−400, respectively) than the CLQ sample from MacLeod et al. (2019) (with $f_{\rm high}/f_{\rm low} = 1-7$ and 2−8 for continuum and Hβ, respectively), shown in Figure 2.14. When restframe flux at 3240 Å was not available to us due to inconsistent spectral coverage, we measured flux at the shortest available comparable wavelength.

2.3.5 Eddington Ratio Estimates

We compute the Eddington ratio ($L_{\rm bol}/L_{\rm Edd}$) for the sample in their "on" state assuming $L_{\rm bol} = 9\lambda L_{5100A}$ (Kaspi et al., 2000), summarized in the final column of Table 2.2. $L_{\rm bol}$ in the "on" state is measured using difference imaging in the filter with central wavelength closest to rest-frame 5100 Å for each source (r-band for higher-redshift sources iPTF16bco, ZTF18aaidlyq, and ZTF18aasszwr, and g-band for all others). $L_{\rm bol}$ in the "off" state is measured from the reddening corrected $L_{\rm [O\ III]}$ narrow line luminosity correlation to $L_{2-10\ \rm keV}$ for type 2 AGN (Equation 1 in Netzer et al. (2006)) and using the same bolometric correction as Elitzur et al. (2014), $L_{\rm bol} = 15.8 L_X$.

While virial black hole masses based on the broad Hβ line and continuum luminosity are more generally used for AGN, those relations are based on reverberation mapping studies which were never done specifically for NLS1s. Thus, for the remainder of this work, we adopt BH mass estimates for the sample to be consistent with $M_{\rm BH}$ from stellar velocity dispersions as described in Section 2.3.2 and summarized in Table 2.2.

The Seyfert CLAGN with appearing broad emission lines in the variability-selected MacLeod et al. (2019) sample (summarized in Section 2.3.4) have $-2 \lesssim \log(L/L_{\rm Edd}) \lesssim -1$, slightly below that of a control sample of extremely variable quasars and normal SDSS DR7 quasars. For the relatively large range of this small sample ($-1.7 \lesssim \log(L/L_{\rm Edd}) \lesssim -0.3$), it is difficult to distinguish which population's Eddington ratios to which they are better matched in their "on" state. The corresponding upper limits of $\log\,(L/L_{\rm Edd}) < -2$ in the "off" states of the LINER host galaxies are in good agreement with that of the MacLeod et al. (2019) CL population that has dimmed.

Elitzur et al. (2014) predict a natural sequence within the disk-wind scenario in which AGN evolve from displaying to lacking broad optical emission lines. This evolution is driven by variations in accretion rate (with the critical value parameterized by $L_{\rm bol}/M_{\rm BH}^{2/3}$), as well as the availability of ionizing radiation from the central engine. The BLR is therefore posited to be assembled following an increase in accretion rate (likely due to instabilities to match the fast timescales observed; Rumbaugh et al. (2018)). Due to an insufficient cloud flow rate and lack of ionizing photons, no BLR can be sustained below the critical accretion rate or bolometric luminosity ($L_{\rm bol} \leq 5 \times 10^{39} M_7^{2/3}$ erg s^{-1}, Elitzur & Ho (2009)). This spectral evolutionary pathway is supported by modeling an SDSS-selected sample of Seyferts of various types and spanning $L/L_{\rm Edd} \sim 10^{-3}$ to 0 (Stern & Laor, 2012), for which accretion rate progressively decreased with luminosity from type 1s to type 2-like AGN. In Figure 2.15 we recreate this sequence represented by AGN with different spectral classifications occupying distinct regions of the $L_{\rm bol} - M_{\rm BH} - L/L_{\rm Edd}$ parameter space and roughly separated by the critical threshold of Elitzur & Ho (2009). We overplot the CL LINER sample in their "on" states which overlap roughly with the Seyfert type 1 sources, and in the "off" LINER states which overlap largely with

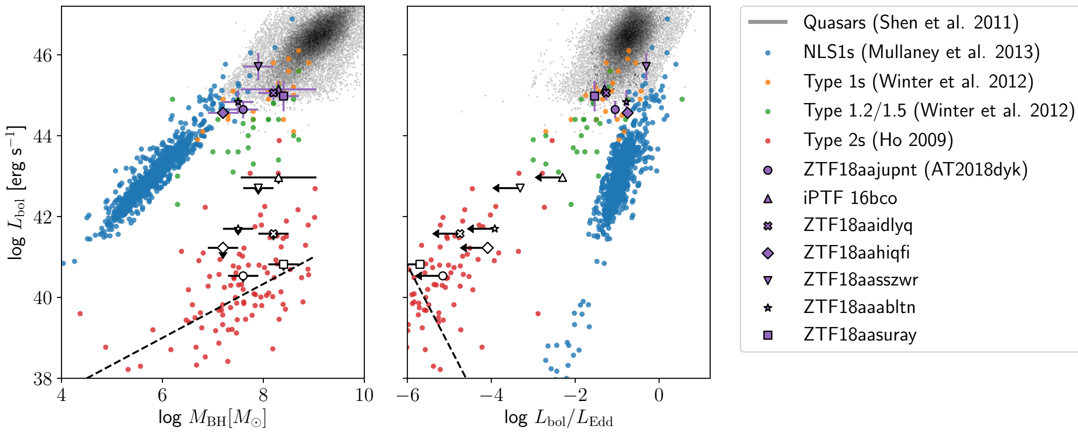

Figure 2.15: AGN, when separated by spectral classification, show the rough evolutionary sequence in parameter space of black hole mass $M_{\rm BH}$, bolometric luminosity $L_{\rm bol}$, and Eddington ratio $L_{\rm bol}/L_{\rm Edd}$ described in Section 2.3.5. The dotted lines denote the critical values above which a BLR can be sustained from Elitzur & Ho (2009) described in Section 2.3.5, to which we compare the measured values for the sample (filled, purple shapes with same mapping as in Figure 2.14) and their hosts (unfilled, black). The CL LINER sample in their "on" state is consistent with the type 1s (orange points), with ZTF18aajupnt in its high state (filled circle) toward the high luminosity end of the NLS1 distribution (blue points). We note that the type 2 sample from Ho (2009) contains LINER2s and LLAGN. Adapted from Figure 1 in Elitzur et al. (2014).

the type 2s and border on the intermediate type 1.2/1.5 Seyferts.

The bolometric luminosities (and therefore the Eddington ratios) are upper limits in Figure 2.15 due to the "off" spectra being almost entirely host dominated. iPTF16bco, ZTF18aasuray, ZTF18aaidlyq, and ZTF18aasszwr approach the quasars in their "on" states, and ZTF18aajupnt does not fall squarely among the NLS1s but instead in the border region between types. The least luminous sources in the sample, ZTF18aajupnt and ZTF18aasuray, approach most closely the critical Eddington ratio for the existence of a BLR in their "off" states, and the most luminous iPTF16bco is closest to the intermediate types in its LINER state.

2.3.6 ZTF18aajupnt: A LINER Changing-Look to a NLS1

For the following analysis we focus on ZTF18aajupnt, for which we have the most extensive follow-up data, and which showed the appearance of coronal lines along with X-ray variability. The difference imaging light curve of this event displays a plateau similar to that of iPTF16bco (Gezari et al. (2017); see comparison in Figure 2.5), before fading gradually over several months in a manner similar to that of CL LINER ZTF18aasszwr, rather than the power-law decline characteristic of an optical TDE light curve (e.g. Hung et al. 2018).

The lack of IR variability in NEOWISE leading up to the turn-on of ZTF18aajupnt constrains the presence of any IR AGN activity or dust echo in this host to < 10 months. W1-W2 is never greater than $\sim$0.02 during this time, far below the 0.8 threshold AGN diagnostic value from Stern et al. (2012). Stability in the CRTS light curve similarly confirms that no AGN-like variability was present for 13 years prior to its discovery with ZTF. There was, however, a hint of some $\sim$0.1 mag flaring in the CRTS light curve in June 2006 and April 2007. Additionally, we extracted forced photometry (Masci et al., 2017) for ZTF18aajupnt from the PTF database covering June 2011 to June 2016, and there were only 8 marginal detections near the limiting magnitude of PTF (from 20 to 20.9 r-band mag) for the last 15 days of this range.

To reproduce the photometry of ZTF18aajupnt, any physical explanation must explain a rise time of $\sim$50 days and a slow decline rate of $\sim$0.5 mag in 60 days, both quite unusual for a TDE or supernova (e.g. van Velzen et al. 2019). Arcavi et al. (2018) note that the difference imaging light curve of ZTF18aajupnt peaks at an absolute magnitude of -17.4 mag, which is much fainter than the majority of TDEs by several magnitudes, excluding iPTF16fnl (Blagorodnova et al., 2017). A power law and blackbody give nearly identical fits to the UV spectra (with $\overline{T_{\rm bb}} = 4.5 \times 10^4$

K) with no change in the slope as the continuum fades over $\sim$140 days; Figure 2.9). The optical continuum in Figure 2.7 is well fitted with a power-law, consistent with the Rayleigh-Jeans tail of a blackbody.

In the UV, the observed spectrum does not resemble that of a TDE in a LINER (e.g. ASASSN-14li, Cenko et al. (2016)). Instead, the UV spectrum of ZTF18aajupnt is very similar to the UV spectra of normal NLS1s, with a similar spectral slope and peaked, broad emission line shapes (see Figure 2.9). In particular, ZTF18aajupnt has a strong C IV $\lambda\lambda 1548, 1551$ line and C III] $\lambda 1909$ line, which is typical of NLS1s, but not detected in all the TDEs with HST UV spectra: ASASSN-14li (Cenko et al., 2016), iPTF15af (Blagorodnova et al., 2019), iPTF16fnl (Brown et al., 2018), AT2018zr (Hung et al., 2019). Interestingly though, ZTF18aajupnt does show N IV] $\lambda 1486$ emission, which is just barely detected in NLS1s (Constantin & Shields, 2003) and *is* detected in the UV spectrum of TDE ASASSN-14li, which was argued to be N-rich. The critical density 3.4×10^{10} cm^{-3} of the intercombination N IV] $\lambda 1486$ line provides an upper limit to the density of this gas in ZTF18aajupnt (Nussbaumer & Storey, 1979). The late-time increase in the Mg II line has not been detected in a TDE; in fact the opposite trend has potentially been observed: the brightening of broad Mg II with the fading of the transient in TDE AT2018zr (Hung et al., 2019). Finally, ZTF18aajupnt demonstrates none of the broad absorption features seen in the UV spectra of TDEs, and has been associated with powerful outflows launched by the accretion process in a TDE.

2.3.6.1 Coronal Line Emission from ZTF18aajupnt

We report line measurements of the Keck spectrum of ZTF18aajupnt in Table 2.4. We choose to analyze the spectrum from this instrument because of its sufficiently high SNR and spectral resolution to measure the presence of coronal lines. For each of these measurements, the stellar population of the host galaxy represented by the ppxf fit has been subtracted (See Figure 2.12 for a visual of the stellar model template).

The width of the majority of the coronal lines is narrower than the widths of the broad permitted AGN emission lines (see Figure 2.16), as is expected from forbidden high-ionization collisionally-excited emission because it originates from a larger distance from the ionization source. However, there is no strong evidence that the coronal emission lines in ZTF18aajupnt are observed with widths between the BL and NL emission, as expected in the scenario in which gas is outflowing from an intermediate coronal line region (CLR; e.g. Mullaney & Ward 2008). The [Fe X] line is unlikely to be broader than expected due to blending with the [O I] λ6364 line (e.g. Pelat et al. 1987), as it is in a 1:3 ratio with the [O I] λ6300 line which is observed to be weaker than [Fe X] in this source. In Sy 1s, [Fe X] tends to be relatively stronger than the other coronal lines (e.g. Pfeiffer et al. 2000). However, in Seyferts the CL emission is typically measured to be only a few percent of the strength of [O III] λ5007).

The fact that [Fe X] λ6374 is stronger than [O III] λ5007 places ZTF18aajupnt away from other Seyferts and instead among the $<$10 known extreme coronal line emitters (ECLEs) in this parameter space. We discuss further the ECLE scenario in Section 2.4.2. We note that the weakness of [O III] may be due to light travel time effects, and thus may strengthen with time.

We note the significant spectral differences between ZTF18aajupnt and SN 2005ip post-peak (Smith et al., 2009). SN 2005ip has much more prominent coronal lines than even the example ECLEs, as well as a strong hydrogen emission series, much broader than the quasar iPTF16bco plotted alongside it.

Korista & Ferland (1998) presented a model by which coronal lines are the result of ISM interaction with bare Seyfert nuclei, i.e. AGN lacking any X-ray/UV evidence of intrinsic absorption by ionized gas along the line of sight to the AGN.

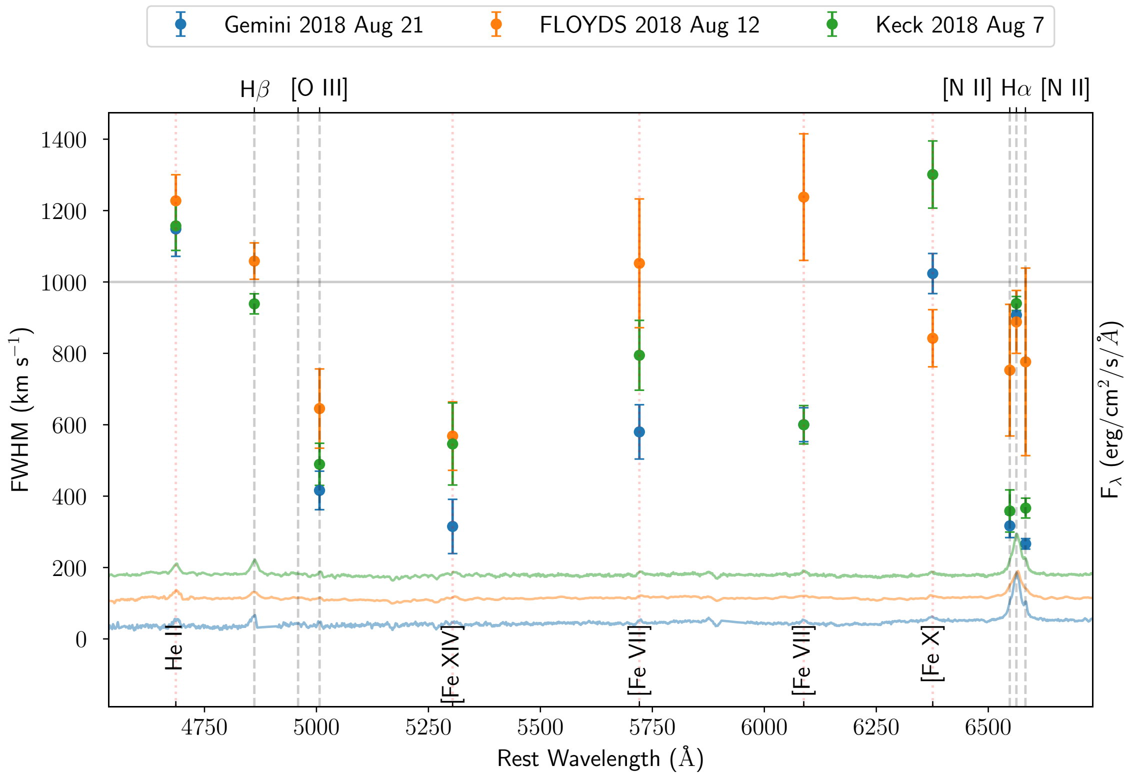

Figure 2.16: FWHM of Hα, Hβ, and the coronal lines for each high-resolution optical observation of ZTF18aajupnt in its "on" state. The stellar population of the host galaxy has been subtracted.

This model is consistent with our finding of no intrinsic absorption in the X-ray spectra of ZTF18aajupnt.

2.3.6.2 ZTF18aajupnt as a NLS1 in its "On" State

At the other extreme of eigenvectors of AGN spectral properties are narrow-line Seyfert 1 galaxies (NLS1s), a subclass of AGN that are characterized by relatively narrow Balmer lines (FHWM < 2000 km s^{-1}), strong broad Fe II emission, [O III] $\lambda 5007/\mathrm{H}\beta_{\mathrm{tot}} < 3$, a prominent soft X-ray excess (e.g. Puchnarewicz et al. 1992), and dramatic variability, especially in the X-rays (e.g. Frederick et al., 2018; Pogge, 2000). These spectral properties of NLS1s are attributed to lower-mass central black holes ($5 < \log(M_{\mathrm{BH}}[M_\odot]) < 8$; e.g. Mathur et al. 2001) that are thought to accrete at high Eddington ratios (Grupe et al., 2010; Pounds et al., 1995; Wang et al., 1996; Xu et al., 2012).

We measure $1000 \lesssim \mathrm{FWHM(H}\beta) < 2000$ km s^{-1} which is indicative of a narrow-line Seyfert 1 galaxy in the AGN interpretation (Goodrich, 1989), as well as the fact that the Balmer lines are significantly better fits to Lorentzian line profiles than Gaussians (Nikołajuk et al., 2009). However, the FWHM limits between Sy 2s, NLS1s and Sy 1s is somewhat arbitrary (Mullaney & Ward, 2008; Véron-Cetty et al., 2001), and may even be better set at 2200 km s^{-1} (Rakshit et al., 2017). The fact that some of the line measurements fall short of this cutoff could speak to the intermediate nature of this transitioning object in the changing-look scenario. The virial mass measurement for ZTF18aajupnt is consistent with the NLS1 interpretation, as NLS1s display properties consistent with AGNs with lower masses (Grupe & Mathur, 2004), though it is toward the high end of the NLS1 mass distribution (Xu et al., 2012). Also consistent with the NLS1 scenario is that [O III] λ5007 / Hβ = 0.1 < 3 (Osterbrock & Pogge, 1985). However, [O III] λ5007 appears to be relatively quite weak when compared to that of of prototypical NLS1, Mrk 618, in Figure 2.6. It should also be noted that the coronal lines in ZTF18aajupnt appear to be symmetric and at the same systematic redshift as the Balmer series and low-ionization forbidden lines, whereas coronal lines in Seyferts can be significantly broadened, asymmetric, and blueshifted consistent with an outflowing wind launched between the BLR and NLR (Rodríguez-Ardila et al. (2006); in NLS1s: Erkens et al. (1997); Mullaney & Ward (2008); Porquet et al. (1999)). This is less common, but not unheard of, for ECLEs (See Section 2.4.2).

It is evident from all follow-up spectra of ZTF18aajupnt in Figure 2.6 that it is also missing the prominent Fe II pseudo-continuum complex characteristic of NLS1s. Therefore we do not utilize an Fe II template in subsequent optical nor UV spectral fitting. The intense ionizing radiation and high temperatures inferred from the presence of the coronal line emission should make visible the multiply ionized Fe II were it present. The fact that Fe II lags behind Hβ in reverberation mapping studies of AGN (Barth et al., 2013) could mean that not enough time has passed for this component to be irradiated, consistent with the weak presence of [O III] (Figure 2.17). Runnoe et al. (2016) also found that, for some CLAGN, the Fe II complex was only present in the "on" state. In AGN there is a robust negative correlation between [O III] and Fe II (the so-called Eigenvector 1; Boroson & Green (1992)), which manifests typically as weak [O III] in NLS1s (e.g. Rakshit et al. 2017), possibly indicating we should expect Fe II to become stronger in ZTF18aajupnt after the light-travel delay time.

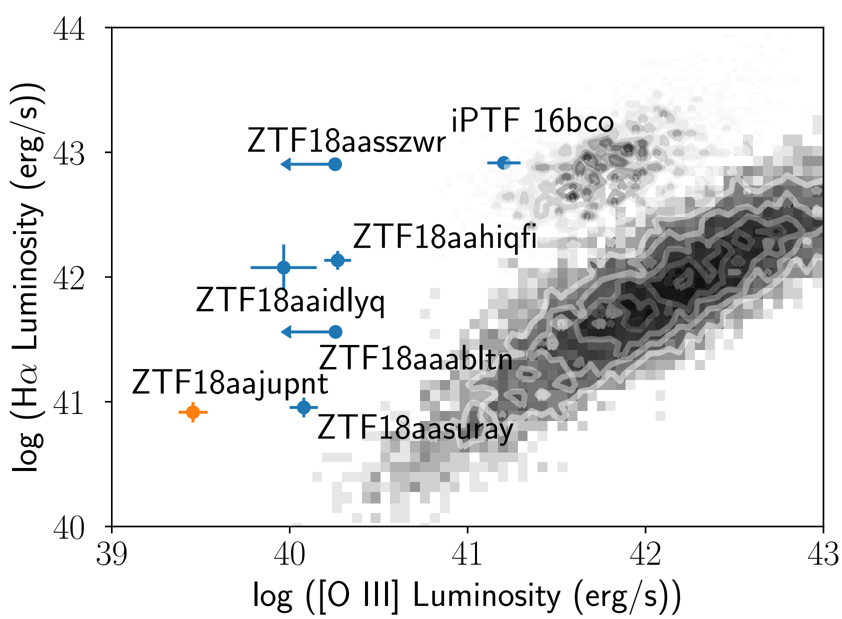

Figure 2.17: Hα and [O III] λ5007 line luminosities measured for this sample of CL LINERs, in the high state. The upper and lower contours representing log $L_{\mathrm{H}\alpha}$ vs. log $L_{[\mathrm{O\ III}]}$ measurements of SDSS DR7 quasars and Sy 1 galaxies from Shen et al. (2011) and Mullaney et al. (2013) show that this sample is up to an order of magnitude underluminous in [O III], due to light-travel time delays of an extended narrow line region that has yet to respond to the continuum flux change. The lower limits of ZTF18aasszwr and ZTF18aaabltn are due to the [O III] λ5007 emission line not being resolved in the low-resolution ($R \sim 100$) follow-up spectra. Adapted from Figure 6 in Gezari et al. (2017).

Narrow He II is frequently observed in AGN, however we measure strong He II broader than the Balmer emission lines (Figure 2.16), possibly revealing an inner nuclear region not typically probed by the Balmer emission lines alone. This has been seen in a number of Seyferts such as the Sy1 Mrk 509, but is far less common.

He II λ1640 and [C III] λ1909 observed in the UV spectrum are consistent with the presence of higher ionization coronal lines in the optical. All prominent emission features are similar in strength and width to those in the *HST* FOS spectrum of NLS1 Mrk 335 and Mrk 478, shown in Figure 2.9 for comparison, however, with a Mg II λ2798, which is only marginally detected in the first *HST*/STIS epoch, and then brightens significantly 4 months later. However, like [O III], the late-time brightening of Mg II is likely a result of light travel time delays if the Mg II and [O III] line emitting gas resides further out from the central black hole.

2.3.6.3 The Accretion Rate of ZTF18aajupnt

The Eddington ratio of ZTF18aajupnt ranged between 0.02 and 0.09 from 2018 June to September, assuming the average BH mass of log $M_{\rm BH}[M_{\odot}]$=7.1 (estimates described in Section 2.3.2 from stellar velocity dispersion as well as from the standard virial method; Shen et al. 2011). Note that we assume a constant for the bolometric correction, but the SED is likely changing throughout the evolution of this source given the dramatic variability in $\alpha_{\rm OX}$ described below. This $L/L_{\rm Edd}$ is toward the low end of the NLS1 distribution, and on the high end for that of CLQs (MacLeod et al., 2019; Xu et al., 2012). The range of Eddington ratios for the remainder of the sample is 0.03$-$0.8. ZTF18aajupnt is probing a critical inflection point in $\alpha_{\rm OX}$ and Eddington ratio space related to accretion rate driven state changes analogous to that of X-ray binaries (Ruan et al., 2019a).

2.3.6.4 X-ray Light Curve and Spectra of ZTF18aajupnt

We initially measure a soft X-ray luminosity of a few $\times 10^{41}$ erg s^{-1} from the first *Swift* XRT observations of ZTF18aajupnt on 2018 July 30. Wang et al. (2011) require at least a few $\times 10^{42}$ erg s^{-1} to power the CLR, a level which ZTF18aajupnt did not reach until ∼40 days later. The XRT light curve in the right panel of Figure 2.10 shows that ZTF18aajupnt is a variable X-ray source (we note that high-amplitude X-ray variability is characteristic of NLS1s; e.g. Nikołajuk et al. 2009). The excess variance (or fractional amplitude of variability) defined by Nandra et al. (1997) as $\sigma^2_{\rm rms} = \frac{1}{N\bar{x}}\sum_{i=1}^{N}(x_i - \bar{x})^2 - \delta x^2$ of the 0.3-10 keV 130-day light curve[27] is 0.41, similar to that of the most variable NLS1s, but high for Sy 1s (Grupe et al., 2000). We measure a maximum luminosity of $L_X = (3.7 \pm 0.4) \times 10^{42}$ erg s^{-1}. This X-ray luminosity is difficult to obtain with even the brightest supernova explosions, which have been observed up to $\sim 10^{41}$ erg s^{-1} (Immler & Lewin, 2003), and it is toward the lower end for both Seyferts and NLS1s (Hasinger, 2008). The hardness ratio light curve in the right panel of Figure 2.10 shows that the X-ray flare is primarily in the soft band i.e. 0.3−1.5 keV, while the 1.5−10 keV light curve tracks the variability but with a much smaller amplitude. In contrast, the optical and UV photometry displays a plateau during this time, reminiscent of that of iPTF16bco (Figure 2.1, 2.5), before declining over several months in a manner similar to ZTF18aasszwr.

The simultaneous optical-to-X-ray spectral slope ratio ($\alpha_{\rm OX}$) defined as

$$\alpha_{\rm OX} = 0.3838 \log(L_{2\ {\rm keV}}/L_{2500{\rm A}})$$

by Eq. 4 of Tananbaum et al. (1979), and Eq. 11 of Grupe et al. (2010), over several epochs, measures roughly how an object's SED is changing with time, and is strongly correlated with Eddington ratio (Poole et al., 2008). However, Grupe

[27] The detections used to compute the excess variance were in units of counts.

et al. (2010) argue that this correlation is only a reliable estimator for Eddington ratio for sources with $\Gamma \leq 1.6$, above which the relationship saturates. We derive $\alpha_{\rm OX}$ from the multi-epoch concurrent observations between 2018 July 30 (61 days after discovery) and Dec 08 by *Swift* XRT and UVOT (taken with the UVW2 filter, which has a central wavelength of 1928Å and FWHM 657Å; Poole et al. (2008)).

ZTF18aajupnt shows dramatic variability in the X-rays (rising by an order of magnitude in 5 months with L_X that varied between (0.4− 3.1) $\times 10^{42}$ erg s^{-1}; see Figure 2.10). However, the range of $\alpha_{\rm OX}$ for ZTF18aajupnt (-1.15−-0.67) is fairly consistent with that of typical LINER values ($-1.4 < \alpha_{\rm OX} < -0.8$; Maoz (2007)) and systematically shallower than that of Type 1 Seyferts ($-2.0 < \alpha_{\rm OX} < -1.2$ (Elvis et al., 1994; Steffen et al., 2006)) and most NLS1s ($-1.8 < \alpha_{\rm OX} < -0.9$; Gallo (2006).

The soft X-ray spectrum and coronal line emission in ZTF18aajupnt are shared characteristics with NLS1s. The soft X-ray component in excess above the extrapolation of hard X-ray power-law continuum is observed in a large fraction of Seyfert AGN (Singh et al., 1985), but is particularly strong in NLS1s. The full extent of the soft excess component remains unknown, and its origin is debated. It has been ruled out as the tail of the UV thermal emission from the accretion disk (Gierliński & Done, 2004; Miniutti et al., 2009; Piconcelli et al., 2005; Porquet et al., 2004) but Comptonization of those seed photons by an optically thick medium is now one of the favored scenarios (e.g. Done et al. 2012), as is blurred ionized disk reflection García et al. (2019).

Due to their high ionization potentials ($\chi > 100$ eV), coronal lines can probe the soft X-ray excess indirectly, as well as the SED in the vicinity of 200 eV, which is difficult to observe otherwise because of both Galactic and intrinsic photoelectric absorption, but important due to their significant contribution to $L_{\rm bol}$. Erkens et al. (1997) found that coronal lines were more likely to be present in Seyferts with steeper X-ray spectra. Gelbord et al. (2009) found in a sample of Seyfert galaxies a correlation between soft X-rays and [Fe VII], [Fe X], and [Fe XI] lines, proposed by Murayama & Taniguchi (1998a,b) to originate from the innermost wall of the dusty torus (see also Rodríguez-Ardila et al. (2002)).

NLS1s also display strong coronal line emission (e.g. Stephens 1989). Optical coronal lines include the forbidden transitions of iron, [Fe XIV] λ5304, [Fe VII] λ6088, [Fe X] λ6376 and [Fe XI] λ7894, as well as [Ar XIV] λ4414 and [S XII] λ7612. The coronal lines in NLS1s can be blueshifted with asymmetric velocity profiles and broad wings, consistent with an outflow (Erkens et al., 1997; Nagao et al., 2000; Porquet et al., 1999). Gelbord et al. (2009) found [Fe X]/[O III] to be the most extreme (by a factor of 2-3) in NLS1s with the narrowest broad lines (FWHM(Hα)$\sim$800 km s^{-1}) during a search for AGN with strong coronal lines in SDSS, and interpreted these sources as having strong soft excesses.

2.4 Discussion

While the number of CLAGN is steadily increasing, there has yet to be a large-scale systematic study of newly-discovered candidates that simultaneously tracks the appearance of continuum variability and the broad-line emission in real-time using high-cadence difference imaging photometry.

The best-studied target-of-interest in this sample was identified from ZTF based on its TDE-like rise time, and therefore we obtained several epochs of supporting data in real-time throughout its evolution. Its months-long plateau, UV/optical spectra, and high-energy properties were indicative of having changed look to a NLS1. Although they are typically highly X-ray variable, such dramatic optical variability of a NLS1 has only been seen in three other sources to-date, including CLAGN NGC 4051 (Guainazzi et al., 1998; Uttley et al., 1999), although it changed from an obscured Sy 2 and not a LINER. ZTF18aajupnt is therefore unique not only among this sample, but among CLAGN overall.

2.4.1 A New Class of changing-look LINERs

We establish this particular class of CLAGN associated with extreme order-of-magnitude changes in continuum and emission line flux compared to less dramatic changing looks occurring in Seyferts (shown in Figure 2.14).

Although most CLAGN reported to-date are Seyferts, this may be due to sample selection bias, as the high numbers of LINERs may cause them to be seen as galaxy contaminants in such searches. Difference imaging offers a unique mechanism to discover variability in known LINERs.

2.4.2 Is ZTF18aajupnt a TDE or AGN activity?

We focus specifically on ZTF18aajupnt, which shows the appearance of broad Balmer and coronal lines within 16 years of being spectroscopically confirmed as a LINER, accompanied by an order-of-magnitude soft X-ray flare. Given a ROSAT All-Sky Survey flux upper limit of $F_{0.1\text{–}2.4\ \mathrm{keV}} < 5 \times 10^{-13}$ ergs s^{-1} cm^{-2} at the location of the host from 1990 to 1991 (Voges et al., 1999), ZTF18aajupnt has therefore displayed a changing look in both the optical and X-ray usages of this term. The lower limit for this change in soft X-ray flux (0.1-2.4 keV) was by a factor of 7 at the time of the most recent observation.

Although highly photometrically variable on their own, flares due to non-AGN mechanisms are not unheard of in NLS1s. For example, CSS100217:102913+404220 displayed a high state ($M_V = -22.7$ at 45 days post-peak) accompanied by broad Hα and was interpreted either as a Type IIn SN (Drake et al., 2011) or TDE (Saxton et al., 2018) near the nucleus ($\sim$150 pc) of a NLS1. It eventually faded back to its original level after one year. PS16dtm (or iPTF16ezh/SN 2016ezh) was a $\sim 1.7 \times 10^4$ K, and near-Eddington but X-ray-quiet nuclear transient with strong Fe II emission which plateaued over $\sim$100 days while maintaining a constant blackbody temperature. The event was interpreted as a TDE exciting the BLR in a NLS1 (Blanchard et al., 2017), although Oknyansky et al. (2018) claimed it may instead be a CLAGN transitioning into a Sy 1. No X-rays were observed during follow-up, dimming at least by an order of magnitude compared to archival observations, but were predicted to reappear after the obscuring debris had dissipated. SDSS J1233+0842 was discovered as a CLQ when it changed into a composite type galaxy or transition object (with [O III]/H$\beta = -0.10$ and [N II]/H$\alpha = -0.17$ from Figure 2.a. in MacLeod et al. (2019)). It shows variable Fe II emission (similar to PS16dtm), with the broad line emission disappearing between 2005 and 2016.

A nuclear transient in the nearby ULIRG F01004-2237 was classified as a TDE—despite an unusually long peak time of 1 year—partially based on the strength of its He II compared to Hβ (Tadhunter et al., 2017). This ratio was unprecedented for AGN activity, even for AGN in the high state of a changing look. We note that although it is broad, He II/H$\beta \sim 0.4$ for ZTF18aajupnt is far below that measured for F01004-2237. It was later argued that the nature of this transient may instead be due to changes in the accretion flow, similar to that of OGLE17aaj, which also showed a slow optical rise and long plateau and slow decline and UV and X-ray properties similar to that of ZTF18aajupnt, although it lacked spectral classification prior to discovery of the transient (Gromadzki et al., 2019). The transient AT2017bgt was classified as a dramatic SMBH UV/optical flare which irradiated the BLR and was interpreted as the result of increased accretion onto the SMBH (Trakhtenbrot et al., 2019a). Unlike ZTF18aajupnt, it showed no decrease in flux over several months. The persistence of the UV emission distinguished it from SNe and TDEs, and the extremely intense nature of the UV continuum as well as presence of Bowen fluorescence He II, [N III] λ4640, and [O III] double-peaked features in the unobscured optical spectrum distinguished it from CLAGN. As in the "on" state of ZTF18aajupnt, the Balmer FWHM in all 3 sources are consistent with that of NLS1 galaxies.

ECLEs are most typically thought to be the echoes of TDEs via the accretion of tidal disruption streams by previously non-active SMBHs (Wang et al., 2012). However, less than 10 ECLEs have been reported in the literature, most notably SDSS J0952+2143 (Komossa et al. (2008, 2009); Palaversa et al. (2016); also technically a NLS1 using the unconventional cutoff in Rakshit et al. (2017), see Section 2.3.6.2 for details), and SDSS J0748+4712 (Wang et al., 2011). We confirm that ZTF18aajupnt is technically an "extreme" CLE by the definition put forth by Wang et al. (2012), because the strength of [Fe X] λ6376 is comparable to that of [O III] λ5007, as well as by the presence of [Fe XIV] in the optical spectrum (seen in Figures 2.6 and 2.21) following the independent definition of Palaversa et al. (2016). We note, however, that it is the present weakness of [O III] that is driving this diagnostic, and the coronal lines overall do not appear nearly as strong when compared to the prototypical ECLEs, SDSS J0952+2143 and J0748+4712, in Figure 2.6. This strong, slowly variable transient nuclear coronal line emission necessitates soft X-ray flaring outbursts from an accretion disk, which may be formed as tidal debris settles, illuminating the outermost debris as well as intervening ISM (Komossa & Bade, 1999). The coronal lines in these sources, some blueshifted, faded on timescales of 1-5 years, with strong [O III] appearing even later. Because strong coronal line emission is not a TDE diagnostic in isolation, some ECLE galaxies with persistent coronal lines may instead be Seyferts.

IC 3599 is an optical changing-look (displaying dramatic variability in not only Balmer lines but also [Fe VII] and [Fe XIV]) Sy 1.9 galaxy with strong soft X-ray repeating outbursts from its galactic nucleus which can be modeled by a disk instability with a rise time of $\sim$1 year whereby the inner disk is vacated and subsequently refills (Brandt et al., 1995; Campana et al., 2015; Grupe et al., 1995, 2015; Komossa & Bade, 1999). It is the only AGN which has shown fading of its coronal lines (though this variability is common among non-active ECLEs).

The *Swift*/XRT and *XMM* spectra of ZTF18aajupnt fit well to a steep power law ($\Gamma \sim 3 \pm 0.2$) below 2 keV, not a disk blackbody as would be expected in the TDE scenario (see Figures 2.10 and 2.11). The large covering factor measured for ZTF18aajupnt by *Spitzer* is also more consistent with mid-infrared studies of CLAGN (Sheng et al., 2017), than the covering factor derived for TDEs with dust echoes (with $f_{\mathrm{dust}} = E_{\mathrm{dust}}/E_{\mathrm{absorb}}$ at the $\sim$1% level; van Velzen et al. 2016). This could imply appreciable accretion happening recently, because that is very likely required for a dusty torus with a large covering factor. In an accretion event unrelated to disk physics, a self-gravitating molecular cloud with low enough angular momentum could also be efficiently accreted on the correct timescales, activating radiation which subsequently illuminates the BLR (e.g. Hopkins et al. 2006). One way to obtain a larger covering factor would also be via chaotic cold accretion, by which interaction via inelastic collisions is made easier, boosting the funneling of molecular clumpy clouds toward the SMBH, and therefore enhancing the accretion rate. (Gaspari & Sadowski, 2017). The high blackbody temperature measured from UV spectroscopy implies the line of sight to the transient is not significantly dust obscured. Sheng et al. (2017) argue that mid IR light echoes of CLAGN (with $\Delta W1|W2 \gtrsim 0.4$ mag) was additional evidence to support the reprocessing scenario driven by changing accretion rate instead of variable obscuration. $W1 - W2$ for that sample varied between 0.1 and 1.2 mag, so $[3.6] - [4.5]$ μm = 1.4 mag for ZTF18aajupnt was consistent with the lowest end of that sample for mid IR color (it would not have been selected based on its variability amplitude for the short duration of the *Spitzer* observations reported here).

LINERs may have inefficient accretion disks surrounding a low-luminosity AGN, occupying a unique physical parameter space compared to other CLAGN.

Similar to the unification scheme derived for AGN (Antonucci, 1993; Urry & Padovani, 1995), broad- and narrow-line LINERs can be categorized into LINER1s and LINER2s (e.g. González-Martín et al. 2015; Ho et al. 1997a,b). Yan et al. (2019) reported the discovery of the "turning on" of a type 1 Seyfert occurring in LINER SDSS1115+0544 which flared for ∼1 year and subsequently plateaued, followed by a mid-IR dust echo delayed with respect to the optical by 180 days and a late-time UV flare, although no soft X-rays were detected then. Narrow coronal lines appeared in the spectrum along with Hα and Hβ consistent with broad line emission. As was done in Yan et al. (2019), we measured the soft X-ray-[Fe VII] ratio for ZTF18aajupnt to be log $L_{2\ \mathrm{keV}}/L_{[\mathrm{Fe\ VII}]\lambda6088}$ =1.25 at maximum, still significantly below the average of 3.37 and pointing to an X-ray deficit compared to normal AGN (Gelbord et al., 2009), although we note that the soft X-rays changed by a factor of 10 and likely continued to rise beyond our last *Swift* observation. We also measure a minimum L/L_{Edd} equivalent to that of SDSS1115+0544. Yan et al. (2019) concluded an instability was required to "turn on" an AGN from a quiescent galaxy within hundreds of days. They argued that (despite a rate in tension with the AGN duty cycle) given the discovery of iPTF16bco and SDSS1115+0544 one year apart, such events should not be uncommon, a prediction this sample supports. There must be a connection between the LINER hosts and the state that is enabling these rapid transitions.

2.4.3 The nature of the high-ionization forbidden "coronal" lines in ZTF18aajupnt

Noda & Done (2018) posited that in the well-studied changing-look AGN Mrk 1018, the coming and going of the soft X-ray excess (the main ionization source) drives the appearance and disappearance of the BLR and therefore the changing-look phenomenon. We observe strong soft X-rays increasing in luminosity over time, which are required to form the coronal lines, although we note that the peak of the

X-ray flaring appears to lag behind the UV/optical flaring.

The nuclear outburst in UV and X-ray required is similar to cataclysmic variable or black hole binary thermal-viscous disk instability flares, which have been discussed as a possible mechanism for powering optical changing-looks, although the observed time scales are much faster than predicted (e.g. Lawrence 2018; Ross et al. 2018; Siemiginowska et al. 1996; Stern et al. 2018).

Ross et al. (2018) attribute changing looks to a thermal (cooling) front propagating inward through the accretion disk or disk surface opacity changes, which have the correct timescales for observed transitions, unlike other proposed CLAGN mechanisms.

We posit that this quiet LINER suddenly goes into an active outbursting state, the rise in ionizing radiation at first confined to the innermost BLR, turning on into a NLS1, then flash ionizing the ambient gas in the CLR, whereas the NLR (where [O III] lines are formed) is at larger distances, and thus light-travel time effects delay their response. Mg II, though still broad, is formed further out on average (Cackett et al., 2015; Goad et al., 1993; O'Brien et al., 1995).

2.4.4 The nature of the soft X-ray excess during the NLS1 state of ZTF18aajupnt

The preceding interpretation does not explain the soft X-ray rise, which is clearly delayed at least ∼60 days with respect to the end of the UV/optical rise (shown in Figure 2.8), and may speak instead to a lag in an "outside-in" sense following the direction of an accretion flow, rather than photon propagation from a central "lamp post". This is in contrast to the clear inter-band time lags on the order of days in support of the reprocessing scenario measured by Shappee et al. (2014) in high cadence multiwavelength observations of CLAGN NGC 2617, which transitioned from a Sy 1.8 to a Sy 1 in 10 years. The ∼2 month lag observed in

ZTF18aajupnt also suggests that this delay is not simply from light-travel time. X-ray inter-band time delays in NLS1s measured via Fourier based spectral timing, due to either X-ray reverberation or propagating fluctuations, are typically on the order of tens to hundreds of seconds (e.g. Kara et al. 2016; Uttley et al. 2014).

This delayed X-ray response may tell us something fundamental about the origin of the soft X-ray excess in AGN in general. The long delay of the soft X-ray flare relative to the expected light-travel time delays between the UV/optical emitting accretion disk and the compact, hot corona suggests that we are witnessing the real-time assembly of the corona plasma itself, possibly due to structural changes due to the dramatic change of state in the inner accretion disk (García et al., 2019).

If the Balmer emission is indeed from a BLR, we predict the Hα and Hβ lines should get broader as the UV luminosity decreases. Continued spectroscopic monitoring to look for evolution in line widths and strengths, particularly the narrow [O III] emission line and Mg II, and monitoring of the soft X-rays will be critical to map out the structure of this system and distinguish between the scenarios presented here.

2.5 Conclusions

We present the changing looks of six known LINERs caught turning on into type-1-like AGN found in Year 1 of the ZTF survey. It is the first systematic study of its kind performed in real time using difference imaging variability as the discovery mechanism for selecting nuclear transients in these previously quiescent galaxies.

1. We establish a class of changing-look LINERs, distinct from Seyfert changing-look AGN, with unique spectroscopic and photometric variability properties intrinsically due to the LINER accretion state.

2. In their "on state" the changing-look LINERs have suppressed narrow [O III]

line emission compared to normal AGN of the same broad Hα luminosity, and inferred Eddington ratios 1−4 orders of magnitude above their LINER state.

3. This sample includes a multiwavelength study between 2018 June to 2019 March of the first case of a LINER changing look to a NLS1 — ZTF18aajupnt — which transitioned within 3 months based on its archival light curve.

4. We observed the delayed response of the NLR and broad Mg II with respect to the appearance of broad (yet < 2000 km s^{-1}) Balmer lines, and X-ray flaring delayed $\sim$60 days with respect to the optical/UV rise of this nuclear transient, indicative of an "outside-in" transition.

5. We interpret this particular object to be a dramatic change of state in a pre-existing LINER accretion disk, which eventually forms an optically thick inner structure that up-scatters the UV/optical seed photons to produce a delayed soft X-ray excess.

This class of previously-weak AGN has the potential to be a laboratory with which to map out the structure of the accretion flow and surrounding environment. We plan to continue to monitor the behavior of these transients, and expect to build upon the sample at a rate of $\sim$4 year^{-1} for the next two years of the ZTF survey.

2.6 Appendix

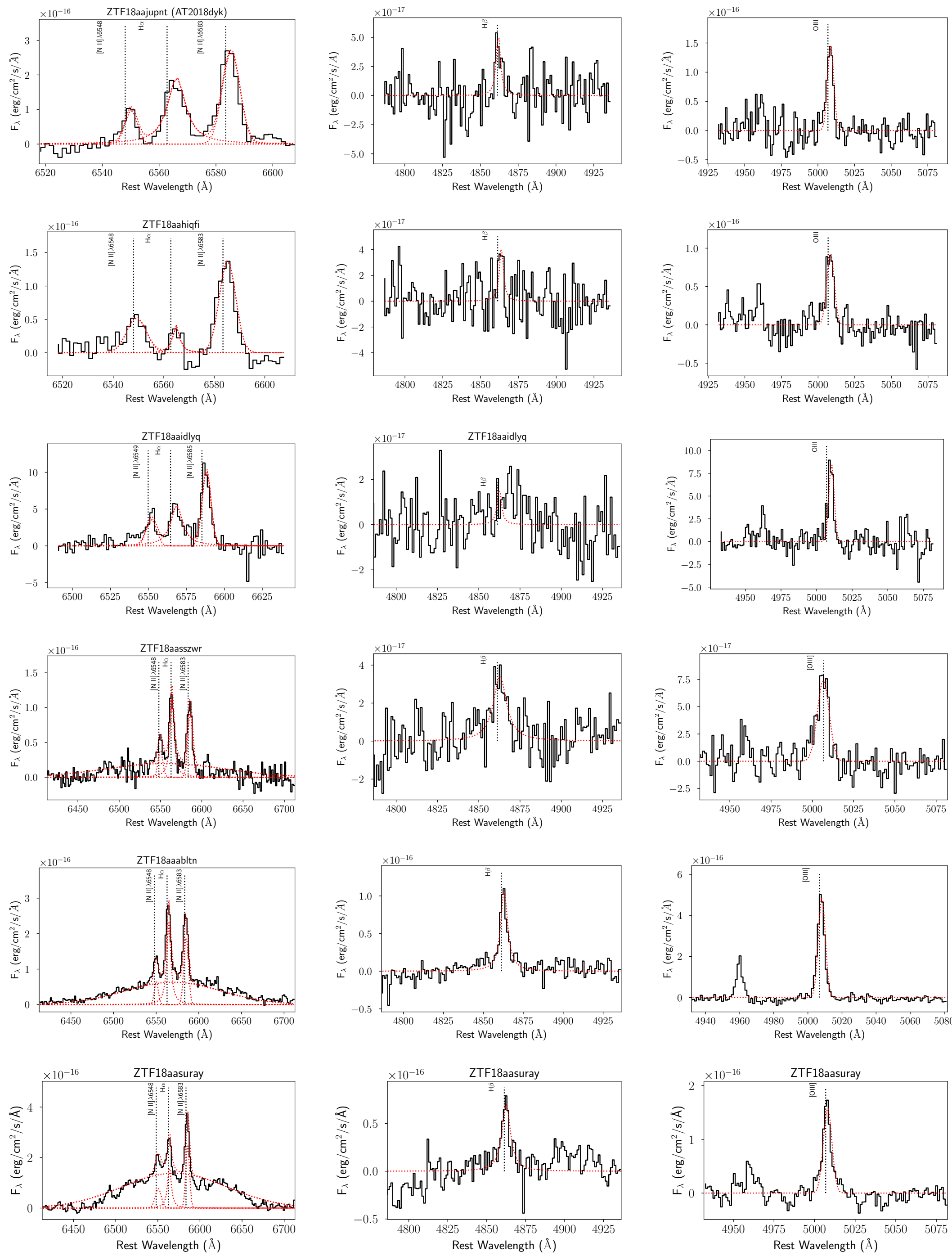

Figure 2.18: Stellar-continuum-subtracted Hα line complex, Hβ, and [O III] (first, second, and third columns, respectively) with best fits to Gaussians for the sample in their “off” state used in Figure 2.13. While fitting Hβ in ZTF18aaidlyq only, the FWHM in the model fit has been fixed to the FWHM of [N II] λ6585, due to Hβ being only marginally detected in that host. Note the differences in scale.

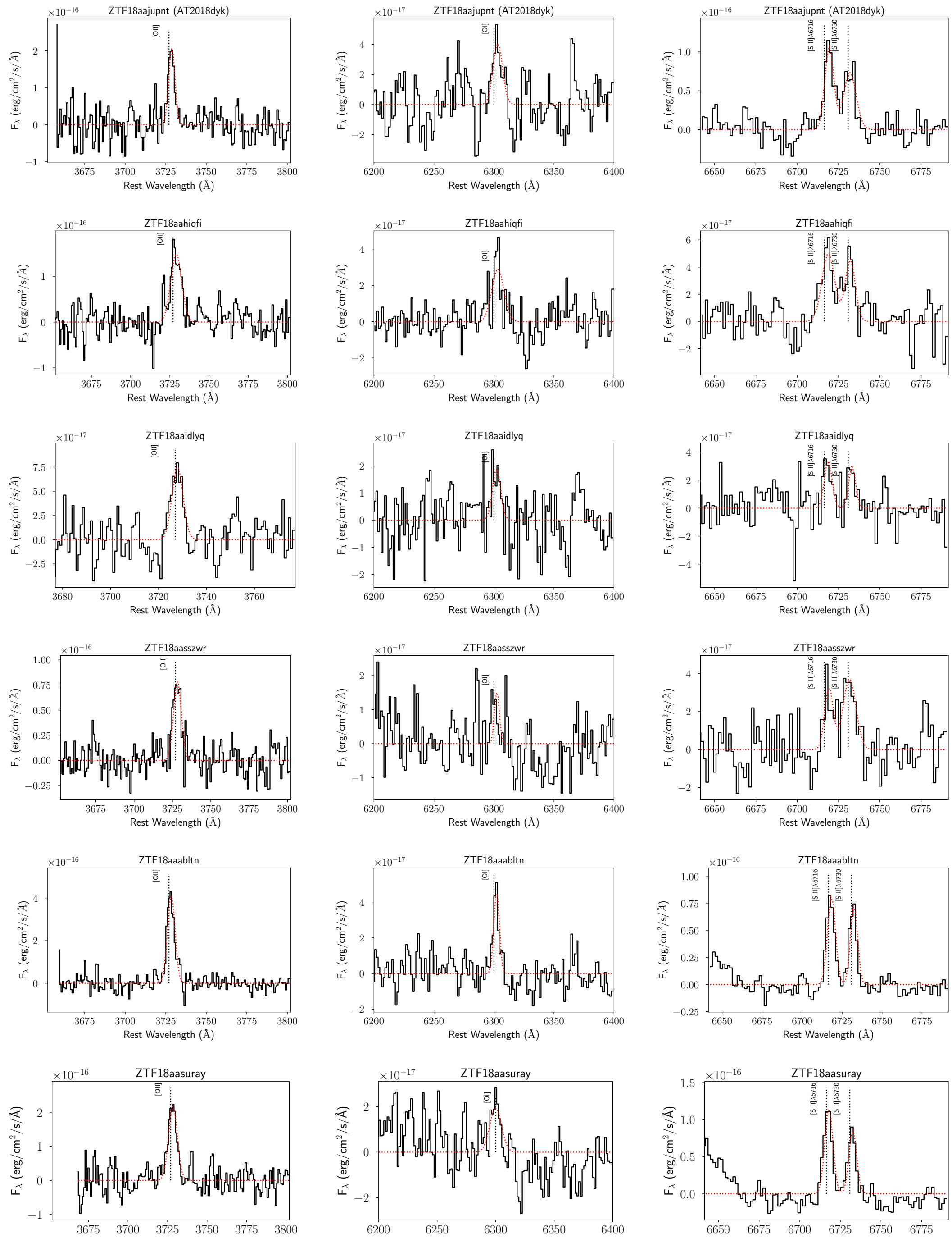

Figure 2.19: Stellar-continuum-subtracted [O II], [O I], and the [S II] doublet (first, second, and third columns, respectively) line profiles and best fits to Gaussians for the sample in their “off” state used in Figure 2.13. Note the differences in scale.

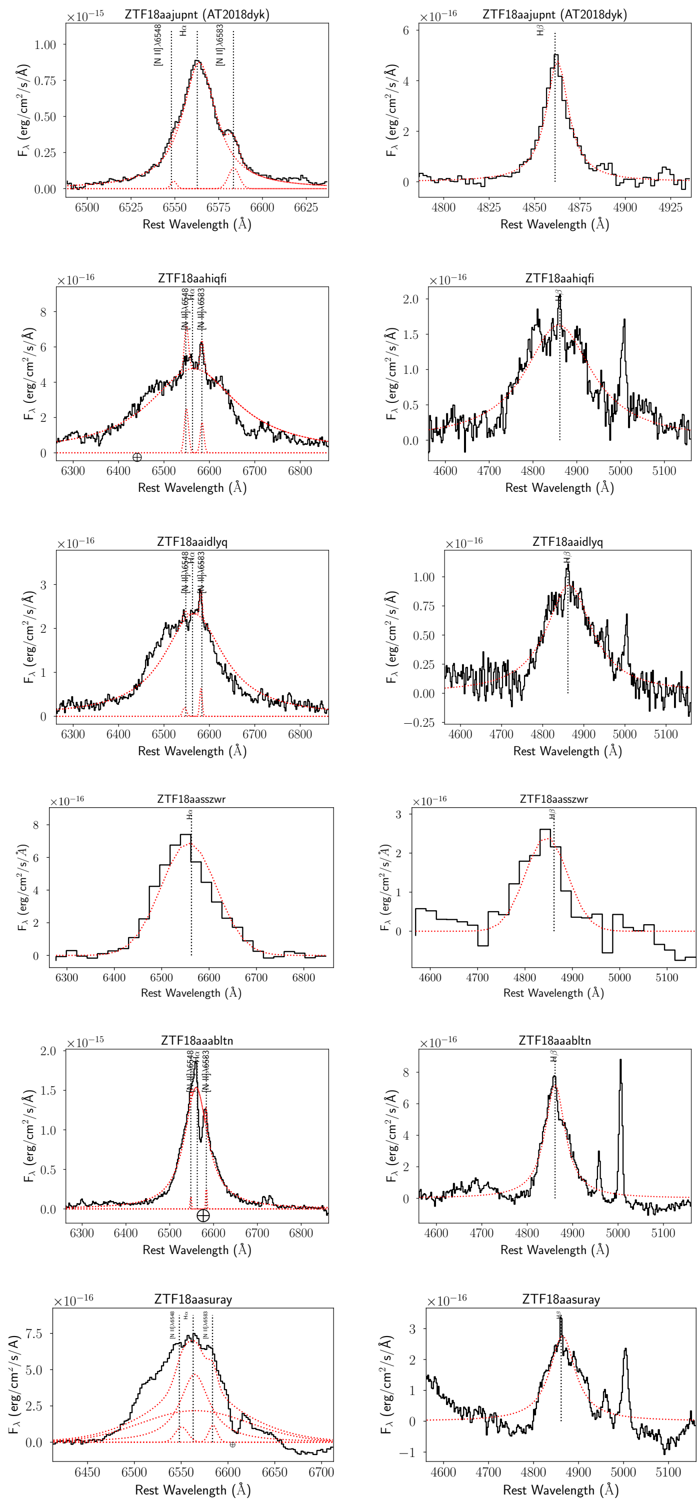

Figure 2.20: Balmer line profiles and best fits to Gaussians/Lorentzians for the sample in their "on" state. Note the difference in scales. See Section 2.2.5 for more details.

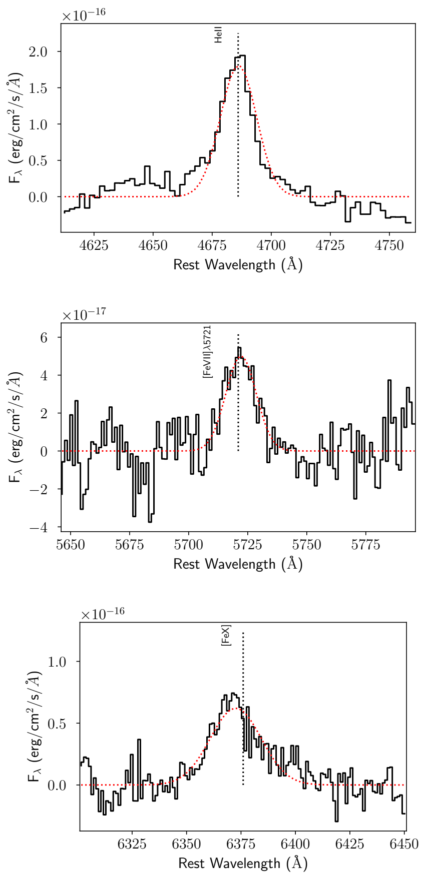

Figure 2.21: Coronal line profiles and best fits to Gaussians for the ZTF18aajupnt in its "on" state. The residual of the spectrum to the stellar continuum was fit. See Section 2.3.6.1 for more details.

Chapter 3: A Family Tree of Optical Transients from Narrow-Line Seyfert 1 Galaxies

The Zwicky Transient Facility (ZTF) has discovered five events ($0.01 < z < 0.4$) belonging to an emerging class of AGN undergoing smooth, large-amplitude, and rapidly rising flares. This sample consists of several transients initially classified as supernovae with narrow spectral lines. However, upon closer inspection, all of the host galaxies display Balmer lines with FWHM(Hβ) $\sim 900 - 1400$ km s^{-1}, characteristic of a narrow-line Seyfert 1 (NLSy1) galaxy. The transient events are long-lived, over 400 days on average in the observed frame. We report UV and X-ray follow-up of the flares and observe persistent UV emission, with two of the five transients detected with luminous X-ray emission, ruling out a supernova interpretation. We compare the properties of this sample to previously reported flaring NLSy1 galaxies and find that they fall into three spectroscopic categories: 1) Balmer line profiles and Fe II complexes typical of NLSy1s, 2) strong He II profiles, and 3) He II profiles including Bowen fluorescence features. The latter are members of the growing class of AGN flares attributed to enhanced accretion reported by Trakhtenbrot et al. (2019). We consider physical interpretations in the context of related transients from the literature. For example, two of the sources show high amplitude rebrightening in the optical, ruling out a simple tidal disruption event scenario for those transients. We conclude that three of the sample belong to the Trakhtenbrot et al. (2019) class, and two are TDEs in NLSy1s. We also hypothesize as to why NLSy1s are preferentially the sites of such rapid enhanced flaring activity.

3.1 Introduction

A galaxy center hosting an active galactic nucleus (AGN) is dominated by its continuum emission. Therefore, a flare originating from this nuclear region requires a distinctly powerful event to be detectable above this stochastically variable continuum. A small number of rapid[1], smoothly evolving flares have been observed to be associated with AGN (e.g. Blanchard et al. 2017; Drake et al. 2011), with few known mechanisms that can cause these events to occur.

Intrinsic UV/optical flares, such as those due to enhanced accretion onto the central supermassive black hole (SMBH) in the form of gaseous material or stars passing too close to the nucleus, have been observed in the form of: tidal disruption events (e.g. Gezari et al. 2012; van Velzen et al. 2020a), UV-bright flaring events that are associated with accretion rate changes (Trakhtenbrot et al., 2019a), transients with double peaked line profiles linked to accretion disk emission (e.g. Halpern & Eracleous 1994), or changing-look AGN — the dramatic change in spectroscopic AGN classification following a rise in continuum level, thought to be connected to unstable changes in accretion state (e.g. Frederick et al. 2019; Gaskell & Sparke 1986; Graham et al. 2020; LaMassa et al. 2015; MacLeod et al. 2016; Ross et al. 2018; Ruan et al. 2016; Runnoe et al. 2016; Stern et al. 2018; Trakhtenbrot et al. 2019b).

Phenomena extrinsic to the SMBH accretion engine, such as microlensing of a quasar by a foreground Galactic source (e.g. Lawrence et al. 2012) or slowly evolving super-luminous supernova (SLSN) explosions, have also been observed to cause smooth large-amplitude flares from galaxies with AGN (Graham et al., 2017). In rare cases these can be astrometrically indistinguishable from the galactic nucleus, and therefore it becomes difficult to discern whether an explosive disruption to the

[1] We refer to flare timescales as "rapid" when they occur on week to month timescales.

accretion flow has occurred, and to differentiate this from AGN variability (Terlevich et al., 1992).

Multiwavelength approaches are required to disentangle this diverse family of observed flaring behaviors from AGN. In the golden era of time domain astronomy, even with many multichromatic instruments trained on the sky, a number of newly-discovered objects continue to defy placement into a clear-cut observational category.

In order of discovery, we present a photometric class comprised of five rapid flares with similar smooth light curve shapes occurring in a subclass of AGN observed by the Zwicky Transient Facility (ZTF) survey:

a) ZTF19aailpwl/AT2019brs ($z = 0.37362$)

b) ZTF19abvgxrq/AT2019pev ($z = 0.097$)

c) ZTF19aatubsj/AT2019fdr ($z = 0.2666$)

d) ZTF19aaiqmgl/AT2019avd ($z = 0.0296$)

e) ZTF18abjjkeo/AT2020hle ($z = 0.103$)

In Section 3.2 we present the follow up of these flares. In Section 3.3 we compare the results of their respective multiwavelength follow up campaigns to observations of a variety of related objects found in recent years, and in Section 3.4 we attempt to place them into a classification scheme based on observational properties, summarized in Section 3.5. All transients in the sample are referred to by their ZTF alert names throughout. All magnitudes are reported in the AB system and light curves are shown in the observed frame unless otherwise stated. We have adopted the following cosmology: $H_0 = 70$ km s^{-1} Mpc^{-1}, Ω_Λ= 0.73 and $\Omega_M = 0.27$.

3.2 Observations

The Zwicky Transient Facility Survey (Bellm et al., 2019a; Graham et al., 2019) is comprised of the automated Palomar 48-inch Samuel Oschin Telescope (P48) as well as the Palomar 60-inch SED Machine (P60 SEDM; Blagorodnova et al. 2018; Rigault et al. 2019), and has surveyed the Northern Sky with g- and r-band filters with a 3-night cadence since 2018 (Bellm et al., 2019b). At least 15 images meeting good quality criteria were stacked to build a coadded reference image of each observing field and quadrant in each filter band. Science images are subtracted by their references and processed each night by the Infrared Processing and Analysis Center (IPAC) pipeline (Masci et al., 2019). The candidate transient alert stream (Patterson et al., 2019) is distributed by the University of Washington Kafka system, and filtered through the AGN and black holes Science Working Group's Nuclear Transients[2] parameter criteria (outlined in van Velzen et al. 2019, 2020b) by the Ampel broker (Nordin et al., 2019; Soumagnac & Ofek, 2018), with the GROWTH Marshal user interface utilized for the coordination of follow-up efforts (Kasliwal et al., 2019).

All 5 transients included in the sample presented here were selected based on the following criteria: large amplitude, nuclear variability ($\Delta g > 1$ mag in difference imaging photometry, and within $0.5''$ of the center of the host galaxy in the reference image) with follow-up or pre-flare spectra consistent with an AGN classification. This selection was not systematic (and therefore not complete), but rather the result of ongoing intersecting and collaborative searches for changing look AGN (Frederick et al., 2019), TDEs (van Velzen et al., 2019, 2020b), and superluminous supernovae (Lunnan et al., 2019; Yan et al., 2020) relying on partial human vetting from the

[2] A nuclear transient was defined as that within 0.5" of the reference galaxy center. Over 9000 nuclear transients passed this filter and were ranked during ZTF Phase I, of which 27 were TDEs, over 7% were classified as SN, and over half were AGN or candidate AGN.

ZTF transient alert stream, from which this sample emerged as more examples were collected. A systematic search for NLSy1 transients in ZTF will be the focus of a future study.

3.2.1 Optical Photometry

All transients in the sample were detected pre-peak using ZTF difference imaging photometry. The smooth light curve shapes (with scatter $\Delta g < 0.1$ mag) of the sample are shown in Figure 3.1. All magnitude changes are reported in g band unless otherwise noted. An analysis of the rise times to peak are measured and reported in Section 3.3.1.1. We report the g-band magnitude-weighted offsets for each transient, calculated using Equation 3 in van Velzen et al. (2019). ZTF forced photometry for the sample is shown in Figure 3.10 of the Appendix.

AT2019brs — (RA=14:27:46.41, Dec=+29:30:38.6, J2000.0) was first detected on 2019 Feb 08 as a nuclear transient within $0\farcs17$ of the host galaxy center. The host galaxy displayed some variability at the < 1 mag level in the Catalina Real-Time Transient Survey (CRTS; Drake et al. 2009) from 2005 to 2013.

AT2019pev[3] — (RA=04:29:22.72, Dec=+00:37:07.6, J2000.0), also known as Gaia19eby, was first detected on 2019 Sept 04 as a nuclear transient within $0\farcs15$ of the host galaxy center. ATLAS, Gaia, and PanSTARRs also reported observations of this source on the Transient Name Server (TNS) with discovery dates of 2019 Sep 04, 2019 Sep 13, and 2019 Sep 26, respectively. The host galaxy displayed no variability above the 0.5 mag level in CRTS.

AT2019fdr — (RA= 17:09:06.86, Dec=+26:51:20.7, J2000.0) was detected on 2019 Apr 27 with a significant flux increase with respect to the reference image and

[3]AT2019pev passed the ZTF TDE working group's tidal disruption event criteria, and was given the nickname "Stannis Baratheon" for ease of discussion. When it was found to be among a class of AGN-associated objects serendipitously detected by ZTF, the other sources in the class were retroactively given the names of other Game of Thrones characters in the same Great House - and collectively referred to fondly as "The Baratheons", whose motto is, appropriately, "Ours is the Fury".

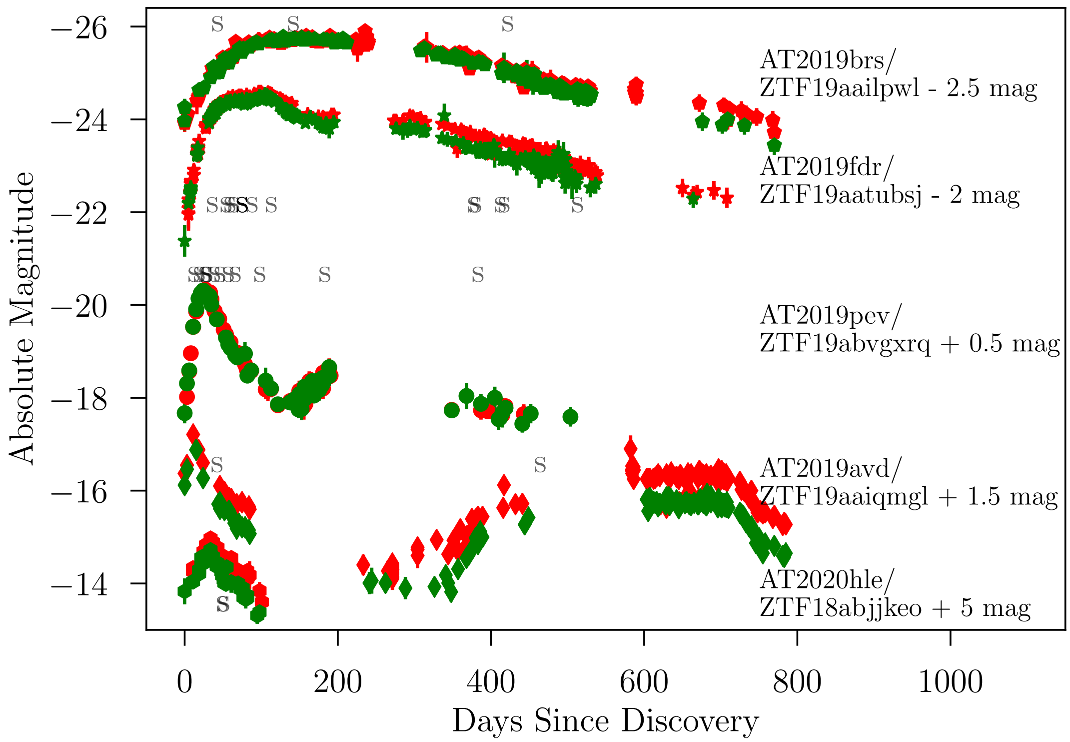

Figure 3.1: Comparison of the ZTF g- and r-band difference imaging light curve shapes and absolute magnitudes of the sample. AT2019fdr decreases before reaching a second plateau stage, and undergoes significant reddening after the first plateau while the others never do. AT2019pev rises again symmetrically after decreasing to pre-flare levels, as does AT2019avd. The light curves have been shifted in absolute magnitude space for visual purposes, as indicated alongside the object name. Overlap of the g and r light curves reflects true colors such that the initial colors approach $g - r = 0$ mag for all transients in the sample. Observations at other wavelengths are shown in Figure 3.2. Spectroscopic epochs are labeled for each light curve with an 'S' below AT2019fdr and AT2020hle and above the rest.

with an offset from the nucleus of its host of 0.″13. During a coverage gap in the first 40 days of the rise, ATLAS reported an intriguing "bump" feature (Smartt et al., 2019). The host galaxy displayed variability at the 2 mag level in V-band CRTS data from 2009 to 2013 (variability which was not observed in ZTF forced photometry prior to the transient).

AT2019avd — (RA=08:23:36.77, Dec=+04:23:02.5, J2000.0), also known as eRASSt J082337+042303[4], was detected by ZTF beginning on 2019 Feb 09 within $0\farcs06$ of its host galaxy. The host showed no variability in CRTS for 15 years prior to its rapid rise to peak.

AT2020hle — (RA=11:07:42.91, Dec=+74:38:02.0, J2000.0) was detected beginning on 2020 Apr 05 within $0\farcs02$ of its host galaxy center. The ZTF forced photometry for this source shows no variability above the level of the galaxy for > 400 days. The host galaxy of AT2020hle was beyond the survey limits of CRTS.

3.2.2 Optical Spectroscopy

All spectroscopic follow-up observations for the sample are summarized in Table 3.1, and each epoch is shown in Figure 3.11 of the Appendix. The phases of the optical follow-up spectra with respect to the features in the ZTF light curves are annotated on Figure 3.1. All transients in this sample have spectral characteristics of NLSy1 galaxies, i.e. strong Balmer line emission with FWHM < 2000 km s^{-1}, along with other spectral features which are highlighted below and explored in detail in Section 3.3.2. We reduced Palomar 60" SED Machine (P60/SEDM; Program PIs: Gezari, Sollerman, Kulkarni) spectra with `pysedm` (Rigault et al., 2019), and all other spectra with `pyraf` using standard procedures.

AT2019brs — showed a striking difference to the SDSS spectrum showing it was a NLSy1 as early as 2006 (Abolfathi et al., 2018; Rakshit et al., 2017). The follow-up Folded Low Order whYte-pupil Double-dispersed Spectrograph North (FLOYDS-N; Arcavi et al. 2019 and Lowell Discovery Telescope (LDT, formerly DCT; PI: Gezari) spectra showed a steep blue continuum and a strong He II profile with Bowen fluorescence features, indicating it became a flaring SMBH belonging

[4]This was the only source in the sample to be detected by the extended ROentgen Survey with an Imaging Telescope Array (eROSITA, part of the Russian-German "Spectrum-Roentgen-Gamma" (SRG) mission; Cappelluti et al. 2011), and was given the name eRASSt J082337+042303. This X-ray detection coincident with the transient's host galaxy is described in Section 3.2.4.

Table 3.1: Summary of spectroscopic follow-up observations of the sample.

Name	Obs UT	Instrument	Exp (s)	Reference
AT2019brs	2006 Jul 01	SDSS	3000	Abolfathi et al. (2018)
	2019 Mar 15	FLOYDS-N	3600	Arcavi et al. (2019)
	2019 Jun 22	LDT Deveny	900	This work
AT2019fdr	2019 May 25	Palomar 60" SEDM	2250	This work
	2019 Jun 17	LT SPRAT	900	This work
	2019 Jun 22	LDT Deveny	900	This work
	2019 Jul 03	Palomar 200" Hale	600	This work
	2020 Apr 30	NOT ALFOSC	1750	This work
AT2019pev	2019 Sep 08	Palomar 60" SEDM	2250	This work
	2019 Sep 15	LT SPRAT	500	This work
	2019 Sep 22	Palomar 60" SEDM	2250	This work
	2019 Sep 24	LDT Deveny	600	This work
	2019 Sep 25	Keck LRIS	300	This work
	2019 Sep 25	NICER	2000	Kara et al. (2019)
	2019 Oct 01	Chandra LETG	45400	Miller et al. 2019
	2019 Oct 05	Lick 3-m KAST	1500	This work
	2019 Oct 12	LT SPRAT	500	This work
	2019 Oct 15	Chandra LETG	91000	Mathur et al. 2019
	2019 Oct 23	LDT Deveny	900	This work
	2019 Nov 01	Palomar 60" SEDM	2250	This work
	2019 Dec 03	LDT Deveny	2400	This work
	2020 Feb 26	LDT Deveny	2600	This work
	2020 Jan 30	*Swift XRT*	94700	This work
AT2019avd	2020 Mar 15	NOT ALFOSC	1800	Malyali et al. (2021)
	2020 Apr 28	eROSITA SRG	140	Malyali et al. (2021)
	2020 May 10	FLOYDS-S	3600	Trakhtenbrot et al. (2020)
AT2020hle	2020 May 16	Palomar 60" SEDM	2250	This work
	2020 May 18	LT SPRAT	1000	This work

to the observational class established by Trakhtenbrot et al. (2019a).

AT2019pev — was spectroscopically identified as a NLSy1 on 2019 Sept 15 with the Liverpool Telescope (LT; PI: Perley) SPectrograph for the Rapid Acquisition of Transients (SPRAT), based on the width of the Balmer emission lines and the strength of the [O III] λ5007 emission line. Gezari et al. (2019) reported that the LT spectrum showed evidence for blue-shifted He II λ4686 emission as well as

N III $\lambda4640$ emission, due to the Bowen fluorescence mechanism, placing it again in the observational subclass of the Trakhtenbrot et al. (2019a) objects. Near peak it was observed with Keck 10-m Low Resolution Imaging Spectrometer (LRIS; PI: Graham) as well as the LDT Deveny Spectrograph (PI: Gezari) and the KAST Double Spectrograph on the Lick 3-m Shane Telescope (PI: Foley), which confirmed the strong blue continuum and clearly defined and persistent Bowen fluorescence features.

AT2019fdr — was observed 8 days after peak on 2019 Jul 03 with the Double Spectrograph (DBSP) on the Palomar 200-inch Hale Telescope (P200; PI: Yan). We measured a significant "blue horn" component of Hβ and marginally detected He II. The transient continuum of AT2019fdr faded to reveal an underlying Fe II complex in the Nordic Optical Telescope (NOT; PI: Sollerman) spectrum taken nearly 368 days after peak on 2020 Apr 30, with no evidence for He II emission.

AT2019avd — The spectrum taken with NOT (PI: Sollerman) on 2019 Mar 15 near the first optical peak showed strong Balmer line emission, no detection of a He II line complex, and evidence for a Fe II complex, characteristic of NLSy1 galaxies. A follow-up FLOYDS-S spectrum taken 444 days after peak and reported to the Transient Name Server (TNS) by Trakhtenbrot et al. (2020) showed the appearance of He II and Bowen fluorescence features and a "blue horn" in Hβ. Again this event was classified as a member of the Trakhtenbrot et al. (2019a) observational class of flaring NLSy1s.

AT2020hle — In the LT (PI: Perley) spectrum of AT2020hle taken on 2020 May 18 8 days after peak, the narrow component of the He II profile is significantly blueshifted. No Fe II line complex was detected in the spectra of this transient.

3.2.3 UV Photometry

We triggered target-of-opportunity monitoring observations with the Neil Gehrels *Swift* Telescope (Gehrels et al., 2004) for all transients in the sample. Using the HEASOFT command `uvotsource` we extracted *UVOT* photometry within a 5″-radius circular aperture and using an annular background region centered on the coordinates of the optical transient.

Figure 3.2 shows the νL_ν light curves of all flares in the sample. We compare ZTF g and r band difference imaging, WISE difference imaging, *Swift XRT* monitoring, and *Swift UVOT* detections subtracted by the archival *Galaxy Evolution Explorer* (*GALEX*; Bianchi et al. 2017) All-Sky Imaging Survey (AIS) near-UV (NUV, $\lambda_{\rm eff} = 2310$ Å) host measurements (measured with a 6-″radius aperture).

We found all transients in the sample to be UV-bright, but with varying UV colors. The UV color of AT2019avd ($UVW1 - g = -0.2$ mag) was similar to that of AT2019pev ($UVW2 - g = -0.2$ mag) and AT2019brs (ranging from $UVW2 - g = -0.1$ mag to -0.7 mag in 80 days), but AT2019fdr was the only transient in the sample with positive UV color ($UVW2 - g = 0.8$ mag). The UV light curves of the sample tend to follow the shape of the optical. AT2019pev became host dominated over time as the transient faded. but with strong scatter in the light curve as it approached the host magnitude.

3.2.4 X-rays

We found only two transients in the sample to be X-ray bright in follow-up *Swift XRT* observations: AT2019pev and AT2019avd. AT2019brs was detected only once, and then only at a low level. We measured an *XRT* upper limit of 0.004 counts s^{-1} for AT2019fdr. X-ray follow-up spectra are reported in Table 3.1. *Swift* photometry compared to WISE W1- and W2-band and ZTF g and r-band photometry is shown in Figure 3.2. The X-ray bright flares in this sample tend to vary in lockstep with the slow UV/optical flares.

AT2019brs — was detected only once in 11 observations during a 16-month monitoring campaign between 2019 Mar 21 and 2020 Jul 7. We measured a 3-σ detection of 0.003 counts s^{-1} on 18 Apr 2019, just brighter than the limiting flux.

AT2019pev — Similar to the UV light curve, the shape of the X-ray flare of AT2019pev followed the optical, from its fade through its second rise (See Figure 3.2 and Section 3.3). The unabsorbed $0.3-10$ keV flux from the stacked *XRT* spectrum of AT2019pev was $7.3\pm0.1\times10^{-12}$ erg cm^{-2} s^{-1}. AT2019pev was previously detected in ROSAT, and NICER observations show an increase in flux from this by 100 times (1×10^{-11} erg cm^{-2} s^{-1}), variable from 11 to 14 counts s^{-1} in 3 hours (Kara et al., 2019). A 50 ks Chandra LETG grating observation taken just 8 days after peak and reported by Miller et al. (2019) found a flux consistent with this, with the spectral shape a good fit to a $kT = 0.24$ keV blackbody, and the source variable at the 25% level on $2-3$ ks timescales. Mathur et al. (2019) reported a decrease in $0.3-2.5$ keV flux to 7.7×10^{-12} erg cm^{-2} s^{-1}; their 91 ks Chandra LETG observation was a good fit to a consistent blackbody model and a power law component typical of AGN with spectral index $\Gamma = 1.8$, with no intrinsic absorption required.

AT2019avd — was observed only during the second optical flare (on 2020 Apr 28, 350 days after the first ZTF detection), and was the only X-ray bright transient in the sample with much fainter X-ray νL_ν than that of the optical (shown in Figure 3.2). Like AT2019pev, the shape of the X-ray rise followed that of the second rise. It was detected by eROSITA as eRASSt J082337+042303, a soft X-ray transient consistent with the galaxy 2MASX J08233674+0423027 (Malyali et al., 2020, 2021). Prior to this, the XMM Slew Survey reported a non-detection at the location of the host galaxy, with an upper limit of $< 1.7\times10^{-14}$ erg^{-1} s^{-1} cm^{-2} assuming $kT_{\rm bb} = 100$ eV and $N_H = 3\times10^{20}$ cm^{-2}. The SRG flux of 1.5×10^{-12} erg^{-1}

s^{-1} cm^{-2} was 90 times brighter than this upper limit. No hard X-ray component was detected above 2.3 keV. No strong short-term variability on hours-long timescales was detected, and no strong variability was detected between SRG and the 3 *Swift XRT* monitoring observations taken afterward with a week-long cadence. Swift and NICER observations over the next 5 months showed an additional increase in X-ray flux by a factor of 10 (Pasham et al., 2020). A careful study of the X-ray properties of this transient is forthcoming (Malyali et al., 2021).

3.2.5 IR

Malyali et al. (2020) reported that the WISE color of AT2019avd was atypically low ($W1-W2 \simeq 0.07$ mag) compared to typical AGN values ($W1-W2 = 0.7-0.8$ mag, Assef et al. 2013; Stern et al. 2012). The WISE colors of AT2020hle (neoWISE: 0.35 mag, AllWISE: 0.036 mag) and AT2019pev ($W1 - W2 = 0.45$ mag) are also inconsistent with an AGN, though not quite as low as that of AT2019avd. Only AT2019brs truly appeared as an AGN in IR, with $W1-W2 = 0.98$ mag. The WISE AGN classification of the sample is summarized in Table 3.3 in Section 3.4.

A flare in the IR was detected in NeoWISE at the location of AT2019avd and concurrent with the optical and X-ray transient. Though the IR flare began much sooner in 2009, Figure 3.2 shows that the peak of the flare was delayed with respect to the first optical peak. Prior to this flare, WISE photometry detected no variability at the location of AT2019avd for nearly 5 years.

3.3 Analysis

3.3.1 Photometry

The difference imaging light curves for the sample are shown in terms of absolute magnitudes in Figure 3.3.

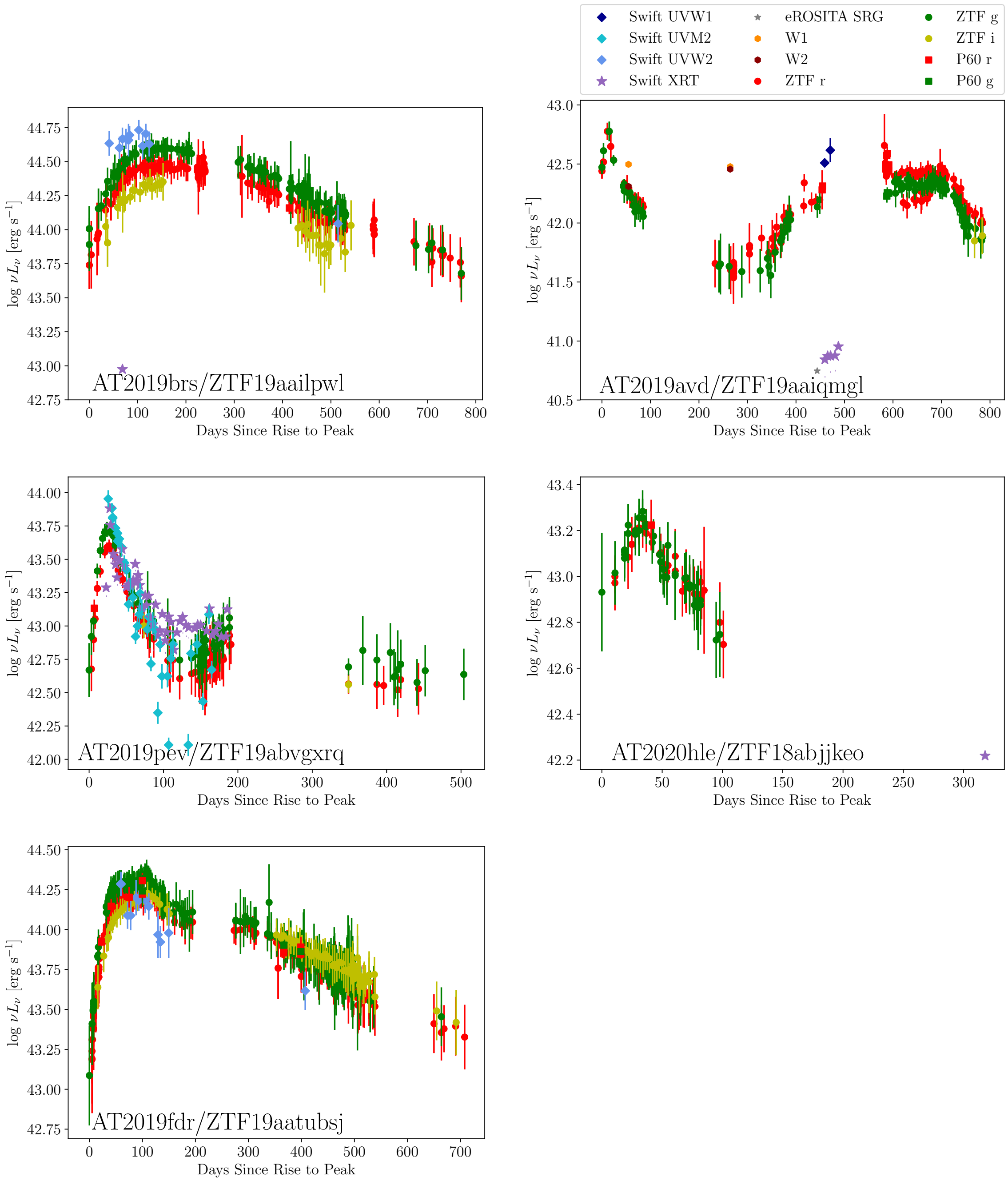

Figure 3.2: We track the colors of the transients in the sample with a νL_ν light curve, comparing the ZTF and WISE data to concurrent high cadence *Swift UVOT* and *XRT* monitoring observations. The X-ray rise and fade of AT2019pev tracks the optical/UV with no significant delay. We subtracted the host galaxy light as estimated by *GALEX* NUV measurements from the *Swift UVOT* observations. Times are given in days since first ZTF detection. The X-ray errorbars are comparable to the size of the data points. See Figure 3.10 for pre-outburst forced photometry.

We show the sample alongside various NLSy1-related events from the literature, which are described in more detail in Section 3.4. CSS100217 displayed some variability prior to the transient, unlike any of the events in this sample. AT2017bgt was observed only during its fade in difference imaging, so we instead show its aperture photometry (from the ASAS-SN Photometry Database[5]; Jayasinghe et al. 2019) which also shows the rise of the source. AT2018dyk is by far the least luminous transient shown. We note the similarity of the shapes of the light curves of AT2019fdr and PS16dtm, which is discussed further in Section 3.4.

3.3.1.1 Light Curve Timescales

We measured the rise-to-peak timescales of the sample by fitting Gaussians to the light curves shown in Figure 3.3 using the `lmfit` package built from `scipy.optimize`. We observe a correlation between the luminosity (specifically the absolute magnitudes M_V and M_g) and rise-to-peak timescales of the sample ($t_{\rm rise}$) with the following relation: $M = -0.04t_{\rm rise} - 18.59$, shown in Figure 3.4. Fitting the light curves with quadratic functions resulted in the same correlation within the error estimates. Interestingly, TDEs also show a positive correlation between rise time to peak and luminosity (van Velzen et al., 2020b). AT2018dyk appears under-luminous for how fast it rises. AT2017bgt was observed only during its fading phase in difference imaging, and so was excluded from this portion of the analysis.

3.3.1.2 Rebrightening

It is noteable that two sources in the sample, AT2019pev and AT2019avd, each have a dramatic rebrightening episode. Following a flare and an approximately $\sim$2 mag fade from peak, both return to nearly half their maximum luminosity before seasonal gaps in visibility. This is in contrast to that of almost all TDEs and

[5]`https://asas-sn.osu.edu/photometry`

SN in the literature (e.g. Sollerman et al. 2019, 2020), although they can show plateaus and "humps" (e.g. Hammerstein et al. 2020, in prep.)[6] We explore possible interpretations of this rebrightening in Section 3.4.

3.3.1.3 UV/Optical to X-ray Ratio

We derive the simultaneous UV/optical-to-X-ray spectral slope ratio ($\alpha_{\rm OX}$) from the *Swift UVOT* and *XRT* observations of the sample, (as well as upper limits assuming $\Gamma_X = 2$, when applicable). We compute unabsorbed X-ray flux densities at 2 keV using the `PIMMS` v4.10 web tool[7]. Following Eq. 4 of Tananbaum et al. (1979) and Eq. 11 of Grupe et al. (2010), the definition of this ratio is $\alpha_{\rm OX} = 0.3838 \log(L_{2\,\rm keV}/L_{2500\rm A})$. Of the transients detected in X-rays, the $\alpha_{\rm OX}$ of AT2019pev evolves over 150 days between 1.1 and 1.4, and AT2019brs is observed in X-rays during only one epoch with $\alpha_{\rm OX} = 1.7$, equivalent to that of the late time detections of AT2019avd. The range of $\alpha_{\rm OX}$ measured for the sample is consistent with that of NLSy1s ($0.9 < \alpha_{\rm OX} < 1.8$; Gallo 2006).

3.3.2 Spectroscopy

From the FWHM of the broad Balmer emission lines, we classified all sources in the sample as NLSy1s. We fit the Hα and Hβ line profiles of the host (when available) and transient spectra of the sample with the non-linear least-squares minimization and curve-fitting routine in the `lmfit` Python package. The results of these fits are shown in Figure 3.5. Using a Lorentzian profile for the broad Hα component fit provided an improvement of the fit over that of a Gaussian profile, as would be expected based on studies of NLSy1s (e.g. Nikołajuk et al. 2009).

We compare the host (when available) and transient spectra of this sample to

[6]We note that ASASSN-15lh showed a large amplitude "double-humped" structure in its UV light curve.

[7]`https://cxc.harvard.edu/toolkit/pimms.jsp`

other transients in NLSy1s in Figures 3.6 (showing the full wavelength range of the observations) and 3.7 (rest wavelength 3700 − 5150 Å, showing clearly the He II, Fe II, and Hβ line profiles). In Figure 3.7 we color-code the sample (as well as these known NLSy1-related transients in the literature) based on the observational classification scheme we establish in Section 3.4.3, named after the features discussed in the following sections: "He II only", "He II+N III", and "Fe II only"[8].

When compared to the newly discovered flaring events to those in the literature, it is clear that AT2017bgt (Trakhtenbrot et al., 2019a) has a much stronger He II+N III Bowen fluorescence profile, CSS100217 (Drake et al., 2009) has stronger narrow emission lines overall, and AT2018dyk (Frederick et al., 2019) has a weaker blue continuum. The presence and strength of Fe II is uncorrelated with other spectroscopic properties of the transients shown. Of the ZTF sample, the transient spectrum of AT2019fdr shows the strongest Fe II complex. However, AT2019fdr shows no strong He II + Bowen fluorescence features while the others in the ZTF sample do. AT2019fdr and AT2019avd both show offset blue components of Hβ.

3.3.2.1 Strong He II profiles in AGN?

In the discovery paper for transient ASASSN-18jd, Neustadt et al. (2020) emphasized the relatively rare nature of strong He II emission in AGN in general, noting the exceptions in the Trakhtenbrot et al. (2019a) observational class of flares as well as the rapid changing-look AGN event AT2018dyk (Frederick et al., 2019). A strong He II line profile is common (but not ubiquitous) in the spectra of TDEs, and they are typically accompanied by Bowen fluorescence features (e.g. Blagorodnova et al. 2019; van Velzen et al. 2020b). AT2019avd, AT2019pev, AT2019brs look the most similar to AT2017bgt spectroscopically. They are spectroscopically classified as "He II+N III"-type flares in Figure 3.7.

[8]We note that although "only" is used in the categorization naming based on the presence of spectral features, all have strong Balmer features.

3.3.2.2 The Fe II complex

A strong Fe II line complex (blueward and redward of Hβ+[O III] in optical spectra, between 4434 Å and 5450 Å) is a distinguishing feature of NLSy1 galaxies. Reverberation mapping studies of AGN show that the line complex emitting region is measured farther than the Balmer line emitting region (e.g. Barth et al. 2013; Rafter et al. 2013). The Fe II complex seen in PS16dtm was interpreted as evidence of the system being a NLSy1 prior to the onset of the flare. CSS100217 also displayed a strong Fe II complex and was interpreted as a SN in a NLSy1 (Drake et al., 2011). TDE AT2018fyk also showed low ionization lines including an Fe II (37,38) emission multiplet emerging for 45 days during the tidal disruption event, and forms a class of Fe-rich TDEs along with ASASSN-15oi and PTF-09ge (Wevers et al., 2019). Therefore, this feature may indicate the presence of an AGN, but is not always useful in determining the nature of a particular AGN-related flare. For two of the transients in this sample, whether or not the Fe II complex can be seen in optical spectra depends on the phase and the continuum brightness of the transient — for AT2019fdr it was not observed for 368 days, and for AT2019avd it became no longer visible during the second rise 444 days after the initial spectrum was taken.

3.3.3 X-rays

There are only two significantly X-ray detected transients in the sample: AT2019pev and AT2019avd. We show their X-ray spectra in Figure 3.8 fit to power law models. The third, AT2019brs, was only detected in one epoch and not at a level that allowed for the signal-to-noise necessary for a spectrum.

The X-ray spectrum of AT2019pev is measured by *Swift XRT* with a power law index of $\Gamma = 2.99 \pm 0.02$, typical of the strong soft X-ray excess observed below 1 keV in NLSy1s ($\overline{\Gamma} = 2.8 \pm 0.9$; Boller et al., 1996; Forster & Halpern, 1996;

Molthagen et al., 1998; Rakshit et al., 2017). The spectrum of AT2019pev could also be explained by a 150 eV blackbody with a $\Gamma = 2$ power law component and no intrinsic absorption (Kara et al., 2019). We note that the soft excess observed in NLSy1s can mimick the blackbody temperatures expected for TDEs (e.g. Boller et al. 1996).

The spectral index of AT2019pev ($\Gamma \sim 3$) was similar to that of AT2018fyk, interpreted as a TDE with late-time disk formation (Wevers et al., 2019), as well as AT2018dyk, interpreted as a changing-look LINER "turning-on" into a NLSy1 (Frederick et al., 2019). The X-ray spectral index of AT2019avd was quite high even with regard to these events, with $\Gamma \sim 4 - 6$.

3.3.4 Black Hole Masses

We measured the black hole masses of the sample using two different methods, each with important caveats: The virial mass method, which may systematically underestimate BH masses for NLSy1s, and the host galaxy luminosity, which may be contaminated by the presence of an AGN. The $M_{\rm BH}$ calculated from the host galaxy luminosity is $M_{\rm BH,M_r} = -0.5 M_{r,\rm host} - 2.96$ following McLure & Dunlop (2002), and the standard virial method (e.g. Shen et al. 2011) was employed to obtain the virial black hole masses from FWHM Hβ reported in Table 3.2. The transient Eddington ratio estimates depend on the BH masses ($M_{\rm BH}$) as $L_{\rm Edd} = 1.3 \times 10^{38}$ $(M_{\rm BH}/M_\odot)$ erg s^{-1}, For each transient in the sample, we report a range of Eddington ratios in Table 3.2 bracketed by the Eddington ratio measured assuming the virial mass estimate for the BH mass, and the Eddington ratio measured assuming BH mass derived from the host galaxy luminosity. The range in BH masses, and therefore Eddington ratios, shown in Table 3.2 is quite large. We estimate statistical and systematic uncertainties of $0.3 - 0.5$ dex on these mass and Eddington ratio measurements, due to the typical scatter associated with single-epoch mass scaling relationships as well as the unknown BLR geometry (e.g. Liu et al. 2018a, 2020; Merloni et al. 2015; Runnoe et al. 2016).

Miller et al. (2019) obtained an independent measurement of the BH mass of AT2019pev. They measured $M_{\rm BH} = 3.7 \times 10^6 M_\odot$ from the observed Chandra X-ray luminosity (this observation is described in more detail in Section 3.2.4). This is closer to, but not consistent with, the virial mass estimate, meaning that the transient may not have been accreting near the Eddington limit at the time of the X-ray observation.

Table 3.2: Black hole mass measurements of the sample from optical spectra and host galaxy properties. NLSy1s are typically thought to be lower mass, highly accreting systems, but we show here that the uncertainty in the mass estimates generates significant uncertainty in the estimates of the Eddington ratios (described in Section 3.3.4). $M_{r,\rm host}$ is the r-band de Vaucouleurs and exponential disk profile model fit magnitude from the SDSS DR14 photometric catalog. The host of AT2020hle is not in the SDSS footprint, and so we instead use the Pan-STARRS1 r-band Kron magnitude of this source (Chambers et al., 2016).

Name	$M_{r,\rm host}$	λL_{5100A}	FWHM$_{H_\beta}$	log $M_{\rm BH,M_r}$	log $M_{\rm BH,vir}$	$L/L_{\rm Edd}$
	(mag)	(10^{43} erg s^{-1})	(km s^{-1})	[$M_\odot$]	[$M_\odot$]	
AT2019pev	-21.36	5.00 ± 0.04	878 ± 49	7.7	6.4	0.066-1.5
AT2020hle	-20.94	2.24 ± 0.02	1199 ±270	7.5	6.4	0.048-0.62
AT2019brs	-22.38	42.6 ± 0.8	1050 ± 77[a]	8.2	7.2	0.17-1.97
AT2019avd	-20.35	0.553 ± 0.008	1433 ± 35	7.2	6.1	0.023-0.29
AT2019fdr	-21.51	21.9 ± 0.2	1208 ± 57	7.8	7.1	0.24-1.2

a. The FWHM(Hβ) for AT2019brs agrees with the measurement in Rakshit et al. (2017) within the error estimates.

3.4 Discussion

In this section, we rule out possible physical scenarios for each outburst, beginning with core collapse supernovae IIn. We review why the supernova interpretation was quickly ruled out in favor of a supermassive black hole accretion scenario, and discuss how many of the characteristics of the objects are consistent with both

NLSy1s and TDEs. We compare the available evidence with other scenarios including TDEs, extreme AGN variability, and binary SMBHs in detail. We also discuss NLSy1 galaxies as the preferential hosts for these and other similar events, and outline a scheme for classifying future events based on the presence of spectral features.

3.4.1 "IIn or not IIn?": Preliminary Observational Classification of the Flare Sample

Identification of the sample presented here occurred with a slew of conflicting preliminary classifications at early times, which we describe below.

The narrow emission lines in the spectra of some SLSN (Type IIn) are a result of the highly luminous interaction of supernova ejecta from a massive progenitor with dense circumstellar medium. Therefore, under special circumstances, nuclear SNe can look spectroscopically very similar to rapid[9] flares from NLSy1s in the optical (e.g. Moriya et al. 2018). The shapes of the light curves of the transients in this sample looked rather like those of such supernovae, in the absence of additional observations. The smoothness of the flares in particular was unique with respect to typical stochastic AGN variability, and made these transients noteworthy for allocation of follow-up resources. Therefore, the narrow Balmer features in the spectra of these transients, coupled with their light curve shapes, left uncertainty in their early classifications. They could have been either Type IIn supernovae or NLSy1 AGN, while those with persistent strong He II λ4686 features in their spectra looked similar to that of TDEs. To illustrate this, Figure 3.9 shows spectra of the sample alongside a Type IIn SN as well as a TDE with Bowen fluorescence features. Additional follow-up observations in the UV/X-rays helped distinguish this sample of transients from SNe.

[9]With rise times on the order of days to weeks.

3.4.2 A Preponderance of Rapid Optical Transients in Narrow-line Seyfert 1 Host Galaxies

In the Analysis section (§3.3), we compared our sample to data from nuclear transients in the literature that happened to be hosted in NLSy1 galaxies. In this and the next sections, we discuss NLSy1s as an interesting AGN subtype, and observationally classify and link these events to one another on the basis of their shared host properties.

The narrower broad-line Balmer profiles and high amplitude variability, (especially in the X-rays, e.g. Frederick et al. 2018; Pogge 2000) in NLSy1s may be evidence of smaller black hole masses in these systems ($5 < \log(M_{\rm BH}[M_\odot]) < 8$; e.g. Mathur et al. 2001), and/or higher observed accretion rates (Grupe et al., 2010; Marconi et al., 2008; Pounds et al., 1995; Wang et al., 1996; Xu et al., 2012). The virial masses derived from spectral measurements of the population may also be explained with geometrical effects, when interpreted as the classic broad-line AGN seen along a lower inclination angle between the broad-line emitting region and the line of sight (Baldi et al., 2016; Decarli et al., 2008; Rakshit et al., 2017).

Studies of NLSy1s typically find them to be highly photometrically variable only in the X-rays. At optical wavelengths, however, Klimek et al. (2004) found that rapid, high amplitude variability was rare in a sample of 172 observations of NLSy1s across 33 nights. Ai et al. (2010) also found that NLSy1s had systematically lower optical variability amplitudes ($\lesssim 0.2$ mag) than broad-line Seyfert 1s in a sample of 275 AGN at $0.3 < z < 0.8$ in 3 years of SDSS data.

However, optical flares are not unheard of in NLSy1s (e.g. NGC 4051, Guainazzi et al. 1998; Uttley et al. 1999). Klimek et al. (2004) noted the exception of IRAS 13224-3809, which showed both dramatic X-ray and optical variability on short timescales (Miller et al., 2000). Here we describe a number of distinct events, including the Trakhtenbrot et al. (2019a) observational class of optical flares, the "on" state of AT2018dyk, and the host of PS16dtm and CSS100217:102913+404220, which were all consistent with NLSy1 related activity.

Trakhtenbrot et al. (2019a) established a new observational class of dramatic AGN flares accompanied by Bowen fluorescence features. The events in this class all originated from active black holes that were classified as NLSy1 galaxies by their Balmer FWHMs. Their optical spectra were unusual for NLSy1s in that they showed strong "double-peaked" He II profiles with contributions from the N III λ4640 Bowen fluorescence feature, indicating the presence of a strong UV ionizing continuum. This was consistent with the UV brightness observed in the small sample of objects as well as the steep blue continua in these sources. The slow UV and spectral emission line evolution over a period of $\sim$450 days ruled out a TDE, and these were instead interpreted as enhanced accretion onto the SMBH of a pre-existing AGN. AT2017bgt was presented as the prototype of these dramatic SMBH UV/optical flares irradiating the BLR. It showed a very slow decrease in optical flux over several months following a relatively shallow ($\sim$0.5 mag) rise to peak over $\sim$80 days from a previous non-variable state. During the transient, the X-rays increased by a factor of $2-3$ from a previous measurement by ROSAT. The persistence of the UV emission over 500 days distinguished it from SNe, and the extremely intense nature of the UV continuum as well as presence of the Bowen fluorescence features in the optical spectrum distinguished it from CLAGN. Two other NLSy1s, OGLE17aaj (Gromadzki et al., 2019) and ULIRG F01004-2237 (Tadhunter et al., 2017) (the latter previously interpreted as a TDE), were retroactively reclassified as belonging to this new observational class of NLSy1s.

We compare with AT2018dyk, a changing-look AGN which transformed from a LINER galaxy to a NLSy1. It was identified as such primarily based on X-ray and UV spectra. It displayed strong high ionization forbidden (i.e. "coronal") emission in the optical and UV spectra, an X-ray flare delayed by 60 days, and showed a late-time $g-r$ color change as it faded slowly over 1 year. This was the only AGN with Balmer lines consistent with a NLSy1 among a new class of "changing-look LINERs", including SDSS 1115+0544 (Yan et al., 2019).

PS16dtm (iPTF16ezh/SN 2016ezh) was a near-Eddington but X-ray-quiet nuclear transient with strong Fe II emission and $T_{\rm BB} \sim 1.7 \times 10^4$ K. It rose over ~50 days to "superluminous" levels (log $L_{\rm bol}$ [ergs s^{-1}] > 44) at peak before plateauing twice over ~50 and ~100 days while maintaining a constant blackbody temperature. The event was interpreted as a TDE exciting the BLR in a well studied, spectroscopically-confirmed NLSy1 with $M_{\rm BH} \sim 10^6 M_\odot$(Blanchard et al., 2017). X-ray upper limits showed dimming by at least an order of magnitude compared to archival observations, but Blanchard et al. 2017 predicted the X-rays would reappear after the obscuring debris (oriented perpendicularly to the accretion disk) had dissipated. We show the V-band ASASSN photometry for PS16dtm in Figure 3.4 which appears similar in shape and absolute magnitude to AT2019fdr, though longer in duration.

CSS100217:102913+404220 displayed a high state ($M_V = -22.7$ at 45 days post-peak) accompanied by broad Hα and was interpreted either as a Type IIn SN (Drake et al., 2011) or a TDE (Saxton et al., 2018) near the nucleus (~150 pc) of a NLSy1 in a star forming galaxy. It eventually faded back to slightly below its original level after one year, which was interpreted as interacting with and subsequently flushing a portion of the accretion disk.

Similar events are not unheard of in broad-line AGN systems, though they may be comparatively more rare. Neustadt et al. (2020) reported a candidate for such a rapidly flaring event with quasar-like properties, ASASSN 18jd, although continued observations of this transient will be critical for a better understanding of the properties of the host.

3.4.3 Observational Classification: The "Family Tree" of NLSy1-associated Transients

In Table 3.3, we use this sample to motivate a framework for quickly classifying similarly ambiguous flaring events. We investigate the following:

- AGN/NLSy1 characteristics (an empirical $W1 - W2$ WISE color cutoff from Assef et al. 2013; Stern et al. 2012, which is comparable between NLSy1s and broad-line Seyfert 1s; Chen et al. 2017; a strong Fe II complex; narrow Balmer emission; and [O III]/H$\beta < 3$; Rakshit et al. 2017),

- TDE characteristics (host black hole mass below the Hills mass ($\sim 10^8 M_\odot$), and a lack of cooling or significant rebrightening),

- X-ray properties (the presence of which can occur in both AGN and TDEs, but are less likely in the SN scenario).

We apply these criteria in Table 3.3 and color code them as blue or green based on whether they favor the TDE or AGN scenario, respectively (as the SN scenario has been ruled out in Section 3.4.1). The spectroscopic class, based on the presence of N III Bowen fluorecence features, Fe II, and/or He II λ4686, which can occur in both TDEs as well as flaring NLSy1s, is then interpreted in the context of one of these scenarios. Based on this table, we confirm the interpretations for three of the four NLSy1-associated transients reported in the literature, except for CSS100217 for which we favor the AGN scenario over the SN interpretation.

Summarized briefly: We expect transients with strong Fe II complexes are most likely associated with AGN, those with very steep soft X-ray spectra ($\Gamma > 5$) and no intrinsic absorption are most likely associated with TDEs, and those with strong Bowen fluorescence profiles and slow UV and spectral evolution are likely associated with enhanced accretion onto supermassive black holes from a pre-existing accretion disk. The timing of a mid infrared flare may also help to distinguish between an AGN and a TDE — if it precedes the optical, it is likely associated with AGN variability, but if it follows as an echo, it may be associated with a TDE (van Velzen et al., 2016).

van Velzen et al. (2020b) established a spectroscopic classification scheme for the sample of TDEs discovered during the first half of the ZTF survey, distinguishing those with and without He II in a single epoch. About half of the TDEs in that sample were "H-only", and only one was "He-only". They found that higher density conditions were likely for the rest of the TDEs which had H and He lines, as well as Bowen features.

For the flaring NLSy1 sample presented here, we establish the following spectroscopic classes to describe each of the transients based on the presence or absence emission features crucial to their physical interpretations:

1. "He II only",
2. "He II+N III", and
3. "Fe II only",

and we propose the following naming convention for these classes: "NLSy1-HeII", "NLSy1-HeII+NIII", and "NLSy1-FeII".[10]

3.4.4 Physical Interpretation of the Transient Flares

In the following section we consolidate all that is known about the relevant properties of each object in the sample, and compare them with the related transients in NLSy1s in the literature, to explore each of the following scenarios: A

[10]We note that although hydrogen features are not explicitly named in this feature classification scheme, all spectra of the transients show resolved narrow ($1000 < \mathrm{FHWM} < 2000$ km s^{-1}) Balmer features (see Section 3.3.2).

Table 3.3: Comparison of the properties of individual objects in the sample (upper table) and NLSy1-related transients in the literature (lower table). "✓" means that property is observed, and "×" indicates that characteristic was not observed. See the extended published version in Frederick et al. 2021 (in prep.) for the full table including UV and emission line diagnostics (uniform for all sources and representing one for each class such that the interpretations in the final column are unchanged). "Rebrighten" refers to a significant recovery of at least half the peak luminosity of the source. Following the convention of Figure 3.7, blue (green) indicates a property associated with the TDE (flaring AGN) scenario.

Name	$\log M_{BH}<8$ $[M_\odot]$	$H\beta<2000$ km s^{-1}	Fe II	$\Delta g - r \sim 0$ mag	X-ray Γ	W1-W2 >0.7 mag[a]	Re-brighten	Spec. class	Interp.
AT2019brs	×	✓	✓	✓	✓[b]	✓	×	HeII+NIII	AGN
AT2019pev	✓	✓	×	✓	3	×	✓	HeII+NIII	AGN
AT2019fdr	✓	✓	✓	×	×	×	×	FeII	TDE
AT2019avd	✓	✓	✓	×	5	×	✓	HeII+NIII	AGN
AT2020hle	✓	✓	×	✓	✓[b]	×	×	HeII	TDE
CSS100217	✓	✓	✓	×	3	✓	×	FeII	AGN
PS16dtm	✓	✓	✓	✓	2[c]	×	×	HeII+FeII	TDE
AT2017bgt	✓	✓	✓	✓	2	×	✓	HeII+NIII	AGN
AT2018dyk	✓	✓	×	×	3	×	×	HeII	AGN
PS1-10adi	✓	✓	✓	✓	✓[b]	×	×	FeII	TDE

a. We select the less conservative color cut presented in Stern et al. (2012).
b. The single low level XRT detection of AT2019brs and AT2020hle occurred only once throughout the follow-up campaign and was not enough to take a reliable spectral measurement. Similarly, the late stage X-ray detection of PS10adi reported in Jiang et al. (2019) was not sufficient to measure the softness of the spectrum.
c. The host of PS16dtm displayed X-rays only prior to and following the fading of, but not for the duration of, the transient.

PS16dtm-like TDE in a NLSy1, A Sharov-21-like microlensing event, a CSS100217-like SN in a NLSy1, and a binary SMBH scenario.

3.4.4.1 Association of the Transients with AGN

There is evidence that all sources in the sample are associated with AGN rather than distinct explosive events occurring in a normal galaxy. Although these outbursts may not necessarily be the result of an intrinsic enhancement in AGN accretion activity, transients with fast-rise/slow-decay (such as those in this sample, along with slow-rise/fast-decay, and symmetric light curve shapes) were well-represented in a sample of 51 AGN flares discovered in CRTS (Graham et al., 2017).

Rakshit et al. (2017) spectroscopically classified the SDSS spectrum of the host galaxy of AT2019brs as harboring an AGN NLSy1 > 12 years prior to the onset of the smoothly flaring transient reported here.

As evident in Figure 3.9, the strengths of the Balmer lines in the transient spectra are most consistent with that of a NLSy1. Ne V λ3426, when observable, is typically associated with AGN, and is present in the spectra of these sources. Strong He II profiles, although somewhat rare in association with normal stochastic AGN variability (Neustadt et al., 2020), have been observed before and interpreted as the signature of a sudden enhancement of accretion (e.g. Frederick et al. 2019; Trakhtenbrot et al. 2019a).

Persistent X-rays are a likely signature of accretion onto a SMBH rather than a SN. A strong soft X-ray excess is characteristic of NLSy1s. However, it is typically accompanied by a hard X-ray continuum component (not present in either X-ray detected transient in this sample), and not nearly as ultra-soft as the X-rays seen in AT2019avd ($4 \lesssim \Gamma \lesssim 6$), which are slopes more frequently observed in the X-ray spectra of TDEs.

3.4.4.2 The SN Scenario

It is highly improbable that these flares are the result of normal SN explosions. We observe long-lived U-band emission in AT2019fdr, persistent UV emission in all transients in the sample, and strong transient X-ray detections in AT2019pev and AT2019avd. There is also only a small likelihood of a SN in the host galaxy along the line of sight unassociated with the AGN. The strongest evidence against the normal supernova scenario is the persistence of the He II emission features $\sim 10-100$ days after the onset of the flare — such flash ionization signatures are only visible in supernova spectra at very early times (e.g. Bruch et al. 2020; Khazov et al. 2016).

At least one of these transients (AT2019fdr) shares a number of properties with

CSS100217, which displayed soft X-rays and was interpreted as a SN IIn explosion in an AGN disk. The SN interpretation of CSS100217 was largely based on light curve energetics, which are similar to those of this sample. The $g - r$ color change, and the peak magnitude of $-23 \lesssim M_V \lesssim -22$ are very similar in particular between CSS100217 and AT2019fdr. Type IIn supernovae can exhibit strong Fe II lines in late spectra, such as AT2019fdr did.

However, in contrast, the light curve evolution differs in that CSS100217 fades at least twice as quickly as AT2019fdr. Also, the Fe II complex of CSS100217 was always visible throughout the flare, and Drake et al. (2011) observed a broad ∼3000 km s^{-1} component in Hα which got broader with time in subsequent follow-up spectra of CSS100217. Strong P Cygni profiles are observed in the optical spectra of SN, and from such profiles we would expect an absence of absorption on the blue end of the Balmer line profiles, rather than emission as in the spectra of AT2019avd and AT2019fdr. Therefore, based on this evidence we rule out the SN Type IIn scenario.

3.4.4.3 The TDE Scenario

The Hills mass is the mass for which the tidal Roche radius is equivalent to the gravitational Schwarzschild radius of the black hole, beyond which a star (that would otherwise be tidally pulled apart) is instead left intact as it passes the event horizon (Hills, 1975). This maximum mass to tidally disrupt a solar-type star just outside the event horizon is $10^8 M_\odot$. Therefore a SMBH mass significantly above this limit would likely rule out a TDE. Of the supermassive black hole masses derived for the host galaxies, only that of AT2019brs is inconsistent with a TDE scenario, (although we note that it is consistent within the typical uncertainty for such mass measurements). The range of absolute magnitudes of the flares in this sample ($-23 < M_r < -19$ mag) also tend to be intrinsically brighter at peak than all but one of the ZTF TDEs ($M_r > -20$ mag) reported in van Velzen et al. (2020a), AT2018iih ($M_r = -21.5$ mag).

Similar to TDEs PS16dtm and AT2018fyk, AT2019fdr showed two distinct plateau stages on month-long timescales after fading, with some slight fading in between. Color evolution is rare but not unheard of for TDEs, and the cooling AT2019fdr shows post-peak is slow, with the transient still detected in the UV at late times as would be expected for a TDE. Optical rebrightening following the intial flare has been interpreted as the result of late time disk formation in a number of TDEs (e.g. van Velzen et al. 2019; Wevers et al. 2019). However, rebrightening with high amplitudes returning nearly to pre-flare levels such as that seen in AT2019pev and AT2019avd has neither been observed[11] nor predicted (e.g. Chan et al. 2020, 2019) from a TDE. In these cases with rebrightening, a TDE is strongly ruled out.

AT2019avd and AT2019fdr, like AT2018fyk, only showed Fe II at certain times during the flare. AT2019avd only displayed Fe II during its first peak, and in AT2019fdr, the Fe II complex got more visible as the transient faded. AT2019fdr is the only transient in the sample with a lack of He II features in its spectra. Within the van Velzen et al. (2020b) spectral classification scheme for optical TDEs, AT2019fdr would be a H-only TDE, with the Fe II complex attributed to the NLSy1 host. It is important to note that the transients with blue horn features in Hβ, AT2019avd and AT2019fdr, may be signatures of wind ejecta with a velocity distinct from the AGN.

Enhanced N III lines such as that seen in the NLSy1-HeII+NIII spectroscopic class (AT2019pev, AT2019brs, and AT2019avd) are a prediction of TDEs in AGN when compared to the host spectrum (Gallegos-Garcia et al., 2018; Kochanek, 2016; Liu et al., 2018b). Unfortunately, a pre-flare spectrum was only available to test this for AT2019brs (Figure 3.6).

Many properties of the hosts do not align with what we expect from AGN.

[11] Except in the case of the periodicity of ASASSN 14ko, which was interpreted as a possible repeating partial TDE (Payne et al., 2020).

The WISE colors, for example, span a broad range of $0.06 - 0.98$ mag (Table 3.3). The IR flare associated with AT2019avd could be interpreted as a dust echo, similar to those seen in a number of TDEs (van Velzen et al., 2016). A host-subtracted SED fit to the *Swift* photometry of AT2019avd gives a blackbody temperature consistent with that of known TDEs, $10^{4.25}$ K.

The X-ray variability of TDEs can vary erratically during a flare (e.g. van Velzen et al. 2020b; Wevers et al. 2019). Although soft X-ray excesses with $\Gamma \sim 3$ are characteristic of NLSy1s, AT2019avd displays an X-ray power law index much higher than typically seen in NLSy1s, and more characteristic of the extremely soft X-ray spectra observed in TDEs.

Based on the combination of properties shown in Table3.3, we conclude that two of the flares, AT2020hle and AT2019fdr, are better explained as TDEs than AGN flares, although the interpretation is not clear-cut. However, if we assume that their spectra are a combination of the host NLSy1 galaxy and the transient line emission from the TDE, then given their spectral classes given here of NLSy1-FeII and NLSy1-HeII, respectively, then the TDE spectra themselves, in these NLSy1 galaxies, would have to be of the TDE subclasses of TDE-H (H only lines) and TDE-He (He II only lines), respectively, in order to match the observed spectra.

3.4.4.4 The Extreme AGN Variability Scenario

Graham et al. (2017) presented a sample of quasars displaying extreme variability in CRTS. Some had similar profiles and amplitudes (rising by $2-2.5$ mag) but longer timescales (500-1000 days) compared to the flares presented here, For example, J002748-055559 rose by nearly $\sim$2 mag compared to the steady level it maintained for several years prior.

The optical spectra of the transients in the sample presented here belonging to the "NLSy1-HeII+NIII" spectroscopic class, as well as the UV brightness of the sample, are consistent with the properties of the observational class of flares with Bowen fluorescence established in Trakhtenbrot et al. (2019b). However, all of the transients presented here have faster fading timescales than AT2017bgt. Trakhtenbrot et al. (2019b) stated that the fade timescale of AT2017bgt was longer than expected for a TDE. However, we note that at least one TDE in the van Velzen et al. (2020b) sample (that also displayed Bowen fluorescence features) was observed to fade over nearly 15 months,

3.4.4.5 The Gravitational Microlensing Scenario

Flares due to microlensing are expected to be observable in difference imaging surveys with the combined baseline of iPTF and ZTF. The rise portions of the light curve shapes of all the transients measured in Section 3.3.1.1 being well-fit by quadratics is consistent with a lensing event, however, all but AT2020hle have a longer decay with respect to the initial rise. Microlensing by multiple foreground sources can give rise to a symmetric (with respect to the fade) double peak with a dip in the middle of the optical light curve such as that seen in AT2019pev (Hawkins, 1998, 2004; Schmidt & Wambsganss, 2010). The cuspy shape of the first peak is also characteristic of microlensing light curves. AT2019avd also showed a second peak in its light curve, but the first peak was a lot more rapid and luminous than the second. To test this scenario in AT2020hle would require continuing to observe for an additional flare.

The microlensing scenario, however, would not account for the strong transient Bowen fluorescence features that appear only at late times in AT2019avd, and only at early times in AT2019pev (Figure 3.11). Meusinger et al. (2010) explained a similar event as a background quasar with a UV flare in J004457+4123, also known as Sharov 21, being microlensed by a foreground star in M31.

Microlensing is characteristically achromatic, and therefore would be ruled out by the clear evidence for $g - r$ color change observed in AT2019fdr.

3.4.4.6 The SMBH Binary Scenario

Variability on the timescales of years due to a binary SMBHB system would require a subparsec separation (e.g. Graham et al. 2015). In such a system, two SMBHs induce tidal torques carving out a cavity in the circumbinary accretion disk, and may be surrounded by their own minidisks at sufficient separations. The interaction of accretion streams with the cavity could cause an outburst on the approximate timescales seen in this sample, which is dependent on the properties of the system. This phenomenon is seen in simulations of SMBH binaries (e.g. Gold 2019; Ryan & MacFadyen 2017).

We see evidence of offset narrow Balmer emission lines in the spectra of AT2019fdr and AT2019avd, which may indicate a significant separate physical component, although it is unclear what is contributing to those blueshifted velocities.

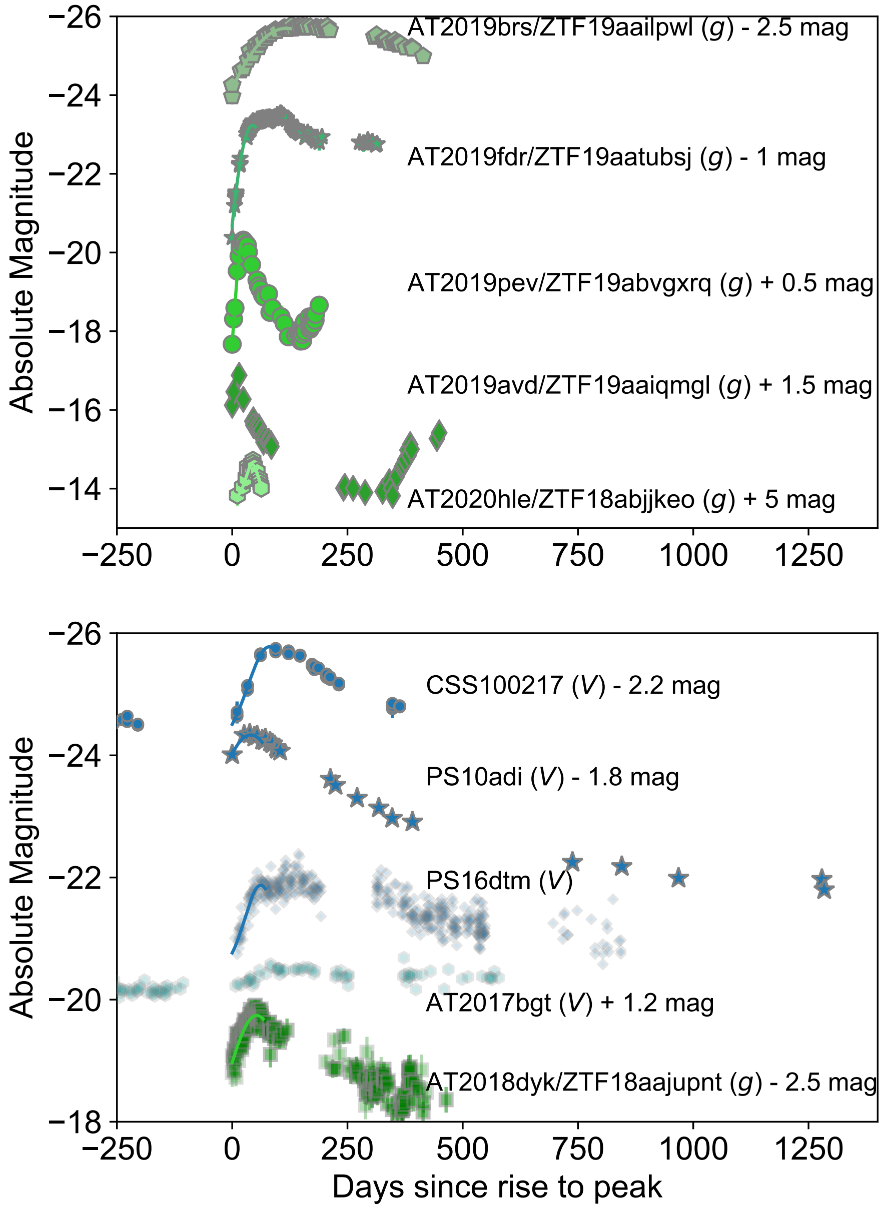

Figure 3.3: The difference imaging light curves of the ZTF sample (upper panel) compared to the published light curves of NLSy1-related events from the literature (lower panel): changing-look LINER AT2018dyk (Frederick et al., 2019), TDE in a NLSy1 PS16dtm (Blanchard et al., 2017), SN in a NLSy1 CSS100217 (Drake et al., 2011), and the aperture photometry of flaring NLSy1 AT2017bgt (Trakhtenbrot et al., 2019a). We show only $g-$band observations for the ZTF sample (upper panel), and omit errorbars for visual purposes. Note the differences in optical filters shown (g in green, V in blue), the differences in colors and markers used to represent the same filters for visual clarity, as well as the difference in y-axis scale between the panels. CRTS data for CSS100217 $>$ 200 days prior to the transient is not shown on this scale, but showed no significant activity for $>$ 5 years.

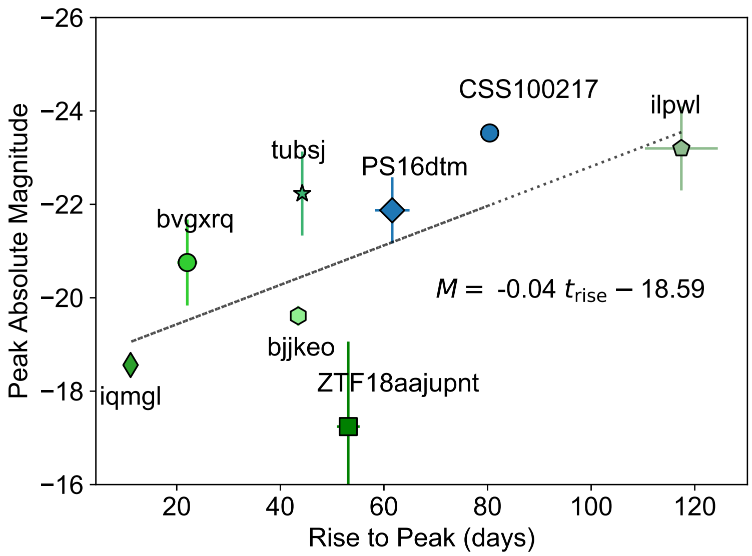

Figure 3.4: Correlation of the rise times of the sample light curves with the maximum absolute magnitude. Fits to light curves are described in Section 3.3.1.1. The same color scheme and markers are used as in Figure 3.3.

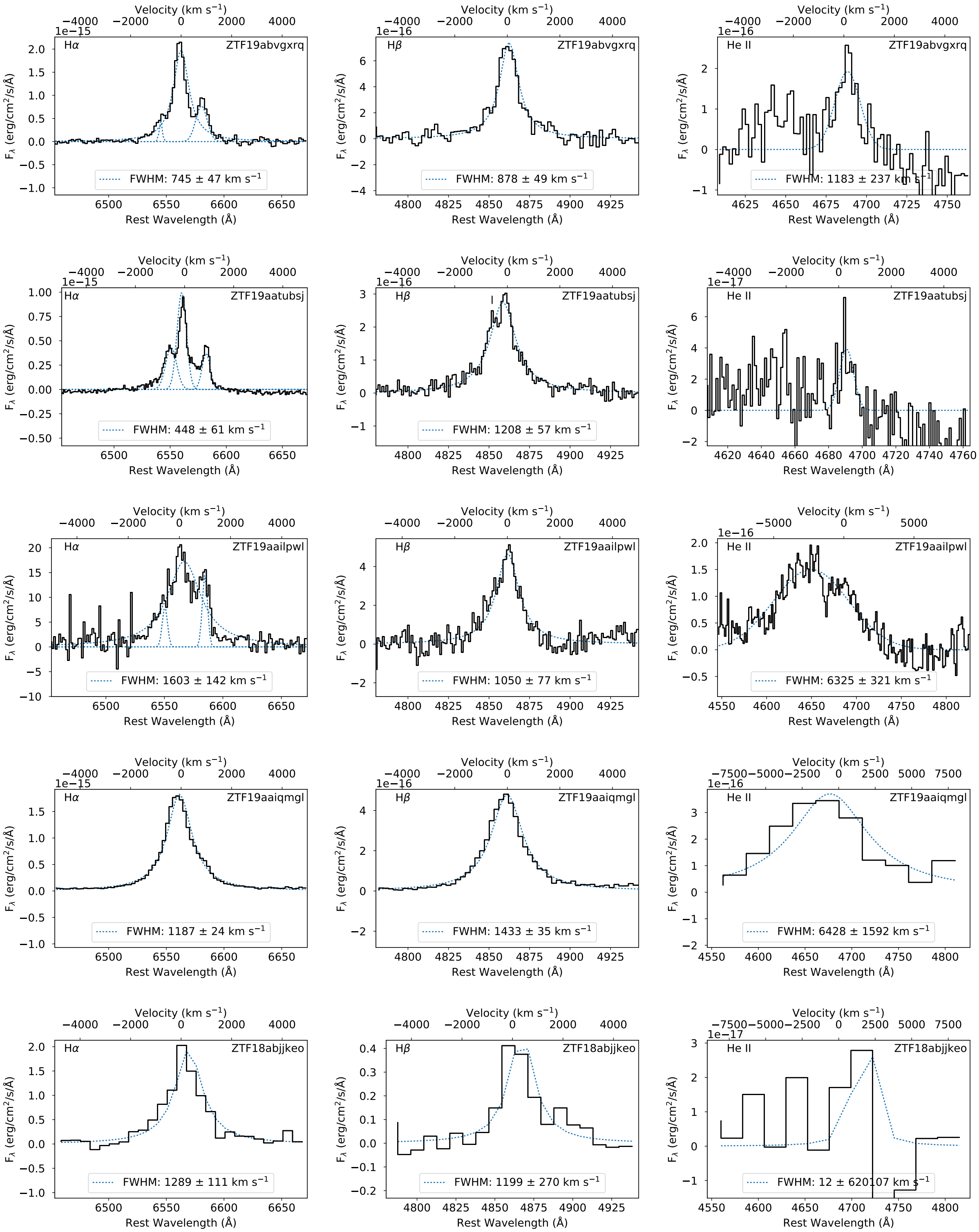

Figure 3.5: Gaussian fits to the Hα+[N II] and Hβ line profiles of all transients in the sample show that their Balmer lines have a FWHM consistent with (and Lorentzian Balmer profiles characteristic of) that of narrow-line Seyfert 1s. The offset blue peak in the Hβ profile of AT2019fdr is marked by a vertical line.

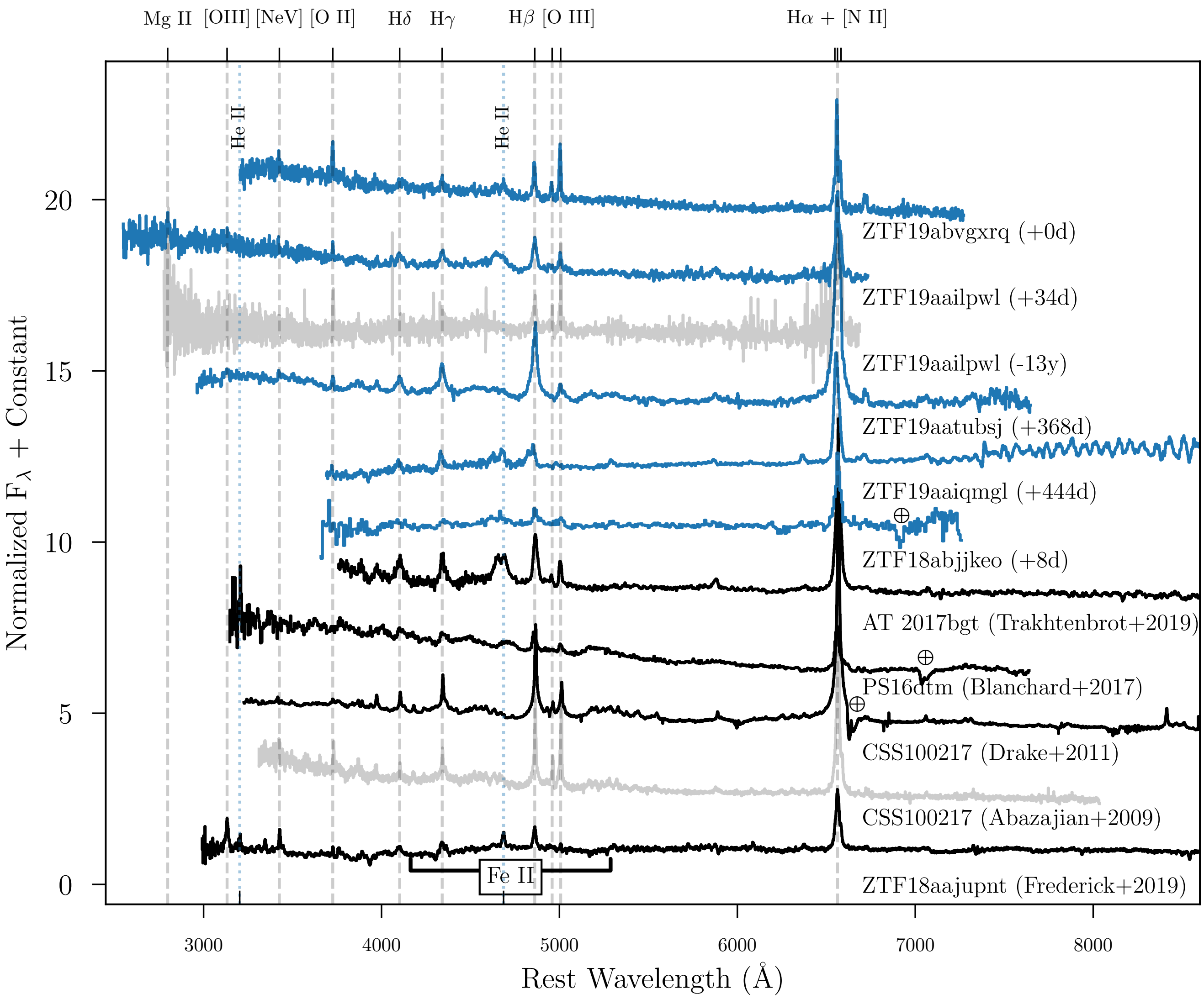

Figure 3.6: Comparison of the ZTF sample of flares (in blue), as well as discovery spectra for the NLSy1-related events from the literature (in black): changing-look LINER AT2018dyk (Frederick et al., 2019), TDE in a NLSy1 PS16dtm (Blanchard et al., 2017), SN in a NLSy1 CSS100217 (Drake et al., 2011), and Bowen fluorescent flare AT2017bgt (Trakhtenbrot et al., 2019a), and their pre-event spectra when available (in grey). For AT2019fdr and AT2019avd here and in Figure 3.7, we plot the spectra after continuum fading rather than the discovery spectra, to display the features used in the spectroscopic classification scheme discussed in Section 3.4.3. AT2019fdr and AT2019avd show offset blue peaks in Hβ, and the peak of He II is offset from 4686 Å in AT2020hle.

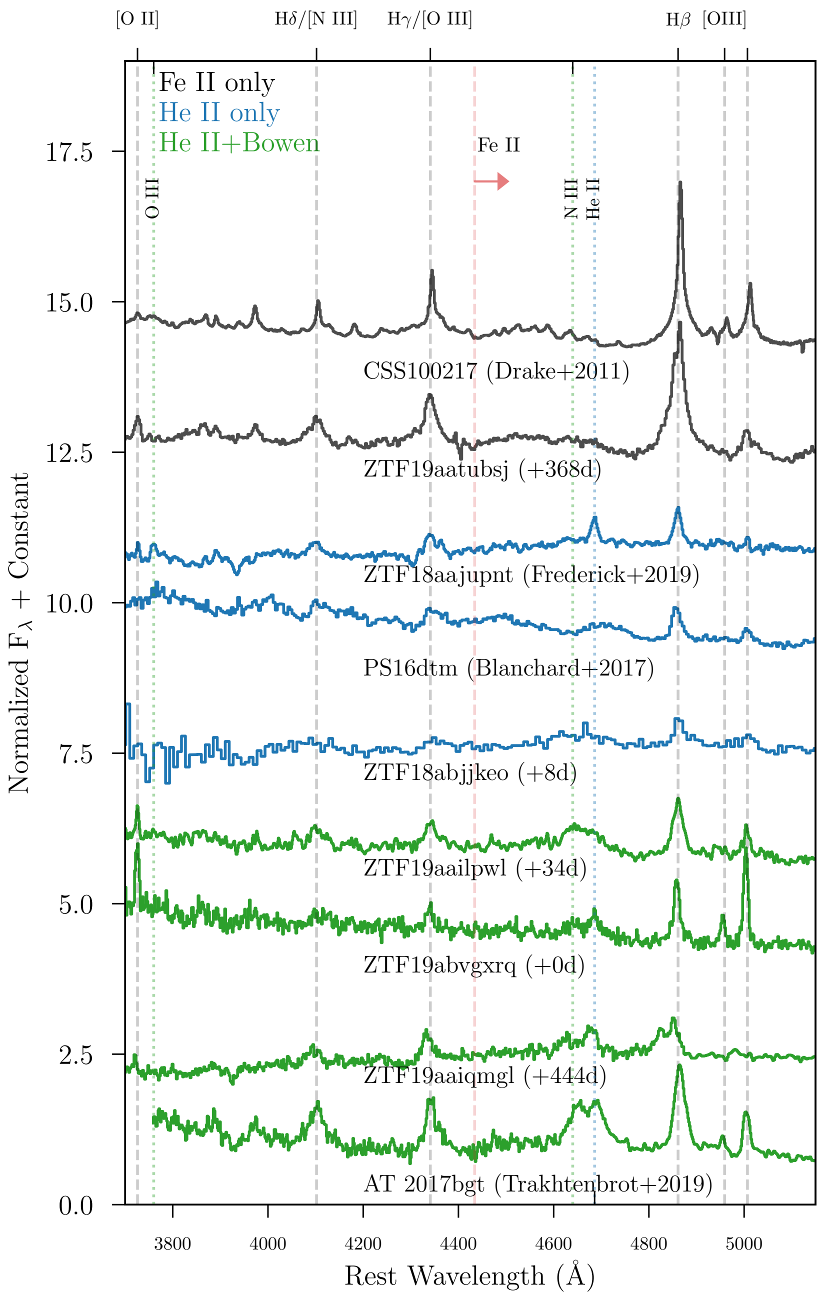

Figure 3.7: Zoom-in on the 4000-5000 Å region of Figure 3.6 showing the comparison of the strength of Hβ, Fe II, and [O III] of the sample with NLSy1-related events in the literature. We color-code the sample and establish categories based on the presence and absence of key emission line features as described in Section 3.4.3. Blue spectra indicate the presence of He II, and black spectra indicate transients which displayed Fe II only, (though we note that PS16dtm showed both features). Those in green display Bowen fluorescence features in addition to He II, and are most spectroscopically similar to AT2017bgt and the other AGN flares comprising the sample in Trakhtenbrot et al. (2019a).

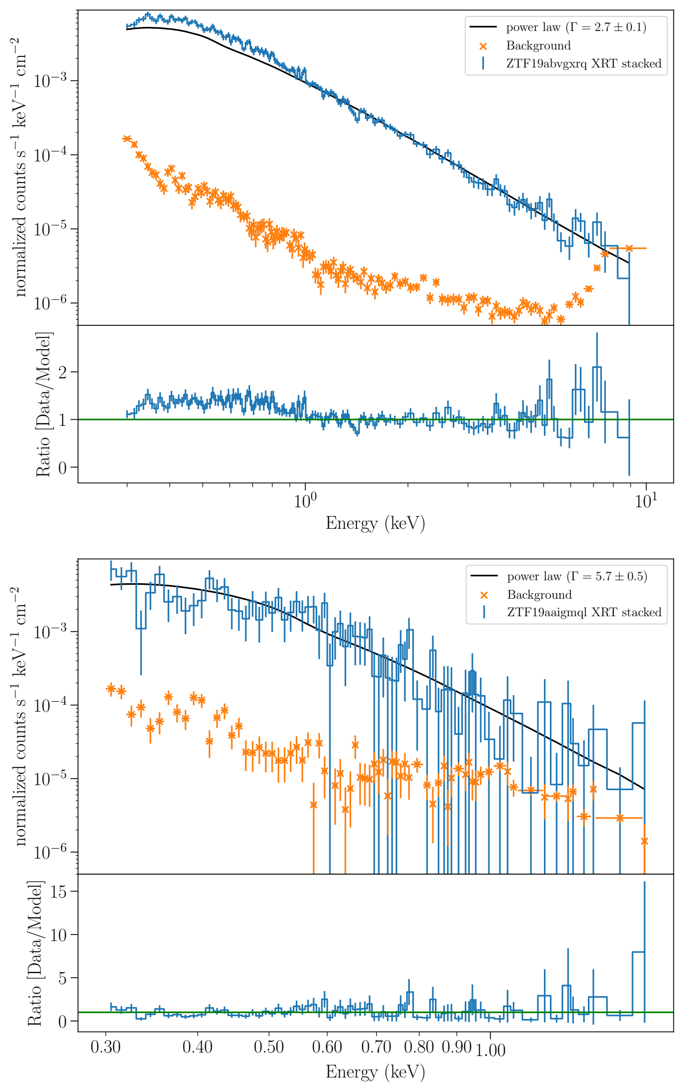

Figure 3.8: Upper panel: An absorbed power law fit and ratio residuals to the ∼100 ks stacked *Swift XRT* spectrum of AT2019pev (spectral index $\Gamma = 2.7 \pm 0.1$). Lower panel: The ∼4 ks stacked spectrum of AT2019avd ($\Gamma = 5.7 \pm 0.5$).

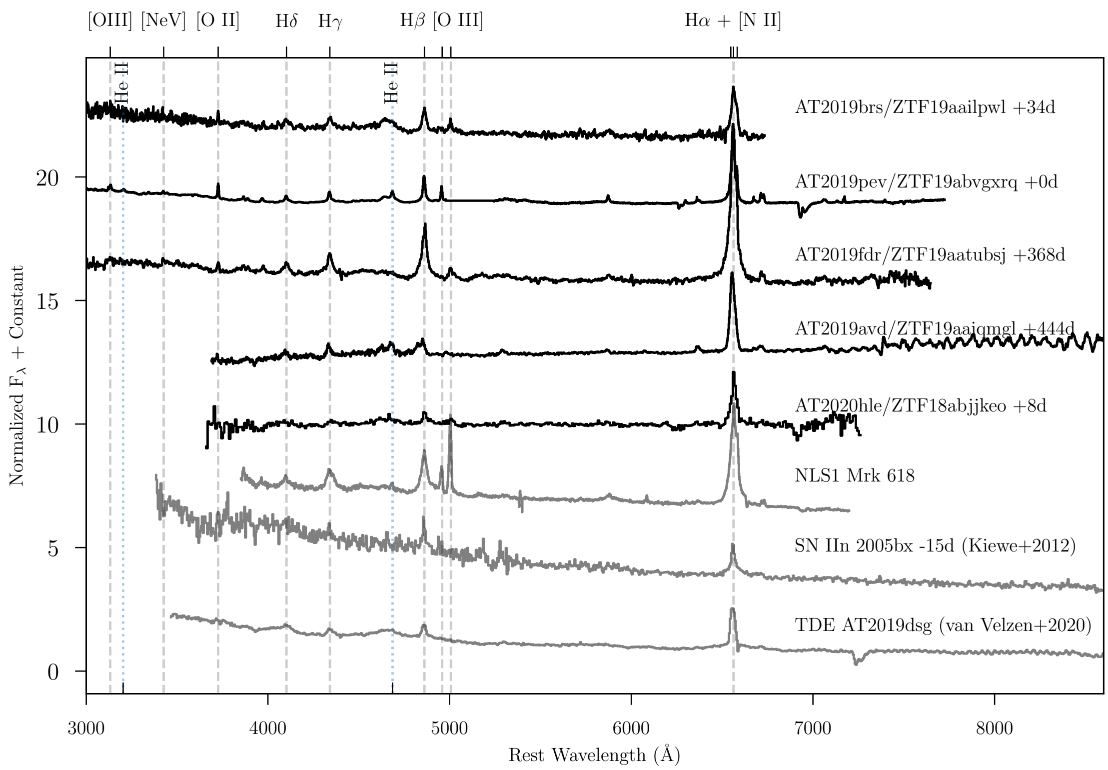

Figure 3.9: We compare the spectra of the transient sample (in black) to archetypal NLSy1 Mrk 618, as well as a normal Type IIn supernova, SN 2005bx (Kiewe et al., 2012), and AT2019dsg, a normal TDE in a star forming galaxy with Bowen fluorescence features and a coincident neutrino detection (Stein et al., 2020; van Velzen et al., 2020b).

3.5 Conclusions

We report five nuclear flaring events associated with NLSy1s, all serendipitously[12] discovered in ZTF. We measured their photometric characteristics (such as light curve shape, $g - r$ color, and rise to peak luminosity, finding a correlation between rise time and absolute magnitude), and spectroscopic properties. We then established groupings of the objects in the sample based on analyses of the months-long follow-up campaigns of these objects. Based on observed groupings of the sample, we propose the following naming scheme of spectroscopic classes of such transients for use in future optical surveys: "NLSy1-HeII", "NLSy1-HeII+NIII", and "NLSy1-FeII". We ruled out the possibility that these are Type IIn supernovae occurring in NLSy1 systems. Despite the heterogeneity of the sample's properties, two of the flares presented in this work have multiwavelength characteristics which could be consistent with TDEs in NLSy1s (AT2019fdr and AT2020hle), with spectral classes of NLSy1-FeII and NLSy1-HeII, respectively. This is a high TDE rate relative to quiescent galaxies, which are more abundant than NLSy1s. The prevalence of TDE candidates in the NLSy1 AGN class could be a natural result of their hosting smaller black holes compared to typical broad-line AGN, and therefore satisfying the Hills mass criterion for an observable TDE. However, without pre-event spectra and X-ray imaging to isolate the contribution of the putative TDE to the composite NLSy1+TDE emission, flaring due to extreme AGN variability cannot be definitively ruled out. For two in the sample (AT2019pev and AT2019avd), we can rule out the simple TDE scenario from rebrightening in their light curves, and we determine that they, along with AT2019brs (which had a pre-flare NLSy1 spectral classification and a black hole mass estimate too large to host a canonical TDE), are

[12] As the Trakhtenbrot et al. (2019a) observational class was established midway through the ZTF survey, we had not been systematically filtering such events when the population became apparent in the nuclear transients alert stream search.

likely outbursts related to enhanced accretion in excess of typical AGN variability, and with spectral features we classify as "NLSy1-HeII+NIII", and members of the Trakhtenbrot et al. (2019a) class of AGN flares.

Given this sample, together with the growing number of interesting rapid optical transients associated with NLSy1s we reviewed in the literature, we posed the question of why such environments are observed to preferentially host these outbursts. Given the relative fraction of NLSy1s found with respect to other AGN classes in spectroscopic surveys such as SDSS ($\sim$15%; e.g. Rakshit et al. 2017; Zhou et al. 2006), there is likely an underlying factor enhancing this rate. We suggest four different possible explanations for this enhancement:

1. A selection bias due to shorter timescales for lower mass BH systems (like NLSy1s), which are therefore more likely to be captured within the baseline of wide field optical surveys,

2. A systematic disregard of smooth flares in broad line AGN during transient searches, or

3. A true intrinsic rate enhancement due to instabilities causing rapid changes in the observable environments or accretion efficiencies of these systems.

Follow-up strategies of optical transients in AGN that are similarly ambiguous at early times may stand to benefit from the framework we offer here. We hope this classification scheme will guide real-time predictions for potential future behavior of large amplitude flares in NLSy1s, which are clearly an interesting population for future study. The next step will be to perform a systematic study of the variability of NLSy1s detected in ZTF, to assess the completeness and rate of this sample of transients with smoothly flaring light curves, and compare to a sample of broad-line AGN. Expanding on the small number of unusual transients associated with NLSy1s not only sheds light on the parameter space in which they reside, but also provides the framework for a decision tree for understanding such outbursts when they are inevitably captured at higher rates in upcoming wide field surveys. This will be imperative to establish in advance of larger and deeper surveys such as ZTF Phase II and the Vera C. Rubin Observatory (formerly known as LSST; Ivezić et al. 2019), to which the timescales of these flares are well-suited. Continued multiwavelength monitoring of the entire sample will be important to determine the host properties for those with sparse data prior to the transient, and for understanding the evolution and nature of these flares.

3.6 Appendix

The light curves in Figure 3.10 are from the second IPAC data release of ZTF forced photometry. Figure 3.11 shows the region of interest around He II, Hβ+[O III], and the Fe II complex for all follow-up spectra taken of the sample.

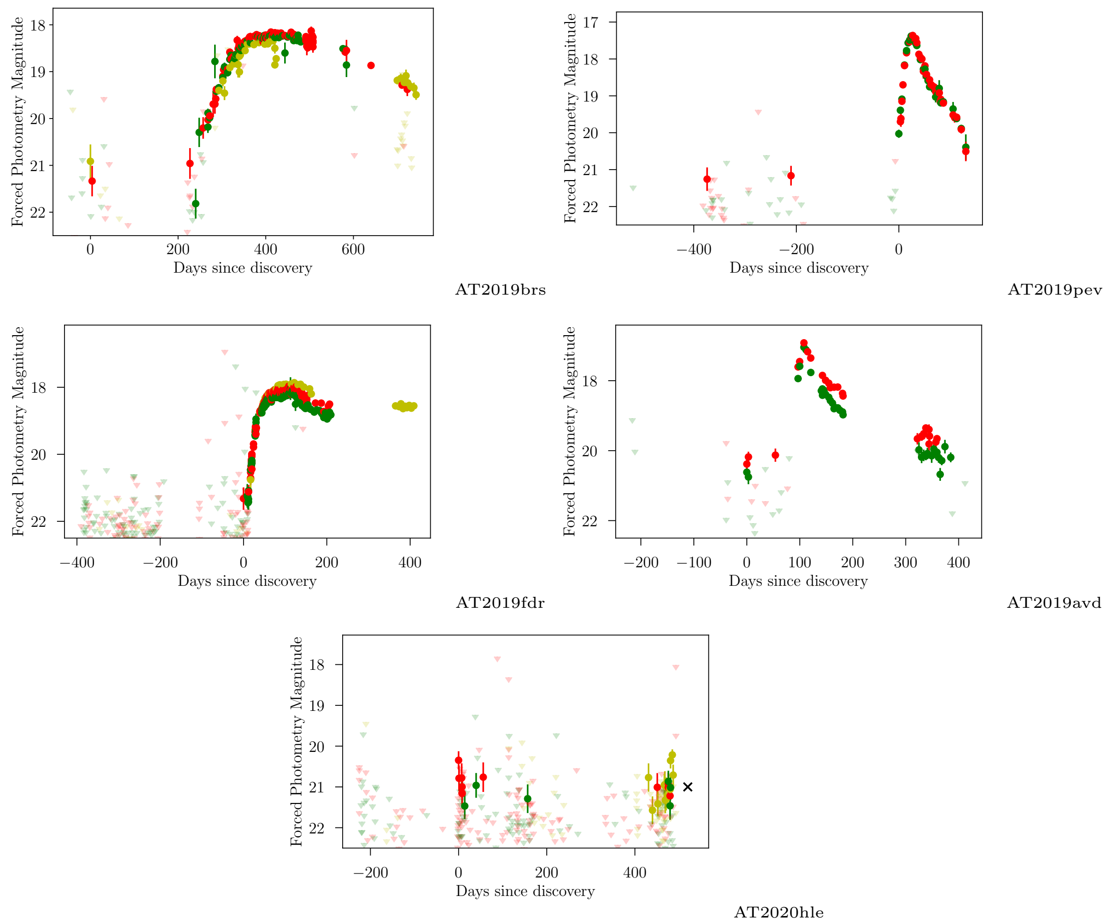

Figure 3.10: Forced photometry of the sample from ZTF Data Release 3. Colors correspond to r-, g-, and i-band 3-σ detections, and triangles correspond to 5-σ upper limits. An 'X' marks the rise to peak in the difference imaging light curve of AT2020hle, which was discovered in data too recent to be included in the ZTF DR3, and therefore only shows the flux level of the host galaxy. The data points in the light curves beyond 2020 will be released in the final ZTF photometry data release.

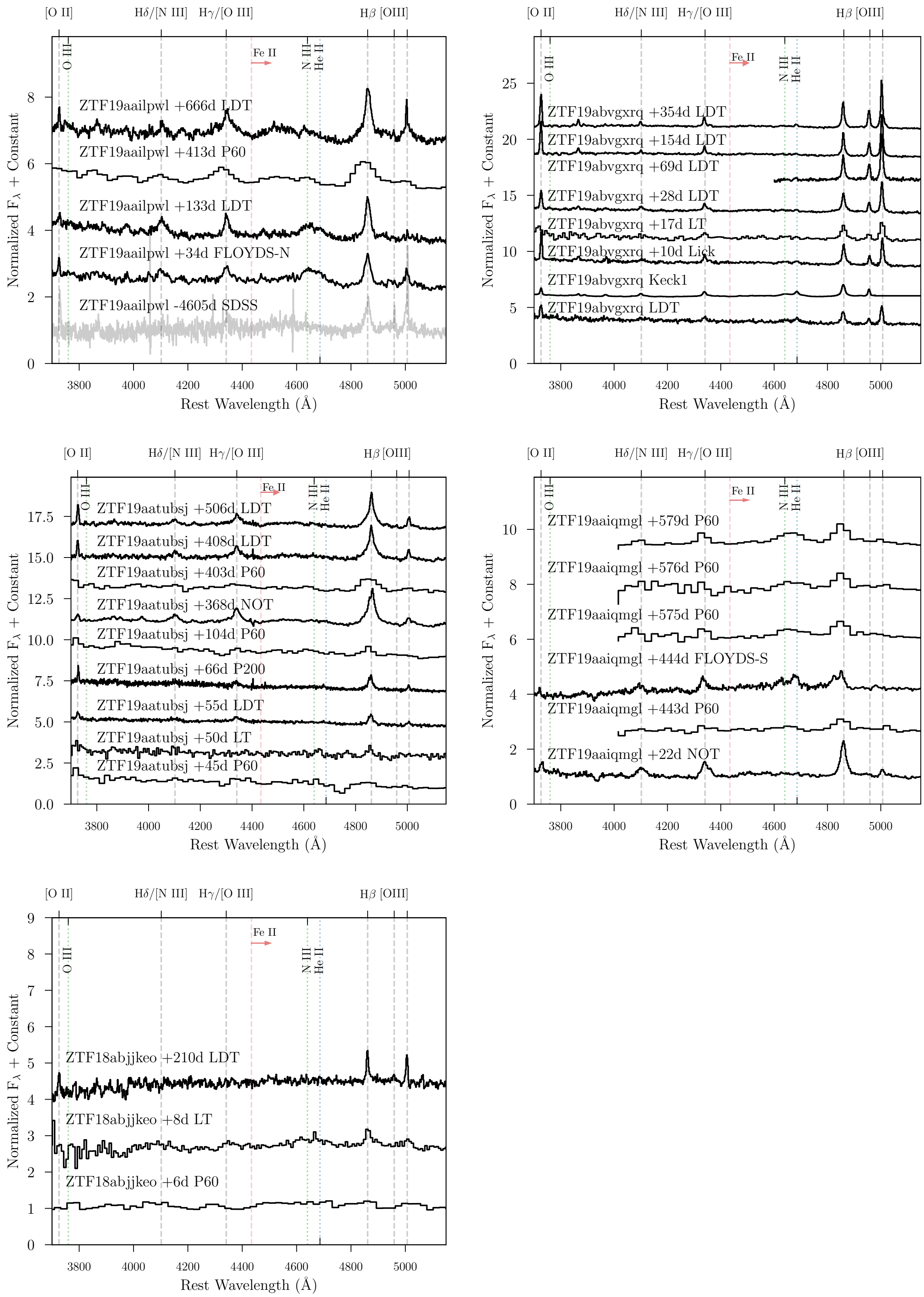

Figure 3.11: Spectroscopic follow-up of the sample summarized in Table 3.1, showing the evolution of the He II, Hβ, and Fe II line complexes.

Chapter 4: The X-ray View of a New Class of Changing-look LINERs

ZTF has enabled the discovery of a new class of LINERs "turning on" into AGN with dramatic optical spectroscopic transformations. For the most rapid transition into a narrow-line Seyfert 1, real-time monitoring revealed the presence of a prominent soft excess and a luminous X-ray flare delayed with respect to the optical rise by 2 months. We present new Swift, XMM-Newton, and NuSTAR follow-up observations of this sample, as well as optical spectroscopic follow-up data, and introduce additional sources discovered in the second half of the 3-year ZTF Phase I survey. We also view for the first time this new class of changing-look LINERs in the hard X-rays, and contrast their optical, UV, and X-ray properties with that of broad-line and changing-look Seyferts. We observe a change in Hα and [O III] line ratios over several years of follow-up observations of the sample, and observe the sample in various stages of X-ray hardening with $1.0 < \alpha_{\rm OX} < 1.6$. The X-ray data in particular point to an intriguing connection between the accretion modes of this observational class of changing-look AGN and the strength of the observed X-ray spectral components, specifically a hardening over time.

4.1 Introduction

"Changing-look" active galactic nuclei (CLAGN, also referred to as "changing-state" AGN)[1] are a growing class of objects that are a challenge to the simple AGN unification picture. They demonstrate the appearance (or disappearance) of broad emission lines and a non-stellar continuum, changing their classification between narrow-line and broad-line AGN on a timescale of months to years. Systematic studies at various wavelengths show that the nature of these spectral transformations is predominantly driven by changes in accretion rate, but the mechanism or mechanisms driving these sudden changes is still not well understood (LaMassa et al., 2015; MacLeod et al., 2016, 2019; Ruan et al., 2016; Runnoe et al., 2016). Evidence in recent years points to changing-state AGN including heterogenous observational sub-classes of objects (e.g. Mg II CLQs; Guo et al. 2019), with some occupying a higher echelon of the continuous distribution of stochastic AGN variability, and others representing more extreme and exotic accretion events than previously observed (e.g. Frederick et al. 2019).

During the first year of the Zwicky Transient Facility Survey, a new class of dramatic changing look AGN (CLAGN) was uncovered to occur in LINER galaxies (Frederick et al., 2019). One of these (ZTF18aajupnt/AT2018dyk) showed soft X-ray flaring delayed by 2 months with respect to the optical rise. As this was the only object in the sample to be promptly followed up with multiwavelength resources, it is therefore largely unknown what their X-ray properties are as a class.

Parker et al. (2016) show that X-ray observations of CLQs can be a powerful tool in understanding the physical mechanisms of an optical changing look (distinct from X-ray changing-look AGN, which show variability in hydrogen column densities) by measuring the response of the reprocessed hard X-ray continuum. Coupled

[1] Optical CLAGN are distinct from X-ray AGN "changing-look" between Compton-thick/-thin class.

with mapping out the structure of the accretion flow state change in optical spectra, a more complete story can be told about what is occurring in each region of an AGN during its state transition. Ruan et al. (2019a) showed a direct analogy of samples of changing-look quasars with the well-studied state transitions X-ray binaries (XRBs). In XRBs, the ratio of the X-ray and UV flux densities probe the disk-corona relationship as the system passes through cyclical states characterized by accretion rate. In the low/hard state, the coronal emission dominates over the dimmer UV emission from a truncated disk caused by a jet or advection dominated accretion flow (ADAF), and in the high/soft state, the UV emission from the disk dominates the spectrum. Ruan et al. (2019a) scaled state changes of X-ray binaries to changing-look AGN in various stages of accretion and showed similar state changes in both according to predicted $\alpha_{\rm OX}$ and Eddington ratios. Ruan et al. (2019b) showed the evolution of the state change in individual CLAGN (including AT2018dyk) followed a well-studied XRB along this parameter space. They measure softening below a critical Eddington ratio threshold of $\sim 1\%$ explained as disk reprocessing of Comptonized X-rays from the corona. Jin et al. (2021) found further agreement with this work by comparing Eddington ratios and flux densities from multi-epoch X-ray and UV/optical snapshots for a sample of 10 known CLQs in various stages of evolution to simulated XRB data. They also uncovered a link between dramatic changes in the strength of optical emission lines and the evolution of objects across this inversion point.

To better understand the evolution of both the optical and X-ray properties of the sample of CL-LINERs, we undertook a 3-year follow-up campaign consisting of optical and X-ray spectroscopic observations with XMM-Newton, NuSTAR, Swift, and various ground based facilities. We sought to detect any evolution of both the broad and narrow lines in the optical spectra as well as the continuum, and the presence of components signaling reflection in the X-ray spectra. Coronal

X-rays irradiating the accretion disk induce fluorescence, the most prominent emission being from Fe (George & Fabian, 1991). A number of features arise from the resulting reflection spectrum, due to reflection at all distances along the accretion disk, and elucidate the interplay between absorption, line emission, and scattering at these high energies (Fabian & Ross, 2010). One of these features, the "Compton hump", is evident in X-ray spectra above 10 keV and interpreted as reflection of > 80 keV continuum photons by the accretion disk or as far out as the molecular torus via Compton down-scattering. Another prominent feature is the iron line, and when relativistically broadened it can be a robust measurement of how emission is reprocessed in the strong gravity region near the central black hole. The presence or absence of these X-ray spectral features following a changing-look transition provides an alternate method for mapping the environment of the accretion flow in these sources, contributing to an understanding of the nature of the related physical processes, and exhibiting how they compare to normal AGN.

We present these X-ray and optical follow-up observations of this new class of CL-LINERs, and introduce additional sources discovered in the second half of the 3-year ZTF Phase I survey.

We assume the following cosmology for calculations relying on distance measurements: $H_0 = 70$ km s^{-1} Mpc^{-1}, $\Omega_\Lambda = 0.73$ and $\Omega_M = 0.27$. RA and Dec are reported at J2000.0.

4.2 Observations

All follow-up observations for this sample are summarized in Table 4.7 of the Appendix.

4.2.1 Target Selection

For this study we largely follow the sample selection criteria and multiwavelength data reduction procedures outlined in Frederick et al. (2019). CL-LINER candidates were triggered for follow-up on the basis of their variable ZTF photometry and cross-matching with galaxies classified as LINERs and displaying Balmer emission in the Portsmouth Sloan Digital Sky Survey (SDSS) DR12 catalog (Thomas et al., 2013). The CL LINERs were selected for follow-up on the basis of having consecutive detections in ZTF difference imaging, with variability above the threshold of photometric error ($\gtrsim$0.1 mag).

4.2.2 Archival Data

The host galaxies of this sample all had Balmer and low ionization forbidden line ratios consistent with that of LINER galaxies, as published in the Portsmouth catalog. The "off" state of ZTF19aambzmf was additionally classified as a Sy1.9 type galaxy in the Véron-Cetty et al. (2001) catalog, due to having a broad base in the profile of the Hα emission line in the 2007 SDSS spectrum. The optical archival observations of the sample were presented in Frederick et al. (2019).

To compare with the new X-ray follow-up data, we summarize the available X-ray archival observations of the sources presented in this work, from NASA High Energy Astrophysics Science Archive Research Center (HEASARC), the XMM-Newton science archive, and the UK Swift Science Data Centre. The detections as well as most recent 3-σ X-ray upper limits[2] of the sample are provided in Table 4.1. For these upper limit calculations, Galactic column densities were estimated as $N_H = 1 \times 10^{20}$ cm^{-2} for all sources except for ZTF18aaabltn, which is approximated as $N_H = 3 \times 10^{20}$ cm^{-2}, following the HI4PI Collaboration et al. (2016)

[2] `http://xmmuls.esac.esa.int/upperlimitserver/`

Table 4.1: Archival ROSAT, *Swift* XRT, and XMM-Newton Slew Survey 3-σ Detections and Upper Limits of CL LINER candidates

Source Name	z	Instrument Name	Observation Date (UTC)	Exposure Time (s)	Energy Range (keV)	Count Rate (counts s^{-1})	F_X (10^{-12})	L_X (10^{43})
ZTF18aajupnt	0.0367	ROSAT	1990 Jul 30	742.9	0.2−2	< 0.0347	< 0.2452	< 0.1
		XMM-Newton	2014 Aug 17	4.0	0.2−12	< 2.2	< 4.6	< 1.5
ZTF18aahiqfi	0.067	ROSAT	1990 Nov 19	470.4	0.2−2	< 0.03	< 0.2	< 0.3
		XMM-Newton	2003 Dec 26	8.7	0.2−12	< 1.2	< 2.5	< 2.8
ZTF18aaidlyq	0.1	ROSAT	1990 Oct 10	398.5	0.2−2	< 0.05	< 0.4	< 1.0
		XMM-Newton slew	2011 May 05	6.6	0.2−12	< 1.2	< 2.5	< 6.4
ZTF18aasszwr	0.168	ROSAT	1990 Nov 21	399.9	0.2−2	0.03 ± 0.01	0.19 ± 0.07	1.5 ± 0.6
		XMM-Newton	2014 May 15	4.5	0.2−12	1.7915 ± 0.7375	3.6941 ± 1.5209	30 ± 10
ZTF18aaabltn	0.045841	ROSAT	1990 Oct 13	327.3	0.2−2	< 0.07	< 0.7	< 0.3
		XMM-Newton	2015 Apr 08	9.3	0.2−12	0.8 ± 0.3	1.7 ± 0.8	0.9 ± 0.4
ZTF18aahmkac	0.0699	ROSAT	1990 Nov 30	436.8	0.2−2	< 0.05	< 0.3	< 0.4
		Swift-XRT	2012 Apr 07	942.7	0.2−12	0.0044 ± 0.0037	0.17 ± 0.14	0.21 ± 0.17
ZTF18aaavffc	0.0654	ROSAT	1990 Dec 05	504.8	0.2−2	0.14 ± 0.02	1.0 ± 0.1	1.0 ± 0.1
		XMM-Newton	2018 Dec 30	6.9	0.2−2	< 2.0	< 2.5	< 2.7
ZTF19aambzmf	0.122	ROSAT	1991 Jan 03	387.0	0.2−2	< 0.06	< 0.4	< 1.7

measurements presented in Section 4.4.1. The count rate to flux conversion calculation was performed assuming an X-ray power law spectral index of Γ=2.

Similar to the photometric analysis of the sample presented in Frederick et al. (2019), we investigate the archival Catalina Real-time Transient Survey (CRTS) V-band light curves and All-Sky Automated Survey for Supernovae (ASASSN[3]; Jayasinghe et al. 2019; Kochanek et al. 2017; Shappee et al. 2014) aperture photometry of the newest objects in this CL-LINER sample in order to constrain the transition timescales prior to their discovery in ZTF difference imaging. This δt listed in Table 4.2 is defined from the gradual increase in the optical variability to the confirmation of the classification change in spectroscopic follow-up data.

ZTF18aaavffc — The CRTS data of this source has an upward trend but shows no variability from a baseline of $V = 15.7$ mag above the 0.2 mag level prior to 2013, 6 years before its discovery in ZTF. It was detected in ASASSN starting in Feb 2012, and showed a slow gradual rise from 16.0 to 15.5 mag in g-band difference imaging photometry starting around 2017.

ZTF19aambzmf — This source was detected steadily at $V = 17.1 \pm 0.2$ mag

[3] `https://asas-sn.osu.edu/`

in CRTS between 2005 and 2013, 6 years before its discovery in ZTF. This source was also detected in ASASSN difference imaging at a similar level starting in 2012.

ZTF18aahmkac — The sparse CRTS data of this source shows no variability from $V = 16.35$ mag above the 0.1 mag level prior to 2012, 6 years before its discovery in ZTF.

4.3 Optical

The majority (5 out of 9) this sample were discovered in ZTF difference imaging for the first time in April and May of 2018, soon after ZTF Phase I Science Commissioning commenced. This indicates these sources were likely variable prior to their detections in ZTF, and is therefore not a representative sample selection. This was confirmed for the subset of this sample discovered in year 1 of ZTF Phase I presented in Frederick et al. (2019), which showed the slow onset of the optical variability in forced and PSF photometry from ZTF and other transient surveys, which define the optical transition timescales presented in that study as being earlier, sometimes by several years, than the discovery in ZTF difference imaging. These transition timescales, as well as other properties of the host galaxies and changing-look states, are listed in Table 4.2 for the sources in the original sample as well as 3 additional sources discovered in the final half of ZTF Phase I (from mid 2019 through Oct 2020). iPTF 16bco (Gezari et al., 2017), which is included in this sample as the first CL-LINER, was observed with ZTF in 2018 (2 years after its discovery in iPTF and ~1 year after detection by the XMM Slew Survey), and is also known by its ZTF name as ZTF18aajarpg.

Table 4.2: Summary of the optical properties of the changing-look LINER sample from the Zwicky Transient Facility (ZTF) Survey Phase I, adapted and extended from Frederick et al. (2019), with sources new to this sample listed in the top panel. We list redshifts from the Portsmouth SDSS DR12 catalog (Thomas et al., 2013). Transition timescales δt are roughly constrained based on the time delay between the onset of variability detected in the host in the archival light curves, and the time of the first spectrum taken in the type 1 AGN state. Estimates of star formation rate by Chang et al. (2015) are from SDSS+WISE SED model fitting. Δm is the variability magnitude change with respect to the host galaxy magnitude defined in Eq. 3 of Hung et al. (2018).

Name	RA (hh:mm:ss.ss)	Dec (dd:mm:ss.ss)	z	$D_{\rm Lum}$ (Mpc)	Discovery Date	$M_{\rm Discovery}$ (mag)	δt (yr)	Host Type[4]	log SFR [$M_\odot$ yr^{-1}]	$\Delta m_{\rm var}$ (mag)	High State
ZTF18aahmkac	11:58:18.02	+10:03:22.6	0.0699	310	2018 Apr 8	−17.82	<0.4	Spiral	0.162	−0.06	quasar
ZTF18aaavffc	12:31:55.15	+32:32:40.3	0.0654	290	2019 Oct 23	−18.37	<0.5	Elliptical	0.907	−0.27	quasar
ZTF19aambzmf	14:40:21.48	+14:11:25.9	0.122	570	2019 Mar 1	−18.53	<1.0	Elliptical	0.232	−0.10	NLSy1
ZTF18aajupnt	15:33:08.01	+44:32:08.2	0.0367	158	2018 May 31	−16.59	<0.3	Spiral	0.177	−0.18	NLSy1
ZTF18aasuray	11:33:55.83	+67:01:08.0	0.0397	171	2018 May 10	−17.80	<6.8	Spiral	0.147	−0.06	Seyfert 1
ZTF18aahiqfi	12:54:03.80	+49:14:52.9	0.0670	296	2018 April 8	−18.25	<0.6	Elliptical	−0.058	−0.12	quasar
ZTF18aaidlyq	09:15:31.06	+48:14:08.0	0.1005	457	2018 April 11	−19.09	<0.7	Spiral	0.092	−0.29	quasar
ZTF18aaabltn	08:17:26.42	+10:12:10.1	0.0458	199	2018 Sept 15	−17.62	<2.6	Elliptical	0.227	−0.81	quasar
ZTF18aasszwr	12:25:50.31	+51:08:46.5	0.1680	813	2018 Nov 1	−20.40	<5.3	Elliptical	1.267	−0.72	quasar
iPTF16bco[5]	15:54:40.26	+36:29:52.4	0.2368	1197	2016 June 1	−20.76	<1.1	Elliptical	1.007	−0.69	quasar

4.3.1 ZTF Photometry

We show the heterogeneous set of ZTF g and r band photometry for this sample in Figure 4.1, beginning with their discovery which requires a 5-σ significance detection above the reference image of the LINER host galaxy. The absolute magnitudes at the time of discovery are given in Table 4.2. The objects display a large range in absolute magnitudes, with minimum and maximum values of M between -16 and -21. Some, like ZTF18aahiqfi, ZTF18aaabltn, and ZTF19aambzmf show stochastic variability in the ZTF difference imaging photometry, while ZTF18aasszwr, AT2018dyk, ZTF18aasuray, and ZTF18aaavffc show in addition to this some smoother, larger amplitude flare features.

In Figure 4.2 we also show the ZTF forced photometry provided by the NASA/IPAC Infrared Science Archive[6] for the latest discovered sources ZTF18aahmkac, ZTF19aambzmf, and ZTF18aaavffc. These light curves show the timing of the rise to peak not seen in difference imaging, which requires a 5-σ detection above the level of the reference

[6] https://irsa.ipac.caltech.edu/Missions/ztf.html

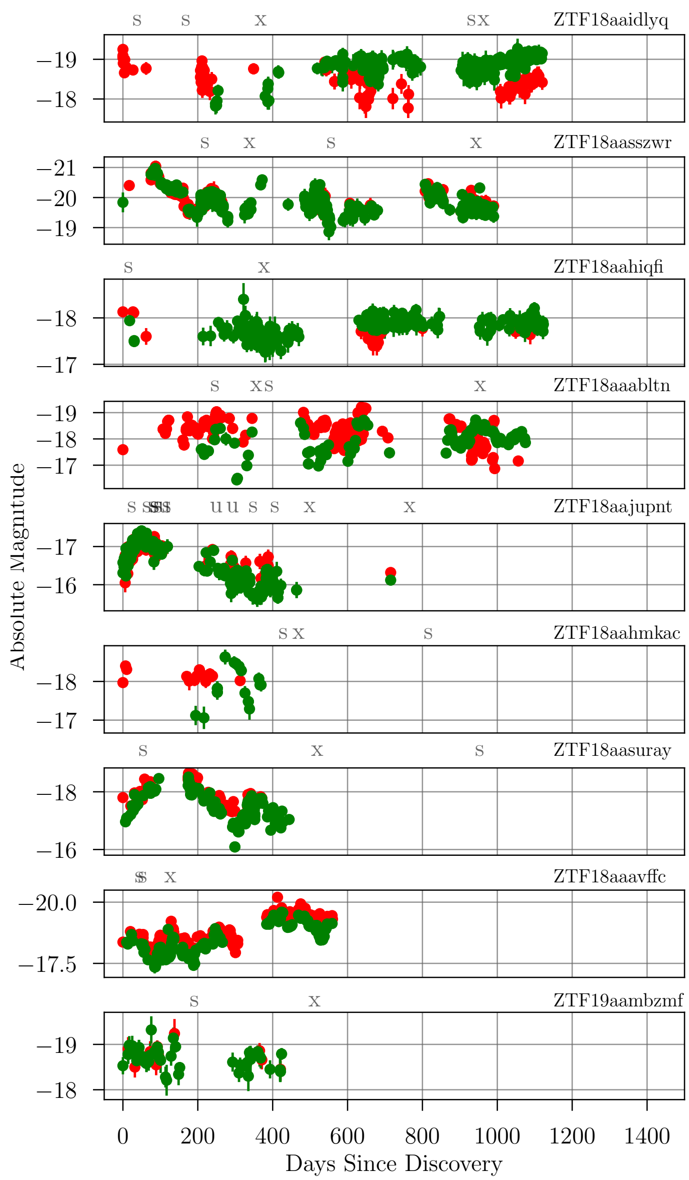

Figure 4.1: Comparison of the ZTF *g*- and *r*-band difference imaging light curve shapes of the sample. The timing of the optical spectroscopic follow-up epochs with respect to the ZTF photometry in absolute magnitude are indicated alongside each light curve with an 's', X-ray follow-up with an 'x' and *Swift* UVOT follow-up with a 'u'. All follow-up data are summarized in detail in Table 4.7 of the Appendix.

image and therefore does not capture the entirety of the optical transition to a larger amplitude variability state. See Figure 2 of Frederick et al. (2019) for the remainder of the sample.

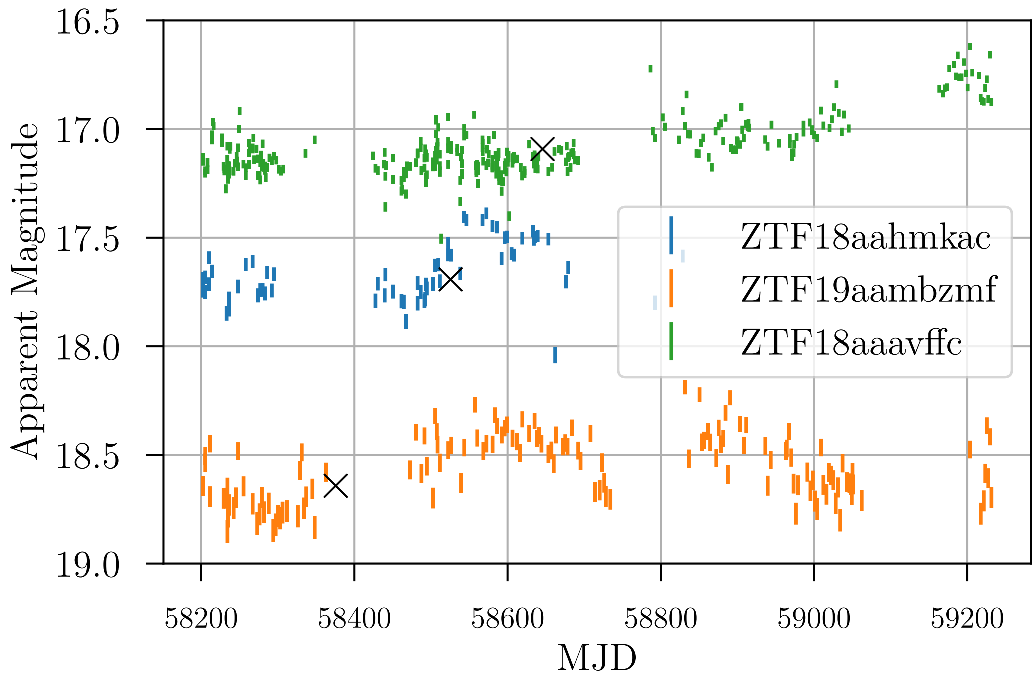

Figure 4.2: The ZTF g-band forced photometry for the three new objects in this sample introduced in this work. The rise time for each source corresponding to the changing-look transition timescale δt measured in Table 4.2 is marked with "$\times$".

4.3.1.1 Optical Monitor

We use the SAS command `omichain` to reduce the UVW1 (effective wavelength 2910 Å) XMM Optical Monitor data. The Vega magnitudes for the sample ranged widely from 12 to 20 mag. See Section 4.3.3.2 for more details about the XMM observations.

4.3.2 Spectroscopy

The data from the follow-up campaign for this sample are shown in Figures 4.11 and 4.3, and summarized in the Appendix in Table 4.7. This set of follow-up data included spectroscopy taken by the robotic SED Machine mounted on the Palomar 60-inch Observatory (SEDM/P60; Program PIs: Gezari, Sollerman, Kulkarni), the Hale Telescope at the Palomar 200-inch Observatory (PI: Yan), the Deveny Spectrograph at the Lowell Discovery Telescope (PI: Gezari), and GMOS-North at Gemini Observatory (PIs: Hung, Frederick). We reduced P60 spectra with `pysedm` (Rigault et al., 2019), and all other spectra with `pyraf` using standard procedures.

Compared to these archival spectra, all sources in the sample showed dramatic changes in their broad emission line profiles, often with bright blue continua. These spectral transformations for the three latest CL-LINERs added to the sample (ZTF18aahmkac, ZTF18aaavffc, ZTF19aambzmf) are shown in Figure 4.3. ZTF18aahmkac shows broad double peaked emission in Hα and Hβ in addition to a strong blue continuum emergent from a LINER spectrum 15 years prior. ZTF18aaavffc shows a broad component in Hα only in the archival spectrum and the Balmer emission lines appear broader in both follow up spectra. ZTF19aambzmf shows broader Balmer emission compared to the archival spectrum from 12 years prior, but relatively less change in the continuum compared to the other CL-LINERs in the sample. Follow up spectral epochs for the rest of the sample are described in detail in Section 4.4.2.

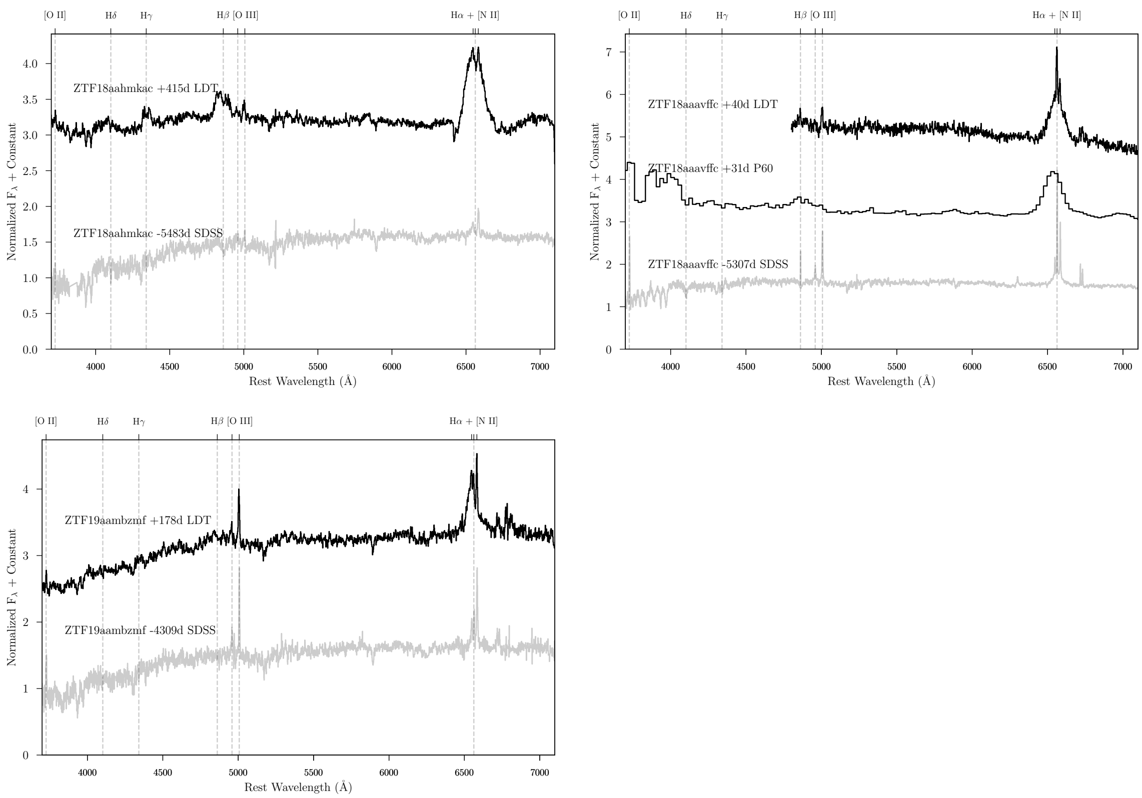

Figure 4.3: Archival SDSS and follow-up spectroscopy from the subset of the sample of CL-LINERs new to this work, showing their dramatic changes from LINER galaxies to AGN.

4.3.3 X-rays

4.3.3.1 Swift

All sources in this sample were observed with the Neil Gehrels *Swift* Observatory's (Gehrels et al., 2004) X-ray Telescope (XRT). The XRT data were processed[7] (Evans et al., 2009) using HEASOFT v6.22[8]. A subset of the Swift Target of Opportunity (ToO) observations for AT2018dyk are described in Frederick et al. (2019). Measured X-ray properties of this sample from multiple epochs taken with XRT on cadences from months to years are given in Table 4.4.

[7] `http://www.swift.ac.uk/user_objects/`

[8] `https://heasarc.gsfc.nasa.gov/docs/software/heasoft/`

4.3.3.2 XMM

We observed a subset of 6 of the sources in this sample with the *XMM* EPIC pn camera (Strüder et al., 2001) during guest observing cycle AO 19 from June to November in 2020 (program 086505; P.I. Frederick). The XMM-Newton EPIC-pn observations were taken in Full Frame Window Mode (except for ZTF18aaabltn due to nearby stellar sources within 20″) and using the Medium Filter for ZTF18aaidlyqand the Thin Filter for all other sources. The data were reduced using standard techniques with the XMM-Newton Science Analysis System v16.0 (SAS; Gabriel et al. 2004), and EPIC-pn calibration database files updated as of April 2021. We used a 35″ source extraction region and a 108″ circular source-free background region, except for ZTF18aaabltn for which we used a 72″ background region, shown in Figure 4.4. We also adopted CCD event patterns 0 to 4, corresponding to single- and double-pixel events. The broadband (0.3−10 keV) XMM-Newton light curves of the six CL-LINERs in this sample are shown in Figure 4.16 the Appendix.

For non-detected sources, we computed upper limits from the XMM EPIC-pn data at the 3-σ level using the XMM SAS/HEASARC command `eregionanalyse`, and converted to 0.3-10 keV fluxes with the PIMMS count rate calculator[9] assuming a power law with Γ=2, a typical value for AGN. We assessed best-fit models utilizing χ^2 statistics and XSPEC version 12.9.1a (Arnaud, 1996). Uncertainties are quoted at 90% confidence intervals. Model fits and upper limits are given in Table 4.5 in Section 4.4.1.

Archival XMM-Newton Slew Survey observations of iPTF 16bco indicate the onset of the X-ray source detected by Swift in its broad-line state to < 1.1 years before the optical transition observed in (Gezari et al., 2017). ZTF18aasszwr was previously detected in the *XMM Newton* Slew Survey with $F_{0.2-12\mathrm{keV}} = 4.76 \times 10^{-12}$ erg cm^{-2} s^{-1} (XMM-SSC, 2018). As the only CL-LINER observed in real time

[9] `https://heasarc.gsfc.nasa.gov/cgi-bin/Tools/w3pimms/w3pimms.pl`

during the ZTF Phase I Survey, AT2018dyk is the only source in the sample in this follow-up campaign with an archival X-ray spectral observation taken with XMM-Newton concurrent with its changing-look transition in 2018, 20 days after the optical peak (PI: Gezari, Program 082204). AT2018dyk was once again faintly detected by XMM-Newton on 2020 Jun 19, after it had faded in the optical. It is also the only source in this sample to show significant X-ray variability in the XMM exposure, exhibiting flaring at the 0.2 cps level during the first 6 ks of the observation.

4.3.3.3 NuSTAR

NuSTAR observed 4 of the CL-LINERs as part of a joint observing program with XMM-Newton (program 086505), summarized in Table 4.3. NuSTAR data were processed (dead-time corrected) with NuSTARDAS version v1.9.2 and with CALDB updated as of April 2020. We used 50-arcsecond regions to extract the source events from the NuSTAR images, shown overlaid in Figure 4.5. Images of the NuSTAR 3−79 keV events in Figure 4.5 show clear high-energy X-ray detections for 2 of the 4 objects, ZTF18aasszwr and ZTF18aahmkac. Light curves of the observations are shown in Figure 4.17 of the Appendix. Single focal plane module (FPM) NuSTAR spectra are shown in Figure 4.7.

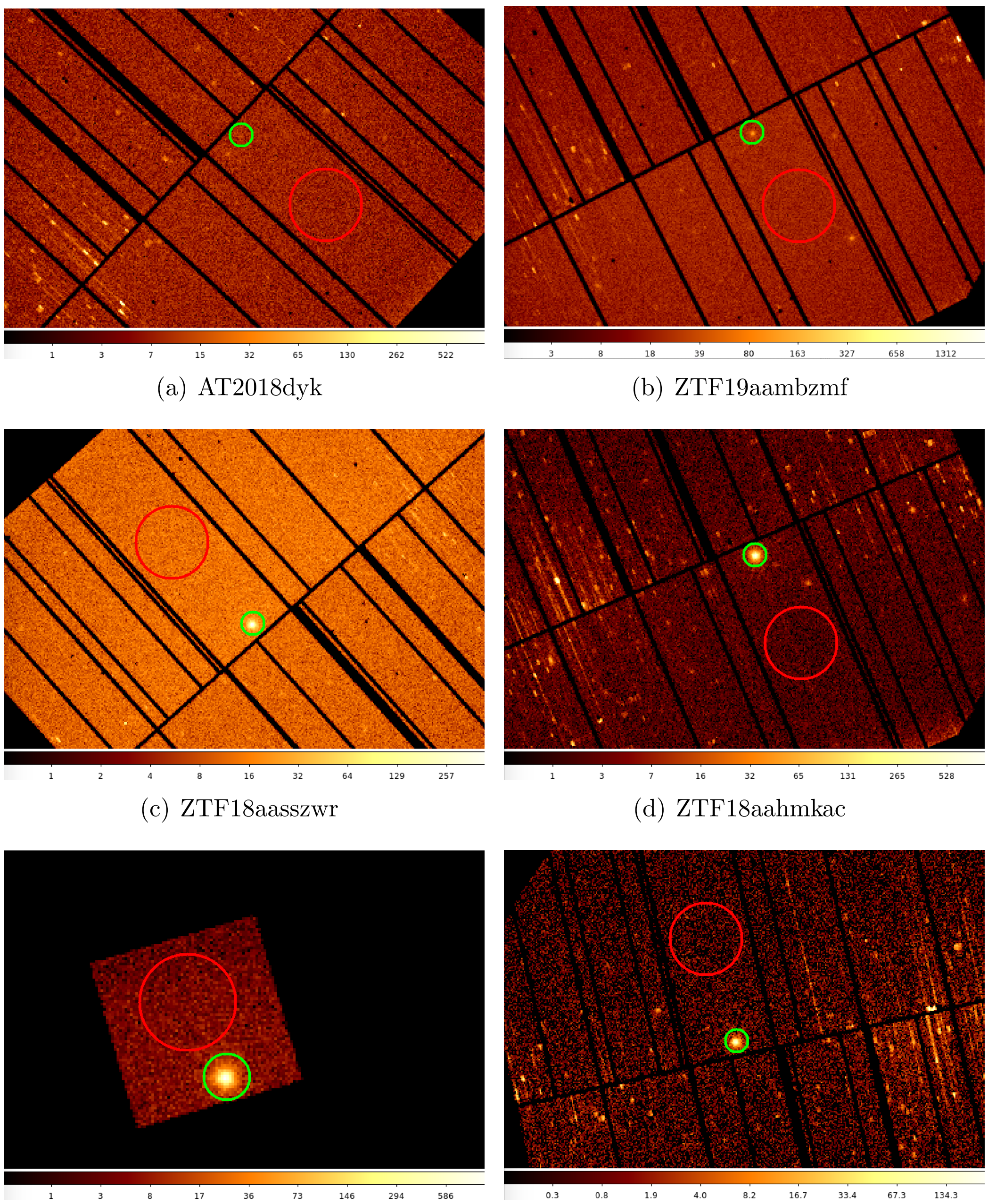

(a) AT2018dyk
(b) ZTF19aambzmf
(c) ZTF18aasszwr
(d) ZTF18aahmkac
(e) ZTF18aaabltn
(f) ZTF18aaidlyq

Figure 4.4: Source and background extractions regions overlaid on *XMM-Newton* images.

Table 4.3: NuSTAR Observations of CL LINER candidates

Source Name	z	Observation ID	Observation Date (UTC)	Exposure Time (s)	Count Rate (counts s^{-1})
ZTF18aajupnt	0.0367	60660001002	2020 Jun 19	21891	<0.03
ZTF19aambzmf	0.122	60660002002	2020 Jul 11	19325	<0.03
ZTF18aasszwr	0.168	60660003002	2020 Dec 01	19762	0.08±0.04
ZTF18aahmkac	0.0699	60660004002	2020 Jun 20	20580	0.09±0.05

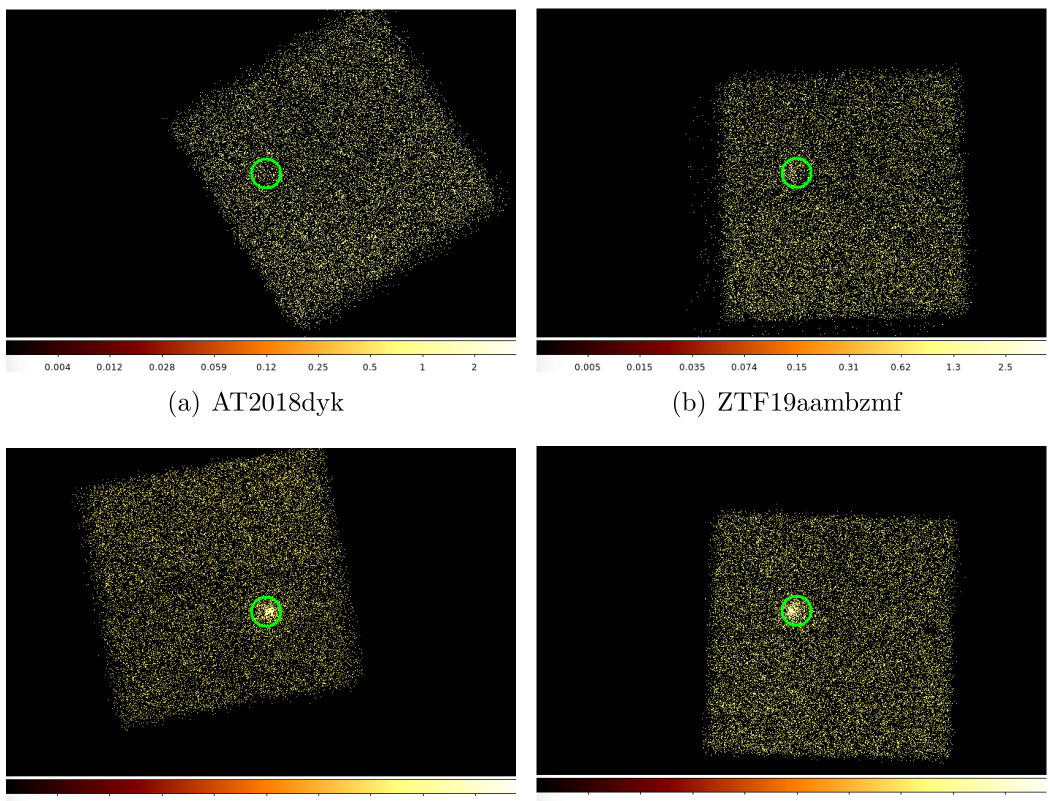

(a) AT2018dyk (b) ZTF19aambzmf

(c) ZTF18aasszwr (d) ZTF18aahmkac

Figure 4.5: 50-arcsec source regions overlaid on NuSTAR event file images taken concurrently with XMM exposures for four sources in the CL-LINER sample. Only two of the four (ZTF18aasszwr and ZTF18aahmkac) were clearly detected, the other two (AT2018dyk and ZTF19aambzmf) were not.

Table 4.4: *Swift* XRT Observations of CL LINER Candidates

Source Name	z	Observation ID	Observation Date (UTC)	n_{H} (10^{20})	Γ	Count Rate (counts s^{-1})	F_X (0.3-10 keV) (10^{-14})	L_X (0.3-10 keV) (10^{42})
ZTF18aaidlyq	0.1000	00011217001	2019 Mar 28	1.72	$1.9^{0.2}_{-0.2}$	0.086 ± 0.007	1.3 ± 0.1	3.4 ± 0.3
ZTF18aasszwr	0.1680	00011216001	2019 Mar 28	1.30	$2.0^{0.7}_{-0.6}$	0.083 ± 0.011	1.2 ± 0.2	9.9 ± 1.3
ZTF18aahiqfi	0.0670	00011214001	2019 Apr 04	1.16	$1.6^{0.4}_{-0.3}$	0.019 ± 0.003	0.3 ± 0.1	0.3 ± 0.1
ZTF18aaabltn	0.0458	00011215001	2019 Mar 25	2.96	$2.0^{0.3}_{-0.2}$	0.176 ± 0.011	2.9 ± 0.2	1.5 ± 0.1
ZTF18aajupnt	0.0367	00095703001	2019 Sep 26	1.59	$2.8^{0.3}_{-0.3}$	0.004 ± 0.003	0.1 ± 0.1	0.0 ± 0.0
ZTF18aahmkac	0.0699	00011466001	2019 Jul 05	1.49	$1.8^{0.5}_{-0.3}$	0.045 ± 0.005	0.7 ± 0.1	0.8 ± 0.1
ZTF18aasuray	0.0397	00011565001	2019 Sep 25	1.11	$1.7^{0.6}_{-0.3}$	0.021 ± 0.003	0.3 ± 0.0	0.1 ± 0.0
ZTF18aaavffc	0.0654	00013203001	2020 Feb 11	1.21	$1.8^{0.3}_{-0.2}$	0.037 ± 0.004	0.6 ± 0.1	0.6 ± 0.1
ZTF19aambzmf	0.1220	00013280001	2020 Mar 05	1.43	$1.8^{0.9}_{-0.6}$	0.012 ± 0.002	0.4 ± 0.1	1.6 ± 0.3
iPTF 16bco	0.2370	00011565001	2016 Oct 21	1.55	$2.1^{0.5}_{-0.5}$	0.027 ± 0.004	0.4 ± 0.1	7.0 ± 1.1

4.4 Analysis

4.4.1 X-rays

For model fitting and calculating luminosities, we used the values for the Galactic column densities and redshifts given in Table 4.5.

Table 4.5: XMM EPIC pn Observations of CL LINER candidates

Source Name	z	Observation ID	Observation Date (UTC)	On/Exposure[a] Time (s)	n_H^b (10^{20})	Γ	Count Rate[c] (counts s^{-1})	F_X^d (0.3-10 keV) (10^{-14})	L_X^e (0.3-10 keV) (10^{42})
AT2018dyk	0.0367	0822040701	2018 Aug 11	1868/11906	1.59	3.02±0.15	0.27±0.01	40±3	1.21±0.09
AT2018dyk	0.0367	0865050101	2020 Jun 19	10492.8/12332	1.59	1.36±0.4	0.023±0.005	6±2	0.18±0.06
ZTF19aambzmf	0.122	0865050301	2020 Jul 09	19423.9/22833	1.43	1.96±0.1	0.075±0.004	15±1	11±1
ZTF18aasszwr	0.168	0865050401	2020 Nov 22	7820.9/9833	1.30	1.8±0.4	0.87±0.01	190±10	148±
ZTF18aahmkac	0.0699	0865050501	2020 Jun 20	17714.5/20668	1.49	1.66±0.02	0.624±0.006	179±3	20±3
ZTF18aaabltn	0.0458	0865050701	2020 Nov 12	7099.7/10284	1.72	1.94±0.03	1.66±0.06	436±7	21.3±0.3
ZTF18aaidlyq	0.1	0865050901	2020 Nov 12	5822.9/6833	1.72	1.87±0.07	0.350±0.008	87±2	21±1

a. Ratio of effective filtered exposure time to total observation duration.
b. Total Galactic column density N_H (in units of cm^{-2}) as a weighted average of measurements from the HI4PI Collaboration et al. 2016, Kalberla et al. 2005, and Dickey & Lockman 1990.
c. The broadband (03−10 keV) background-subtracted *XMM-Newton* count rate is given when available. We report background-subtracted statistical upper limits at the 3-σ level.
d. Fluxes (in units of ergs s^{-1} cm^{-2}) were measured from the best-fit spectral model.

As many of the XMM observations were affected by high levels of background radiation, only single epochs were taken. Only ZTF19aambzmf shows evidence of a broad Fe emission feature near 6.4 keV in the spectra shown in Figure 4.6, approximately 500 days following its discovery in ZTF, although careful modeling of this potential emission line feature is required. This feature would be expected in typical broad line AGN, however more time is needed for the narrow Fe emitting region, located far from the innermost accretion flow and the X-ray continuum emitting region, to respond to the dramatic continuum change in these sources, compared to the broad Fe line which shows variations on timescales of less than 1 day (Parker et al., 2016; Vaughan & Edelson, 2001). ZTF18aaabltn is the only source with a soft excess detected in the XMM follow-up campaign, and is well fit to a broken power law model with $\Gamma = 1.66 \pm 0.06$ above 2 keV and $\Gamma = 2.6 \pm 0.2$ below 2 keV. All other CL-LINERs were detected and modeled by a simple $\Gamma \sim 2$ power law, as expected for normal AGN (Brandt et al., 1995), with Galactic absorption described by the `phabs` model in `XSPEC` v12.9.1 (Arnaud, 1996). The majority showed no indication of a strong Fe line near 6 keV. ZTF18aasszwr is dominated by background at high energies, and data are therefore only shown below 3 keV.

As expected from the XMM data, power law continua with $\Gamma \approx 2$ are present

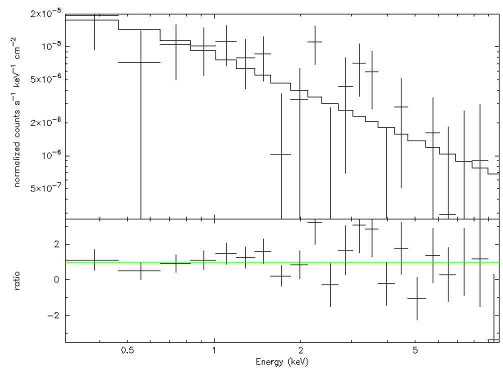

(a) AT2018dyk

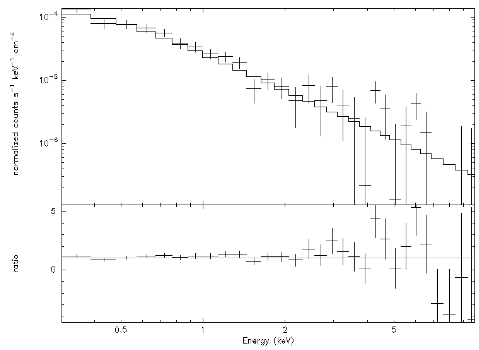

(b) ZTF19aambzmf

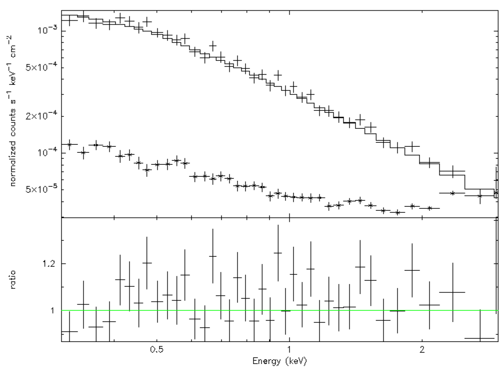

(c) ZTF18aasszwr

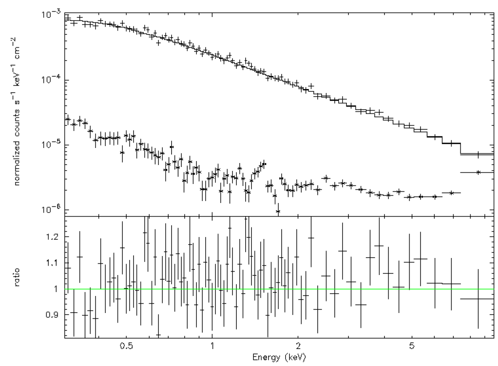

(d) ZTF18aahmkac

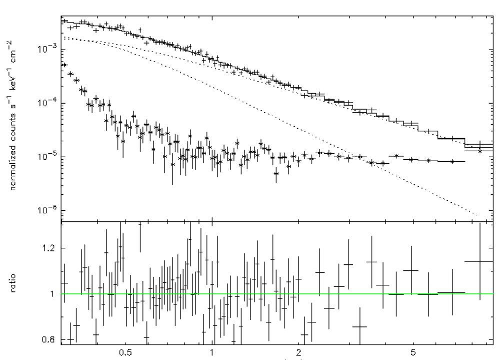

(e) ZTF18aaabltn

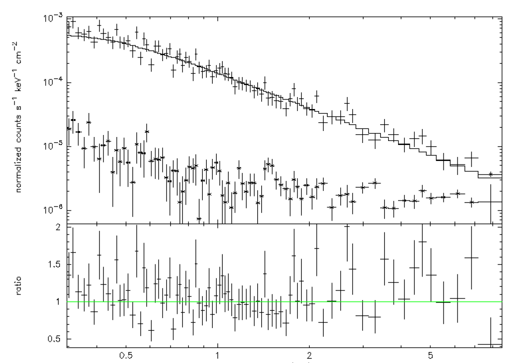

(f) ZTF18aaidlyq

Figure 4.6: X-ray spectra of the 6 sources in the sample observed with XMM-Newton (in chronological order of the exposures): AT2018dyk, ZTF19aambzmf (note the difference in energy scale), ZTF18aasszwr, ZTF18aahmkac, ZTF18aaabltn, and ZTF18aaidlyq. The model parameters for Galactic absorption and power law spectral indices are listed in Table 4.5. The top panel of each figure shows the data modeled by the simple absorbed power law (solid line), except for ZTF18aaabltn with a soft excess which is modeled by a broken power law (the 2 power law models are represented as dotted lines). The lower panel of each figure shows the residuals defined as the ratio of the data over the model, and the background level is indicated by crosses.

.

in the NuSTAR data between 3−79 keV. For the sources in the sample observed with NuSTAR, emergent features are present at high energies (near 50 keV, close in energy to where the Compton hump would be expected) at varying strengths in the X-ray spectra shown in Figure 4.7. We discuss the implications of this further in Section 4.5. A more detailed analysis of the combined concurrent NuSTAR and XMM data is forthcoming in a future study.

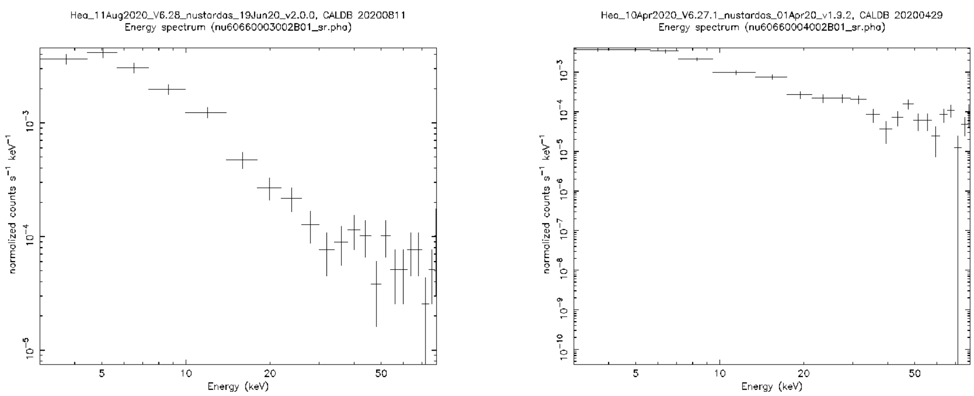

(a) ZTF18aasszwr (b) ZTF18aahmkac

Figure 4.7: X-ray spectra of the two sources in the sample observed with NuSTAR concurrently with the XMM-Newton observations, ZTF18aasszwr and ZTF18aahmkac (note the difference in energy scale). The observation details are listed in Table 4.3. AT2018dyk and ZTF19aambzmf were not detected above the background limit, and no clear Compton hump feature is observed in either ZTF18aasszwr or ZTF18aahmkac above 10 keV as seen in X-ray spectra of normal AGN.

Following the work of Jin et al. (2021); Ruan et al. (2019a), we compare the X-ray and UV flux densities of the sources in this sample with other broad line and changing-look AGN in Figure 4.8. To do so, we measure the simultaneous optical-to-X-ray flux density ratio ($\alpha_{\rm OX}$) defined as

$$\alpha_{\rm OX} = 0.3838\ \log(L_{2\ \rm keV}/L_{2500\rm A})$$

by Eq. 4 of Tananbaum et al. (1979), and Eq. 11 of Grupe et al. (2010). Most sources in this sample are probing the critical inflection point in Eddington ratio which has been shown to be an important condition for triggering the changing-look transition (see e.g. Noda & Done (2018)). We show the sensitivity of the Eddington ratio metric to the choice of black hole mass measurement, which affects this result especially for narrow-line Seyfert 1 sources such as AT2018dyk.

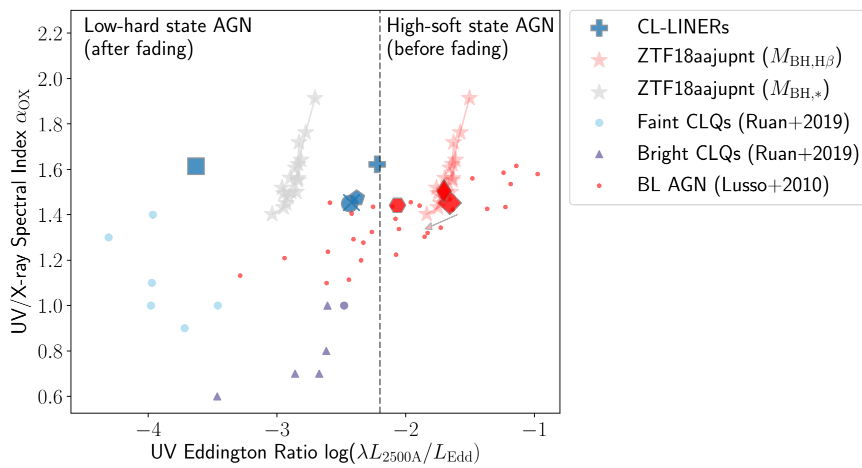

Figure 4.8: We demonstrate that recent detections are broadly in agreement with, and are currently probing the critical inversion point in $\alpha_{\rm OX}$ vs UV Eddington ratio, the trend established by Ruan et al. (2019a), who scaled state changes of X-ray binaries (XRBs) to changing-look (also called changing-state) AGN and showed similar state changes in both. However, we show this trend is sensitive to black hole mass measurements, which for narrow line sources vary in orders of magnitude between virial and other methods (see Section 4.4.3). We use this empirical cutoff to separate the sample into low-hard (blue, left) and high-soft (red, right) states, analogous to the state changes in XRBs. Shapes used to identify individual sources are the same as in Figure 4.12.

Figure 4.9 shows the evolution of AT2018dyk along X-ray spectral index and X-ray Eddington ratio (which is less sensitive to choice of bolometric correction, see discussion in Ruan et al. 2019a) as measured by all available Swift ToO epochs. We compare this source to all other CL-LINERs in this sample as well as to 2 X-ray studies of broad-line AGN, Brightman et al. (2013) and Yang et al. 2014, and find that the sample do not quite approach them in this parameter space, despite transitioning to broad line quasars in the optical (Frederick et al., 2019). We speculate on reasons for this discrepancy in Section 4.5.

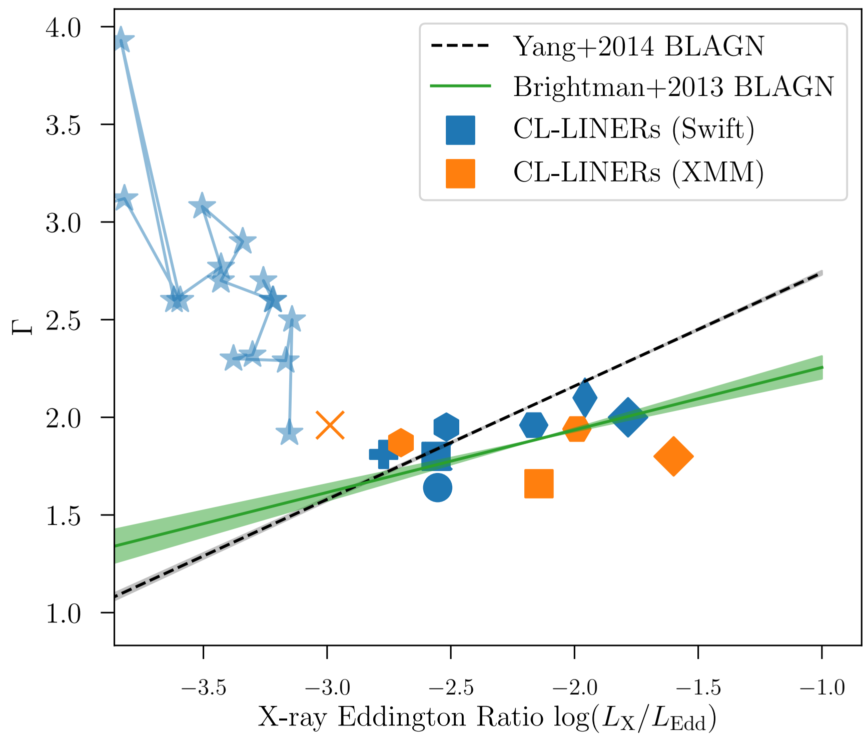

Figure 4.9: *Swift* data of AT2018dyk (the source in the sample caught in a real time transition "turning-on" and subsequently fading) shows it gradually "settling" to where the rest of the sample lies in the parameter space of Γ_x vs. $L_x/L_{\rm Edd}$. The sample in their "on" states has X-ray power law indices comparable to average broad line AGN (BLAGN; green and black lines), and undergoes changes in Eddington ratio between the Swift (2018) and XMM (2020) campaigns.

We also show the measurements and evolution of the ratio of UV (measured at 2500 Å) and X-ray (measured at 2 keV) flux densities, $\alpha_{\rm OX}$, compared to the overlapping ranges from populations of LINER galaxies (Maoz, 2007) and broad-line AGN (Steffen et al., 2006). The majority of the sample lies between the overlapping region of $\alpha_{\rm OX}$ within error, and may decrease over time as evidenced by multi-epoch measurements of AT2018dyk. Although this correlation is weak for the remaining sources in the sample, this would indicate a relative strengthening of the X-ray emission while the UV decreases along with the optical, as shown by Frederick et al. (2019). An increase in the X-ray with time in tidal disruption events is indicative of the formation of the accretion disk, and may scale with the evolutionary sequence of XRBs (Wevers et al., 2021), behavior for which there is evidence in some CLAGN as well (Ruan et al., 2019a).

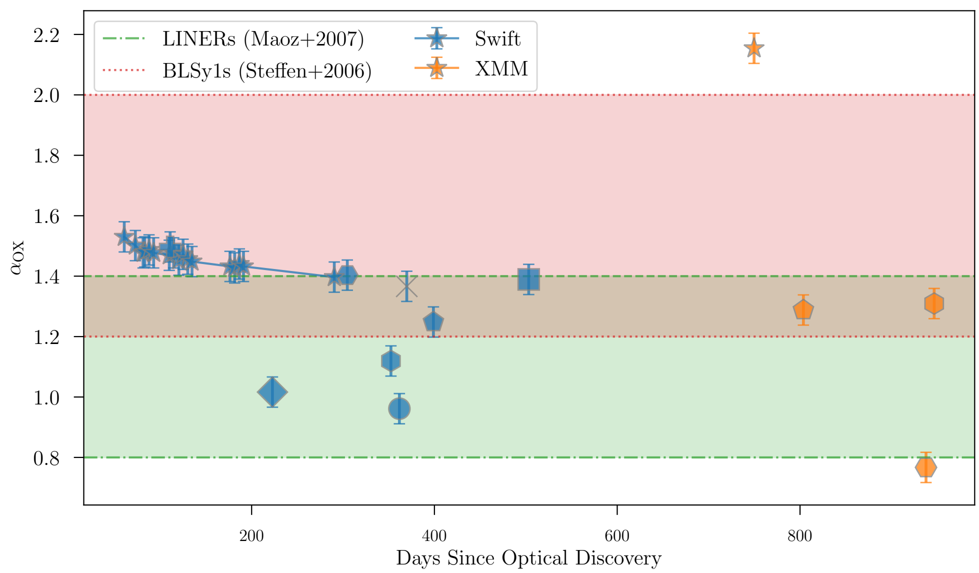

Figure 4.10: Ratio of UV to X-ray flux densities, $\alpha_{\rm OX}$, of the CL-LINER sample as measured from *Swift* UVOT and XRT observations, compared to that of samples of broad line AGN in red (Steffen et al., 2006) and LINER galaxies in orange (Maoz, 2007).

4.4.2 Optical Spectroscopy

We focus on the broad spectral changes for each source. All follow-up optical spectra for the sample are summarized in Table 4.7 of the Appendix and selected spectra are shown in Figure 4.11. Spectra for sources not presented in the Frederick et al. (2019) sample are shown in Figure 4.3.

Spectra taken with Lowell Discovery Telescope (LDT, formerly DCT) Deveny spectrograph (PI: Gezari), the Alhambra Faint Object Spectrograph and Camera (ALFOSC) on the 2.56-m Nordic Optical Telescope (NOT; PI: Sollerman), and the KAST Double Spectrograph on the Lick 3-m Shane Telescope (PI: Foley) were reduced using standard IRAF procedures. We performed wavelenth calibration using arc lamps and flux calibration using a spectrophotometric standard star. Spectra obtained with the Low-Resolution Imaging Spectrometer (LRIS) on the Keck1 10-m telescope were reduced automatically with the LRIS reduction pipeline `Lpipe` Perley (2019). Spectroscopy obtained with the Double Beam Spectrograph (DBSP) on the Palomar 200-inch Hale Telescope (P200; PI: Yan) were reduced using the `pyraf-dbsp` pipeline (Bellm & Sesar, 2016; Science Software Branch at STScI, 2012). Data taken by the robotic 2-m Liverpool Telescope (LT) SPectrograph for the Rapid Acquisition of Transients (SPRAT; PI: Perley) were reduced by the standard pipeline provided by the Observatorio del Roque de Los Muchachos. Lower resolution ($R \sim 100$) spectra taken by the Palomar 60-inch SEDM were reduced automatically with `pysedm` (Rigault et al., 2019).

ZTF18aaidlyq— Both the broad double peaked Hβ profile and the blue continuum appear to be fading in the follow-up spectrum taken 3 years post discovery compared to the spectrum taken 25 days after the discovery in difference imaging.

ZTF18aasuray — The Fe II complex and broad seemingly double peaked Balmer emission in this source has remained prominent while the blue continuum

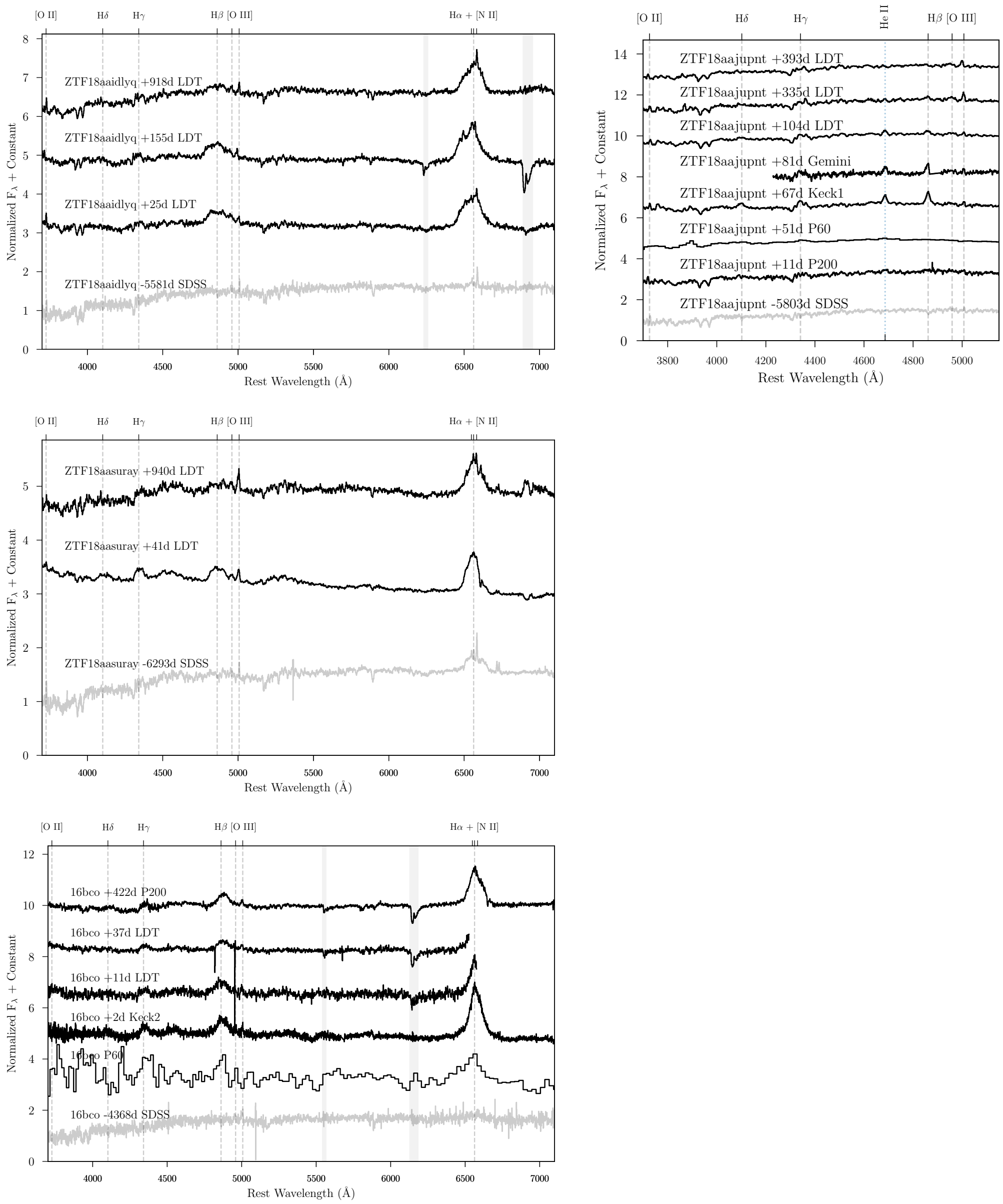

Figure 4.11: Selected multi-epoch spectroscopy from the 3-year follow-up campaign of the CL-LINER year 1 sample compared to a SDSS spectrum of the host from several years prior to the onset of the changing-look transition. Both ZTF18aaidlyq and ZTF18aasuray (upper left) show potential double peaked emission with a fading in blue continuum over 3 years, ZTF18aaidlyq shows a fading in Hβ flux over 3 years, and AT2018dyk (upper right, with a difference in scale to emphasize the spectrum in the vicinity of features of interest) shows a fading in Hβ and He IIλ4686 over 1 year. Telluric absorption features are indicated by gray shading.

has faded over 2.5 years resulting in the [O III]λ5007Ådoublet appearing to have relatively strengthened over that time.

AT2018dyk— Spectra taken over 1 year after the optical flare and subsequent plateau shows a fading in the strong profile of He IIλ4686Å, and a possible strengthening of [O III]λ5007Å.

We fit the emission lines of the follow-up spectra with Gaussian models using `lmfit`, and present the FWHM measurements in Table 4.6 and Figure 4.14 of the Appendix. Models of the forbidden lines such as the narrow [N II] emission lines included in the multi-Gaussian models of the Hα profiles are fixed to the width of the [O III] lines.

We update Figure 14 from Frederick et al. (2019) in Figure 4.12, showing measurements of the Hβ and continuum flux ratios of the CL-LINERs compared to a sample of normal CLQs from MacLeod et al. (2019), to include the latest sources in this sample as well as additional epochs of the original sample taken months to years after the initial classification spectra. ZTF18aahmkac is an outlier with respect to both flux ratios, and ZTF19aambzmf is at the high end of the Hβ flux ratios compared to the CLQ sample, although we note the low measurement of the continuum ratio is due to an issue with the flux calibration in the follow-up spectrum of ZTF19aambzmf blueward of Hβ.

We also recreate Figure 17 of Frederick et al. (2019) to include the updated follow-up data set in Figure 4.13. The emission line model fits to Hα, Hβ, and [O III] that these measurements are based on are shown in Figure 4.14 in the Appendix, as well as in the Appendix of Frederick et al. (2019).

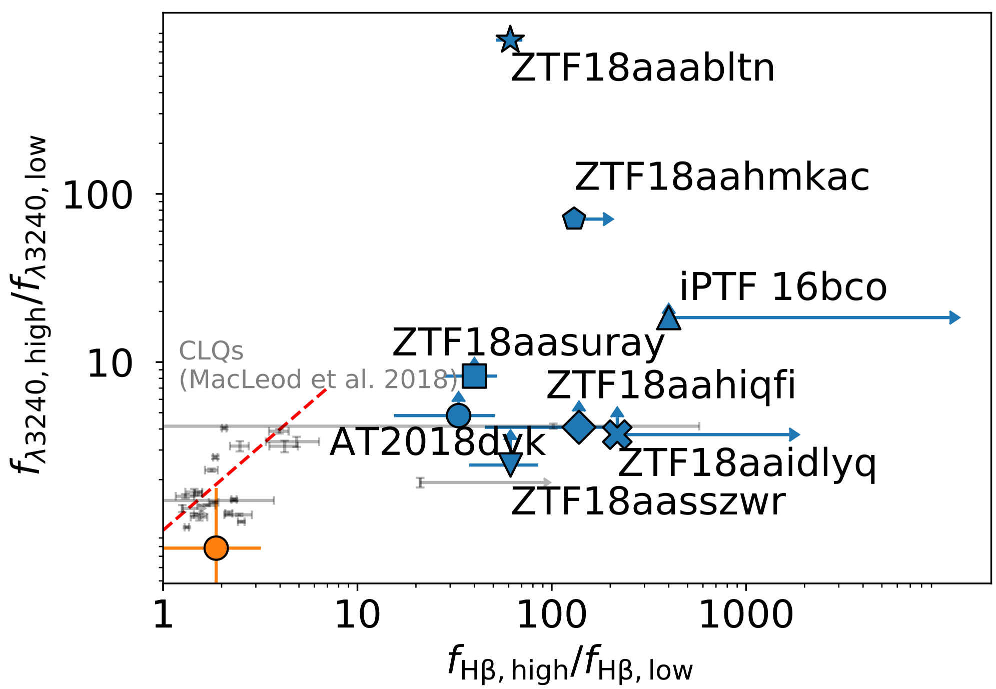

Figure 4.12: Ratio of continuum flux change as a function of broad line flux change for our changing-look LINER sample (filled shapes) in comparison to changing-look AGN (shown in gray). All have much larger (by a factor of > 10) changes in broad line flux than the changing-look quasar sample. Measurements from a follow-up epoch of AT2018dyk is shown in orange. The $f_{\lambda 3240}$ ratio measurements are represented as lower limits, as there is stellar contamination in the low (LINER) state. We note that there was an error in the flux calibration in the follow-up spectrum blueward of Hβ for ZTF19aambzmf, so we do not include the continuum ratio of that source. Adapted from Figure 6 in MacLeod et al. (2019) and Figure 14 in Frederick et al. (2019).

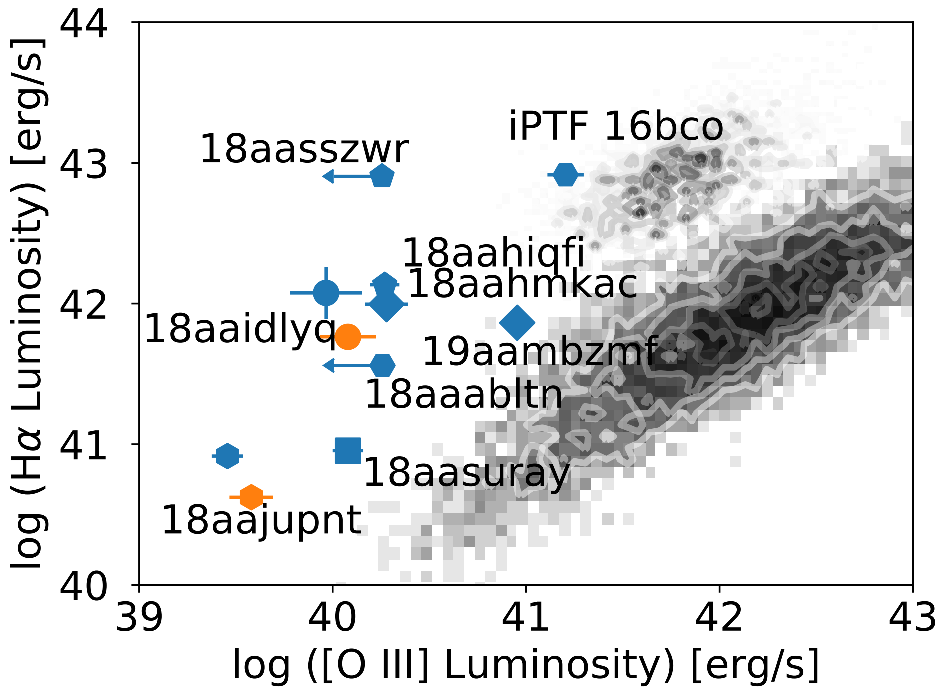

Figure 4.13: Hα and [O III] λ5007 line luminosities measured for the sample of CL LINERs, showing that they exist in an extreme region of this parameter space in the high state. The upper and lower contours representing log $L_{\mathrm{H}\alpha}$ vs. log $L_{\mathrm{[O\ III]}}$ measurements of SDSS DR7 quasars and Sy 1 galaxies from Shen et al. (2011) and Mullaney et al. (2013) show that this CL-LINER sample is up to an order of magnitude underluminous in [O III], due to light-travel time delays of an extended narrow line region that has yet to respond to the continuum flux change. We begin to see this response of [O III] as Hα fades in sources with spectra taken years after discovery (orange). Fits to these emission lines are shown in Figure 4.15 in the Appendix. Adapted from Figure 6 in Gezari et al. (2017) and Figure 17 of Frederick et al. (2019).

4.4.3 Black Hole Mass Estimates

We measure the black hole masses and resulting range of Eddington ratios for the sample through various methods, presented in Table 4.6, modified from Frederick et al. (2019) to include the additional sources discovered during the second half of the ZTF Phase I Survey. The gaussian fits to the Hβ lines are shown in Figure 4.14. See the caveats and equations presented in Frederick et al. (2019) for more details.

Table 4.6: Properties of the host galaxies of the sample of changing-look LINERs from ZTF and iPTF. $M_{\rm BH}$ for each object is calculated by various methods from the host galaxy luminosity, mass, and velocity dispersion, respectively, and described in Section 4.4.3.

Name	$M^{a}_{r,\rm host}$ (mag)	log $M^{b}_{\rm Bulge}$ [$M_\odot$]	$\sigma^{c}_{\star}$ (km s^{-1})	λL_{5100A} (10^{43} erg s^{-1})	FWHM$_{H_\beta}$ (km s^{-1})	log $M^{d}_{\rm BH,M_r}$ [$M_\odot$]	log $M^{e}_{\rm BH,Bulge}$ [$M_\odot$]	log $M^{f}_{\rm BH,\sigma\star}$ [$M_\odot$]	log $M_{\rm BH,vir}$ [$M_\odot$]	$L/L^{g}_{\rm Edd}$
ZTF18aahmkac	-21.20	10.67	230	0.55±0.01	5599±408	7.6	7.8	7.6	7.4	0.009
ZTF18aaavffc	-21.59	10.61	160	2.9±0.2	7020±2060	7.8	7.8	7.7	8.0	0.06
ZTF19aambzmf	-21.80	10.74	200	1.13±0.03	1319±318	7.9	7.9	7.9	6.3	0.06
ZTF18aajupnt	-22.00	10.66	150	0.49±0.11	939±28	8.0	7.8	7.6	6.4	0.09
ZTF18aasuray	-21.70	10.73	230	10.6±0.4	4270±218	7.9	7.9	8.4	8.0	0.03
ZTF18aaidlyq	-21.64	-	120	12.7±2.3	7726±458	7.9	-	8.2	8.5	0.06
ZTF18aahiqfi	-21.63	-	210	4.1±0.5	8809±723	7.9	-	7.2	8.3	0.2
ZTF18aasszwr	-22.19	11.19	180	57.0±1.9	6461±846	8.1	8.3	7.9	8.8	0.5
ZTF18aaabltn	-20.62	-	140	0.8±0.2	5195±648	7.3	-	7.5	8.0	0.2
iPTF16bco	-22.21	-	176	17.3±11.0	4183±213	8.4	-	7.9	8.1	0.05

a. Computed from the r-band de Vaucouleurs / exponential disk profile model fit magnitude from the SDSS DR14 photometric catalog, with errors between 0.003−0.005.
b. Computed from broadband SED fits to photometric measurements of SDSS DR 7 galaxies (Mendel et al., 2014), with error on the measurement of 0.15 dex.
c. Measured from the SDSS spectrum using the PPXF method.
d. McLure & Dunlop (2002)
e. Häring & Rix (2004)
f. Tremaine et al. (2002)
g. In the high state of the source; $M_{\rm BH,\sigma\star}$ was employed to obtain the black hole masses used in computing the Eddington ratio).

4.5 Discussion

The detection of hard X-rays in 2 of the 4 sources in this sample observed with NuSTAR (ZTF18aasszwr and ZTF18aahmkac) indicates the likely existence of an accretion disk several years after the optical rise associated with the changing-look transition, as defined in Table 4.2. As there was an X-ray flare observed with AT2018dyk, this may be evidence for the assembly of some accretion components occurring concurrently with the changing-look transition observed in 2018 for that object (Frederick et al., 2019). However, as the host galaxies for the sample are LINERs, there may have been a pre-existing accretion disk at the time of the changing-look transition. The physical properties for the persistent LINER accretion flow may have been importantly different to that of a type 1 AGN, e.g. smaller in physical extent or lower in density, which may make these a unique physical as well as observational class of changing-look events, and may explain their more dramatic nature compared to normal CLAGN (e.g. Figure 4.12).

For the subset of sources with weak or no tentative Compton hump detections

[9] Measured from the SDSS spectrum using the PPXF method.

with NuSTAR, due to the light crossing time from the molecular torus component being on the order of years, there may not have been sufficient time for any change following the changing look transition to fully propagate and induce a response. Fitting the X-ray spectral data with fully physical reflection model is forthcoming in future work. Additionally, detection of the Compton hump in future X-ray spectroscopic observations would be independent support for the (changing-look) AGN scenario for these nuclear transients, as opposed to other accretion related or flaring events, as it is a reflection signature of the molecular torus.

In Frederick et al. (2019), the Swift XRT spectrum of AT2018dyk required an additional strong soft excess component below 1-2 keV modeled by a power law with $\Gamma \sim 3$, which was no longer seen in the epoch taken 2 years later. Present in more than 50% of Seyfert 1 galaxies, and prominent in high-mass-accretion-rate narrow-line Seyfert 1 AGN, it is possible this component is a crucial artifact or driver of the changing look phenomenon observed in real time in this source. Swift XRT provides an important insight into the intermediate evolution of the X-ray spectral slope, shown in Figure 4.9 to approach that of the other objects in the sample over time. What effects the LINER environment has on the longevity of this component is an intriguing focus for future theoretical and systematic studies with a larger sample of CL-LINERs. In tidal disruption events, X-rays are seen to appear initially from the accretion flow of debris immediately following the destruction of the star, are sometimes obscured, and later re-emerge in some objects several months to years later following the formation of the accretion disk (e.g. Gezari et al. 2017; Wevers et al. 2019).

The fact that AT2018dyk was not strongly detected with XMM-Newton two years later in 2020 is quite unusual for a NLSy1, which typically display luminous and variable soft X-rays. It is possible this source is behaving similarly to a non-canonical X-ray bright TDE that has faded and changed color, despite having a

NLSy1-like UV spectrum (the sparse UV spectral data of TDEs are heterogeneous in the literature; see van Velzen et al. 2020a and references therein). The line strength of He II, which is directly photoionized by the X-rays and a common but not ubiquitous spectral signature of TDEs, has also faded with time in this source. Alternatively, the X-ray emitting region may be partially obscured by Compton-thick accreted material along the line of sight to the AGN, possibly associated with the changing-look event.

4.6 Conclusions

As automated discovery and follow-up efforts increase in efficiency, we find more examples of changing-look AGN which push the limits of what we know of this population's properties such as transition timescales and multiwavelength emission in real time. Such systematic multiwavelength follow up efforts are necessary to track the evolution of these events in real time. With observations with XMM and NuSTAR, coupled with multi epoch optical spectroscopy, we attempt to map out the environments of a growing sample of changing-look LINERs. We find that this observationally distinct class of objects generally follows trends of X-ray spectral hardening with time established by Ruan et al. (2019b) and Jin et al. (2021) for changing-look quasars. We also find a strengthening of the narrow line region tracer [O III] over several years with respect to the broad line region as expected from a light travel time delayed response to the dramatic continuum changes observed from these sources. We observe differences in the directionality of the time evolution of these sources through various parameter spaces representing accretion rate, hardness, and strengths of emission features tracing various regions of the accretion flow. Inclusion of intermediate epochs, including from a follow-up campaign with Gemini GMOS-N undertaken between 2019 and 2020, will track this directionality with finer granularity. Additionally, with statistical samples which will be possible in the near future, these diagnostics may be a way to distinguish heterogeneous accretion modes or chaotic or unstable phases within this observational class through their spectroscopic evolution. Systematic searches and follow-up with multi-epoch and all-sky spectroscopic and X-ray surveys such as SDSS-V and eROSITA will have the capability to extend this sample to better understand the time evolution of such events.

4.7 Appendix

Details of the optical and UV spectroscopic follow-up of the CL-LINER sample are presented in Table 4.7. In Figures 4.15 and 4.14 we present additional Gaussian profile model fits for selected emission lines of the sample used in Figures 2.17 and 4.12 with methods described in Section 4.4. we present the XMM-Newton and NuSTAR light curves of the X-ray observed subset of the sample in Figures 4.16 and 4.17, respectively.

Name	Obs UT	Instrument	Exposure (s)	Reference
ZTF18aajupnt	2002 July 11	SDSS	28816	Abolfathi et al. 2018
	2018 June 12	Palomar 200" DBSP	2400	Frederick et al. 2019
	2018 July 22	Palomar 60" SED Machine	2430	Frederick et al. 2019
	2018 Jul-Dec	Swift XRT	40400	Frederick et al. 2019
	2018 Aug 7	Keck DEIMOS	300	Frederick et al. 2019
	2018 Aug 11	XMM EPIC pn	11906	Frederick et al. 2019
	2018 Aug 12	Palomar 60" SED Machine	2430	Frederick et al. 2019
	2018 Aug 12	FTN FLOYDS-N	3600	Arcavi et al. 2018
	2018 Aug 21	Gemini GMOS-N	600	Frederick et al. 2019
	2018 Sept 1	HST STIS	2859	Frederick et al. 2019
	2018 Sept 12	DCT Deveny	2400	Frederick et al. 2019
	2018 Sept 17	NICER	1856	This work
	2019 Jan 18	HST STIS	2502	Frederick et al. 2019
	2019 Mar 3	HST STIS	2502	Frederick et al. 2019
	2019 Mar 17	Swift	2900	This work
	2019 May 2	LDT Deveny	600	This work
	2019 Jun 29	LDT Deveny	2400	This work
	2019 Sep 26	Swift	1800	This work
	2019 Dec 15	Swift	2800	This work
	2020 Jan 3	Gemini GMOS-N	1200	This work
ZTF18aasuray	2001 Feb 15	SDSS	8699	Abolfathi et al. 2018
	2018 Jun 21	LDT Deveny	1400	Frederick et al. 2019
	2019 Sep 25	Swift	2300	This work
	2019 Dec 18	Gemini GMOS-N	1200	This work
	2020 Dec 6	LDT Deveny	900	This work
ZTF18aahiqfi	2003 Apr 7	SDSS	20314	Abolfathi et al. 2018
	2018 Apr 11	LDT Deveny	1800	Frederick et al. 2019
	2019 Apr 4	Swift	2000	This work
	2019 May 25	Swift	5000	This work
	2019 Dec 19	Gemini GMOS-N	1200	This work
ZTF18aaidlyq	2002 Dec 29	SDSS	17642	Abolfathi et al. 2018
	2018 May 6	LDT Deveny	1200	Frederick et al. 2019
	2019 Mar 28	Swift	2000	This work
	2019 Nov 29	Gemini GMOS-N	1200	This work
	2020 Oct 15	LDT Deveny	1400	This work
ZTF18aaabltn	2007 Feb 18	SDSS	42982	Abolfathi et al. 2018
	2018 Dec 9	Palomar 60" SED Machine	1200	Frederick et al. 2019
	2019 Mar 25	Swift	1700	This work
	2019 May 2	LDT Deveny	600	Frederick et al. 2019
	2019 Nov 29	Gemini GMOS-N	1200	This work
	2020 Oct 14	LDT Deveny	1000	This work
ZTF18aasszwr	2003 Jan 5	SDSS	17891	Abolfathi et al. 2018
	2018 Dec 3	Palomar 60" SED Machine	2250	Frederick et al. 2019
	2019 Mar 28	Swift	857	This work
	2019 Nov 5	LDT Deveny	1200	This work
	2019 Dec 4	Gemini GMOS-N	1200	This work
	2020 Jan 3	Gemini GMOS-N	1200	This work
	2021 Mar 3	LDT Deveny	1200	This work
ZTF18aahmkac	2003 Apr 4	SDSS	20200	Abolfathi et al. 2018
	2019 May 29	LDT Deveny	900	This work
	2019 July 5	*Swift*	6000	This work
	2019 Dec 4	Gemini GMOS-N	1200	This work
ZTF18aaavffc	2005 Apr 12	SDSS	44907	Abolfathi et al. 2018
	2020 Jan 29	Gemini GMOS-N	1200	This work
ZTF19aambzmf	2007 May 14	SDSS	44907	Abolfathi et al. 2018
	2019 Dec 5	*Swift*	-	This work
	2020 Jan 3	Gemini GMOS-N	1200	This work
	2020 Jan 24	Gemini GMOS-N	1200	This work
iPTF 16bco	2004 June 16	SDSS	27205	Abolfathi et al. 2018
	2016 June 2	Palomar 60" SED Machine	1200	Gezari et al. 2017
	2016 June 4	Keck DEIMOS	240	Gezari et al. 2017
	2016 June 13	LDT Deveny	600	Gezari et al. 2017
	2016 July 9	LDT Deveny	1200	Gezari et al. 2017
	2016 July 24	Palomar 60" SED Machine	2700	Gezari et al. 2017
	2017 July 29	Palomar 200" DBSP	600	This work
	2019 Sep 29	*Swift*	2000	This work
	2020 Jan 9	Gemini GMOS-N	1200	This work
	2020 Jan 24	Gemini GMOS-N	1200	This work

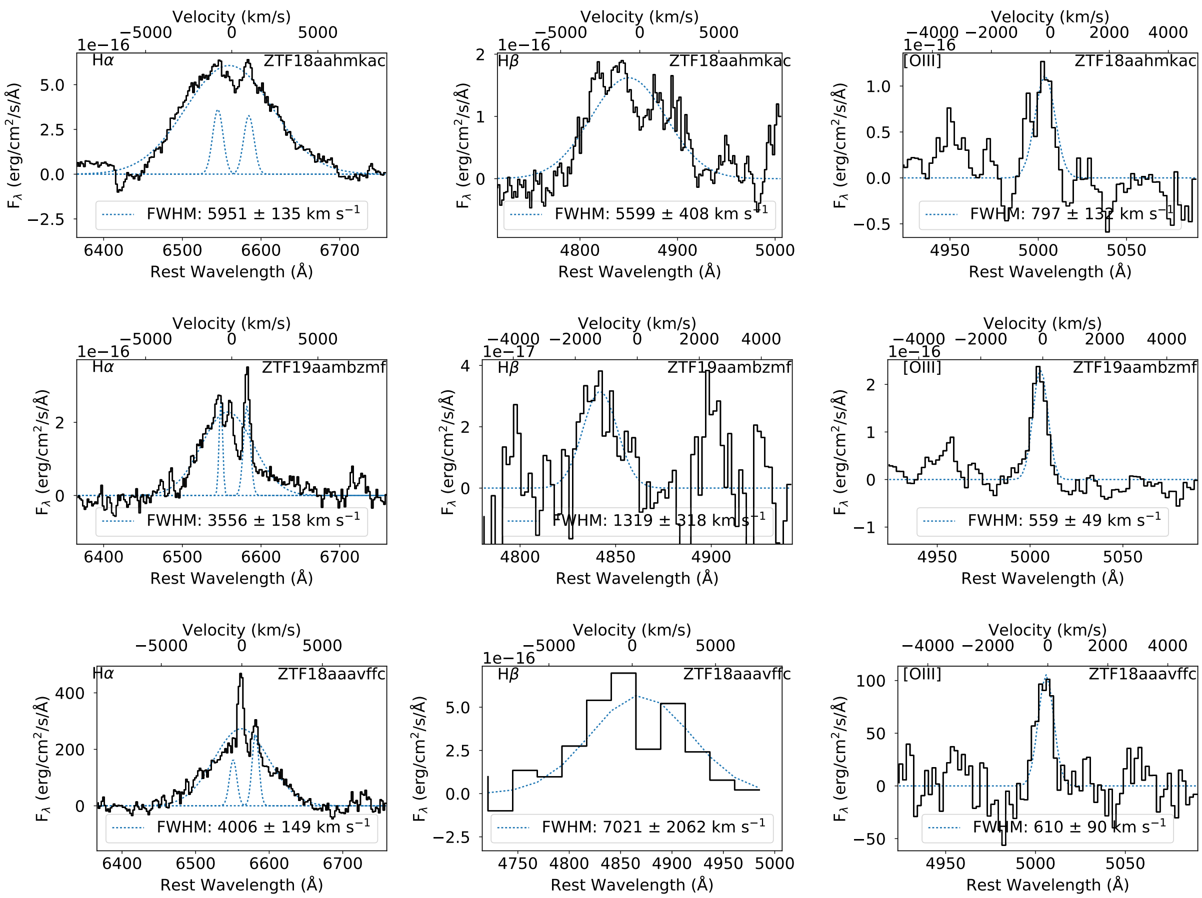

Figure 4.14: Gaussian fits to the Hα+[N II], Hβ, and [O III] line profiles of the latest sources added to the sample. Measurements from these fits are used in Table 4.6 and Figure 4.13. Note the differences in scale.

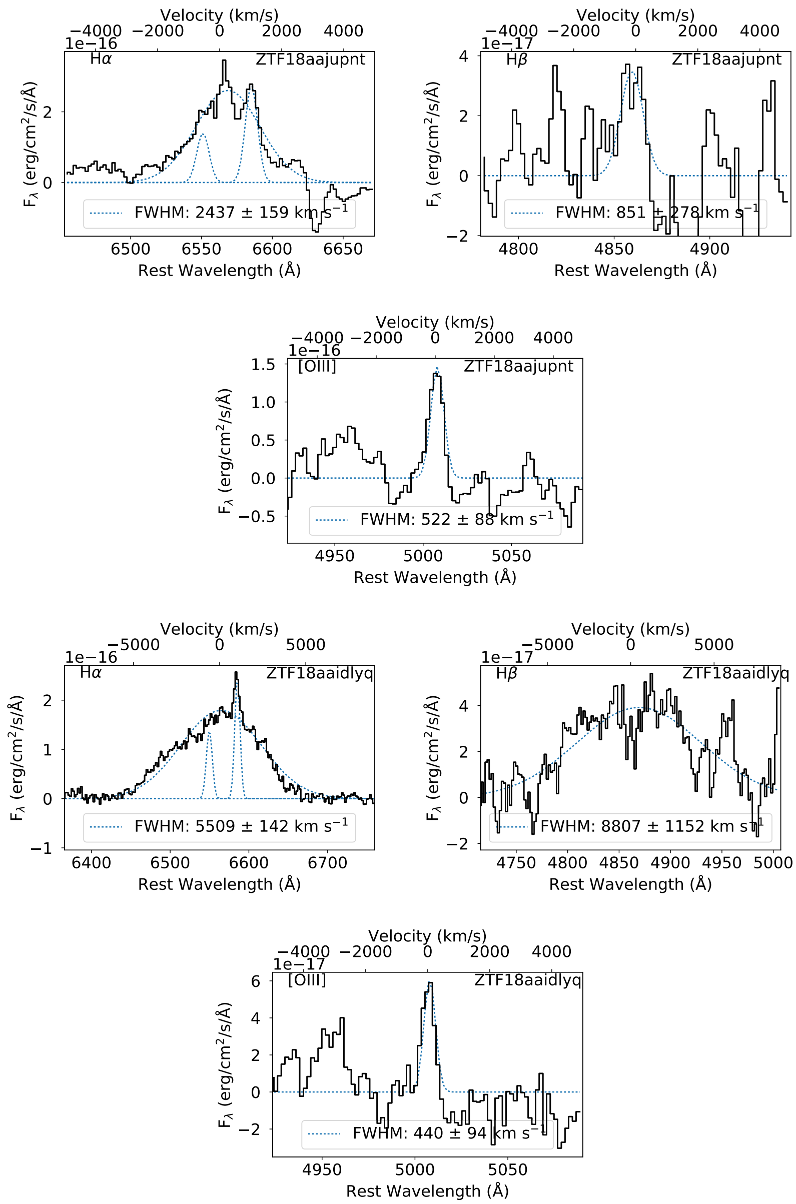

Figure 4.15: Gaussian fits to the Hα+[N II], Hβ, and [O III] line profiles using the latest follow-up data of the original sample displaying spectral changes in Figure 4.11. Measurements from these fits are used in Table 4.6 and Figure 4.13. Note the differences in scale.

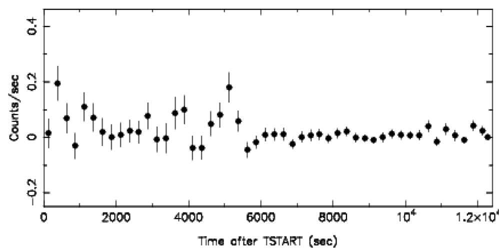

(a) AT2018dyk

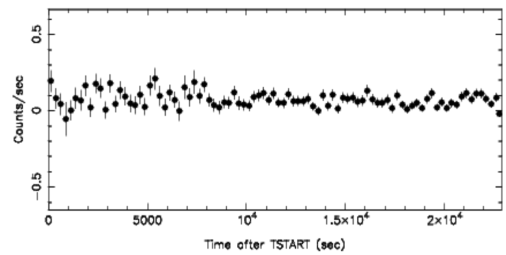

(b) ZTF19aambzmf

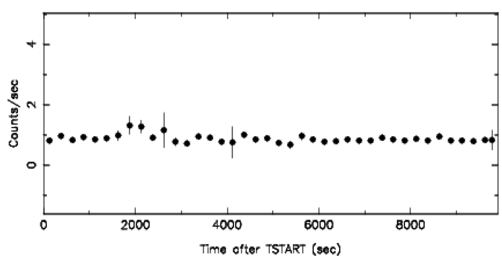

(c) ZTF18aasszwr

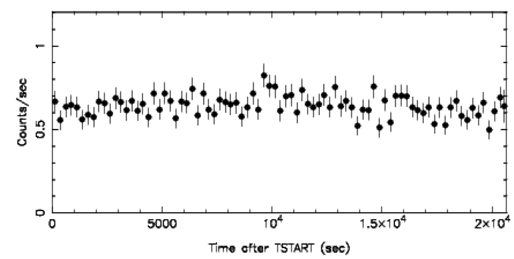

(d) ZTF18aahmkac

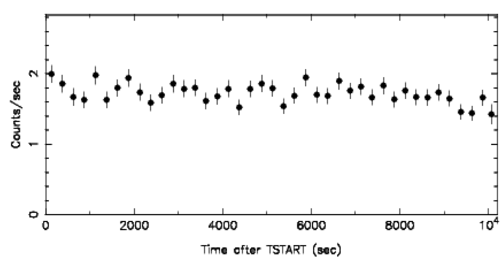

(e) ZTF18aaabltn

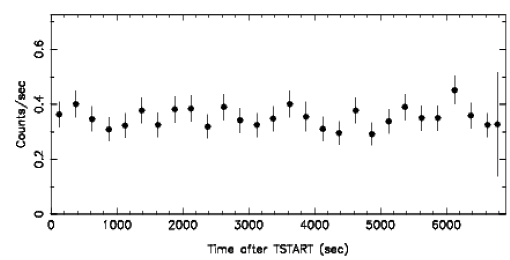

(f) ZTF18aaidlyq

Figure 4.16: Broadband (0.3−10 keV) light curves of the 6 sources in the sample observed with XMM-Newton.
.

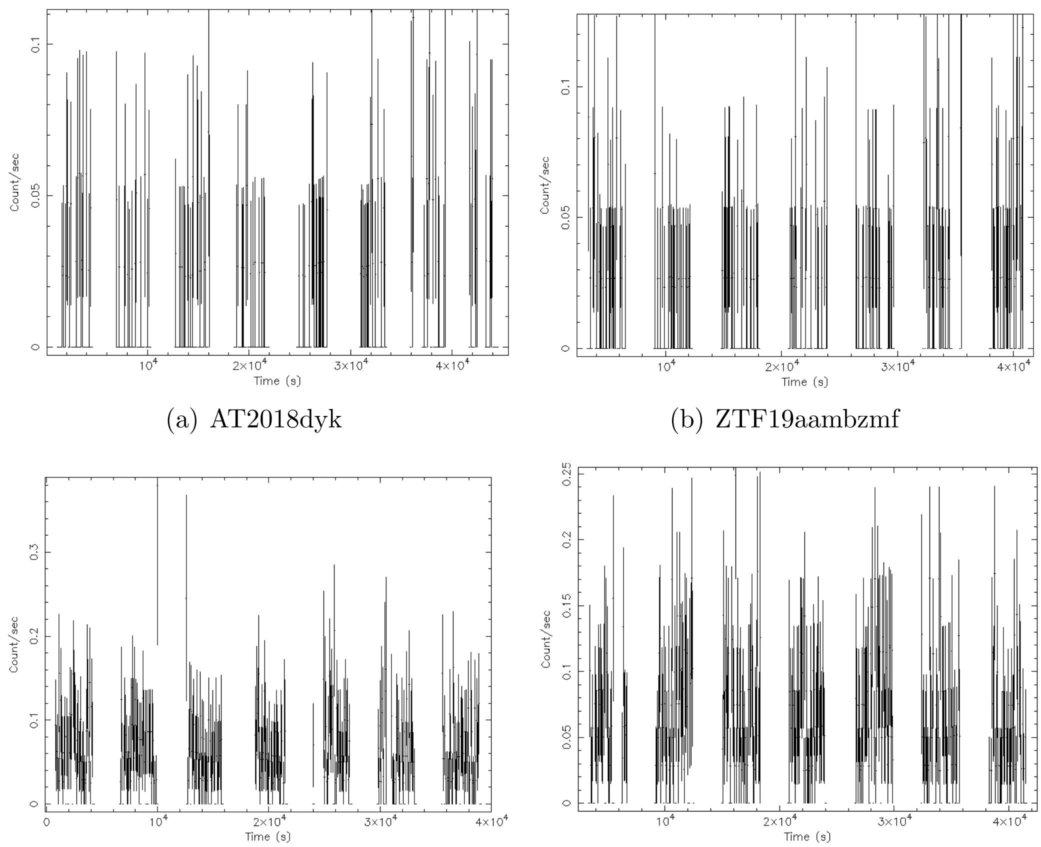

(a) AT2018dyk

(b) ZTF19aambzmf

(c) ZTF18aasszwr

(d) ZTF18aahmkac

Figure 4.17: Broadband (3−79 keV) finely binned light curves of the 4 sources in the sample observed with NuSTAR.
.

Chapter 5: Conclusions and Future Work

5.1 Lessons Learned

Discoveries of new observational classes of changing-look AGN in the past decade have uncovered a diverse set of exotic new laboratories for understanding the relationship between SMBHs at the centers of galaxies and their environments, specifically how feeding episodes leading to AGN ignition and black hole growth may proceed differently than we currently understand. Both are processes which affect how galaxies evolve over cosmological timescales, despite the small relative size of the central black hole compared to the rest of its host galaxy and the short timescales of these observations.

In terms of experimental design, ZTF Phase I provided a proof-of-concept that such new and exciting discoveries could be made in the realm of AGN science with a survey intended to discover transients such as supernovae. These ambitious efforts to tease out these events from the alert stream were inevitably met with difficulties, namely we find that in certain transient events the observational distinctions between tidal disruption flares, superluminous supernovae, and extreme AGN variability are subtle, and this should certainly inform how future searches proceed.

We nonetheless found that these relatively small scale studies of heterogeneous observational classes of events, of which we conducted intensive follow-up campaigns and provided detailed accounts across wavebands, were useful for identifying important characteristics and generating hypotheses for more systematic searches and studies to eventually test models and theories for exotic accretion-powered phenomena. With this open attention to exciting yet incomplete samples emerging from various approaches to collecting events from the ZTF alert stream, we found unexpected avenues for future study, such as characteristics of nuclei in certain galaxy subtypes which were far more conducive to hosting such dramatic changes. For example, Frederick et al. (2019) found a proximity in the BPT diagram to the cross-over point between LINER and Seyfert galaxies for the sample of CL-LINERs presented in Chapter 2. Such studies contextualizing these samples within new theoretical and empirical frameworks are already beginning to be carried out (e.g. Dodd et al. 2021; Ruan et al. 2019b).

5.2 Future Work

ZTF, along with its wide field survey contemporaries and building off of the legacy of the Palomar Transient Factory, has revolutionized the field of transient science beyond even what was intended. Though enabling this work, these predecessors to the Rubin Observatory have opened up a new time domain field of following up rapid and unique AGN behavior as it occurs, to better and earlier understand the nature of processes associated with rapid shifts in SMBH accretion on human timescales, to investigate why they occur.

There exist many interesting future avenues of research to explore, from modeling the chemical abundances of the accretion flow with high resolution spectroscopy, to systematic matched sample studies of the unique host galaxies of these flares, which will serve to deepen our understanding of the mechanisms driving these new and exotic events.

For example, Dodd et al. (2021) recently conducted an observational study of CLAGN host galaxies to understand the conditions for triggering an instability that could result in a change in accretion state, and confirmed this result that LINERs are conducive to hosting transitions. They found that changing look AGN are likely linked to periods of galaxy transformation and quenching of star formation in galaxies undergoing evolution processes that drive gas toward the high-density nucleus, terminating in episodic bursty accretion as the reservoir is diminished.

5.2.1 Looking Forward to the Landscape of Real-time All-sky and High Energy Observations

Thanks to technological advancements across instrumentation to data science, discoveries from the ever-expanding field of multimessenger astrophysics is rich and growing richer. In the near future (i.e. in the next several years to decades), panoptic surveys will uncover many more exciting unforeseen avenues for disocvery as well as systematic exploration into the physical mechanisms underlying these events.

The observational classification scheme presented in Frederick et al. (2020) will allow for more rapid distinctions to be made between the physical mechanisms resulting in transients in AGN, to better tailor follow-up efforts in forthcoming synoptic surveys. Ground-based facilities with multi-epoch imaging photometry such as PTF/iPTF, ZTF, PanSTARRS, and ASAS-SN have been the workhorses for photometric surveys discovering and monitoring flaring events of all kinds including AGN variability, whereas space-based facilities like Kepler have laid the groundwork for the Transiting Exoplanet Survey Satellite (TESS) to follow AGN with both high cadence and regular observations (Smith et al., 2018). The Vera Rubin Survey, formerly LSST, will drastically increase the rate of discovery of candidates for exotic SMBH accretion events by orders of magnitude, improving our understanding of their temporal properties on short timescales, and allowing for more rapid follow-up.

The Sloan Digital Sky Survey, consisting of multi-epoch imaging surveys such as Stripe-82[1] as well as spectroscopic follow-up like the TDSS variability selected AGN sample, has been instrumental in defining the catalogues from which CLAGN may be discovered (e.g. LaMassa et al. 2015; MacLeod et al. 2016; Ruan et al. 2016; Runnoe et al. 2016). The Black Hole Mapper Project as part of SDSS-V (Kollmeier et al., 2017) utilizes the legacy of the BOSS fibre multi-object spectrograph and will provide 800,000 new spectra of more than 6 million total objects with both Northern and Southern sky coverage as well as spectroscopic monitoring. It joins large scale IFU surveys such as MUSE to provide shorter cadences (down to 20 minutes) and longer baselines between epochs (up to 20 years), as well as reaching unprecedented volumetric depths, with a median galaxy redshift of $z = 0.1$. Large scale spectroscopic surveys such as those carried out by SDSS-V and the Dark Energy Spectroscopic Instrument (DESI) will dramatically expand the parameter space in which changing-state transitions will be found, and thereby growing the samples and searches of such exotic sources to be both statistical and systematic. Such samples will allow for tests of the hypotheses put forward here, that certain environments such as narrow-line Seyfert 1 galaxies and LINER galaxies are more conducive to hosting these accretion state changes, the most dramatic of this class seen to-date.

Based on studies of individual objects, it is possible that the accretion mode changes of CLAGN may be heralded in the X-rays concurrent with (or even prior to) the optical (e.g. Frederick et al. 2019; Parker et al. 2016; Trakhtenbrot et al. 2019b). The advent of major all-sky X-ray surveys such as eROSITA will complement rapid follow-up facilities for bright targets such as NICER and Swift XRT, and will be tracked systematically (completely and homogenously) with large-scale spectroscopic follow-up campaigns like the SPectroscopic IDentfication of ERosita Sources (SPIDERS; Clerc et al. 2016) and SDSS-V.

[1]Stripe-82 was completed between 2000−2008.

Complementary to the observational advances made by large scale photometric and spectroscopic surveys alike, computational advancements in data science as well as machine learning could be utlized to learn on the photometric datasets of these now-exotic rapid and smooth AGN flares as they become not-so-unique when hundreds of thousands are observed throughout the lifetimes of these wide area surveys, to hone search techniques and identify crucial shared properties of such events. Future expanded searches may also turn up even more interesting variants on these flares types, for example SMBH binaries displaying optical flare counterparts. It will be important for large scale surveys to be positioned to follow up these binary AGN gravitational wave sources that will be visible to LISA in the same way as done for stellar mass systems with LIGO. Additionally, there will be on-going multimessenger searches for neutrinos from TDEs and AGN with IceCube, which will help us to understand the higher energy emission and processes associated with SMBH systems accelerating these astroparticles (Stein et al. 2021, in prep.)

5.3 Overview of Contributions

While the number of CLAGN continues to steadily increase, prior to this work there had yet to be a large-scale systematic study that simultaneously tracks the appearance of continuum variability and the broad-line emission of changing-look candidates in real-time using difference imaging as a discovery mechanism. The Zwicky Transient Facility (ZTF) has allowed for real-time detection and rapid multiwavelength follow-up of events related to accretion onto supermassive black holes like never before. Here we presented real-time investigations of extreme transients associated with sudden changes in the environments of the SMBHs in active galaxy centers. Possible modes of SMBH accretion ascribed to these outbursts span from tidal disruption events in active galactic nuclei (AGN), to the curious established and growing class of "changing-look" active galactic nuclei (CLAGN). A pilot study with the intermediate Palomar Transient Factory (iPTF) discovered one CL LINER (Gezari et al., 2017), and ZTF expanded this sample by an order of magnitude, discovering 9 more (Frederick et al. 2019 and Frederick et al. 2021, in prep.) This search also resulted in the serendipitous discovery of a sample of 6 new exotic optical transients in NLSy1s (Frederick et al., 2020), growing the number of such flares by a factor of three (Trakhtenbrot et al., 2019a).

Filtering the ZTF alert stream for nuclear transients over the past three years resulted in a surprisingly broad range of accretion powered phenomena associated with AGN, from flares to changes in accretion state. In studying these extreme outbursts, we found they were associated with enhanced accretion onto certain types of supermassive black hole environments. Specifically, we have found a connection to dramatic flares with spectroscopic changes and LINERs (Chapter 2) and NLSy1s (Chapter 3), and investigated those new observational classes with multiwavelength data in real time (Chapter 4).

Through searching for nuclear transients coincident with previously narrow-line AGN, we discovered eight quiescent galaxies caught "turning on" into quasars (Frederick et al., 2019). We showed that the LINER galaxies, classified previously by weak narrow forbidden line emission in their archival optical spectra, had transformed dramatically into broad-line AGN reminiscent of iPTF 16bco (Gezari et al., 2017). Comparing the dramatic on-to-off continuum and Hβ flux ratios with a sample of CL-Seyferts, we identified that this was a unique class of optical CLAGN related to physical processes associated with the LINER accretion state. In one case, follow-up UV and optical spectra revealed the transformation from a LINER into a narrow-line Seyfert 1 (NLS1) with strong coronal lines. *Swift* monitoring of this source revealed bright UV emission that tracked the optical flare, accompanied by a luminous soft X-ray flare that peaked ∼60 days later. Archival light curves of the sample revealed similar smooth, flare-like deviations from quiescence, and constrained the onset of the optical nuclear flaring (transition timescales shown in Section 3 Table). This unique class of transients found in ZTF "turning on" from quiescent galaxies into broad line AGN on timescales of months to years, promises to shed light on the nature of LINERs, the nature of coronal line emission, the nature of the soft X-ray excess in NLSy1s, and the physical mechanism powering changing-look AGN.

Appendix A: Facilities and Software

This thesis work would not have been possible without the following resources:

1. Zwicky Transient Facility

   www.ztf.caltech.edu

   The ZTF camera is mounted on the Samuel Oschin 48-inch telescope at Palomar Optical Observatory (Bellm et al. 2019a, Graham et al. 2019).

2. The SED Machine

   www.ztf.caltech.edu

   The SEDM is an IFU spectrograph mounted on the 60-inch telescope at Palomar Optical Observatory.[1]

3. Lowell Discovery Telescope

   https://lowell.edu/research/research-facilities/4-3-meter-ldt/

   This dissertation relied on data taken by the Deveny Spectrograph at the Lowell Observatory in Happy Jack, Arizona.

4. SDSS

   http://skyserver.sdss.org/dr16/en/home.aspx

5. SAS

   https://www.cosmos.esa.int/web/xmm-newton/home

[1] Blagorodnova, N., Neill, J. D., Walters, R., et al. 2018, PASP, 130, 035003. doi:10.1088/1538-3873/aaa53f

Data in this dissertation was reduced using the XMM-Newton Science Analysis System distributed by ESA.[2]

6. lmfit

   https://zenodo.org/record/11813#.YDqxgGNOnNY

   The lmfit package is Free software, using an MIT license.[3,4]

7. IPAC, NED

   NED.ipac.caltech.edu

   This work made use of archival optical spectra made available by the NED NASA/IPAC Extragalactic Database online interface.[5]

8. ASASSN Sky Patrol

   https://asas-sn.osu.edu

9. SIMBAD

   simbad.u-strasbg.fr/

   The SIMBAD database is operated at CDS, Strasbourg, France. [6]

[2] Gabriel et al. 2004

[3] Newville, Matthew, Stensitzki, Till, Allen, Daniel B., & Ingargiola, Antonino. (2014, September 21). LMFIT: Non-Linear Least-Square Minimization and Curve-Fitting for Python (Version 0.8.0). Zenodo. http://doi.org/10.5281/zenodo.11813

[4] Newville, M., Stensitzki, T., Allen, D. B., et al. 2016, Astrophysics Source Code Library. ascl:1606.014

[5] Madore, Barry, 1998, "Astrophysics and Algorithms: a DIMACS Workshop on Massive Astronomical Data Sets", meeting abstract, id. 6.

[6] 2000,A&AS,143,9 , "The SIMBAD astronomical database", Wenger et al.

Bibliography

Abolfathi, B., Aguado, D. S., Aguilar, G., et al. 2018, *ApJS*, 235, 42, doi: 10.3847/1538-4365/aa9e8a

Agüeros, M. A., Ivezić, Ž., Covey, K. R., et al. 2005, *AJ*, 130, 1022, doi: 10.1086/432160

Ai, Y. L., Yuan, W., Zhou, H. Y., et al. 2010, *ApJL*, 716, L31, doi: 10.1088/2041-8205/716/1/L31

Antonucci, R. 1993, Annual Review of Astronomy and Astrophysics, 31, 473, doi: 10.1146/annurev.aa.31.090193.002353

Arcavi, I., Trakhtenbrot, B., & Hiramatsu, D. 2019, Transient Name Server AstroNote, 4, 1

Arcavi, I., Gal-Yam, A., Sullivan, M., et al. 2014, *ApJ*, 793, 38, doi: 10.1088/0004-637X/793/1/38

Arcavi, I., Burke, J., French, K. D., et al. 2018, The Astronomer's Telegram, 11953

Arnaud, K., Branduardi-Raymont, G., Culhane, J., et al. 1985, Monthly Notices of the Royal Astronomical Society, 217, 105

Arnaud, K. A. 1996, in Astronomical Society of the Pacific Conference Series, Vol. 101, Astronomical Data Analysis Software and Systems V, ed. G. H. Jacoby & J. Barnes, 17

Assef, R. J., Stern, D., Kochanek, C. S., et al. 2013, *ApJ*, 772, 26, doi: 10.1088/0004-637X/772/1/26

Baldi, R. D., Capetti, A., Robinson, A., Laor, A., & Behar, E. 2016, *MNRAS*, 458, L69, doi: 10.1093/mnrasl/slw019

Baldwin, J. A., Phillips, M. M., & Terlevich, R. 1981, Publications of the Astronomical Society of the Pacific, 93, 5, doi: 10.1086/130766

Barth, A. J., Pancoast, A., Bennert, V. N., et al. 2013, *ApJ*, 769, 128, doi: 10.1088/0004-637X/769/2/128

Belfiore, F., Maiolino, R., Maraston, C., et al. 2016, *MNRAS*, 461, 3111, doi: 10.1093/mnras/stw1234

Bellm, E. C., & Sesar, B. 2016, pyraf-dbsp: Reduction pipeline for the Palomar Double Beam Spectrograph. http://ascl.net/1602.002

Bellm, E. C., Kulkarni, S. R., Graham, M. J., et al. 2019a, *PASP*, 131, 018002, doi: 10.1088/1538-3873/aaecbe

Bellm, E. C., Kulkarni, S. R., Barlow, T., et al. 2019b, Publications of the Astronomical Society of the Pacific, 131, 068003, doi: 10.1088/1538-3873/ab0c2a

Bianchi, L., Shiao, B., & Thilker, D. 2017, *ApJS*, 230, 24, doi: 10.3847/1538-4365/aa7053

Bianchi, L., Seibert, M., Zheng, W., et al. 2005, *ApJL*, 619, L27, doi: 10.1086/423710

Blagorodnova, N., Gezari, S., Hung, T., et al. 2017, *ApJ*, 844, 46, doi: 10.3847/1538-4357/aa7579

Blagorodnova, N., Neill, J. D., Walters, R., et al. 2018, *PASP*, 130, 035003, doi: 10.1088/1538-3873/aaa53f

Blagorodnova, N., Cenko, S. B., Kulkarni, S. R., et al. 2019, *ApJ*, 873, 92, doi: 10.3847/1538-4357/ab04b0

Blanchard, P. K., Nicholl, M., Berger, E., et al. 2017, *ApJ*, 843, 106, doi: 10.3847/1538-4357/aa77f7

Blandford, R. D., & Znajek, R. L. 1977, *MNRAS*, 179, 433, doi: 10.1093/mnras/179.3.433

Boller, T., Brandt, W. N., & Fink, H. 1996, *A&A*, 305, 53

Bolzonella, M., Miralles, J.-M., & Pelló, R. 2000, *A&A*, 363, 476

Boroson, T. A., & Green, R. F. 1992, The Astrophysical Journal Supplement Series, 80, 109, doi: 10.1086/191661

Brandt, W. N., Pounds, K. A., & Fink, H. 1995, *MNRAS*, 273, L47, doi: 10.1093/mnras/273.1.L47

Bremer, M., Scharwächter, J., Eckart, A., et al. 2013, *A&A*, 558, A34, doi: 10.1051/0004-6361/201322009

Brightman, M., Silverman, J. D., Mainieri, V., et al. 2013, *MNRAS*, 433, 2485, doi: 10.1093/mnras/stt920

Brown, J. S., Kochanek, C. S., Holoien, T. W. S., et al. 2018, *MNRAS*, 473, 1130, doi: 10.1093/mnras/stx2372

Brown, P. J., Yang, Y., Cooke, J., et al. 2016, *ApJ*, 828, 3, doi: 10.3847/0004-637X/828/1/3

Bruch, R. J., Gal-Yam, A., Schulze, S., et al. 2020, arXiv e-prints, arXiv:2008.09986. https://arxiv.org/abs/2008.09986

Cackett, E. M., Gültekin, K., Bentz, M. C., et al. 2015, *ApJ*, 810, 86, doi: 10.1088/0004-637X/810/2/86

Campana, S., Mainetti, D., Colpi, M., et al. 2015, *A&A*, 581, A17, doi: 10.1051/0004-6361/201525965

Cappellari, M. 2016, Annual Review of Astronomy and Astrophysics, 54, 597, doi: 10.1146/annurev-astro-082214-122432

Cappellari, M., & Emsellem, E. 2004, *PASP*, 116, 138, doi: 10.1086/381875

Cappelluti, N., Predehl, P., Böhringer, H., et al. 2011, Memorie della Societa Astronomica Italiana Supplementi, 17, 159. https://arxiv.org/abs/1004.5219

Cardelli, J. A., Clayton, G. C., & Mathis, J. S. 1989, *ApJ*, 345, 245, doi: 10.1086/167900

Cenko, S. B., Fox, D. B., Moon, D.-S., et al. 2006, Publications of the Astronomical Society of the Pacific, 118, 1396, doi: 10.1086/508366

Cenko, S. B., Cucchiara, A., Roth, N., et al. 2016, *ApJL*, 818, L32, doi: 10.3847/2041-8205/818/2/L32

Chambers, K. C., Magnier, E. A., Metcalfe, N., et al. 2016, arXiv e-prints, arXiv:1612.05560. https://arxiv.org/abs/1612.05560

Chan, C.-H., Piran, T., & Krolik, J. H. 2020, arXiv e-prints, arXiv:2004.06234. https://arxiv.org/abs/2004.06234

Chan, C.-H., Piran, T., Krolik, J. H., & Saban, D. 2019, *ApJ*, 881, 113, doi: 10.3847/1538-4357/ab2b40

Chang, Y.-Y., van der Wel, A., da Cunha, E., & Rix, H.-W. 2015, The Astrophysical Journal Supplement Series, 219, 8, doi: 10.1088/0067-0049/219/1/8

Chatterjee, R., Marscher, A. P., Jorstad, S. G., et al. 2009, The Astrophysical Journal, 704, 1689

Chen, P. S., Liu, J. Y., & Shan, H. G. 2017, *NA*, 54, 30, doi: 10.1016/j.newast.2017.01.005

Choi, Y., Gibson, R. R., Becker, A. C., et al. 2014, *ApJ*, 782, 37, doi: 10.1088/0004-637X/782/1/37

Cid Fernandes, R., Stasińska, G., Mateus, A., & Vale Asari, N. 2011, *MNRAS*, 413, 1687, doi: 10.1111/j.1365-2966.2011.18244.x

Clerc, N., Merloni, A., Zhang, Y. Y., et al. 2016, *MNRAS*, 463, 4490, doi: 10.1093/mnras/stw2214

Constantin, A., & Shields, J. C. 2003, Publications of the Astronomical Society of the Pacific, 115, 592, doi: 10.1086/374724

Corbett, E. A., Robinson, A., Axon, D. J., et al. 1996, *MNRAS*, 281, 737, doi: 10.1093/mnras/281.3.737

Crenshaw, D. M., Kraemer, S. B., & Gabel, J. R. 2003, *AJ*, 126, 1690, doi: 10.1086/377625

Crummy, J., Fabian, A., Gallo, L., & Ross, R. 2006, Monthly Notices of the Royal Astronomical Society, 365, 1067

da Cunha, E., Charlot, S., Dunne, L., Smith, D., & Rowlands, K. 2012, in IAU Symposium, Vol. 284, The Spectral Energy Distribution of Galaxies - SED 2011, ed. R. J. Tuffs & C. C. Popescu, 292–296, doi: 10.1017/S1743921312009283

Davis, S. W., Woo, J.-H., & Blaes, O. M. 2007, *ApJ*, 668, 682, doi: 10.1086/521393

Dawson, K. S., Schlegel, D. J., Ahn, C. P., et al. 2013, *AJ*, 145, 10, doi: 10.1088/0004-6256/145/1/10

Decarli, R., Labita, M., Treves, A., & Falomo, R. 2008, *MNRAS*, 387, 1237, doi: 10.1111/j.1365-2966.2008.13320.x

Dickey, J. M., & Lockman, F. J. 1990, *ARA&A*, 28, 215, doi: 10.1146/annurev.aa.28.090190.001243

Dodd, S. A., Law-Smith, J. A. P., Auchettl, K., Ramirez-Ruiz, E., & Foley, R. J. 2021, *ApJL*, 907, L21, doi: 10.3847/2041-8213/abd852

Done, C., Davis, S., Jin, C., Blaes, O., & Ward, M. 2012, Monthly Notices of the Royal Astronomical Society, 420, 1848

Done, C., Davis, S. W., Jin, C., Blaes, O., & Ward, M. 2012, *MNRAS*, 420, 1848, doi: 10.1111/j.1365-2966.2011.19779.x

Drake, A. J., Djorgovski, S. G., Mahabal, A., et al. 2009, *ApJ*, 696, 870, doi: 10.1088/0004-637X/696/1/870

—. 2011, *ApJ*, 735, 106, doi: 10.1088/0004-637X/735/2/106

Elitzur, M., & Ho, L. C. 2009, *ApJ*, 701, L91, doi: 10.1088/0004-637X/701/2/L91

Elitzur, M., Ho, L. C., & Trump, J. R. 2014, *MNRAS*, 438, 3340, doi: 10.1093/mnras/stt2445

Elvis, M., Wilkes, B. J., McDowell, J. C., et al. 1994, *ApJS*, 95, 1, doi: 10.1086/192093

Eracleous, M., & Halpern, J. P. 2001, *ApJ*, 554, 240, doi: 10.1086/321331

—. 2003, *ApJ*, 599, 886, doi: 10.1086/379540

Erkens, U., Appenzeller, I., & Wagner, S. 1997, *A&A*, 323, 707

Evans, P. A., Beardmore, A. P., Page, K. L., et al. 2009, Monthly Notices of the Royal Astronomical Society, 397, 1177, doi: 10.1111/j.1365-2966.2009.14913.x

Fabian, A. C., & Ross, R. R. 2010, *SSRv*, 157, 167, doi: 10.1007/s11214-010-9699-y

Fazio, G. G., Hora, J. L., Allen, L. E., et al. 2004, The Astrophysical Journal Supplement Series, 154, 10, doi: 10.1086/422843

Filippenko, A. V. 1996, in Astronomical Society of the Pacific Conference Series, Vol. 103, The Physics of Liners in View of Recent Observations, ed. M. Eracleous, A. Koratkar, C. Leitherer, & L. Ho, 17

Forster, K., & Halpern, J. P. 1996, *ApJ*, 468, 565, doi: 10.1086/177715

Frederick, S., Kara, E., Reynolds, C., Pinto, C., & Fabian, A. 2018, *ApJ*, 867, 67, doi: 10.3847/1538-4357/aae306

Frederick, S., Gezari, S., Graham, M. J., et al. 2019, *ApJ*, 883, 31, doi: 10.3847/1538-4357/ab3a38

—. 2020, arXiv e-prints, arXiv:2010.08554. https://arxiv.org/abs/2010.08554

Gabriel, C., Denby, M., Fyfe, D., et al. 2004, in Astronomical Data Analysis Software and Systems (ADASS) XIII, Vol. 314, 759

Galeev, A., Rosner, R., & Vaiana, G. 1979, The Astrophysical Journal, 229, 318

Gallegos-Garcia, M., Law-Smith, J., & Ramirez-Ruiz, E. 2018, *ApJ*, 857, 109, doi: 10.3847/1538-4357/aab5b8

Gallo, L. C. 2006, *MNRAS*, 368, 479, doi: 10.1111/j.1365-2966.2006.10137.x

García, J. A., Kara, E., Walton, D., et al. 2019, *ApJ*, 871, 88, doi: 10.3847/1538-4357/aaf739

Gaskell, C. M., & Sparke, L. S. 1986, *ApJ*, 305, 175, doi: 10.1086/164238

Gaspari, M., & Sadowski, A. 2017, *ApJ*, 837, 149, doi: 10.3847/1538-4357/aa61a3

Gehrels, N., Chincarini, G., Giommi, P., et al. 2004, *ApJ*, 611, 1005, doi: 10.1086/422091

Gelbord, J. M., Mullaney, J. R., & Ward, M. J. 2009, *MNRAS*, 397, 172, doi: 10.1111/j.1365-2966.2009.14961.x

George, I. M., & Fabian, A. C. 1991, *MNRAS*, 249, 352, doi: 10.1093/mnras/249.2.352

Gezari, S., van Velzen, S., Perley, D., et al. 2019, The Astronomer's Telegram, 13127, 1

Gezari, S., Chornock, R., Rest, A., et al. 2012, *Nature*, 485, 217, doi: 10.1038/nature10990

Gezari, S., Hung, T., Cenko, S. B., et al. 2017, *ApJ*, 835, 144, doi: 10.3847/1538-4357/835/2/144

Ghisellini, G. 2013, Radiative processes in high energy astrophysics, Vol. 873 (Springer)

Gierliński, M., & Done, C. 2004, Monthly Notices of the Royal Astronomical Society, 349, L7

Gierliński, M., & Done, C. 2004, *MNRAS*, 349, L7, doi: 10.1111/j.1365-2966.2004.07687.x

Goad, M. R., O'Brien, P. T., & Gondhalekar, P. M. 1993, *MNRAS*, 263, 149, doi: 10.1093/mnras/263.1.149

Gold. 2019, Galaxies, 7, 63, doi: 10.3390/galaxies7020063

González-Martín, O., Masegosa, J., Márquez, I., et al. 2015, *A&A*, 578, A74, doi: 10.1051/0004-6361/201425254

Goodrich, R. W. 1989, The Astrophysical Journal, 342, 224

Graham, M. J., Djorgovski, S. G., Drake, A. J., et al. 2017, *MNRAS*, 470, 4112, doi: 10.1093/mnras/stx1456

Graham, M. J., Djorgovski, S. G., Stern, D., et al. 2015, *MNRAS*, 453, 1562, doi: 10.1093/mnras/stv1726

Graham, M. J., Kulkarni, S. R., Bellm, E. C., et al. 2019, Publications of the Astronomical Society of the Pacific, 131, 078001, doi: 10.1088/1538-3873/ab006c

Graham, M. J., Ross, N. P., Stern, D., et al. 2020, *MNRAS*, 491, 4925, doi: 10.1093/mnras/stz3244

Gromadzki, M., Hamanowicz, A., Wyrzykowski, L., et al. 2019, *A&A*, 622, L2, doi: 10.1051/0004-6361/201833682

Grupe, D., Beuermann, K., Mannheim, K., et al. 1995, *A&A*, 299, L5

Grupe, D., Komossa, S., Leighly, K. M., & Page, K. L. 2010, *ApJS*, 187, 64, doi: 10.1088/0067-0049/187/1/64

Grupe, D., Komossa, S., & Saxton, R. 2015, *ApJL*, 803, L28, doi: 10.1088/2041-8205/803/2/L28

Grupe, D., Leighly, K. M., Thomas, H.-C., & Laurent-Muehleisen, S. A. 2000, *A&A*, 356, 11

Grupe, D., & Mathur, S. 2004, *ApJL*, 606, L41, doi: 10.1086/420975

Guainazzi, M., Nicastro, F., Fiore, F., et al. 1998, *MNRAS*, 301, L1, doi: 10.1046/j.1365-8711.1998.02089.x

Guo, H., Sun, M., Liu, X., et al. 2019, *ApJL*, 883, L44, doi: 10.3847/2041-8213/ab4138

Halpern, J. P., & Eracleous, M. 1994, *ApJL*, 433, L17, doi: 10.1086/187537

Häring, N., & Rix, H.-W. 2004, *ApJL*, 604, L89, doi: 10.1086/383567

Hasinger, G. 2008, *A&A*, 490, 905, doi: 10.1051/0004-6361:200809839

Hawkins, M. R. S. 1998, *A&A*, 340, L23. https://arxiv.org/abs/astro-ph/9810337

—. 2004, Baltic Astronomy, 13, 642

Heckman, T. M. 1980, *A&A*, 500, 187

Hernández-Toledo, H. M., Vázquez-Mata, J. A., Martínez-Vázquez, L. A., Choi, Y.-Y., & Park, C. 2010, *AJ*, 139, 2525, doi: 10.1088/0004-6256/139/6/2525

HI4PI Collaboration, Ben Bekhti, N., Flöer, L., et al. 2016, *A&A*, 594, A116, doi: 10.1051/0004-6361/201629178

Hills, J. G. 1975, *Nature*, 254, 295, doi: 10.1038/254295a0

Ho, L. C. 2009, The Astrophysical Journal, 699, 626

Ho, L. C., Filippenko, A. V., & Sargent, W. L. W. 1993, *ApJ*, 417, 63, doi: 10.1086/173291

—. 1997a, The Astrophysical Journal Supplement Series, 112, 315, doi: 10.1086/313041

Ho, L. C., Filippenko, A. V., Sargent, W. L. W., & Peng, C. Y. 1997b, The Astrophysical Journal Supplement Series, 112, 391, doi: 10.1086/313042

Holoien, T. W. S., Brown, J. S., Auchettl, K., et al. 2018, *MNRAS*, 480, 5689, doi: 10.1093/mnras/sty2273

Holoien, T. W. S., Kochanek, C. S., Prieto, J. L., et al. 2016a, *MNRAS*, 455, 2918, doi: 10.1093/mnras/stv2486

—. 2016b, *MNRAS*, 463, 3813, doi: 10.1093/mnras/stw2272

Hopkins, P. F., Somerville, R. S., Hernquist, L., et al. 2006, *ApJ*, 652, 864, doi: 10.1086/508503

Hung, T., Gezari, S., Blagorodnova, N., et al. 2017, *ApJ*, 842, 29, doi: 10.3847/1538-4357/aa7337

Hung, T., Gezari, S., Cenko, S. B., et al. 2018, The Astrophysical Journal Supplement Series, 238, 15, doi: 10.3847/1538-4365/aad8b1

Hung, T., Cenko, S. B., Roth, N., et al. 2019, *ApJ*, 879, 119, doi: 10.3847/1538-4357/ab24de

Immler, S., & Lewin, W. H. 2003, in Supernovae and Gamma-Ray Bursters (Springer), 91–111

Ivezić, Ž., Kahn, S. M., Tyson, J. A., et al. 2019, *ApJ*, 873, 111, doi: 10.3847/1538-4357/ab042c

Jayasinghe, T., Stanek, K. Z., Kochanek, C. S., et al. 2019, *MNRAS*, 485, 961, doi: 10.1093/mnras/stz444

Jiang, N., Wang, T., Mou, G., et al. 2019, *ApJ*, 871, 15, doi: 10.3847/1538-4357/aaf6b2

Jin, X., Ruan, J. J., Haggard, D., et al. 2021, *ApJ*, 912, 20, doi: 10.3847/1538-4357/abeb17

Kalberla, P. M., Burton, W., Hartmann, D., et al. 2005, Astronomy & Astrophysics, 440, 775

Kankare, E., Kotak, R., Mattila, S., et al. 2017, Nature Astronomy, 1, 865, doi: 10.1038/s41550-017-0290-2

Kara, E., Alston, W. N., Fabian, A. C., et al. 2016, Mon. Not. R. Astron. Soc., 462, 511, doi: 10.1093/mnras/stw1695

Kara, E., Pasham, D., Gendreau, K., & Arzoumanian, Z. 2019, The Astronomer's Telegram, 13132, 1

Kasliwal, M. M., Cannella, C., Bagdasaryan, A., et al. 2019, *PASP*, 131, 038003, doi: 10.1088/1538-3873/aafbc2

Kaspi, S., Smith, P. S., Netzer, H., et al. 2000, *ApJ*, 533, 631, doi: 10.1086/308704

Kataoka, J., Reeves, J. N., Iwasawa, K., et al. 2007, Publications of the Astronomical Society of Japan, 59, 279

Kauffmann, G., Heckman, T. M., Tremonti, C., et al. 2003, *MNRAS*, 346, 1055, doi: 10.1111/j.1365-2966.2003.07154.x

Kelly, B. C., Bechtold, J., & Siemiginowska, A. 2009, in American Astronomical Society Meeting Abstracts, Vol. 213, American Astronomical Society Meeting Abstracts #213, 422.06

Kewley, L. J., Heisler, C. A., Dopita, M. A., & Lumsden, S. 2001, The Astrophysical Journal Supplement Series, 132, 37, doi: 10.1086/318944

Khachikian, E. Y., & Weedman, D. W. 1971, *ApJL*, 164, L109, doi: 10.1086/180701

Khazov, D., Yaron, O., Gal-Yam, A., et al. 2016, *ApJ*, 818, 3, doi: 10.3847/0004-637X/818/1/3

Kiewe, M., Gal-Yam, A., Arcavi, I., et al. 2012, *ApJ*, 744, 10, doi: 10.1088/0004-637X/744/1/10

Klimek, E. S., Gaskell, C. M., & Hedrick, C. H. 2004, *ApJ*, 609, 69, doi: 10.1086/420809

Kochanek, C. S. 2016, *MNRAS*, 458, 127, doi: 10.1093/mnras/stw267

Kochanek, C. S., Shappee, B. J., Stanek, K. Z., et al. 2017, *PASP*, 129, 104502, doi: 10.1088/1538-3873/aa80d9

Kollmeier, J. A., Zasowski, G., Rix, H.-W., et al. 2017, arXiv e-prints, arXiv:1711.03234. https://arxiv.org/abs/1711.03234

Komossa, S. 2002, Reviews in Modern Astronomy, 15, 27. https://arxiv.org/abs/astro-ph/0209007

Komossa, S., & Bade, N. 1999, *A&A*, 343, 775. https://arxiv.org/abs/astro-ph/9901141

Komossa, S., Zhou, H., Wang, T., et al. 2008, *ApJ*, 678, L13, doi: 10.1086/588281

Komossa, S., Zhou, H., Rau, A., et al. 2009, *ApJ*, 701, 105, doi: 10.1088/0004-637X/701/1/105

Korista, K., & Ferland, G. 1998, *ApJ*, 495, 672, doi: 10.1086/305330

Kuminski, E., & Shamir, L. 2016, The Astrophysical Journal Supplement Series, 223, 20, doi: 10.3847/0067-0049/223/2/20

LaMassa, S. M., Urry, C. M., Glikman, E., et al. 2013a, *MNRAS*, 432, 1351, doi: 10.1093/mnras/stt553

LaMassa, S. M., Urry, C. M., Cappelluti, N., et al. 2013b, *MNRAS*, 436, 3581, doi: 10.1093/mnras/stt1837

LaMassa, S. M., Cales, S., Moran, E. C., et al. 2015, *ApJ*, 800, 144, doi: 10.1088/0004-637X/800/2/144

Law, N. M., Kulkarni, S. R., Dekany, R. G., et al. 2009, Publications of the Astronomical Society of the Pacific, 121, 1395, doi: 10.1086/648598

Lawrence, A. 2018, Nature Astronomy, 2, 102, doi: 10.1038/s41550-017-0372-1

Lawrence, A., Gezari, S., Elvis, M., et al. 2012, EPJ Web of Conferences, 39, doi: 10.1051/epjconf/20123903002

Liu, H.-Y., Yuan, W., Dong, X.-B., Zhou, H., & Liu, W.-J. 2018a, *ApJS*, 235, 40, doi: 10.3847/1538-4365/aab88e

Liu, X., Dittmann, A., Shen, Y., & Jiang, L. 2018b, *ApJ*, 859, 8, doi: 10.3847/1538-4357/aabb04

Liu, Z., Li, D., Liu, H.-Y., et al. 2020, *ApJ*, 894, 93, doi: 10.3847/1538-4357/ab880f

Lohfink, A. M., Reynolds, C. S., Miller, J. M., et al. 2012, The Astrophysical Journal, 758, 67

Lunnan, R., Yan, L., Perley, D. A., et al. 2019, arXiv e-prints, arXiv:1910.02968. https://arxiv.org/abs/1910.02968

MacLeod, C. L., Ross, N. P., Lawrence, A., et al. 2016, *MNRAS*, 457, 389, doi: 10.1093/mnras/stv2997

MacLeod, C. L., Green, P. J., Anderson, S. F., et al. 2019, *ApJ*, 874, 8, doi: 10.3847/1538-4357/ab05e2

Mahabal, A., Rebbapragada, U., Walters, R., et al. 2019, Publications of the Astronomical Society of the Pacific, 131, 038002, doi: 10.1088/1538-3873/aaf3fa

Malkan, M. 1983, The Astrophysical Journal, 268, 582

Malyali, A., Rau, A., Arcodia, R., et al. 2020, The Astronomer's Telegram, 13712, 1

Malyali, A., Rau, A., Merloni, A., et al. 2021, *A&A*, 647, A9, doi: 10.1051/0004-6361/202039681

Maoz, D. 2007, *MNRAS*, 377, 1696, doi: 10.1111/j.1365-2966.2007.11735.x

Marconi, A., Axon, D. J., Maiolino, R., et al. 2008, *ApJ*, 678, 693, doi: 10.1086/529360

Martin, D. C., Fanson, J., Schiminovich, D., et al. 2005, *ApJ*, 619, L1, doi: 10.1086/426387

Marziani, P., & Sulentic, J. W. 2012, New Astronomy Reviews, 56, 49, doi: 10.1016/j.newar.2011.09.001

Masci, F. J., Laher, R. R., Rebbapragada, U. D., et al. 2017, Publications of the Astronomical Society of the Pacific, 129, 014002, doi: 10.1088/1538-3873/129/971/014002

Masci, F. J., Laher, R. R., Rusholme, B., et al. 2019, *PASP*, 131, 018003, doi: 10.1088/1538-3873/aae8ac

Mathur, S., Auchettl, K., Kochanek, C. S., et al. 2019, The Astronomer's Telegram, 13213, 1

Mathur, S., Kuraszkiewicz, J., & Czerny, B. 2001, *NA*, 6, 321, doi: 10.1016/S1384-1076(01)00058-6

Mathur, S., Denney, K. D., Gupta, A., et al. 2018, *ApJ*, 866, 123, doi: 10.3847/1538-4357/aadd91

McLure, R. J., & Dunlop, J. S. 2002, *MNRAS*, 331, 795, doi: 10.1046/j.1365-8711.2002.05236.x

Mendel, J. T., Simard, L., Palmer, M., Ellison, S. L., & Patton, D. R. 2014, *ApJS*, 210, 3, doi: 10.1088/0067-0049/210/1/3

Merloni, A., & Fabian, A. 2001, Monthly Notices of the Royal Astronomical Society, 321, 549

Merloni, A., Dwelly, T., Salvato, M., et al. 2015, *MNRAS*, 452, 69, doi: 10.1093/mnras/stv1095

Meusinger, H., Henze, M., Birkle, K., et al. 2010, *A&A*, 512, A1, doi: 10.1051/0004-6361/200913526

Miller, H. R., Ferrara, E. C., McFarland, J. P., et al. 2000, *NAR*, 44, 539, doi: 10.1016/S1387-6473(00)00094-4

Miller, J. M., Kaastra, J. S., Miller, M. C., et al. 2015, *Nature*, 526, 542, doi: 10.1038/nature15708

Miller, J. M., Zoghbi, A., Reynolds, M., et al. 2019, The Astronomer's Telegram, 13163, 1

Miniutti, G., Ponti, G., Greene, J. E., et al. 2009, *MNRAS*, 394, 443, doi: 10.1111/j.1365-2966.2008.14334.x

Molthagen, K., Bade, N., & Wendker, H. J. 1998, *A&A*, 331, 925

Moriya, T. J., Sorokina, E. I., & Chevalier, R. A. 2018, *SSRv*, 214, 59, doi: 10.1007/s11214-018-0493-6

Mullaney, J. R., Alexander, D. M., Fine, S., et al. 2013, *MNRAS*, 433, 622, doi: 10.1093/mnras/stt751

Mullaney, J. R., & Ward, M. J. 2008, *MNRAS*, 385, 53, doi: 10.1111/j.1365-2966.2007.12777.x

Murayama, T., & Taniguchi, Y. 1998a, *ApJ*, 503, L115, doi: 10.1086/311554

—. 1998b, *ApJ*, 497, L9, doi: 10.1086/311264

Nagao, T., Taniguchi, Y., & Murayama, T. 2000, *AJ*, 119, 2605, doi: 10.1086/301411

Nandra, K., George, I. M., Mushotzky, R. F., Turner, T. J., & Yaqoob, T. 1997, *ApJ*, 476, 70, doi: 10.1086/303600

Nemmen, R. S., Storchi-Bergmann, T., & Eracleous, M. 2014, *MNRAS*, 438, 2804, doi: 10.1093/mnras/stt2388

Netzer, H., Mainieri, V., Rosati, P., & Trakhtenbrot, B. 2006, *A&A*, 453, 525, doi: 10.1051/0004-6361:20054203

Netzer, H., & Trakhtenbrot, B. 2007, *ApJ*, 654, 754, doi: 10.1086/509650

Neustadt, J. M. M., Holoien, T. W. S., Kochanek, C. S., et al. 2020, *MNRAS*, 494, 2538, doi: 10.1093/mnras/staa859

Nikołajuk, M., Czerny, B., & Gurynowicz, P. 2009, *MNRAS*, 394, 2141, doi: 10.1111/j.1365-2966.2009.14478.x

Noda, H., & Done, C. 2018, *MNRAS*, 480, 3898, doi: 10.1093/mnras/sty2032

Nordin, J., Brinnel, V., van Santen, J., et al. 2019, *A&A*, 631, A147, doi: 10.1051/0004-6361/201935634

Nussbaumer, H., & Storey, P. J. 1979, *A&A*, 74, 244

O'Brien, P. T., Goad, M. R., & Gondhalekar, P. M. 1995, *MNRAS*, 275, 1125, doi: 10.1093/mnras/275.4.1125

Ofek, E. O., & Frail, D. A. 2011, *ApJ*, 737, 45, doi: 10.1088/0004-637X/737/1/45

Oknyansky, V. L., Malanchev, K. L., & Gaskell, C. M. 2018, in Revisiting Narrow-Line Seyfert 1 Galaxies and their Place in the Universe, 12. https://arxiv.org/abs/1810.08844

Oknyansky, V. L., Gaskell, C. M., Huseynov, N. A., et al. 2016, MNRAS, 000, 1. https://arxiv.org/abs/arXiv:1701.05042v5

Osterbrock, D. E. 1981, *ApJ*, 249, 462, doi: 10.1086/159306

Osterbrock, D. E., & Pogge, R. W. 1985, The Astrophysical Journal, 297, 166

Page, K. L., Schartel, N., Turner, M. J., & O'Brien, P. T. 2004, Monthly Notices of the Royal Astronomical Society, 352, 523

Palaversa, L., Gezari, S., Sesar, B., et al. 2016, *ApJ*, 819, 151, doi: 10.3847/0004-637X/819/2/151

Parker, M. L., Komossa, S., Kollatschny, W., et al. 2016, MNRAS, 461, 1927, doi: 10.1093/mnras/stw1449

Pasham, D., Gendreau, K., Arzoumanian, Z., et al. 2020, The Astronomer's Telegram, 14036, 1

Patterson, M. T., Bellm, E. C., Rusholme, B., et al. 2019, *PASP*, 131, 018001, doi: 10.1088/1538-3873/aae904

Payne, A. V., Shappee, B. J., Hinkle, J. T., et al. 2020, arXiv e-prints, arXiv:2009.03321. https://arxiv.org/abs/2009.03321

Pelat, D., Alloin, D., & Bica, E. 1987, *A&A*, 182, 9

Perley, D. A. 2019, *PASP*, 131, 084503, doi: 10.1088/1538-3873/ab215d

Pfeiffer, M., Appenzeller, I., & Wagner, S. 2000, *NAR*, 44, 547, doi: 10.1016/S1387-6473(00)00096-8

Piconcelli, E., Jimenez-Bailón, E., Guainazzi, M., et al. 2005, *A&A*, 432, 15, doi: 10.1051/0004-6361:20041621

Pogge, R. W. 2000, *NAR*, 44, 381, doi: 10.1016/S1387-6473(00)00065-8

Poole, T. S., Breeveld, A. A., Page, M. J., et al. 2008, *MNRAS*, 383, 627, doi: 10.1111/j.1365-2966.2007.12563.x

Porquet, D., Dumont, A.-M., Collin, S., & Mouchet, M. 1999, *A&A*, 341, 58

Porquet, D., Reeves, J. N., O'Brien, P., & Brinkmann, W. 2004, *A&A*, 422, 85, doi: 10.1051/0004-6361:20047108

Pounds, K. A., Done, C., & Osborne, J. P. 1995, *MNRAS*, 277, L5, doi: 10.1093/mnras/277.1.L5

Pronik, V. I., & Chuvaev, K. K. 1972, Astrophysics, 8, 112, doi: 10.1007/BF01002159

Puchnarewicz, E. M., Mason, K. O., Cordova, F. A., et al. 1992, *MNRAS*, 256, 589, doi: 10.1093/mnras/256.3.589

Rafter, S. E., Kaspi, S., Chelouche, D., et al. 2013, *ApJ*, 773, 24, doi: 10.1088/0004-637X/773/1/24

Rakshit, S., Stalin, C. S., Chand, H., & Zhang, X.-G. 2017, The Astrophysical Journal Supplement Series, 229, 39, doi: 10.3847/1538-4365/aa6971

Rau, A., Kulkarni, S. R., Law, N. M., et al. 2009, Publications of the Astronomical Society of the Pacific, 121, 1334, doi: 10.1086/605911

Rigault, M., Neill, J. D., Blagorodnova, N., et al. 2019, *A&A*, 627, A115, doi: 10.1051/0004-6361/201935344

Rodríguez-Ardila, A., Prieto, M. A., Viegas, S., & Gruenwald, R. 2006, *ApJ*, 653, 1098, doi: 10.1086/508864

Rodríguez-Ardila, A., Viegas, S. M., Pastoriza, M. G., & Prato, L. 2002, *ApJ*, 579, 214, doi: 10.1086/342840

Roming, P. W. A., Kennedy, T. E., Mason, K. O., et al. 2005, *SSRv*, 120, 95, doi: 10.1007/s11214-005-5095-4

Ross, N. P., Ford, K. E. S., Graham, M., et al. 2018, *MNRAS*, 480, 4468, doi: 10.1093/mnras/sty2002

Rowan-Robinson, M. 1977, *ApJ*, 213, 635, doi: 10.1086/155195

Ruan, J. J., Anderson, S. F., Eracleous, M., et al. 2019a, arXiv e-prints, arXiv:1903.02553. https://arxiv.org/abs/1903.02553

—. 2019b, arXiv e-prints, arXiv:1909.04676. https://arxiv.org/abs/1909.04676

Ruan, J. J., Anderson, S. F., Cales, S. L., et al. 2016, *ApJ*, 826, 188, doi: 10.3847/0004-637X/826/2/188

Rumbaugh, N., Shen, Y., Morganson, E., et al. 2018, *ApJ*, 854, 160, doi: 10.3847/1538-4357/aaa9b6

Runnoe, J. C., Cales, S., Ruan, J. J., et al. 2016, *MNRAS*, 455, 1691, doi: 10.1093/mnras/stv2385

Ryan, G., & MacFadyen, A. 2017, *ApJ*, 835, 199, doi: 10.3847/1538-4357/835/2/199

Sarzi, M., Falcón-Barroso, J., Davies, R. L., et al. 2017, GANDALF: Gas AND Absorption Line Fitting. http://ascl.net/1708.012

Saxton, C. J., Perets, H. B., & Baskin, A. 2018, *MNRAS*, 474, 3307, doi: 10.1093/mnras/stx2928

Schawinski, K., Thomas, D., Sarzi, M., et al. 2007, *MNRAS*, 382, 1415, doi: 10.1111/j.1365-2966.2007.12487.x

Schlafly, E. F., & Finkbeiner, D. P. 2011, *ApJ*, 737, 103, doi: 10.1088/0004-637X/737/2/103

Schlegel, D. J., Finkbeiner, D. P., & Davis, M. 1998, *ApJ*, 500, 525, doi: 10.1086/305772

Schmidt, R. W., & Wambsganss, J. 2010, General Relativity and Gravitation, 42, 2127, doi: 10.1007/s10714-010-0956-x

Schneider, D. P., Richards, G. T., Hall, P. B., et al. 2010, *AJ*, 139, 2360, doi: 10.1088/0004-6256/139/6/2360

Science Software Branch at STScI. 2012, PyRAF: Python alternative for IRAF. http://ascl.net/1207.011

Shappee, B. J., Prieto, J. L., Grupe, D., et al. 2014, *ApJ*, 788, 48, doi: 10.1088/0004-637X/788/1/48

Shen, Y., & Ho, L. C. 2014, *Nature*, 513, 210, doi: 10.1038/nature13712

Shen, Y., Richards, G. T., Strauss, M. A., et al. 2011, *ApJS*, 194, 45, doi: 10.1088/0067-0049/194/2/45

Sheng, Z., Wang, T., Jiang, N., et al. 2017, *ApJ*, 846, L7, doi: 10.3847/2041-8213/aa85de

Siemiginowska, A., Czerny, B., & Kostyunin, V. 1996, *ApJ*, 458, 491, doi: 10.1086/176831

Silk, J., & Rees, M. J. 1998, *A&A*, 331, L1. https://arxiv.org/abs/astro-ph/9801013

Singh, K., Garmire, G., & Nousek, J. 1985, The Astrophysical Journal, 297, 633

Singh, K. P., Garmire, G. P., & Nousek, J. 1985, *ApJ*, 297, 633, doi: 10.1086/163560

Singh, R., van de Ven, G., Jahnke, K., et al. 2013, *A&A*, 558, A43, doi: 10.1051/0004-6361/201322062

Smartt, S. J., Smith, K. W., McBrien, O., et al. 2019, Transient Name Server AstroNote, 33, 1

Smith, K. L., Mushotzky, R. F., Boyd, P. T., et al. 2018, *ApJ*, 857, 141, doi: 10.3847/1538-4357/aab88d

Smith, N., Silverman, J. M., Chornock, R., et al. 2009, *ApJ*, 695, 1334, doi: 10.1088/0004-637X/695/2/1334

Sollerman, J., Taddia, F., Arcavi, I., et al. 2019, *A&A*, 621, A30, doi: 10.1051/0004-6361/201833689

Sollerman, J., Fransson, C., Barbarino, C., et al. 2020, arXiv e-prints, arXiv:2009.04154. https://arxiv.org/abs/2009.04154

Soumagnac, M. T., & Ofek, E. O. 2018, *PASP*, 130, 075002, doi: 10.1088/1538-3873/aac410

Steffen, A. T., Strateva, I., Brandt, W. N., et al. 2006, *AJ*, 131, 2826, doi: 10.1086/503627

Stein, R., van Velzen, S., Kowalski, M., et al. 2020, arXiv e-prints, arXiv:2005.05340. https://arxiv.org/abs/2005.05340

Stephens, S. A. 1989, *AJ*, 97, 10, doi: 10.1086/114953

Stern, D., Assef, R. J., Benford, D. J., et al. 2012, *ApJ*, 753, 30, doi: 10.1088/0004-637X/753/1/30

Stern, D., McKernan, B., Graham, M. J., et al. 2018, *ApJ*, 864, 27, doi: 10.3847/1538-4357/aac726

Stern, J., & Laor, A. 2012, *MNRAS*, 423, 600, doi: 10.1111/j.1365-2966.2012.20901.x

Storchi-Bergmann, T., Baldwin, J. A., & Wilson, A. S. 1993, *ApJL*, 410, L11, doi: 10.1086/186867

Strüder, L., Briel, U., Dennerl, K., et al. 2001, Astronomy & Astrophysics, 365, L18

Tadhunter, C., Spence, R., Rose, M., Mullaney, J., & Crowther, P. 2017, Nature Astronomy, 1, 0061, doi: 10.1038/s41550-017-0061

Tananbaum, H., Avni, Y., Branduardi, G., et al. 1979, *ApJL*, 234, L9, doi: 10.1086/183100

Terlevich, R., Tenorio-Tagle, G., Franco, J., & Melnick, J. 1992, *MNRAS*, 255, 713, doi: 10.1093/mnras/255.4.713

Thomas, D., Steele, O., Maraston, C., et al. 2013, *MNRAS*, 431, 1383, doi: 10.1093/mnras/stt261

Tonry, J. L., Denneau, L., Heinze, A. N., et al. 2018, Publications of the Astronomical Society of the Pacific, 130, 064505, doi: 10.1088/1538-3873/aabadf

Trakhtenbrot, B., Arcavi, I., Ricci, C., & Burke, J. 2020, Transient Name Server AstroNote, 105, 1

Trakhtenbrot, B., Arcavi, I., Ricci, C., et al. 2019a, Nature Astronomy, 3, 242, doi: 10.1038/s41550-018-0661-3

Trakhtenbrot, B., Arcavi, I., MacLeod, C. L., et al. 2019b, arXiv e-prints, arXiv:1903.11084. https://arxiv.org/abs/1903.11084

Tremaine, S., Gebhardt, K., Bender, R., et al. 2002, *ApJ*, 574, 740, doi: 10.1086/341002

Turner, T., & Pounds, K. 1989, Monthly Notices of the Royal Astronomical Society, 240, 833

Urry, C. M., & Padovani, P. 1995, Publications of the Astronomical Society of the Pacific, 107, 803, doi: 10.1086/133630

Uttley, P., Cackett, E. M., Fabian, A. C., Kara, E., & Wilkins, D. R. 2014, *Astronomy and Astrophysics Reviews*, 22, 72, doi: 10.1007/s00159-014-0072-0

Uttley, P., McHardy, I. M., Papadakis, I. E., Guainazzi, M., & Fruscione, A. 1999, *MNRAS*, 307, L6, doi: 10.1046/j.1365-8711.1999.02801.x

van Velzen, S., Holoien, T. W. S., Onori, F., Hung, T., & Arcavi, I. 2020a, arXiv e-prints, arXiv:2008.05461. https://arxiv.org/abs/2008.05461

van Velzen, S., Mendez, A. J., Krolik, J. H., & Gorjian, V. 2016, *ApJ*, 829, 19, doi: 10.3847/0004-637X/829/1/19

van Velzen, S., Farrar, G. R., Gezari, S., et al. 2011, *ApJ*, 741, 73, doi: 10.1088/0004-637X/741/2/73

van Velzen, S., Gezari, S., Cenko, S. B., et al. 2019, *ApJ*, 872, 198, doi: 10.3847/1538-4357/aafe0c

van Velzen, S., Gezari, S., Hammerstein, E., et al. 2020b, arXiv e-prints, arXiv:2001.01409. https://arxiv.org/abs/2001.01409

Vaughan, S., & Edelson, R. 2001, *ApJ*, 548, 694, doi: 10.1086/319028

Véron-Cetty, M. P., & Véron, P. 2000, *Astronomy and Astrophysics Reviews*, 10, 81, doi: 10.1007/s001590000006

Véron-Cetty, M.-P., Véron, P., & Gonçalves, A. C. 2001, *A&A*, 372, 730, doi: 10.1051/0004-6361:20010489

Voges, W., Aschenbach, B., Boller, T., et al. 1999, *A&A*, 349, 389. https://arxiv.org/abs/astro-ph/9909315

Wang, T., Brinkmann, W., & Bergeron, J. 1996, *A&A*, 309, 81

Wang, T.-G., Zhou, H.-Y., Komossa, S., et al. 2012, *ApJ*, 749, 115, doi: 10.1088/0004-637X/749/2/115

Wang, T.-G., Zhou, H.-Y., Wang, L.-F., Lu, H.-L., & Xu, D. 2011, *ApJ*, 740, 85, doi: 10.1088/0004-637X/740/2/85

Wevers, T., Pasham, D. R., van Velzen, S., et al. 2019, *MNRAS*, 488, 4816, doi: 10.1093/mnras/stz1976

—. 2021, arXiv e-prints, arXiv:2101.04692. https://arxiv.org/abs/2101.04692

Wilkins, D. R., Gallo, L. C., Grupe, D., et al. 2015, *MNRAS*, 454, 4440, doi: 10.1093/mnras/stv2130

Winkler, H. 1992, *MNRAS*, 257, 677, doi: 10.1093/mnras/257.4.677

Wright, E. L., Eisenhardt, P. R. M., Mainzer, A. K., et al. 2010, *AJ*, 140, 1868, doi: 10.1088/0004-6256/140/6/1868

XMM-SSC. 2018, VizieR Online Data Catalog, IX/53

Xu, D., Komossa, S., Zhou, H., et al. 2012, *AJ*, 143, 83, doi: 10.1088/0004-6256/143/4/83

Yan, L., Wang, T., Jiang, N., et al. 2019, *ApJ*, 874, 44, doi: 10.3847/1538-4357/ab074b

Yan, L., Perley, D., Schulze, S., et al. 2020, arXiv e-prints, arXiv:2006.13758. https://arxiv.org/abs/2006.13758

Zhou, H., Wang, T., Yuan, W., et al. 2006, *ApJS*, 166, 128, doi: 10.1086/504869